TECHNISCHE UNIVERSITÄT MÜNCHEN

Lehrstuhl für Methodik der Fernerkundung

Burst-Mode Wide-Swath SAR Interferometry for Solid Earth Monitoring

Néstor YAGÜE MARTÍNEZ

Vollständiger Abdruck der von der Ingenieurfakultät Bau Geo Umwelt der Technischen Universität München zur Erlangung des akademischen Grades eines Doktor-Ingenieurs (Dr.-Ing.) genehmigten Dissertation.

Vorsitzender: Prof. Dr.-Ing. Uwe Stilla

Prüfer der Dissertation:

1. Hon.-Prof. Dr. rer. nat. Michael Eineder
2. Prof. Dr. Ing. habil. Richard H. G. Bamler
3. Prof. Andrew Hooper
   (schrifftliche Beurteilung)
   Prof. Dr.-Ing. habil. Alberto Moreira
   (mündliche Prüfung)

Die Dissertation wurde am 21.10.2019 bei der Technischen Universität München eingereicht und durch die Ingenieurfakultät Bau Geo Umwelt am 04.12.2019 angenommen.

Abstract

This work addresses the generation of large area maps of ground deformation originated by dynamic processes of the Earth using spaceborne Synthetic Aperture Radar (SAR) systems. The main focus is put on the development of new interferometric processing techniques for SAR data and on the proposal, design, experimental implementation and demonstration with TerraSAR-X of an acquisition mode with wide-swath capabilities, able to improve the accuracy of the measurements.

When designing a SAR system for the study of Earth's dynamic processes, the consideration of spatial sampling, coverage and temporal sampling are of fundamental importance. The temporal sampling can be improved by adjusting the orbital design and/or employing multiple platforms orbiting in such a configuration that the repetition cycle is reduced. Regarding the spatial aspect, high azimuth resolution and wide swath are terms usually in conflict in the design of a SAR system. Keeping in mind that the interest of the scientific community lies in achieving a reduced temporal sampling, the conception of a SAR system should be motivated by its coverage in order to achieve global systematic observations, and by a proper sensitivity in the retrieval of ground deformation measurements rather than achieving the best azimuth resolution.

Since the development of the first SAR spaceborne SAR systems, the StripMap mode has represented the baseline for numerous spaceborne SAR missions. Geoscientists have exploited this mode to generate 2-D deformation maps by combining interferometric and correlation techniques. This approach has been applied in this work to map the M_w9.0 Tohoku-Oki Earthquake occurred in 2011 in Japan by employing TerraSAR-X StripMap (30 km $\times$ 50 km) pairs distributed over the Japanese archipelago. The estimation of the displacement in the along-track direction is an added-value with respect to the use of pure interferometric techniques, only sensitive to displacements in the radar line of sight. In this direction, cross-correlation provides a poorer performance than interferometry, but on the other hand, the measurements are not affected by wrapping, therefore becoming of great interest in case of strong deformation, for which the unwrapping of the phase can become impossible due to phase aliasing. Geophysical corrections, specifically atmospheric disturbances and the consideration of solid Earth tides, have been applied and the results validated against GPS, achieving divergences below 15 cm for regions characterized by vegetation, with rather high temporal baselines - in the order of 100 days. Under this challenging circumstances, the achieved accuracy is still suitable to map such strong events. However, better results are expected for short temporal baseline and lower frequency systems (C- or L- band, more suitable for geophysical applications). For SAR missions acquiring routinely and globally, e.g., Envisat or ERS, the temporal sampling (approx. 35 days, imposed by the 100 km swath) is however too coarse to catch some events. Therefore wide-swath modes become necessary.

The terrain observation by progressive scans (TOPS) mode has been recently implemented as the baseline acquisition mode of the European Sentinel-1 System, providing a swath of 250 km at approximately 20 m resolution. TOPS achieves wide swath coverage by recording bursts of echoes, which allow to reduce the synthetic aperture time. The latter allows switching cyclically the beam in elevation, as with ScanSAR mode, but TOPS additionally performs a steering of the antenna in azimuth in order to equalize the signal-to-noise ratio (SNR) and azimuth ambiguitiy-to-signal ratio (AASR) , i.e., avoiding the so-called "scalloping" effect. The TOPS mode requires special techniques for the interferometric processing of the data, especially regarding accurate coregistration. The

interferometric processing algorithms for handling pairs of Sentinel-1 TOPS data (Interferometric Wide Swath mode) are provided in this work. The coregistration approach exploits the SAR data for the retrieval of the required fine azimuth shifts. Since the performance of the method depends on the coherence, it can become an issue when working with very long time series, as temporal decorrelation dominates. A method for coregistering time series of Sentinel-1 TOPS data exploiting all images of the stack is proposed in this work. The technique is based on the least squares method and validated employing Sentinel-1 data.

The original TOPS mode achieves wide swath at the expense of a degraded azimuth resolution, with a negative impact on the accuracy of the deformation measurements in this direction. In the last contribution of this dissertation, a new mode is proposed which achieves wide swath (employing bursts of data and a steering of the antenna in azimuth, as TOPS) but exploiting spectral diversity techniques, in order to mitigate the poor accuracy on the along-track deformation retrieval. This novel mode, called *2-look TOPS*, is able to record two separated bands of the Doppler spectrum for each target on ground. In this way a higher sensitivity of the azimuth measurements can be obtained when compared to the achievable sensitivity exploiting the available bandwidth of a conventional 1-look system. Taking into account that Earth Observation satellites orbit in quasi-polar configurations, a high sensitivity to the ground deformation in the North-South direction can be obtained. A discussion on the optimization of the scanning timeline design for an azimuth-sensitivity driven design rather than a classical resolution-driven design is provided. With an optimized scanning timeline it is even possible to obtain higher sensitivities than with StripMap to the motion in the azimuthal direction. The 2-look TOPS mode represents the most evolved burst-mode, in terms of equalized azimuth ambiguities and SNR and better sensitivity to the azimuth motion, which provides at the same time wide swath. A demonstration with experimental TerraSAR-X data for mapping fast displacements employing pairs of images (Petermann Glacier, Greenland) and for the mapping of slow displacements with time series covering two years of postseismic deformation over the Hoshab fault, Pakistan, is provided, making evident the high potential of this mode.

Kurzfassung

Diese Arbeit befasst sich mit der Erstellung großflächiger Karten von Bodenverformungen, welche durch dynamische Prozesse der Erde entstanden sind, durch das Verwenden von raumgestützten Radarsystemen mit synthetischer Apertur (SAR). Der Schwerpunkt der Arbeit liegt auf der Entwicklung von neuen interferometrischen Prozessierungsmethoden für SAR Daten und die Ausarbeitung eines neuen Modus mit großer Streifenbreite. Es wurde anhand von TerraSAR-X Daten demonstriert, dass durch diesen Modus eine verbesserte Genauigkeit der Messungen erreicht werden kann.

Wenn ein SAR System für die Untersuchung der dynamischen Prozesse der Erde entwickelt wird, ist die Berücksichtigung der örtlichen und zeitlichen Abtastung und die Abdeckung der Erde von fundamentaler Bedeutung. Die zeitliche Abtastung kann verbessert werden durch geeignete Entwicklung der Umlaufbahn und/oder die Verwendung von mehreren Plattformen, die die Erde in solch einer Art und Weise umrunden, dass der Wiederholungzyklus reduziert wird. Beim Design der örtlichen Abdeckung steht normalweise der Bedarf nach einer hohen Azimutauflösung im Konflikt mit dem Bedarf einer hohen Streifenbreite.

Seit der Entwicklung des ersten raumgestützten SAR Systems, war der sogenannte StripMap Modus der Grundmodus für etliche SAR Missionen. Geowissenschaftler haben diesen Modus verwendet, um 2D-Verformungskarten zu erzeugen, indem sie Interferometrie- und Korrelationstechniken kombiniert haben. Dieser Ansatz wurde in dieser Arbeit verwendet, um das Erdbeben von Tohoku-Oki, das in 2011 in Japan stattfand, zu kartieren. Hierzu wurden Aufnahmen von TerraSAR-X mit dem StripMap Modus (30 km $\times$ 50 km) von den japanischen Inselgruppen verwendet. Die Schätzung des Versatzes in der Vorwärtsrichtung hat einen zusätzlichen Mehrwert im Vergleich zu Interferometrietechniken, die nur sensitiv zu Verschiebungen in der Blickrichtung sind. Bei dieser Richtung hat die Kreuzkorrelation eine schlechtere Genauigkeit als bei Interferometrie, aber sie ist nicht beeinträchtigt von Phasenmehrdeutigkeiten, was vor allem bei starken Deformationen ein Problem ist. Geophysikalische Korrekturen, insbesondere atmosphärische Störungen und die Berücksichtigung der Gezeiten, wurden angewandt und die Ergebnisse wurden mit GPS-Messungen verglichen. Der Vergleich zeigte Divergenzen von unter 15 cm, welche aber in erster Linie in Gegenden mit starkem Bewuchs auftraten. Durch einen Versatz von um die 100 Tage zwischen den einzelnen Aufnahmen, ist die erreichte Genauigkeit immer noch hinreichend, um starke Erdbeben zu kartieren. Es werden jedoch bessere Ergebnisse für kürzer versetzte Aufnahmen bei niedrigeren Frequenzen erwartet (C- oder L- Band Systeme sind besser geeignet für geophysikalische Anwendungen). Bei SAR Missionen, die routinemäßig und global Daten aufnehmen, wie z.B. Envisat oder ERS, ist die zeitliche Abtastung zu groß, um einige Ereignisse zu erfassen. Daher ist es wichtig einen Modus mit einer großen Streifenbreite zu benutzen.

Der sogenannte „Terrain Observation by Progressive Scans“ (TOPS) Modus wurde als Standardmodus bei dem europäischem Sentinel-1 System implementiert, womit eine Streifenbreite von 250 km und eine Auflösung von 20 m erreicht werden konnte. TOPS erreicht große Streifenbreiten indem es gebündelt Echos aufnimmt, wodurch die synthetische Aperturzeit reduziert werden kann. TOPS ändert die Richtung der Keule in Elevation in einer zyklischen Abfolge, wie bei ScanSAR, zusätzlich wird die Keule aber auch in Azimut geschwenkt, um das Signal-zu-Rauschverhältnis (SNR) und die Azimutmehrdeutigkeiten (AASR) auszugleichen, um den sogenannten „scalloping“ Effekt zu vermeiden. Beim TOPS werden spezielle Techniken für die interferometrische Prozessierung benötigt, insbesondere

in Bezug auf die genaue Koregistrierung. In dieser Arbeit wurden Algorithmen entwickelt zum Verarbeiten von Sentinel-1 TOPS Datenpaaren (für den sogenannten „Interferometric Wide Swath Mode“). Der Koregistrierungsansatz nutzt die SAR Daten zum genauen Schätzen der Azimutverschiebung. Da die leistungsfähigkeit diese Methode von der Kohärenz abhängt, können Probleme auftreten, wenn mit langen Zeitreihen gearbeitet wird, wo Dekorrelation auftritt. In dieser Arbeit wird daher ein Ansatz vorgeschlagen, der alle Bilder des Stapels zur Koregistrierung verwendet. Diese Technik basiert auf der Least-Square-Methode und wurde mit Sentinel-1 Daten validiert.

Der originale TOPS Modus erreicht große Streifenbreiten auf Kosten von verminderter Azimutauflösung, das sich auf die Genauigkeit der Verformungsmessungen in dieser Richtung auswirkt. Im letzten Beitrag dieser Arbeit wird ein neuer Modus vorgestellt, welcher große Streifenbreiten erreicht (durch die Bündelung der Daten und das Schwenken der Antenne in Azimut wie bei TOPS) aber die spektrale Diversität wird ausgenutzt, um die Genauigkeit der Verformungsschätzung in der Vorwärtsrichtung zu verbessern. Dieser neue Modus, welcher als „2-look TOPS“ bezeichnet wird, nimmt zwei getrennte Bänder im Dopplerspektrum von jedem Ziel auf. Auf diese Arte kann eine höhere Empfindlichkeit der Azimutmessung erreicht werden im Vergleich zu einem normalen TOPS Modus bei gleichbleibender Bandbreite. Unter Berücksichtigung, dass die Erdbeobachtungssatelliten sich auf quasi Polarumlaufbahnen befinden, kann somit eine höhere Empfindlichkeit der Bodenvervormungsmessung in der Nord-Süd-Richtung erreicht werden. Optimierungsmöglichkeiten des Zeitplans für das sogenannte Scanning zur Verbesserung der Verformungsmessung wird erörtert. Mit einem optimierten Zeitplan kann man sogar eine bessere Genauigkeit als mit einem StripMap Modus erreichen. Der „2-look TOPS“ Modus ist der am meisten entwickelte Burst-Modus in Bezug auf Ausgeglichenheit der Azimutmehrdeutigkeiten, dem SNR und der Empfindlichkeit auf Azimutbewegung bei gleichzeitig großer Streifenbreite. Dieser Modus wurde auch mit TerraSAR-X Daten getestet, um schnelle Verschiebungen anhand von Bildpaaren (Petermann Gletscher, Grönland) und langsame Verformungen mit Zeitreihen über zwei Jahre von der postseismischen Verformung der Hoshab-Bruchstelle in Pakistan zu messen. Das hohe Potenzial dieses Moduses wurde hierbei demonstriert.

Acknowledgements

Pursuing my PhD concurrently with my position as research scientist at DLR has been a long journey full of experiences. Writing this thesis was a lonely endeavor but I want to take a moment to thank all the people who helped me along the way.

For my research activities related to my doctorate, I would like to express my most sincere gratitude to my advisors at the Remote Sensing Technology Institute (IMF) Prof. Dr. Michael Eineder and Prof. Dr. Richard Bamler. My most sincere gratitude during the second half of my PhD is for my advisors at the Microwaves and Radar Institute (HR) Dr. Pau Prats and Prof. Dr. Alberto Moreira, who encouraged me to continue my PhD path from the very first moment I joined their institute. I am very thankful to all for their continuous and insightful support, useful discussions and their careful revision of this thesis. Their vast knowledge in the field of synthetic aperture radar (SAR) and SAR interferometry (InSAR) has been crucial for the fulfillment of this work. I would also like to thank Prof. Andrew Hooper from the University of Leeds for accepting to be my external reviewer.

Special thanks to my colleague Alessandro Parizzi, who was able to simplify the complexity of the SAR and InSAR concepts and had always time to discuss these topics at my early times at DLR. I appreciate his way of explaining technical concepts, as well as his support with his sense of humor. I also thank my colleagues Fernando Rodríguez González, for very fruitful discussions about almost every technical topic, and Ramon Brcic for sharing patiently his signal processing knowledge with me.

There are many colleagues and friends at IMF and HR with whom I have shared very nice moments and thank for their company: Marie Lachaise, Xiao Ying Cong, Wael Abdel Jaber, Sergi Duque, Giorgio Gomba, Francesco De Zan, Daniele Cerra, Silke Kerkhoff, Cristian Rossi, Nico Adam, Christian Minet, Helko Breit, Bettina Bierkampf, Thomas Fritz, Ulrich Balss, Werner Liebhart, Matteo Soccorsi, Antonio Repucci, Yuanyuan Wang, Octavio Ponce, Muriel Pinheiro, Toni Martínez del Hoyo, Marc Rodríguez, Anton Heister, Alejandro Linde Cerezo, Michelangelo Villano, Paola Rizzoli, Paolo Sica, Jalal Matar, Nida Sakar, Daniela Borla Tridon, Felipe Queiroz de Almeida, Paolo Valdo, María José Sanjuán Ferrer, Maron Schlemon, Mariantonietta Zonno, Matteo Nannini, José Luis Bueso, Carolina González, Chris Wecklich, Sushil Joshi, Alberto Alonso, Georg Fischer, Changhyun Choi, Jun Su Kim, Michele Martone, Elisa Fagiolini, Nicola Gollin, Rolf Scheiber, Ryo Natsuaki and many more who crossed along the long way. I thank also my colleague Valeria Gracheva for taking her precious time to translate the abstract of this thesis into german. Finally I would like to express my warmest gratitude to my colleague Víctor Cazcarra for our interesting talks during the 4 pm *Obst-Runde*.

I would also like to thank Valérie Cayol and Jean-Luc Froger from the University of Clermont-Auvergne for inviting me to the MDIS-Form@Ter workshop in Besse en Chandesse in 2017. I had the chance to attend talks from geoscientists about the extraction of the physical signal and its geophysical interpretation for seismic and volcanic applications. The night hike around the lake Pavin gave me moreover the opportunity to swap out my remote sensing activities in the office for an adventure in the analog world.

Finally I want to express my unconditional gratitude and love to my parents, Pascual Yagüe Soriano and Adelina Martínez Rodríguez, who have been at any moment available despite of the distance.

Oberpfaffenhofen, 14 October 2019.

Contents

List of Abbreviations

1-D	one-dimensional
2-D	two-dimensional
3-D	three-dimensional
AAP	**A**zimuth **A**ntenna **P**attern
AASR	**A**zimuth **A**mbiguity-to-**S**ignal **R**atio
APS	**A**tmospheric **P**hase **S**creen
ASR	**A**mbiguity-to-**S**ignal-**R**atio
ATI	**A**long-**T**rack **I**nterferometry
AWGN	**A**dditive **W**hite **G**aussian **N**oise
BiDi	**Bi** **Di**rectional
CCC	**C**oherent **C**ross **C**orrelation
DEM	**D**igital **E**levation **M**odel
DFT	**D**iscrete **F**ourier **T**ransform
DInSAR	**D**ifferential **SAR** **In**terferometry
DPC	**D**isplaced **P**hase **C**enter
DLR	German Aerospace Center
ECMWF	**E**uropean **C**entre for **M**edium-**R**ange **W**eather **F**orecast
Envisat	**Envi**ronmental **sat**ellite
ERS	**E**uropean **R**emote **S**ensing **S**atellites
ESA	**E**uropean **S**pace **A**gency
ESD	**E**nhanced **S**pectral **D**iversity
FFT	**F**ast **F**ourier **T**ransform
FM	**F**requency **M**odulation
GIMP	**G**reenland **I**ce **M**apping **P**roject
GL	**G**rating **L**obe
GNSS	**G**lobal **N**avigation **S**atellite **S**ystem
GPS	**G**lobal **P**ositioning **S**ystem
HRWS	**H**igh-**R**esolution **W**ide-**S**wath
HCRB	**H**ybrid **C**ramér-**R**ao **B**ound
ICC	**I**ncoherent **C**ross **C**orrelation
IRF	**I**mpulse **R**esponse **F**unction
InSAR	**SAR** **In**terferometry
ISLR	**I**ntegrated **S**ide**l**obe **R**atio
IW	**I**nterferometric **W**ide
LEO	**L**ow **E**arth **O**rbit
LO	**L**ocal **O**scillator
LOS	**L**ine **O**f **S**ight
MAI	**M**ultiple **A**perture **I**nterferometry
ML	**M**ain **L**obe
NASA	**N**ational **A**eronautics and **S**pace **A**dministration
NESZ	**N**oise **E**quivalent **S**igma **Z**ero
OT	**O**ffset **T**racking
PBW	**P**rocessed Doppler **B**and**w**idth

PCC	**P**earson **C**orrelation **C**oefficient
PDF	**P**robability **D**ensity **F**unction
PRF	**P**ulse **R**epetition **F**requency
PL	**P**hase **L**inking
PRI	**P**ulse **R**epetition **I**nterval
PSLR	**P**eak **S**ide**l**obe **R**atio
PSI	**P**ersistent **S**AR **I**nterferometry
RADAR	**Ra**dio **D**etection **a**nd **R**anging
RASR	**R**ange **A**mbiguity-to-**S**ignal **R**atio
RX	**R**eceive
S1	**S**entinel-**1**
SAR	**S**ynthetic **A**perture **R**adar
SBAS	**S**mall **Ba**seline **S**ubset
SBI	**S**plit **B**andwidth **I**nterferometry
SD	**S**pectral **D**iversity
SLC	**S**ingle-**L**ook **C**omplex
SNR	**S**ignal-to-**N**oise **R**atio
SPECAN	**Spec**tral **An**alysis
SRTM	**S**huttle **R**adar **T**opography **M**ission
ST	**S**peckle **T**racking
TOPS	**T**errain **O**bservation by **P**rogressive **S**cans
TRM	**T**ransmit / **R**eceive **M**odule
TX	**T**ransmit
TZDS	**T**otal **Z**ero **D**oppler **S**teering
WLS	**W**eighted **L**east **S**quares
ZP	**Z**ero **P**adding

To my parents.

Chapter 1

Introduction

The developments in the last years in the field of remote sensing with synthetic aperture radar[1] (SAR) systems have allowed the establishment of this technology as a reference for the monitoring of Earth's dynamic processes (Ulaby et al., 2014, Moreira et al., 2013). A distinctive feature of SAR systems is their ability to acquire images independently of the sunlight illumination, thanks to the employment of an active instrument. The use of microwaves, usually in the range from P-band (300 MHz - 1 GHz) to K_a-band (27 - 47 GHz) enables moreover its operation in the presence of clouds or fog, since microwaves can propagate through water microdroplets.

The coherent nature of the radar system allows to form 2-D high resolution complex images, by installing the radar instrument on a moving platform, typically an aircraft or a satellite. Assuming stationarity of the illuminated scene, a large antenna can be synthesized by combining coherently the received echoes at the different positions of the platform. This is the working principle of SAR, engineered by the American mathematician Carl Atwood Wiley (Wiley, 1985) in the 50s and patented in 1965 (Love, 1985).

A phase-preserving SAR processing enables the exploitation of the phase of the complex values of the reflectivity. The phase carries information related to the backscattering properties of the illuminated object towards the sensor but also information related to the electromagnetic travel path between both. By combining two SAR acquisitions interferometrically, i.e., performing the phase difference between them, the phase contribution that characterizes the scatterer cancels out and information related to the differential path delay becomes available. This is the fundamental principle of SAR interferometry (Bamler and Hartl, 1998, Rosen et al., 2000), abbreviated as InSAR.

InSAR techniques have become a very powerful instrument for Earth Observation related applications, e.g., the generation of digital elevation models (DEM) of the terrain. Moreover, systematic acquisitions over time allow to monitor deformation of the Earth's crust with high accuracy. An alternative to the use of interferometry is the imaging geodesy concept (Eineder et al., 2011), which is able to obtain pixel location accuracies of a few centimeter.

Data analyses with stacks of acquisitions reach accuracies of the Earth's surface deformation in the millimeter range. First demonstrations were done over urban areas or regions characterized by scatterers with long-time coherence properties, known as permanent scatterers interferometry (PSI) (Ferretti et al., 2001). The analysis of time series in order to measure low-rate deformations has been exploited within a wide range of applications related to the dynamic processes of the Earth, including earthquakes, volcanoes (Hooper et

[1] Radar is an acronym for "radio detection and ranging"

al., 2004), tectonic strain and landslides. Since InSAR provides measurements sensitive to ground displacement, it can for instance determine the particular fault that ruptured during an earthquake. The determination of the fault slip aids the calculation of stress transfer onto surrounding faults, identifying the parts of the fault system that are approaching failure. Moreover since InSAR can also map small displacements, allowing the measurement of, e.g., interseismic strain, the detection of unmapped faults becomes possible (Elliott et al., 2016).

The generation of global strain maps requires the accurate measurement of 3-D ground deformation, in order to be able to perform a full geophysical inversion. Traditionally this has been done by deploying networks of global navigation satellite system (GNSS) stations (typically the global positioning system, GPS) over the area of interest. As a consequence, the spatial resolution is constrained by the network itself. Earth Observation remote sensing SAR satellites allow to obtain high spatial resolution; the achievement of short temporal sampling can be obtained by adjusting the orbital satellite design and/or employing multiple platforms, orbiting in such a configuration that the repetition cycle is reduced. Short repetition cycles require wide-swath capabilities in order to systematically map the whole landmass of the Earth. Fig. 1.1 shows a generalized world stress map generated based on a global compilation of information on the crustal present-day stress field (Heidbach et al., 2018), which indicates the necessity for global coverage of the whole landmass of the Earth.

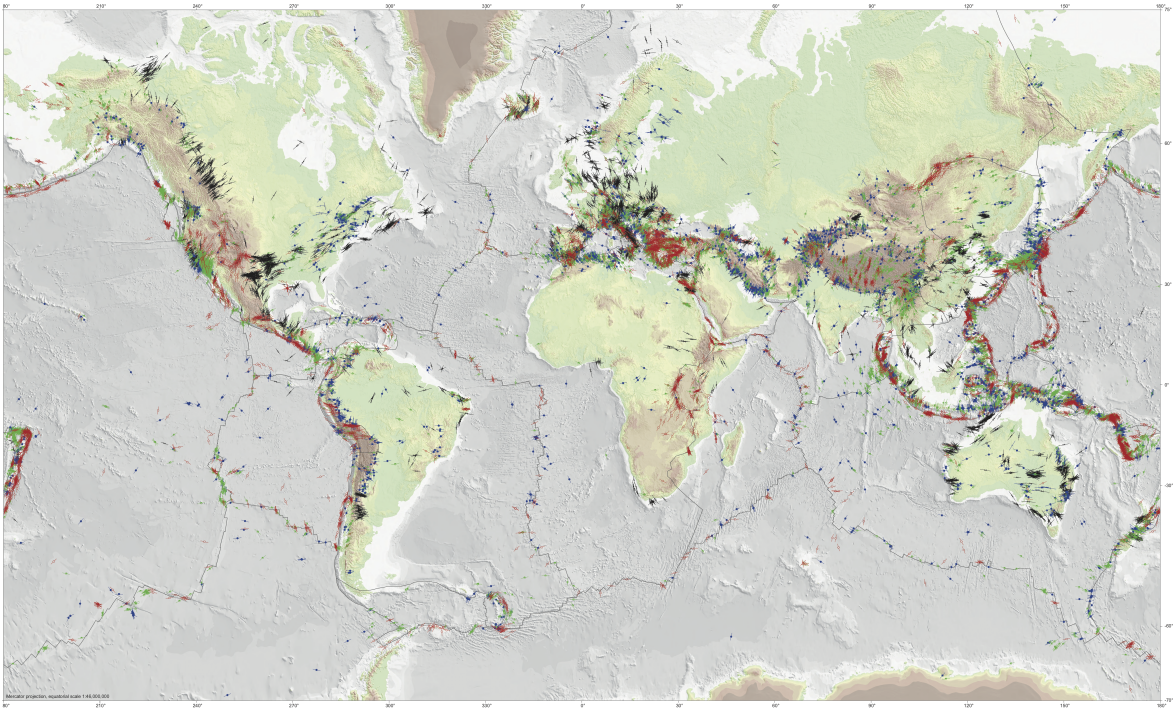

FIGURE 1.1: A generalized world stress map. Lines show the orientation of the maximum horizontal stress. The tectonic regimes – normal faulting (red), strike–slip faulting (green) and thrust faulting (blue) is shown. Source: Heidbach et al., 2016, available on-line at http://www.world-stress-map.org.)

The use of interferometric techniques exploiting spaceborne SAR data allows obtaining 3-D deformation maps by combining acquisitions in ascending and descending geometry (Wright et al., 2004). However, due to the quasi-polar satellite orbits, the sensitivity to the North-South (N-S) direction remains low, since the radar provides measurements in the line-of-sight direction, almost perpendicular to the N-S direction. In order to enhance the sensitivity in this direction, speckle tracking (ST) techniques can be employed, which

provide measurements in the along-track direction. The performance of this technique is, however, dependent on the image resolution, therefore poor performances are expected for mid-resolution acquisition modes.

A prominent example of wide-coverage mode is the terrain observation by progressive scanning (TOPS), an interferometric capable mid-resolution mode, evolution of ScanSAR, with enhanced imaging performance parameters. TOPS is the baseline acquisition mode over land of the ESA's Sentinel-1 mission. Sentinel-1 operates with two C-band satellites, launched in 2014 and 2016, that jointly achieve a six-day repetition cycle, allowing for a great number of observations and rapid detection of deformation. The open data policy of Sentinel-1 along with its wide-swath capabilities has opened a golden age for the remote sensing of the Earth's crust deformation.

1.1 Research scope

The monitoring of geophysical processes of the Earth requires the generation of 3-D ground deformation estimations at short temporal sampling intervals. This thesis aims to *develop and consolidate methods for the interferometric processing of image pairs of wide-swath TOPS data, the coregistration of time series, and the design of a novel acquisition mode able to provide wide-swath capabilities and accurate ground deformation estimates both in along- and across-track directions*.

1.2 Structure

This dissertation is conceived following a publication-based research (cumulative PhD). The dissertation begins with a review of state-of-the-art SAR techniques, interferometric processing and mutual shift estimation algorithms, followed by a summary of four peer-reviewed papers, included in the Appendix.

Fundamentals and state of the art

Chapter 2 presents fundamental concepts on the SAR acquisition geometry, the SAR principle to obtain high resolution in the along-track direction and the basic StripMap acquisition mode. Some aspects related to SAR imaging, namely the ambiguities in azimuth and range direction are summarized. An important issue to achieve wide swath is the consideration of some timing constraints, namely blind ranges, related to the use of a single antenna to transmit and receive, and echoes coming from the nadir direction, which can mask out the signal of interest. The two wide-swath modes ScanSAR and TOPS, based on acquisition by means of bursts of echoes are reviewed. The second part of the fundamentals is a review of the interferometric SAR techniques. The exploitation of phase differences among acquisitions can be used for topography mapping or ground deformation monitoring. Finally the procedures to estimate mutual shift between images, either employing cross-correlation techniques, or by means of spectrum-based approaches, are provided.

2-D ground deformation estimation through correlation techniques

Chapter 3 provides the methodology to apply correlation techniques in order to derive 2-D, i.e., in the slant-range plane, ground deformation maps from StripMap images. Geophysical corrections due to the turbulent troposphere, using numerical weather model (NWM) data, and solid Earth tides are performed in order to validate the measurements against GPS data. The study case corresponds to the 2011 Tohoku-Oki Earthquake, Japan. A total of nine TerraSAR-X co-seismic interferometric acquisitions in StripMap mode, affected by strong decorrelation effects, have been evaluated, which provide 2-D accuracies with a

standard deviation below 15 cm, when compared to GPS.

Sentinel-1 TOPS InSAR processing

Chapter 4 deals with the interferometric processing of pairs of Sentinel-1 TOPS acquisitions, providing a concise and robust methodology. Specifically, the spectral characteristics, taking into account the azimuth antenna steering, the use of deramping functions, burst synchronization requirements, coregistration aspects, spectral shift filtering, interferogram formation and first interferometric results are provided. A special focus is given to the stringent azimuth coregistration requirement along with the methodology based on enhanced spectral diversity (ESD) to be applied to Sentinel-1 data.

Joint-coregistration of stacks of Sentinel-1 TOPS acquisitions

The accuracy of the azimuth fine coregistration for TOPS acquisitions, based on the ESD estimator, suffers from decorrelation effects, which might be a problem when working with long time series. In Chapter 5, a joint coregistration approach based on ESD and weighted least squares is provided and tested with Sentinel-1 data. It is demonstrated that joint approaches deliver a higher quality of the azimuth shifts that can avoid phase biases.

A novel acquisition mode: the 2-look TOPS

Chapter 6 gathers the investigations performed for the design of the novel 2-look TOPS acquisition mode, which provides wide-swath coverage and improved sensitivity to along-track ground motion through spectral diversity techniques, overcoming the limitations of the conventional TOPS mode. The 2-look TOPS acquisition mode provides therefore 2-D sensitivity to ground displacement. A detailed design description, processing methodology, performance assessment and demonstration with experimental TerraSAR-X data over a fast deforming site (glacier flow) and slow-deforming site (post-seismic displacement) is provided.

In Chapter 7 the conclusions are provided.

Chapter 2

Fundamentals and state of the art

2.1 Synthetic Aperture Radar (SAR)

A SAR system consists of a radar sensor which illuminates a scene on ground with a side-looking geometry and boarded on a moving platform, typically an airplane or a satellite. The SAR reference frame is depicted in Fig. 2.1, whose coordinates are defined as:

(i) *range*: refers to the looking direction of the radar, also called line of sight and abbreviated as LOS. A distinction between the range before and after the SAR processing is commonly employed to distinguish between the LOS direction of the single radar pulses/echoes and the LOS direction after the integration of each echo within the synthetic aperture is performed. For systems with a zero-squinted antenna orientation this direction is also called *across-track*. The term *range* is sometimes to be found as *slant-range*, indicating the side-looking orientation of the sensor.

(ii) *azimuth*: corresponds to the direction of movement of the sensor. It is also called *along-track* direction.

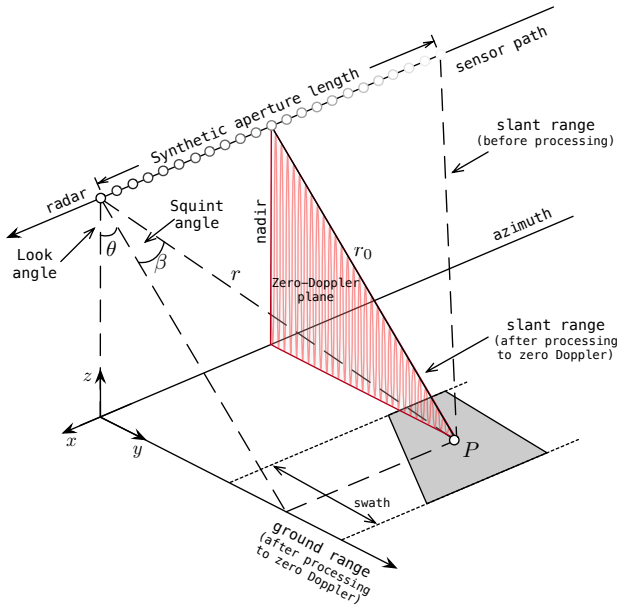

FIGURE 2.1: SAR acquisition geometry

The complex-valued measurement of the backscattered signal after the SAR focusing operation (Cumming and Wong, 2005), contains information on the brightness (amplitude), while the phase is also proportional to the two-way distance traveled by the electromagnetic wave from the sensor to the Earth's surface and back. Section 2.1.1 addresses the resolution that can be achieved in the along-track direction by exploiting the SAR technique. After the SAR processing has been carried out, the (unambiguous) phase can be written as:

$$\phi = -\frac{4\pi}{\lambda} r_0 + \phi_{\text{scat}} + \phi_{\text{noise}}, \tag{2.1}$$

where λ is the radar wavelength, r_0 the distance to a target P (after processing to zero-Doppler geometry), ϕ_{scat} the additional phase due to the *scattering* mechanism and ϕ_{noise} the noise phase. Interferometric techniques take advantage of this feature by exploiting the phase differences between surveys. Depending on the temporal and spatial baseline among them, measurements sensitive to terrain deformation or terrain elevation can be obtained. In Section 2.3 a brief review is provided.

2.1.1 Imaging with radar: the SAR principle

The ability of a real aperture radar system to differentiate two close objects in the azimuth direction is given by the resolution. The azimuth resolution that can be achieved depends on the azimuth dimension of the antenna, the employed wavelength and the distance to the target according to:

$$\rho_{\text{a}} \approx \Theta_{\text{a}} \cdot r_0 = \frac{\lambda}{L_{\text{a}}} \cdot r_0, \tag{2.2}$$

where Θ_a is the azimuth antenna beam width, L_{a} the azimuth antenna dimension and r_0 the distance to the target. Eq. (2.2) indicates that the achievable resolution by a conventional radar would imply to employ a very long antenna if fine azimuth resolution is desired. Moreover the azimuth resolution is range-dependent. For a spaceborne system operating in X-band and orbiting at 514 km altitude, an antenna length of 5m long would result in an azimuth resolution of roughly 4 km for a look angle, θ, equal to 35°.

Synthetic Aperture Radar (SAR) techniques overcome this limitation by creating a virtual larger antenna. This is accomplished by taking advantage of the movement of the platform carrying the radar sensor and by exploiting the coherent nature of the electromagnetic waves.

The azimuth resolution that can be achieved employing a SAR system is provided by the created longer antenna, virtually formed by the platform path and constrained in its extension by the beamwidth and range to the target, according to:

$$L_{\text{sa}} \approx \Theta_{\text{a}} \cdot r_0 = \frac{\lambda}{L_{\text{a}}} \cdot r_0 \tag{2.3}$$

The resulting virtual beamwidth with the synthetic aperture, taking into account the two-way path experienced by the signal, is given by $\Theta_{\text{sa}} \approx \lambda / 2L_{\text{sa}}$. The achievable azimuth resolution becomes:

$$\rho_{\text{a}} \approx \Theta_{\text{sa}} \cdot r_0 = \frac{\lambda}{2L_{\text{sa}}} \cdot r_0 = \frac{L_{\text{a}}}{2}, \tag{2.4}$$

which is independent of the range to the target and depends only on the physical antenna length. Following the same example as before, a SAR system with an antenna length of 5 m would result in an azimuth resolution of 2.5 m.

2.1.2 Statistics of SAR images: distributed targets

SAR images contain information about the interaction of the electromagnetic waves with the illuminated resolution cell. The recorded signal is commonly known as backscattering, being a complex magnitude due to the coherent nature of SAR systems. For each resolution cell, the backscattered field is the coherent sum of many elementary scatterers, which can be described mathematically as:

$$\mathbf{A} = Ae^{j\theta} = \frac{1}{\sqrt{N}} \sum_{n=1}^{N} \mathbf{a_n} = \frac{1}{\sqrt{N}} \sum_{n=1}^{N} a_n e^{j\phi_n}, \tag{2.5}$$

where N represents the number of phasor components, $\mathbf{A}$ is the resultant phasor, A is its length, and θ its phase. $\mathbf{a_n}$ is the n^{th} component phasor, being a_n its length, and ϕ_n its phase. The scaling factor $1/\sqrt{N}$ aids to preserve finite second moments of the sum when the number of components phasors tend to infinity.

When the backscattered signal corresponds to natural terrain, it can be assumed that the weights of each elementary scatterer within the resolution cell are of similar amplitude, i.e., there is no dominant target. This phenomenon applies when the surface is rough compared to the radar wavelength, resulting in a so-called "distributed target". Under these circumstances, the SAR signal can be considered as "speckle", i.e., a signal composed of a multitude of independently phased additive complex components (Goodman, 2007). In the case that there are many scatterers in the resolution cell, which is the case for SAR images over homogeneous areas, the central limit theorem can be applied. According to the latter, the statistics of the sum of N independent random variables is asymptotically Gaussian as $N \to \infty$. The first and second moments of the real and imaginary parts and the correlation between them are given by (Goodman, 2007):

$$\begin{aligned}
\mu_{\mathbb{R}} &= E\{\mathbb{R}\} = 0 \\
\mu_{\mathbb{I}} &= E\{\mathbb{I}\} = 0 \\
\sigma^2_{\mathbb{R}} &= E\{(\mathbb{R} - \mu_{\mathbb{R}})^2\} = \frac{1}{N} \sum_{n=1}^{N} \frac{E\{a_n^2\}}{2} \\
\sigma^2_{\mathbb{I}} &= E\{(\mathbb{I} - \mu_{\mathbb{I}})^2\} = \frac{1}{N} \sum_{n=1}^{N} \frac{E\{a_n^2\}}{2} \\
\Gamma_{\mathbb{RI}} &= E\{\mathbb{RI}\} = 0
\end{aligned} \tag{2.6}$$

Consequently the joint probability density function for the real and imaginary part is given by (Goodman, 2007):

$$p_{\mathbb{R},\mathbb{I}}(\mathbb{R},\mathbb{I}) = \frac{1}{2\pi\sigma^2} e^{-\frac{\mathbb{R}^2+\mathbb{I}^2}{2\sigma^2}}, \tag{2.7}$$

where $\sigma^2 = \sigma^2_{\mathbb{R}} = \sigma^2_{\mathbb{I}}$. Contours of constant probability density are shown in Fig. 2.2. Because of the circular shape of the contour lines, the resultant complex phasor $\mathbf{A}$ is said to be a "circular" complex Gaussian variate.

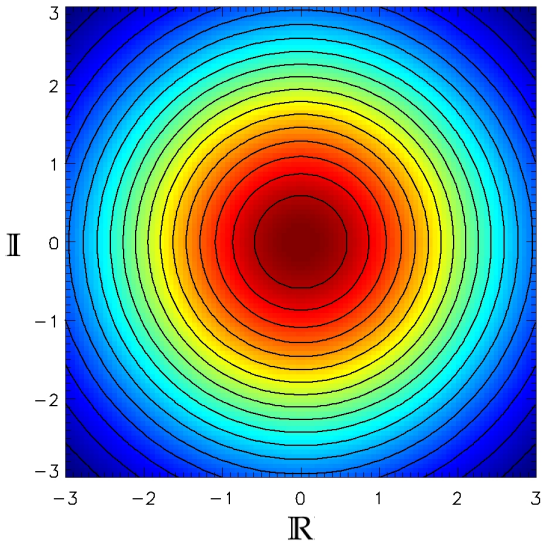

FIGURE 2.2: Contours of constant probability density for a circular complex Gaussian random variate

The probability density function of the amplitude, A, and phase, θ, of the resultant phasor is given by:

$$p_{A,\theta}(A,\theta) = \frac{A}{2\pi\sigma^2} e^{-\frac{A^2}{2\sigma^2}} \tag{2.8}$$

The marginal probability distribution function of the amplitude is given by:

$$p_A(A) = \int_{-\pi}^{\pi} p_{A,\theta}(A,\theta)d\theta = \frac{A}{\sigma^2} e^{-\frac{A^2}{2\sigma^2}}, \tag{2.9}$$

for $A \geq 0$, known as Rayleigh function. The probability density function of the phase is given by:

$$p_\theta(\theta) = \int_0^{\infty} p_{A\theta}(A,\theta)dA = \frac{1}{2\pi}, \tag{2.10}$$

for $(-\pi \leq \theta < \pi)$. We conclude that the phase of the resultant phasor is uniformly distributed in the primary interval, $[-\pi, \pi[$.

2.2 SAR acquisition modes

The illumination of a scene employing SAR techniques is done through directional antennas. This way the radiated microwave energy can be concentrated over the area of interest. The employed antenna technology consists usually of planar antennas, however the use of reflector-based antennas, traditionally used for communications applications, is also possible. In case of choosing planar antennas, arrays of transmit/receive modules (TRM) are usually employed. These modules are fed by a chirp waveform signal (Curlander and Mcdonough, 1991). Controlling phase and amplitude of the TRM provides flexibility to steer the pointing or tune the beam shape. This section provides a review of the fundamental StripMap mode and burst-mode strategies for wide-swath mapping. Additionally an overview of selected acquisition approaches that achieve increased sensitivity in the along-track direction is provided.

2.2.1 StripMap

StripMap represents the primitive SAR acquisition mode. The antenna beam is oriented to the broadside direction, i.e., perpendicular to the antenna plane. A fixed swath is illuminated in a single continuous *strip*, being each target illuminated during the complete synthetic aperture, taking advantage of the platform movement. Fig. 2.3 depicts a simplified acquisition geometry of a radar boarded on a platform moving with velocity v, where a point target, P, is observed. As the sensor advances along its path, pulses are sent every $1/\mathrm{PRF}$ seconds, being PRF the pulse repetition frequency. The pulses reach the illuminated scene on the ground and a fraction of the incident energy is bounced back towards the radar sensor, usually called radar echo. The echoes are received by the radar antenna, digitized and stored.

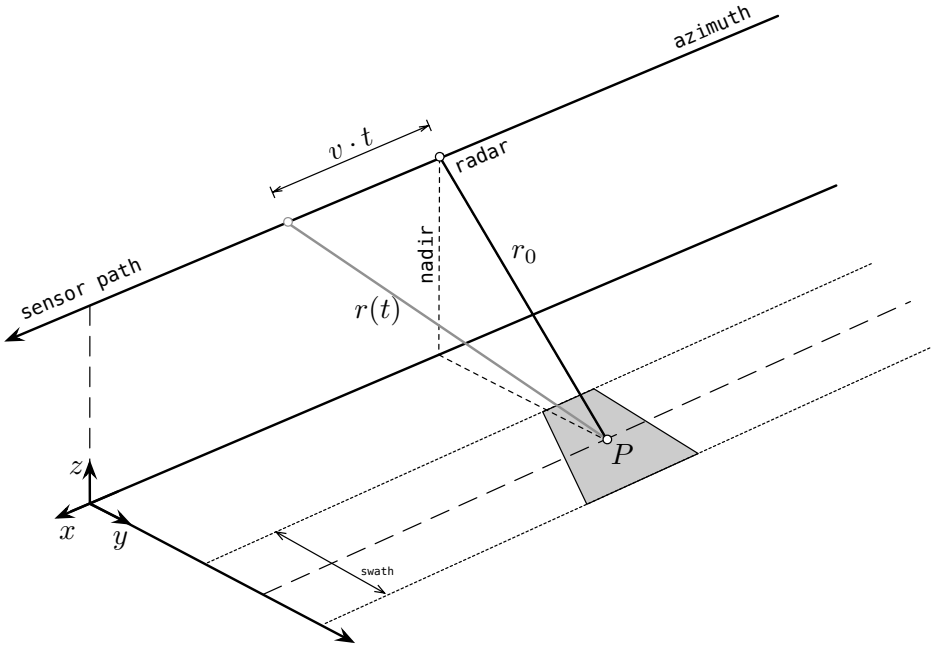

FIGURE 2.3: Range history for the target P.

Assuming linear geometry, the distances from the different positions of the sensor to a target, P, are given by:

$$r(t) = \sqrt{r_0^2 + (v \cdot t)^2}, \tag{2.11}$$

which is known as the hyperbolic form of the range history. The origin of times has been taken at the zero-Doppler position, i.e., when the target is observed at its shortest range, r_0.

Performing a Taylor series expansion around the time origin, $t = 0$, we obtain the parabolic approximation of the range history:

$$r(t) \approx r_0 + \frac{v^2}{2r_0}t^2 \tag{2.12}$$

Since the phase of the complex SAR signal is given by $\theta(t) = -\frac{4\pi}{\lambda}r(t)$, the SAR signal presents an instantaneous Doppler frequency given by:

$$f_\mathrm{d}(t) = -\frac{2}{\lambda}\frac{\mathrm{d}r(t)}{\mathrm{d}t} = -\frac{2v^2}{\lambda r_0}t, \tag{2.13}$$

where λ is the radar wavelength. The Doppler frequency of the target varies thus linearly with time, with a rate $k_\mathrm{a} = -\frac{2v^2}{\lambda r_0}$, which is known as Doppler rate or frequency modulation (FM) rate.

The bandwidth is given by the Doppler frequency excursion experienced by the target during the time in which it is illuminated by the 3-dB width of the antenna beam. In case of an uniform illumination of the elements, $\Theta_\mathrm{a} = 0.89 \cdot \frac{\lambda}{L_\mathrm{a}} \approx \frac{\lambda}{L_\mathrm{a}}$, where L_a is the antenna length in the azimuth direction. The illumination time is given by:

$$T_\mathrm{ill} \approx \frac{r_0 \cdot \Theta_\mathrm{a}}{v}, \tag{2.14}$$

where a small-angle approximation has been used. Thus the Doppler bandwidth can be written as:

$$B_\mathrm{a} = |k_\mathrm{a}| \cdot T_\mathrm{ill} \approx \frac{2v}{L_\mathrm{a}}. \tag{2.15}$$

Usually a slightly narrower bandwidth is considered during the SAR processing, which is called processing bandwidth (PBW).

Fig. 2.4 shows the time-frequency diagram of the acquisition. The horizontal axis indicates the azimuth time, whereas the vertical corresponds to the Doppler frequency. The azimuth antenna pattern is schematically plotted on the left, which indicates the signal strength from a certain target. An acquisition of length T_raw is carried out. The Doppler frequency history, with rate k_a, of the first and last illuminated targets at the same range distance are shown. Note that just the Doppler history corresponding to the established PBW, B_P, is considered. The duration of the focused scene is T_focused.

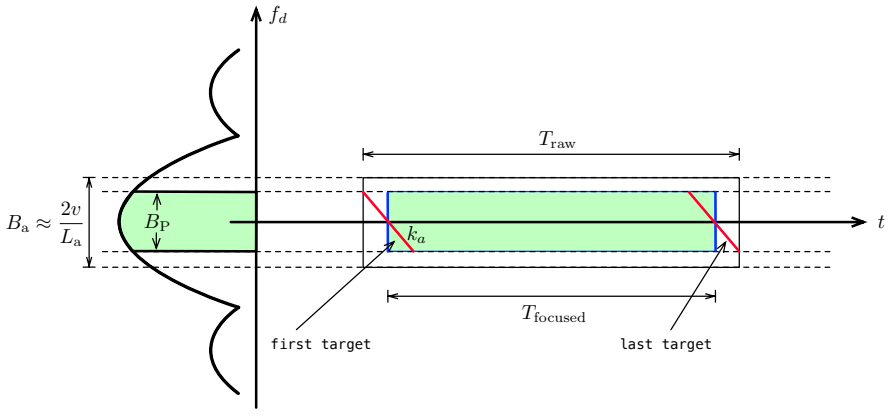

FIGURE 2.4: Time-frequency diagram for the StripMap mode

2.2.1.1 Swath width

The swath width that can be achieved with pulsed SAR systems is limited by the pulse repetition frequency. Since the pulses are transmitted every pulse repetition interval (PRI), the duration of the echoes cannot exceed this interval (Curlander and Mcdonough, 1991). Fig 2.5 illustrates the timing scheme of transmitting radar pulses (TX) and the reception (RX) of the echoes.

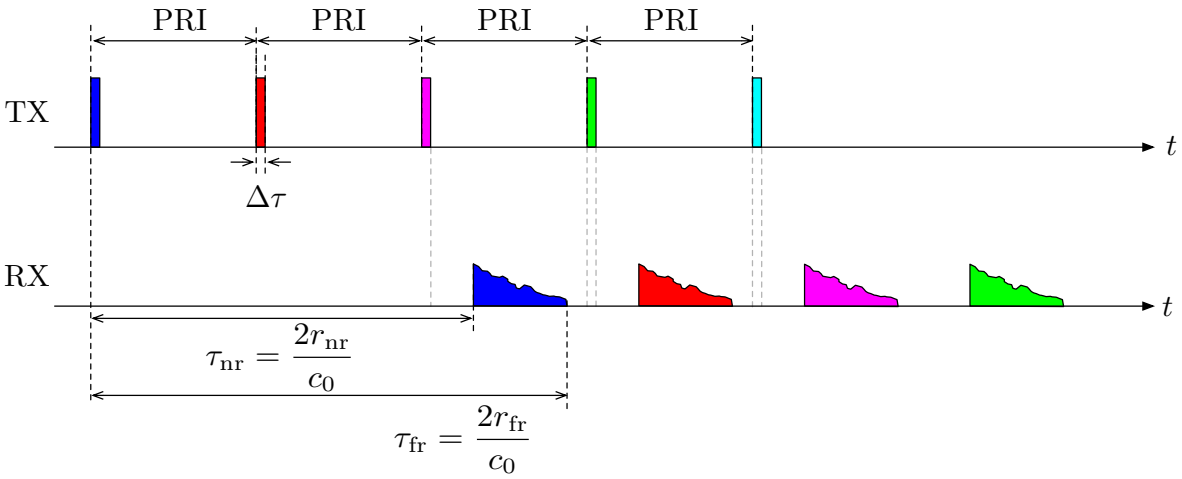

FIGURE 2.5: Transmission-Reception timing scheme

The available time interval to receive an echo, difference between the far range time (τ_{fr}) and the near range time (τ_{nr}), is given by the PRI once the duration of the transmitted pulse, $\Delta\tau$, has been subtracted:

$$\tau_{\mathrm{fr}} - \tau_{\mathrm{nr}} < \frac{1}{\mathrm{PRF}} - \Delta\tau \lessapprox \frac{1}{\mathrm{PRF}}, \tag{2.16}$$

which can be approximated by the inverse of the PRF, if the pulse duration is much smaller, typically fulfilled. Under the same assumption, the maximum swath width (in slant range) can be written as:

$$W_{\mathrm{s}} \lessapprox \frac{c_0}{2 \cdot \mathrm{PRF}}, \tag{2.17}$$

where c_0 is the speed of light.

The Doppler spectrum of the SAR signal has a bandwidth B_{a}, which is sampled at a rate PRF due to the pulsed operation of the system. In order to fulfill the Nyquist sampling theorem, $B_{\mathrm{a}} <$ PRF. The Doppler bandwidth can be written as:

$$B_{\mathrm{a}} \approx \frac{v_{\mathrm{g}}}{\rho_{\mathrm{a}}}, \tag{2.18}$$

where v_{g} is the beam ground velocity. Therefore, $\mathrm{PRF} \geq v_{\mathrm{g}}/\rho_{\mathrm{a}}$. Combining this with (2.17) we obtain the relationship between swath width and azimuth resolution:

$$\frac{W_{\mathrm{s}}}{\rho_{\mathrm{a}}} < \frac{c_0}{2 \cdot v_{\mathrm{g}}}, \tag{2.19}$$

which indicates the trade-off between both parameters.

The swath width in ground range, W_{g}, can be obtained approximately, following the geometry depicted in Fig. 2.6, as:

$$W_g \approx \frac{W_s}{\sin \theta_{avg}}, \tag{2.20}$$

where θ_{avg} is the averaged incidence angle of the swath.

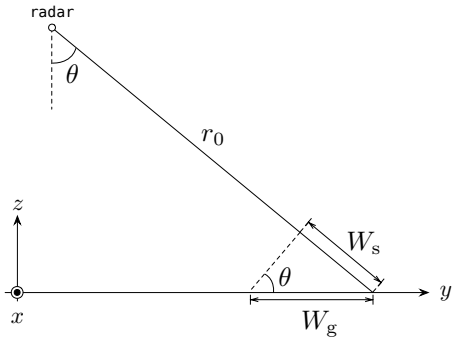

FIGURE 2.6: Relationship between slant-range swath width and ground coverage. A flat Earth has been assumed

2.2.1.2 Azimuth ambiguities

The Doppler spectrum of the SAR signal is not band-limited, presenting sidelobes due to the antenna pattern. The amplitude of the sidelobes decrease progressively when moving away from the center frequency. By sampling the spectrum at a limited frequency, PRF, the components outside the main band, i.e., $[-\text{PRF}/2, \text{PRF}/2[$, fold back into the main band (Curlander and Mcdonough, 1991). These components, which correspond to targets located away from the zero-Doppler position, add coherently to the signal received by the main beam, degrading the quality of the legitimate signal. The contributions of the targets observed by the sidelobes are known as azimuth ambiguities.

Fig. 2.8 shows a scheme of the directivity pattern of a broadside oriented beam. The processed Doppler bandwidth is indicated in green. Due to the sampling with a limited PRF, there is a periodical folding of the components located at multiples of PRF into the main band. The portions of the Doppler spectrum, corresponding to the azimuth ambiguities, are indicated in red. Note that the amplitude of the sidelobes decrease for frequencies moving away from the zero-Doppler position.

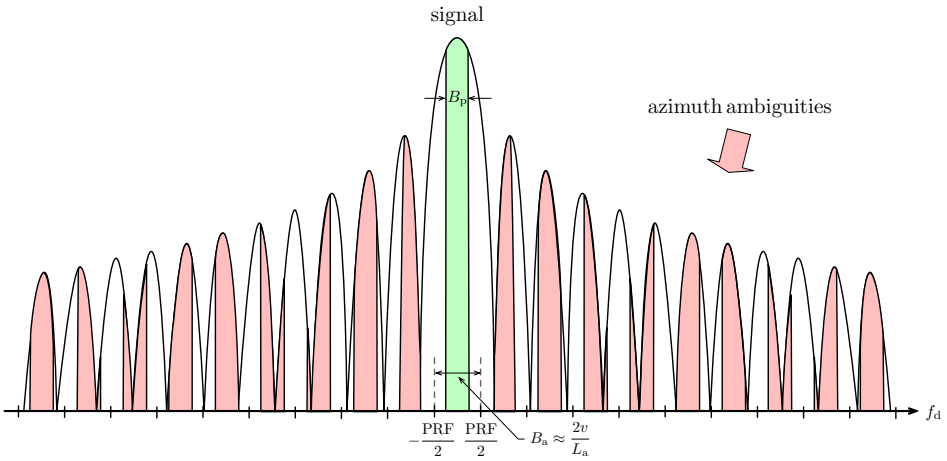

FIGURE 2.7: Azimuth ambiguities

The ambiguity signals are undesired and can be modeled as noise for sites characterized by distributed scatterers. In order to decrease the level of the ambiguities, it is interesting to sample the Doppler spectrum with the highest possible PRF. This is, however, in contradiction with the desired swath width (2.17), which limits the maximum PRF, and the range ambiguities, as will be seen in Section 2.2.1.3.

The level of ambiguities is usually characterized through the ratio of the azimuth ambiguity signal power to the main signal power, and is referred as azimuth ambiguity-to-signal ratio (AASR), defined as:

$$\mathrm{AASR} \approx \frac{\sum_{\substack{k=-\infty \\ k\neq 0}}^{\infty} \int_{-B_a/2}^{B_a/2} T(f_d) \cdot G_a^2(f_d + k \cdot \mathrm{PRF}) \cdot \mathrm{d}f_d}{\int_{-B_a/2}^{B_a/2} T(f_d) \cdot G_a^2(f_d) \cdot \mathrm{d}f_d}, \tag{2.21}$$

where B_a is the azimuth processing bandwidth, $T(f_d)$ is the sidelobe suppression tapering function (Breit et al., 2010) applied during processing, and $G_a^2(f_d)$ is the two-way far field azimuth antenna power pattern.

2.2.1.3 Range ambiguities

A second constraint to limit the sampling of the Doppler spectrum with a high PRF is given by the range ambiguities or second time around. In the case of using a high PRF the spacing of consecutive pulses may be so small that sidelobes returns (from preceding and succeding pulses) are received at the same time as the return through the mainlobe (Curlander and Mcdonough, 1991).

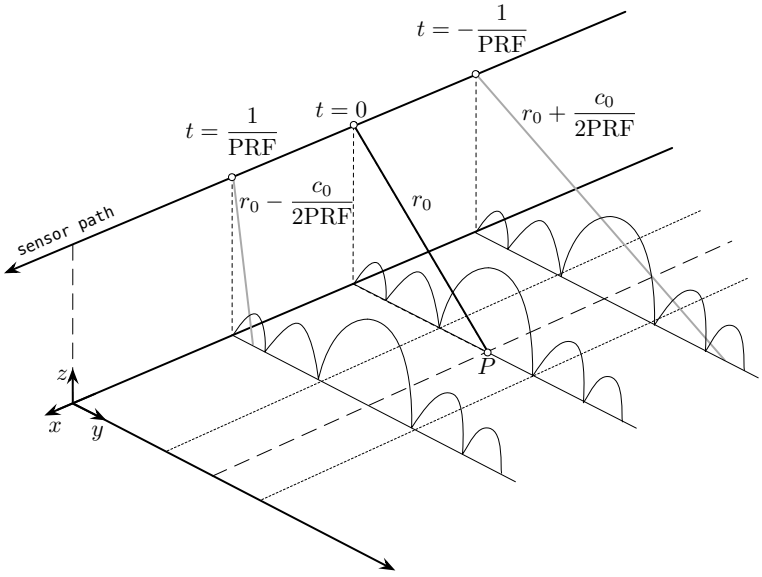

FIGURE 2.8: Range ambiguities

The range ambiguities can be quantitatively characterized through the range ambiguity-to-signal ratio (RASR), defined for planar antennas as (Villano, 2016):

$$\mathrm{RASR} \approx \frac{\sum_{\substack{k=-\infty \\ k\neq 0}}^{\infty} \frac{\sigma_0(\eta_0) G_\theta^2(\theta_k)}{(r_0 + \frac{c_0}{2\mathrm{PRF}})^3 \sin(\eta_k)}}{\frac{\sigma_0(\eta_0) G_\theta^2(\theta_0)}{r_0^3 \sin(\eta_0)}}, \tag{2.22}$$

where $\sigma_0(\eta)$ is the backscattering coefficient as a function of the incidence angle, η, $G_\theta^2(\theta)$ is the two-way far-field elevation antenna pattern power, θ is the look angle and r is the distance to the target on ground. The subscript 0 for the look and incidence angles refers to the desired echo return, whereas the subscript k refers to the ambiguous return.

For the computation of the RASR, the consideration of the geometry and a scatterer model accounting for the incidence angle are necessary. In Ulaby and Dobson, 1989 scattering models for different terrain categories can be found.

2.2.2 Wide swath and timing constraints

Different approaches have been proposed in the literature to achieve wide-swath coverage (Currie and Brown, 1992, Krieger et al., 2009). Some of them are intended to obtain at the same time high resolution. The achievement of high resolution implies that the Doppler bandwidth has to be increased, demanding for higher PRFs, which is in contradiction with the attainment of wide swath coverage (2.2.1.1). Noteworthy is the use of multiple azimuth beam systems, which allow to effectively decrease the acquisition PRF; for instance, the Displaced Phase Center (DPC) multibeam concept foresees the transmission of pulses into a single broad azimuth beam and the reception of the echoes in several broad beams, which are displaced in the along-track direction. Since several channels are available for reception, a suitable distance between phase centers and a certain operating PRF result in independent target returns, allowing the use of a reduced PRF (by a factor equal to the number of channels) keeping the same resolution. A reconstruction algorithm for non-uniform sampling (Krieger et al., 2004) allows to relax the selection of the acquisition PRF and distance between phase centers, making this concept applicable for real single-platform multi channel systems or for multistatic SAR.

Of interest for wide-swath acquisition modes is the consideration of the timing constraints for transmission of pulses and reception of the echo returns. If the same antenna is used for transmission and reception, "blind ranges", i.e., the lack of data at certain range positions will take place. This is due to the fact that the antenna is not able to receive echo returns while it is transmitting. The blind ranges intervals lie at constant ground-range positions for a given geometry and PRF. The interval of ranges, r, that can be stored is given by (Currie and Brown, 1992):

$$\left(\frac{n}{\mathrm{PRF}} + \Delta\tau\right)\frac{c_0}{2} \leq r \leq \left(\frac{n+1}{\mathrm{PRF}} - \Delta\tau\right)\frac{c_0}{2}, \tag{2.23}$$

where possible guard bands, i.e. an extra time margin around $\Delta\tau$ to avoid for partial losses of the echo return at near or far range, have been ignored.

An additional blind range interval might be caused by an eventual saturation from the nadir echo return. The reason is that, since the nadir region lies at closer distance than the scene of interest and corresponds to specular reflection, it can swamp other radar returns arriving at the same time. In order to avoid this situation, an additional constraint to the PRF can be set, which consists in selecting a PRF such that the nadir returns occur at the same time as the pulses are transmitted. This condition can be written as:

$$\mathrm{PRF} = k \cdot \frac{c_0}{2H}, \tag{2.24}$$

where k is an integer number, known as the *rank* of the PRF, and H is the height of the platform carrying the radar antenna. In the general case, the nadir return interferes with the echo from a target located at a range given by (Curlander and Mcdonough, 1991):

$$H + \frac{c_0}{2}\left(\frac{k}{\mathrm{PRF}} + 2\Delta\tau\right) \leq r \leq H + k \cdot \frac{c_0}{2\mathrm{PRF}}, \tag{2.25}$$

where a duration of $2\Delta\tau$ for the nadir return has been assumed.

The previous constraints to the PRF allow to design a coverage diagram that indicates the location of the blind ranges. Fig 2.9 shows an example, considering flat Earth geometry, a platform height of 514 km and a duty cycle[1] of 12%. The blue areas correspond to transmit events, whereas the green zones to nadir returns. The allocation of the swaths between these areas, indicated by the orange lines, avoids loss of data or interference with the nadir returns.

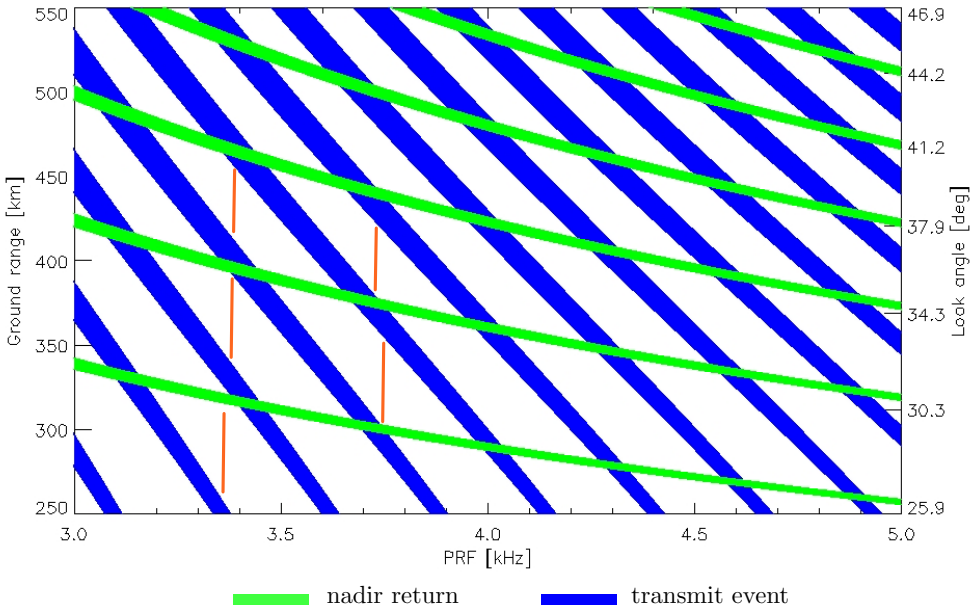

FIGURE 2.9: Example of coverage diagram from timing considerations. A height of 514 km, a duty cycle of 12% and flat Earth geometry have been considered.

The restrictions imposed by the transmit events and nadir returns require to review its impact on a continuous wide-swath coverage. Related to the mitigation of blind ranges, the staggered SAR concept (Villano et al., 2014) suggests to employ a continuous variation of the PRI in order that the locations of the blind ranges vary between consecutive pulses. Consequently, only some of the transmitted pulses are missing, being possible to perform a compression in azimuth. A sequence of PRIs can be chosen so that the blind range areas are almost uniformly distributed across the swath. Another possibility is to design the sequence of PRIs such that, in the raw azimuth signal, two consecutive samples are never missed. In this case, if the mean PRI decreased, i.e., the signal is averagely oversampled, it is possible to recover the missing samples by means of interpolation (Villano et al., 2014). The extension of the staggered SAR concept to multi-channel systems can be found in Queiroz de Almeida et al., 2018. Regarding the nadir return, the use of waveform diversity on transmit has been suggested by Villano et al., 2018 for its removal.

2.2.3 Wide-swath burst-mode acquisitions

Recalling the discussion introduced in Section 2.2.1.1, the use of wide swaths requires sampling with low PRFs, as indicated by (2.17). The use of lower PRFs implies that the Doppler bandwidth has to be reduced in order to sample the azimuth signal correctly, as pointed out

[1] Ratio between the uncompressed pulse duration and the inverse of the PRF

in Section 2.2.1.2. This translates into a narrower antenna beamwidth, which can be implemented with a longer antenna in the along-track direction[2]. Combining (2.19) with (2.4), we obtain the trade-off between swath width and antenna length in the along-track direction:

$$L_a > \frac{4v_g}{c_0} W_s. \tag{2.26}$$

If, e.g., a swath width of 250 km is desired, as employed by the Sentinel-1 system over land, an antenna length of more than 20 m would be required, which is unpractical and costly to implement. An alternative way to degrade the azimuth resolution keeping a practical antenna length, consists in reducing the illumination time of the targets. This means that each target is illuminated by a *burst* of pulses, which represents a fraction of the number of pulses of the whole synthetic aperture. The remaining time is used to acquire consecutive subswaths by switching cyclically the elevation beam. This is the working principle of the Scanned-beam SAR (ScanSAR) mode (Moore et al., 1981, Tomiyasu, 1981), which is briefly described in Section 2.2.3.1. The Shuttle Radar Topography Mission (SRTM) employed the ScanSAR mode in C band, with four subswaths and a coverage of 225 km, as the basis scheme to map interferometrically the Earth's topography in February 2000 in just 10 days (Farr et al., 2007). Following the same burst-acquisition principle, the terrain observation by progressive scans (TOPS) mode introduces additionally a steering of the antenna in the azimuth direction, which solves the problems of scalloping and azimuth varying ambiguities of the original ScanSAR mode, a brief review is provided in Section 2.2.3.2. The Sentinel-1 constellation mission, started in 2014, employs TOPS with three subswaths as the baseline mode over land, providing a coverage of 250 km at 20 m azimuth resolution (Attema et al., 2007, Torres et al., 2012).

It is worthy to mention that in the case of burst-mode acquisitions, the blind ranges and nadir return can be easily avoided, since the PRF can be changed for each subswath. This way, continuous coverage, including some overlapping between subswaths, can be achieved. This is exemplarily illustrated in Fig. 2.9, where five subswaths can be imaged (orange vertical lines), providing a continuous range coverage.

2.2.3.1 ScanSAR

ScanSAR achieves wide-swath coverage by imaging a series of different swaths. The look angle of the elevation beam is cyclically switched, meaning that each target is illuminated during a fraction of the complete synthetic aperture. The time interval in which each target is observed, known as dwell time, matches the burst duration. Fig. 2.10 shows schematically the working operation of ScanSAR for an exemplary three-subswath system.

[2]Note that restricting the processing bandwidth, B_p, is not an option, since the sampling of the azimuth signal takes places during the acquisition.

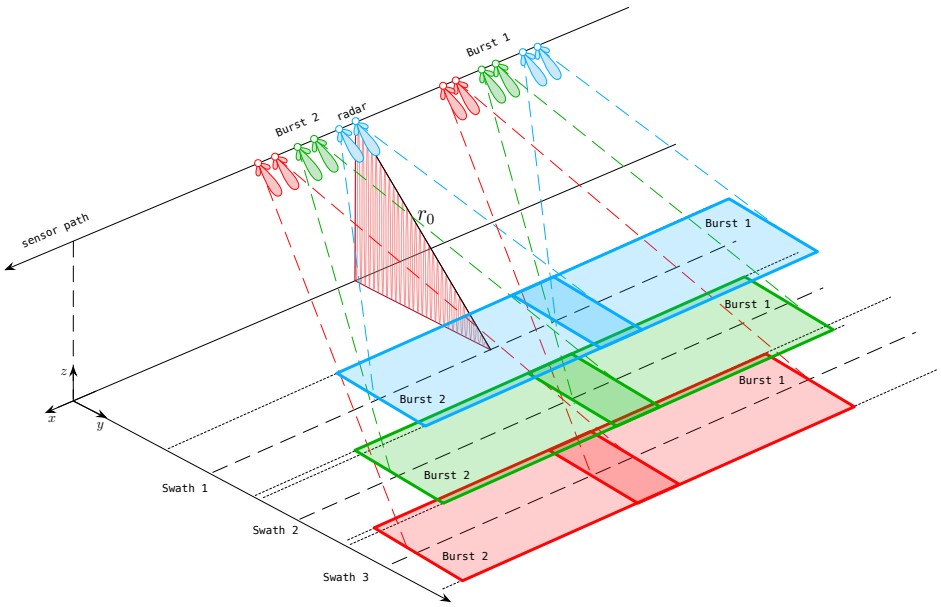

FIGURE 2.10: ScanSAR acquisition operation

The acquisition starts illuminating the first subswath with a burst of pulses, storing the corresponding echoes; afterwards the beam is electronically switched to the second and third subswath, acquiring for each of them a burst of echoes. Afterwards the beam is switched to the first subswath again, repeating the process. The time interval between the beginning of one dwell time and the begin of the next dwell time for the same given subswath is known as cycle time or return time, T_R. Note that the ScanSAR acquisition can be carried out continuously without any constraint in the azimuth dimension, as for StripMap. Fig. 2.11 shows the time-frequency diagram for the acquisition of a burst. By comparing this diagram to the StripMap one of the Fig. 2.4, it can be seen that only a portion of the Doppler bandwidth is recorded for each target. When processing the data to zero-Doppler geometry, the burst presents a linear Doppler variation with slope k_t and excursion Δf_{DC}; this time-variant Doppler change over azimuth has to be considered during the SAR and InSAR processing. Note that the focused burst is longer than the raw burst, being therefore possible to obtain a gap-free focused image, even if the acquisition is not continuous over each subswath.

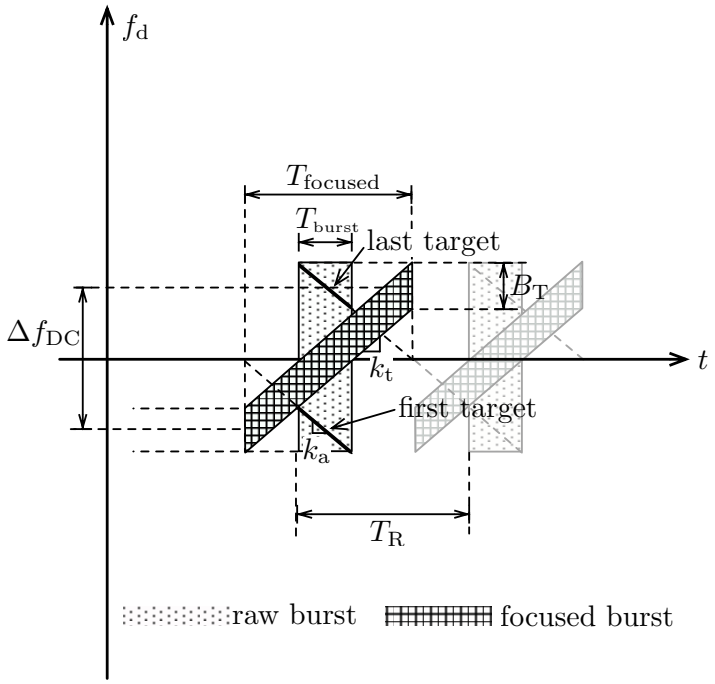

FIGURE 2.11: Time-frequency diagram of two raw burst and their corresponding focused bursts acquired in ScanSAR mode

Combining (2.19), (2.4) and (2.20) and given a desired swath width on ground, $W_\mathrm{g}^\mathrm{ScanSAR}$, the necessary number of subswaths, N_ss, can be approximated by:

$$N_\mathrm{ss} = \left\lceil \frac{4 v_\mathrm{g} \sin\theta_\mathrm{avg}}{c_0 L_\mathrm{a}} W_\mathrm{g}^\mathrm{ScanSAR} \right\rceil, \tag{2.27}$$

where $\lceil x \rceil$ denotes the ceil of a number, i.e., the least integer greater than or equal to x.

The azimuth resolution for any subswath of a ScanSAR acquisition cannot be better than the sum of the resolutions of the equivalent StripMap modes, i.e.:

$$\rho_\mathrm{a}^\mathrm{ScanSAR} > \sum_{i=0}^{N_\mathrm{ss}-1} \rho_\mathrm{a}^\mathrm{StripMap}(i), \tag{2.28}$$

where $\rho_\mathrm{a}^\mathrm{StripMap}(i)$ represent the equivalent StripMap azimuth resolution of each subswath, i.

ScanSAR presents, however, some limitations related to azimuth-dependent ambiguities and SNR, resulting from the so-called *scalloping* effect. This is due to the azimuth non-stationarity of the acquisition, i.e., depending on the azimuth position of the target, they are observed by a different central Doppler frequency and therefore with a different azimuth antenna pattern (AAP), which produces a different amplitude weighting. A way to mitigate this effect is to employ multi-look systems in order to observe each target with different slices of the AAP. This way the amplitude modulation of the AAP is reduced. Fig 2.12 shows the time-frequency diagram of an exemplary 3-look system. Each target is illuminated by 3 bursts with different sections of the AAP, as the shown target located at the zero-Doppler time t_0.

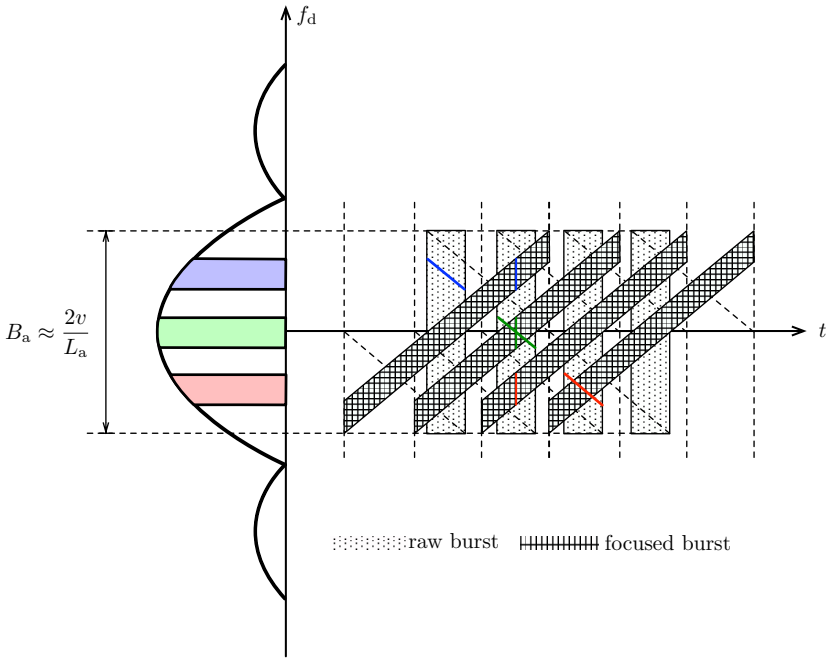

FIGURE 2.12: Time-frequency diagram of a 3-look ScanSAR mode. Four raw bursts with their corresponding focused bursts are displayed.

The classical approach to compress ScanSAR data is the Spectral Analysis method (SPECAN). The basic SPECAN (Sack et al., 1985), originally conceived to process normal SAR data (StripMap), suits very well to burst-mode data because of the individual processing of the bursts. It makes use of the concept of deramping followed by spectral analysis. Deramping comprises the operation of multiplying a linear FM signal with the complex conjugated reference signal, i.e., a signal with the same FM rate but opposite sign. This way the original FM signal is converted into a constant-frequency sinusoid, which can be compressed by a spectral analyzer, such as an FFT (Caputi, 1971). Some deficiencies of the basic SPECAN algorithm have been solved by introducing a modified azimuth scaling function (Moreira et al., 1996), which removes the variation of the azimuth frequency modulation with range and induces a range invariant, linear frequency modulation. Therefore, no interpolation is necessary for the azimuth geometric correction, required in the case of the basic SPECAN algorithm.

A SAR processing alternative to the SPECAN method for burst-mode data consists of using standard high precision algorithms as range-Doppler, wavenumber domain or chirp scaling (Bamler and Eineder, 1996). This is also indicated for multi-look systems, where long bursts trains with zeroes are inserted at the interburst intervals. The drawback of this approach is the higher computation time and the degradation of the azimuth impulse response function due to the interference of the burst images. The latter can be overcome for imaging purposes by low-pass filtering the power detected image at the expense of some resolution loss.

2.2.3.2 TOPS

The terrain observation by progressive scans (TOPS) (De Zan and Monti Guarnieri, 2006) overcomes the limitations of ScanSAR related to azimuth-dependent ambiguities and SNR, and the so-called scalloping effect. TOPS performs the acquisition by recording bursts of echoes, as ScanSAR does, but introduces additionally an azimuth steering of the antenna

beam (from backward to forward) during the acquisition of each burst. This way each target experiences the same AAP weighting, eliminating almost completely the azimuth non-stationarity of the ScanSAR mode, so that ambiguities and SNR become almost constant in azimuth and the scalloping effect is practically eliminated, except for a very small residual scalloping due to the element pattern effect (Wollstadt et al., 2012). As ScanSAR, TOPS switches cyclically the antenna beam in elevation in order to achieve wide-swath coverage. Fig. 2.13 shows the working operation for an exemplary three-subswath system. The acquisition starts by illuminating the first subswath pointing the beam backwards, a burst of pulses is transmitted varying simultaneously the beam azimuth angle. At the end of the burst acquisition, the beam is pointing forward with a squint angle symmetric to the squint angle at the beginning of the burst. Afterwards, the beam is switched in elevation to the next subswath pointing backwards. A new burst is acquired in the same way as for the first subswath. The process is repeated until the last subswath is acquired, switching afterwards the elevation beam to the first subswath and repeating the process until the desired azimuth swath coverage has been achieved.

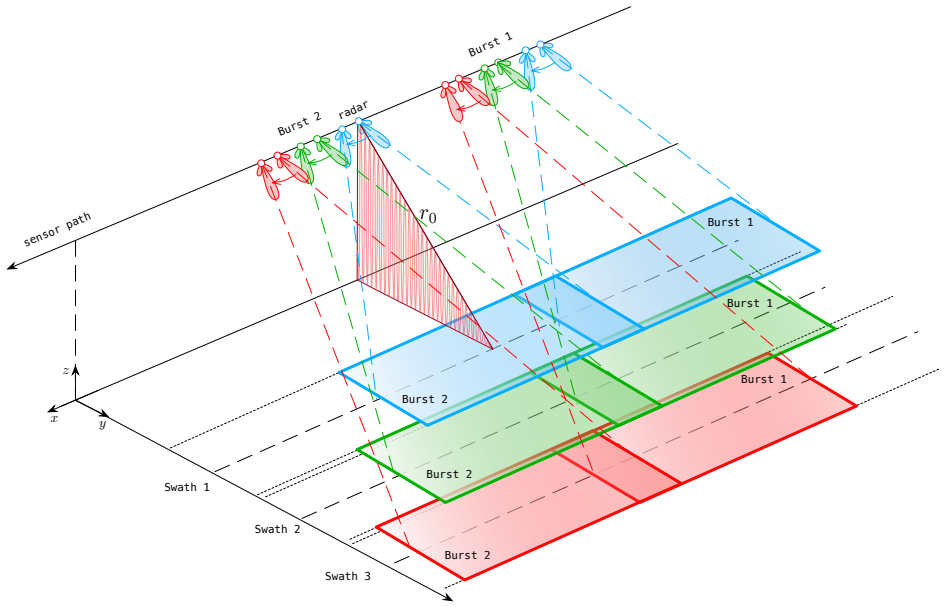

FIGURE 2.13: TOPS acquisition principle

The antenna beam is steered from backward to forward with a rate ω_r, which produces a Doppler rate given by (De Zan and Monti Guarnieri, 2006):

$$k_{\text{rot}} \approx \frac{2v_s}{\lambda}\omega_r, \tag{2.29}$$

where v_s is the satellite velocity. The steering implies that a wider bandwidth than the one corresponding to the 3 dB-beam width is covered. This fact does not require an increase of the PRF, since the instantaneous antenna beam width is the same as for StripMap. Therefore no aliasing of the Doppler spectrum is produced, but just a wrap, that can be easily recovered. A focusing of each burst to zero-Doppler geometry, produces an effective Doppler rate at image level given by (Prats-Iraola et al., 2012):

$$k_t(r) = \frac{k_a(r) \cdot k_{\text{rot}}}{k_a(r) - k_{\text{rot}}}, \tag{2.30}$$

where $k_a(r)$ is the (range-dependent) target frequency modulation rate. Fig. 2.14 shows the time-frequency support for a raw burst acquired in TOPS mode and after focusing to

zero-Doppler geometry. Each target is observed during the dwell time, T_{dwell}, which is much shorter than the burst duration, unlike the ScanSAR mode. The target bandwidth, which determines the azimuth resolution, is given by $B_{\text{T}} = T_{\text{dwell}} \left| k_{\text{a}}(r) \right|$.

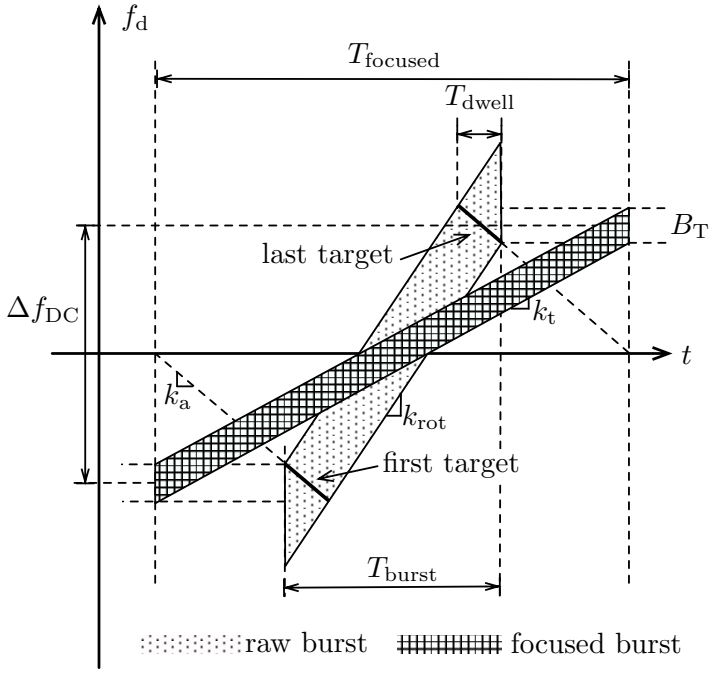

FIGURE 2.14: Time-frequency diagram of a raw burst and its corresponding focused burst acquired in TOPS mode

There are several approaches to process SAR data acquired in TOPS mode as introduced in the literature by Prats et al., 2010, Engen and Larsen, 2011, Sun et al., 2011 and Xu et al., 2011.

2.2.4 Bidirectional SAR

SAR systems are able to measure distances very accurately in the line-of-sight direction by exploiting the interferometric phase. However, the sensitivity to the motion in the along-track direction is limited by the azimuth resolution, resulting in a performance orders of magnitude worse than in the line of sight. If enhanced sensitivity in the along-track direction is desired, dual-beam concepts (Frasier and Camps, 2001) can be applied. If a single platform is employed, two lines of sight can be obtained by mounting a radar instrument with two antennas, looking symmetrically forward and backward, respectively.

The conceptual SuperSAR system (Shepherd and SuperSAR Team, 2010) has been proposed to measure the Earth surface deformation in three dimensions. The SuperSAR concept foresees a SAR system operating in L-band boarded on a single platform with a repetition cycle of 13 days. It operates in ScanSAR mode, in order to achieve wide swath, and acquires the VV- and HH-polarized SAR images from forward- and backward-looking beams, respectively. The beams are squinted at $\pm 30^{\circ}$ and are implemented through a phased-array antenna. SuperSAR system achieves 1 mm/year accuracy over 100 km in all three dimensions after five years of observation (Wright et al., 2011). The feasibility to detect 3-D surface displacement provides accuracies in the sub-centimeter range assuming a coherence of 0.8 (Jung et al., 2015) according to simulations.

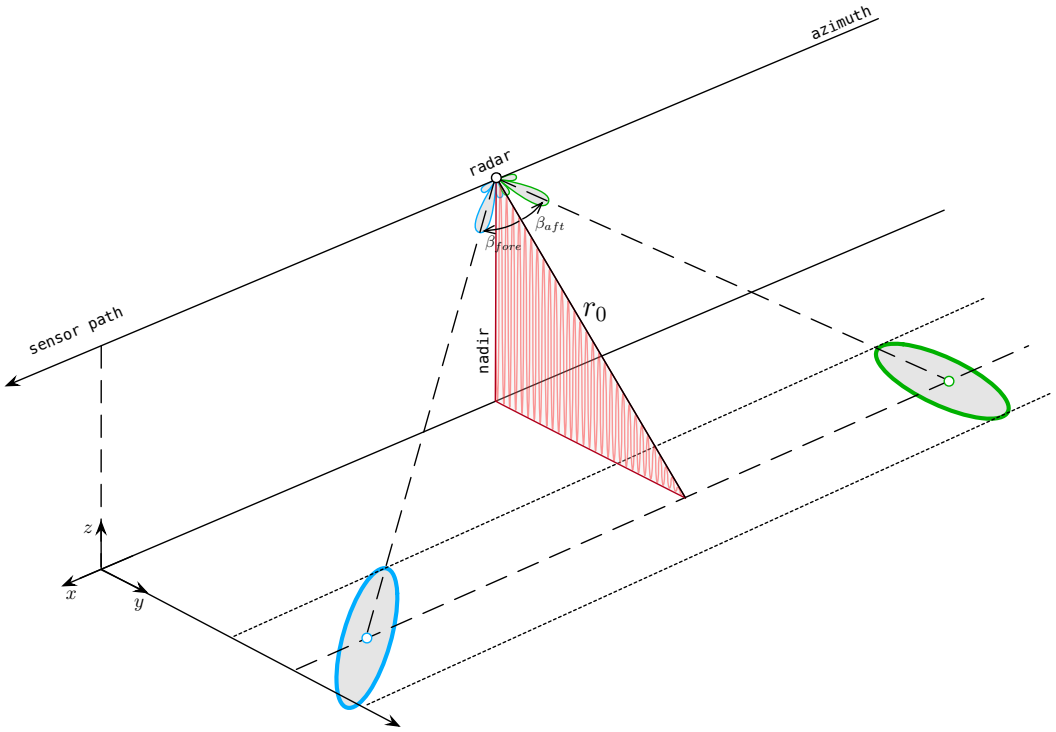

FIGURE 2.15: Bidirectional and squinted acquisition principles

Experimental acquisitions have been already performed with the TerraSAR-X system following a similar approach. The bidirectional SAR (BiDi SAR) mode (Mittermayer et al., 2013) acquires in StripMap mode and obtains two symmetrical beams, looking forward and backward, through a phased array antenna. This mode exploits the periodicity property of an array of antennas, which presents an angular separation between the beam or, main lobe (ML) and the grating lobe (GL), in the visible region, given by (Cardama et al., 1998)[3]:

$$\Delta\theta_{\mathrm{ML-GL}} \approx \frac{\lambda}{d_{\mathrm{a}}}, \tag{2.31}$$

being d_{a} the physical distance between the elements of the array in the along-track direction.

BiDi achieves two simultaneous symmetric lines of sight by feeding the array elements with a progressive phase shift α, such that the main and the grating lobe in the visible region present the same level. For the TerraSAR-X system, with 12 elements in azimuth separated approximately 40 cm, two beams squinted approximately $\pm 2.23^{\circ}$ can be achieved. Fig. 2.16 shows the directivity and element pattern for the BiDi SAR mode, generated by means of a numerical simulation employing the sinus cardinalis function according to the TerraSAR-X antenna dimensions, number of elements and wavelength.

[3] Assuming isotropic antennas. In practical systems, the pattern of the elements of the array have to be taken into account. The directivity pattern of the beam results from the multiplication between the array factor and the element pattern. The effect of the element pattern introduces a slight shift to the beam, or main lobe, and the grating lobe, achieving a slightly smaller angular separation

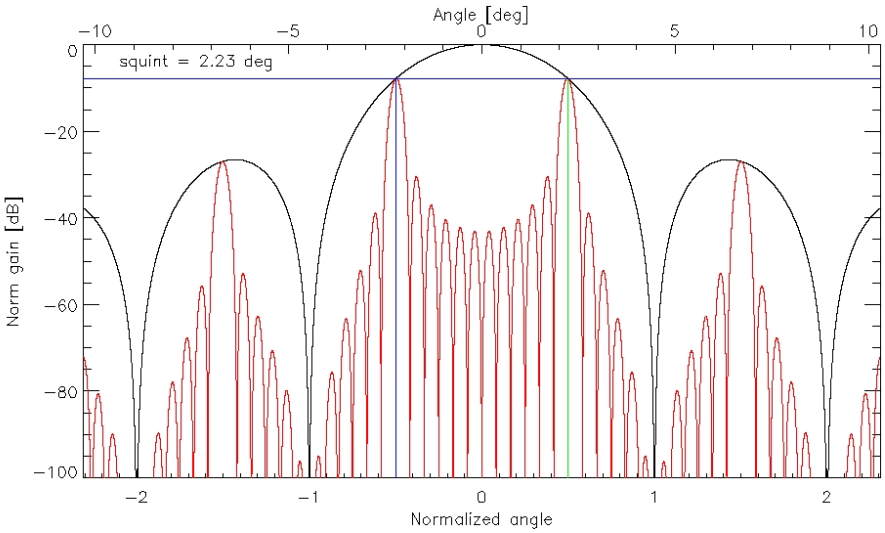

FIGURE 2.16: Element and directivity pattern for the BiDi SAR mode with the TerraSAR-X antenna panel.

The recording of both beams implies that the acquisition PRF has to be approximately doubled. BiDi moreover imposes some constraints on the particular PRF in order to be able to filter the bandwidths of the forward and backward beams during the processing. Since high PRFs are needed, there are additional constraints to the swath width and/or look angles. A detailed discussion can be found in Mittermayer et al., 2013.

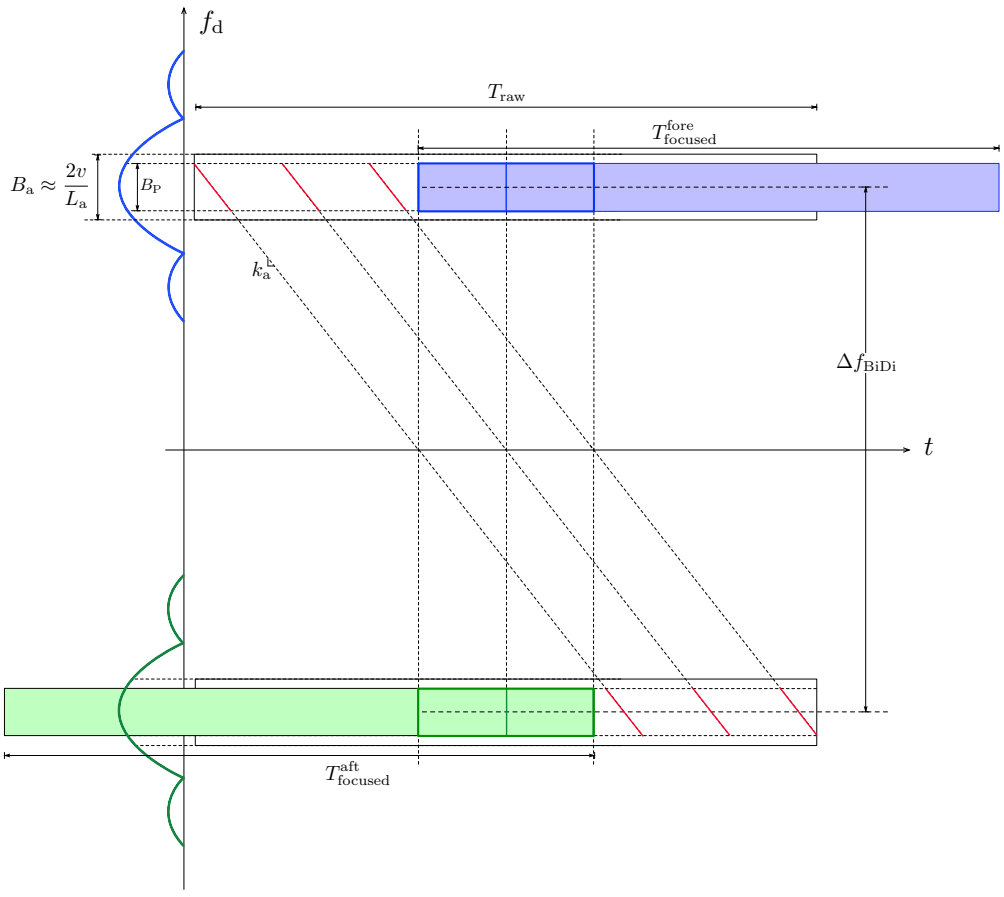

FIGURE 2.17: Time-frequency diagram for the BiDi SAR mode

Fig. 2.17 shows the corresponding (unwrapped) time-frequency support. The spectral separation that can be achieved is $\Delta f_{\text{BiDi}} \approx 38$ kHz. Note that both beams are acquired simultaneously, however, the delay between the observation of a common target is given by $\Delta t_{\text{BiDi}} = t_0^{\text{fore}} - t_0^{\text{aft}} = \Delta f_{\text{BiDi}} / |k_{\text{a}}|$. For a typical TerraSAR-X BiDi acquisition acquired at an incidence angle of 21.5°, the Doppler rate results in about -6.3 kHz, being the delay approximately 6 s.

2.2.5 Multi-platform squinted SAR

An interesting concept related to the retrieval of 2-D ground displacement employing interferometry is the use of constellations of two satellites, working in monostatic mode, one of them oriented according to the zero-Doppler plane and a second one squinted with respect to the first one (Ansari et al., 2016). In each pass the 2-D deformation can be obtained taking advantage of both lines of sight. By combining different geometries, e.g., ascending and descending, the 3-D deformation can be retrieved.

Another possibility, following the same baseline of employing two lines of sight, is the use of a bistatic system based on a companion satellite orbiting ahead or behind of an illuminator satellite. This is the idea of the ESA's Earth Explorer 10 Harmony mission proposal (former STEREOID) (Lopez-Dekker et al., 2018).

The consideration of the correlation of the turbulent troposphere between both lines of sight has been studied in Prats-Iraola et al., 2017, where the 2-D and 3-D achievable performances are provided.

2.3 SAR Interferometry

The exploitation of the phase differences between two or more complex-valued SAR images, acquired either from different orbital positions and/or at different instants of time is known as SAR Interferometry (InSAR). The phase difference between two images can be used to measure different geophysical quantities, such as topography, deformation, glacier flow, ocean currents, etc. In this section a brief review of the interferometric principles following a geometrical approach is presented. A simplified geometry is assumed, considering a flat Earth and rectilinear trajectory of the platform, carrying the SAR antenna.

There are mainly three possibilities for SAR Interferometry:

(i) Single-pass along-track interferometry (ATI): the surface is observed simultaneously with two spatially separated antennas in the direction of the platform movement. This configuration is mainly used to study ocean surface currents or moving objects, as ships or vehicles on ground, (Goldstein and Zebker, 1987).

(ii) Single-pass across-track interferometry: the antennas are separated in the across-track direction. We can moreover differentiate between *monostatic* acquisitions, if each antenna is used to transmit and receive or *multistatic* acquisitions if the backscattered signal is received by multiple receive antennas, different to the antenna that was used to transmit. In the case of having one transmit antenna and a separate receive antenna, we refer to *bistatic* acquisitions. Interferometric acquisitions in single-pass configuration are usually employed for Digital Elevation Model (DEM) generation (Zebker and Goldstein, 1986, Gabriel and Goldstein, 1988), e.g. the NASA Shuttle Radar Topography Mission (SRTM) carried out in 1999 (Farr et al., 2007) or the TanDEM-X mission (Krieger et al., 2004) since 2010.

(iii) Repeat-pass interferometry: repeated acquisitions are performed at different times, enabling the possibility to study dynamic processes of the Earth surface, as e.g., land deformation and glacier flow (Gabriel et al., 1989).

2.3.1 Across-track interferometry

Let us consider the across-track acquisition geometry depicted in Fig. 2.18, in which two SAR images are acquired over the same area. Assuming a repeat-pass scenario, the first SAR image, referred to as master image, is acquired from the position M. A second image, referred to as slave image is taken from the position S. The vector between the phase centers of both antennas, $\mathbf{B}$, is known as baseline.

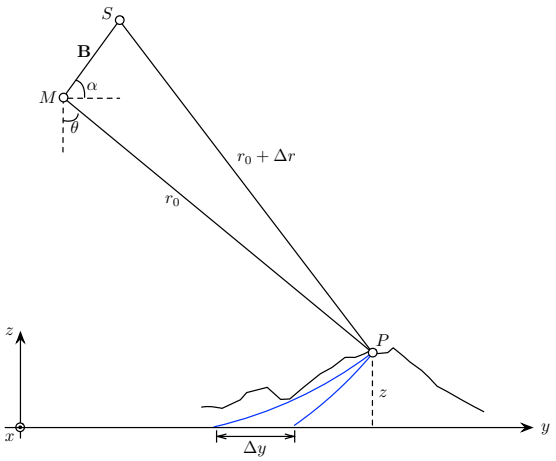

FIGURE 2.18: Schematic representation of the across-track SAR interferometer

If we consider a point target on ground, P, distant r and $r + \Delta r$ to the master and slave antenna phase centers, the baseline vector can be decomposed into its perpendicular, $B_\perp$, and parallel, $B_\parallel$, component, as indicated in Fig. 2.19. Assuming a side looking angle, θ, and an angle α between the baseline vector and the horizontal component:

$$\begin{cases} B_\perp = |\mathbf{B}| \cos(\theta - \alpha) \\ B_\parallel = -|\mathbf{B}| \sin(\theta - \alpha) \end{cases} \tag{2.32}$$

The complex reflectivity functions of the master, u_M, and slave, u_S, signals are given by:

$$a_M = |u_M| \, e^{j\phi_M} \qquad\qquad a_S = |u_S| \, e^{j\phi_S}, \tag{2.33}$$

where $|u_M|, |u_S|$, ϕ_M and ϕ_S are the amplitudes and phases of the master and slave signals, respectively. Assuming monostatic acquisitions in a repeat-pass scenario, the phase values for the master, ϕ_M, and slave, ϕ_S, acquisitions can be written as:

$$\phi_M = -\frac{4\pi}{\lambda} r_0 + \phi_{\text{scat,M}} + \phi_{\text{noise,M}} \qquad \phi_S = -\frac{4\pi}{\lambda}(r_0 + \Delta r) + \phi_{\text{scat,S}} + \phi_{\text{noise,S}}, \tag{2.34}$$

where λ is the radar wavelength, r_0 and $r_0 + \Delta r$ are the distances from the antenna phase centers to the target, $\phi_{\text{scat,M}}$ and $\phi_{\text{scat,S}}$ are the phase contributions due to the scattering mechanism and $\phi_{\text{noise,M}}$ and $\phi_{\text{noise,S}}$ are the phase noise contributions due to thermal noise.

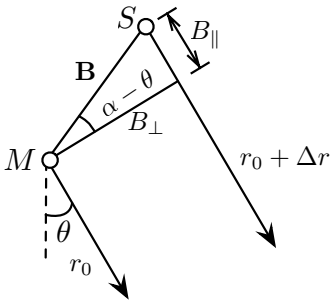

FIGURE 2.19: Interferometric baseline geometry. Detail of perpendicular and parallel baseline components.

The different path of the radar signals between the antenna phase centers and the ground target causes a misalignment between both SAR images, this is due to the parallax effect: assuming the across-track configuration from Fig. 2.18, the apparent position of a common target, P, at height z, is different between surveys by Δy. In general, the larger the perpendicular baseline, the larger the misalignment and its variation across the scene. In order to form an interferogram, precise pixel-by-pixel alignment is necessary. This is achieved through the so-called coregistration procedure (Gabriel and Goldstein, 1988), in which the slave image is warped to the master geometry. After the slave image is overlaid to the master geometry, the interferogram can be formed as the conjugated complex product between both images:

$$v = u_M \cdot u_S^* = a_M a_S e^{j(\phi_M - \phi_S)} = a_M a_S e^{j\phi} \tag{2.35}$$

Assuming that the scattering mechanism does not change between acquisitions, the (non-ambiguous) phase difference only depends on the path length difference, Δr, and the differential thermal noise, $\Delta\phi_{\text{noise}}$ (Just and Bamler, 1994):

$$\phi = -\frac{4\pi}{\lambda}\Delta r + \Delta\phi_{\text{noise}}. \tag{2.36}$$

Nevertheless, due to the cyclic nature of any phase measurement, the interferometric phase is only measurable in the main interval,$[-\pi, \pi[$:

$$\varphi = W(\phi) = mod\{\phi + \pi, 2\pi\} - \pi = \phi - 2\pi \cdot k, k \in \mathbb{Z}, \tag{2.37}$$

with $W(\cdot)$ being the wrapping operator, $mod\{\cdot, 2\pi\}$ the modulo-2π operation and k the index of the ambiguity band. The removal of the ambiguity, i.e., the determination of k is carried out using phase unwrapping algorithms (Ghiglia and Pritt, 1998, Davidson and Bamler, 1999, Pritt and Shipman, 1994, Goldstein et al., 1988, Costantini, 1998, Wei Xu and Cumming, 1996). For further analyses, it is assumed in the following that the unwrapping of the phase has been carried out.

Applying the cosine's rule to the triangle MSP from Fig. 2.18, we obtain:

$$\begin{aligned}(r_0 + \Delta r)^2 &= r_0^2 + B^2 - 2r_0 \cdot B\cos(\frac{\pi}{2} - (\theta - \alpha)) \\ &= r_0^2 + B^2 - 2r_0 \cdot B\sin(\theta - \alpha)\end{aligned} \tag{2.38}$$

Considering the order of magnitude of the previous parameters for a spaceborne scenario and (2.32), Δr can be approximated as:

$$\Delta r \approx \frac{B^2}{2r} - B\sin(\theta - \alpha) \approx -B\sin(\theta - \alpha), \tag{2.39}$$

resulting in an interferometric phase given by $\phi \approx -\frac{4\pi}{\lambda}B\sin(\theta - \alpha)$. The differential interferometric phase between two targets separated in the across-track direction, P and P', observed with looking angles θ and $\theta + \Delta\theta$, is given by:

$$\begin{aligned}\Delta\phi &= -\frac{4\pi}{\lambda}\Delta(\Delta r) \\ &= -\frac{4\pi}{\lambda}\{B\sin(\theta - \alpha) - B\sin(\theta + \Delta\theta - \alpha)\} \\ &= -\frac{4\pi}{\lambda}B\{2\sin(\frac{\Delta\theta}{2})\cos(\theta + \Delta\theta - \alpha)\} \\ &\approx -\frac{4\pi}{\lambda}\Delta\theta B_\perp,\end{aligned} \tag{2.40}$$

having made use of the small-angle approximation for the sine function, i.e., $\sin(\Delta\theta) \approx \Delta\theta$, and taking into account that $\Delta\theta$ is small in comparison to $\theta - \alpha$. From (2.40) we observe that the InSAR phase difference between two ground points depends on the perpendicular baseline, $B_\perp$, and on the differential looking angle, $\Delta\theta$. In the following, we analyze the contributions to the differential interferometric phase.

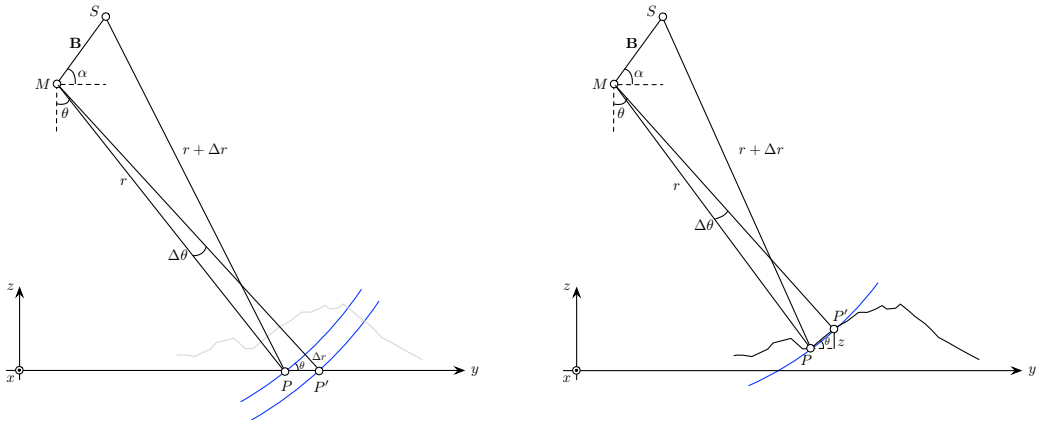

(a) Flat Earth phase contribution

(b) Topographic phase contribution

FIGURE 2.20: Contributions to the interferometric phase

If we assume that both ground points across track are located at the same height, as depicted in Fig. 2.20(a), and applying again a small-angle approximation, we obtain $r\sin(\Delta\theta) \approx r\Delta\theta = \Delta r/\tan(\theta)$. Therefore the contribution of the range difference between two separated ground points across track is given by:

$$\Delta\phi_{\text{flat Earth}} = -\frac{4\pi}{\lambda}\frac{B_\perp}{r}\frac{\Delta r}{\tan(\theta)}. \tag{2.41}$$

Now, if we assume that the ground points are located at the same range but at different heights, as shown in Fig. 2.20(b), the phase difference will account only for the topography. In this case we can apply the approximation $r\sin(\Delta\theta) \approx r\Delta\theta = \Delta z/\sin(\theta)$, being Δz the height difference. The contribution of the topography to the interferometric phase is therefore given by:

$$\Delta\phi_{\text{topography}} = -\frac{4\pi}{\lambda}\frac{B_\perp}{r}\frac{\Delta z}{\sin(\theta)} \tag{2.42}$$

From (2.42) and taking infinitesimal differences, we obtain the height sensitivity of the interferometer:

$$\frac{\partial\phi}{\partial z} = -\frac{4\pi}{\lambda}\frac{B_\perp}{r\sin(\theta)}. \tag{2.43}$$

The height of ambiguity, h_{amb}, corresponds to the height resulting from a complete phase cycle and is given by:

$$h_{\text{amb}} = \frac{\lambda}{2}\frac{r\sin(\theta)}{B_\perp}. \tag{2.44}$$

2.3.2 Differential SAR interferometry (DInSAR)

In repeat-pass acquisition scenarios an additional phase contribution appears if the terrain is affected by deformation (Gabriel et al., 1989, Massonnet et al., 1993). Differential SAR interferometry (DInSAR) profits from the temporal baseline between acquisitions to monitor geodynamic phenomena, as volcano deformation, tectonic strain, urban subsidence, etc. Let us assume that between two interferometric acquisitions, deformation of the ground has taken place, which can be characterized by a ground displacement vector, $\vec{g}$. The projection of the latter vector onto the (normalized) radar line of sight vector, $\vec{g}$, produces a phase given by:

$$\phi_{\Delta r_{\text{defo}}} = \frac{4\pi}{\lambda} < \hat{e}_{\text{LOS}}, \vec{g} >= \frac{4\pi}{\lambda} \Delta r_{\text{defo}}, \tag{2.45}$$

being Δr_{defo} the projection of the ground displacement onto the radar line of sight. The DInSAR technique intends to isolate the phase contribution due to ground displacement from other contributions. The contributions to the InSAR phase are given by:

$$\Delta\phi = \Delta\phi_{\delta r} + \Delta\phi_{\text{topography}} + \Delta\phi_{\text{flat Earth}} + \Delta\phi_{\text{orb}} + \Delta\phi_{\text{prop}} + \Delta\phi_{\text{scat}} + \Delta\phi_{\text{noise}}, \tag{2.46}$$

with $\Delta\phi_{\text{topography}}$ being the topographic phase (2.42) and $\Delta\phi_{\text{flat Earth}}$ the flat Earth phase (2.41). These terms can be reduced to a minimum by synthesizing a phase from an external DEM and employing precise orbital information. Additional terms, that also have to be removed, are the following:

1. $\Delta\phi_{\text{orb}}$: accounts for the additional phase due to the differential orbital error, usually known as baseline error, of the acquisitions in the generation of the synthetic phase.

2. $\Delta\phi_{\text{prop}}$: corresponds to the differential propagation delay of the radar signals through the transmission medium, i.e, the atmosphere. If the atmospheric delay is not compensated, the performance of interferometric techniques in repeat-pass scenarios can be seriously degraded (Goldstein, 1995). The atmospheric delay is split into tropospheric and ionospheric terms. Tropospheric delays are caused by variations in pressure, temperature, and relative humidity in the lower part of the troposphere. The differential tropospheric contribution is, for repeat-pass spaceborne scenarios, correlated spatially (hundreds of meters) but not temporally (hours or days) (Hanssen, 2001) and can introduce delays of a few centimeter and therefore mask out tectonic or volcanic signals of interest. Tropospheric corrections are usually performed employing numerical weather model data (Wadge et al., 2002), GNSS (Williams et al., 1998) and/or spectrometer data (Li et al., 2006). A correction can be also performed from the interferometric phase by assuming a linear relationship between phase and topography regarding the stratified troposphere (Wicks Jr. et al., 2002, Tarayre and Massonnet, 1996). Statistical methods employing time-series analyses, as e.g., PSI (Ferretti et al., 2001) are able to estimate and remove the atmospheric phase screen (APS) contributions. Ionospheric effects are caused by fluctuations in ionospheric electron density. The latter effect results in a phase advance of the radar signal, which introduces moreover an azimuth shift modulation in the SAR images (Gray et al., 2000). There are several techniques to compensate differential ionospheric effects for repeat-pass spaceborne scenarios, e.g., the range split-spectrum method, sensitive to the range variations, which exploits the dispersive propagation of the ionosphere to separate the ionospheric phase delay from the non-dispersive phase term of an interferogram (Gomba et al., 2016). The azimuth shift method, sensitive in the azimuth direction, exploits the proportional relation between differential azimuth shift and the azimuth derivative of the differential ionosphere (Kim et al., 2011).

3. $\Delta\phi_{\text{scat}}$: refers to the extra delay due to variations of the scattering characteristics of the ground. It may be a deterministic phase offset due to a change in the dielectric constant as a consequence of variations of the soil moisture (Morrison et al., 2011, De Zan and Gomba, 2018) or a random phase due to temporal decorrelation (Rocca, 2007).

4. $\Delta\phi_{\text{noise}}$: accounts for the differential phase noise due to thermal noise of the receiver.

2.3.2.1 Accuracy of the interferometric phase

Under the assumption of a scene characterized by distributed scatterers, which are modeled as zero-mean complex Gaussian random variables (Section 2.1.2), the Cramér-Rao bound for the interferometric phase standard deviation, after N samples of the complex interferogram have been averaged (multi-looking factor), is given by (Rodriguez and Martin, 1992):

$$\sigma_{\Delta\phi} = \frac{1}{\sqrt{2N}} \frac{\sqrt{1-\gamma^2}}{|\gamma|}, \tag{2.47}$$

assuming that the number of independent samples, N, is larger than 4 and for values of γ not close to 0.

2.3.2.2 Coherence: decorrelation sources

The complex correlation or coherence of two SAR images is given by (Bamler and Hartl, 1998, Rosen et al., 2000):

$$\gamma = \frac{E\{u_M \cdot u_S^*\}}{\sqrt{E\{|u_M|^2\} + E\{|u_S|^2\}}} = |\gamma|\, e^{j\Delta\phi} \tag{2.48}$$

We refer usually to the modulo of the coherence, $|\gamma|$, when calculating the coherence. The different sources of decorrelation can be written as (Zebker and Villasenor, 1992, Hanssen, 2001):

$$|\gamma| = \gamma_{\text{geom}} \cdot \gamma_{\text{Doppler}} \cdot \gamma_{\text{temp}} \cdot \gamma_{\text{vol}} \cdot \gamma_{\text{noise}}, \tag{2.49}$$

being:

(i) γ_{geom}: corresponds to geometric decorrelation due to the spatial baseline. A slightly different viewing geometry between surveys implies that the coherent sum of all independent scatterers within the resolution cell is also relatively different. The baseline decorrelation is related to the different incident angles of the SAR acquisitions and leads to a critical baseline, above which the interferometric phase is pure noise. The geometric decorrelation can be reduced applying spectral filtering (Gatelli et al., 1994).

(ii) γ_{Doppler} : refers to the decorrelation due to a mismatch of the Doppler spectra. In case of StripMap acquisitions, the Doppler spectra mismatch corresponds to different Doppler centroid frequencies due to a change in the platform attitude:

$$\gamma_{\text{Doppler}} = \frac{B_a - |\Delta f_{dc}|}{B_a} \approx 1 - |\Delta f_{DC}| \frac{L_a}{2v_s}, \tag{2.50}$$

where Δf_{dc} is the difference between Doppler centroid frequencies of master and slave acquisitions, L_a is the antenna length in azimuth, and v_s the platform velocity.

(iii) γ_{temp}: corresponds to temporal decorrelation, especially important in repeat-pass interferometry over areas characterized by distributed scatterers. A mathematical framework has been established in Rocca, 2007 over surfaces characterized by distributed scatterers, where the temporal decorrelation mechanism has been modeled as the motion of the scatterers within a resolution cell according to Brownian or Markovian processes.

(iv) γ_{noise}: refers to thermal noise and can be related to the signal-to-noise-ratio (SNR) of the radar system as (Zebker and Villasenor, 1992, Just and Bamler, 1994):

$$\gamma_{\text{noise}} = \frac{1}{1 + SNR^{-1}} \tag{2.51}$$

(v) γ_{vol}: corresponds to volumetric decorrelation, induced by a finite number of distributed scatterers in the vertical dimension.

When working with real data, coherence is usually estimated by replacing the expectation values by spatial averagings of L independent samples (Bamler and Hartl, 1998). This estimate is biased as it tends to overestimate low coherence. For large numbers of samples L it becomes asymptotically unbiased. Approaches toward unbiasing the coherence can be found in Touzi et al., 1999.

2.3.3 Time series analyses

Repeat-pass interferometry represents a very powerful technique for crustal deformation analyses. However, when very slow deformation processes are intended to be retrieved, consideration of phase noise from different sources (eq. 2.46), that can mask out the geophysical signal, have to be considered. Among the most important contributions, we find the effect of the atmospheric propagation ($\Delta\phi_{\text{prop}}$), errors in the orbital determination ($\Delta\phi_{\text{orb}}$), the residual topographic error of the external DEM ($\Delta\phi_{\text{topography}}$) and the noise introduced due to temporal changes in the scattering properties or due to slightly different observation geometries of the targets ($\Delta\phi_{\text{scat}}$).

A solution to cope with these effects is the use of multi-temporal analysis. This consists on the evaluation of stacks of data through a statistical analysis in order to eliminate noise contributions. One of the first approaches corresponds to the persistent scatterers interferometry (PSI) (Ferretti et al., 2001) technique, which consists on identifying scatterers whose amplitude remains stable over time and for different observation angles. A modified method that exploits the spatial correlation of the phases of scatterers selected based on its phase stability, rather than its amplitude, is more suitable for the observation of temporally-variable processes as volcanic deformation and has been introduced by Hooper et al., 2004. The PSI approach is however more suitable for urban scenarios, where resolution cells are characterized by the presence of dominant point scatterers.

For crustal deformation, the resolution cells are usually characterized by distributed scatterers, implying that temporal decorrelation effects predominate, being more adequate to evaluate subsets of interferograms with small temporal baseline. This is the principle of the small-baseline subsets (SBAS) (Berardino et al., 2002), which moreover minimizes the geometrical baseline and the Doppler differences within each subset of interferograms, in order to minimize geometric decorrelation effects. The procedure consists basically on unwrapping spatially the phases of each subset, applying the single value decomposition method to link them and obtain a phase series, from which the geophysical signal can be extracted.

Combinations of both approaches have been introduced in the literature, for instance a full resolution SBAS method to extract coherent distributed scattering targets (Hooper,

2008). The SqueeSAR technique processes jointly distributed and persistent scatterers taking into account their different statistical behavior (Ferretti et al., 2011). An extension of the latter consists in identifying multiple scattering mechanisms from the analysis of the covariance matrix (Fornaro et al., 2015). Advances have been also done to process large amount of data from current (Sentinel-1) or future missions avoiding to reprocess the whole stack when new acquisitions are available (Ansari et al., 2017).

2.4 Mutual shift estimation

The estimation of the mutual shift between two SAR images is a procedure that can serve to multiple purposes. Related to interferometric processing, it aids the coregistration stage (parallax effect compensation), but it might also be used to determine the absolute phase offset (Madsen et al., 1993) by creating a radargrammetric DEM (Leberl, 1990), as, e.g, done for the generation of the raw DEMs of the TanDEM-X mission (Rossi et al., 2012).

As an additional application, the shift estimation between SAR images acquired in a repeat-pass configuration can provide an unambiguous and absolute estimation of the 2-D ground deformation – in line-of-sight and azimuth directions. This supposes an added value with respect to DInSAR, which is insensitive to azimuth displacements and moreover provides ambiguous shift estimates in the radar line of sight. The ground displacement in the line of sight direction can be obtained by compensating the shifts due to (geometric) parallax error between both acquisitions to the correlation shift. This can be achieved by simulating the acquisition geometry with an external DEM and precise orbital information.

Two different approaches can be employed to measure the relative shifts between SAR acquisitions. The first of them, usually referred as offset tracking (OT) or speckle tracking (ST), relies on the calculation of the mutual shift applying the cross-correlation operation and is described in Section 2.4.1. The second family of approaches, usually known as split-bandwidth interferometry (SBI), or spectral diversity (SD), are based on the extraction of sublooks in range or azimuth, respectively, and the computation of the differential interferogram, whose phase is proportional to the shift. Section 2.4.2 covers these approaches. As it will be seen in the following, both implementations provide the same accuracy (Bamler and Eineder, 2005), however correlation techniques provide unambiguous estimates, whereas the ones based on calculating the differential interferogram of the sublooks interferograms result in ambiguous estimates, due to the wrapped nature of the phase.

The application area of correlation techniques cover the measurement of ground displacements due to seismic events (Michel et al., 1999) and glacier motion estimation (Derauw, 1999, Strozzi et al., 2002).

In the following we assume 1-D signals, without loss of generality. The extension to 2-D signals is immediate.

2.4.1 Cross-correlation

The cross-correlation function between two, one-dimensional, stationary[4] random processes, $X(t)$ and $Y(t)$, is given by (Papoulis, 1991):

$$R_{XY}(\Delta t) = E[X^*(t) \cdot Y(t + \Delta t)], \tag{2.52}$$

where $E[\cdot]$ indicates the expectation, and * the complex conjugate. Assuming that both stationary random processes are ergodic[5], the cross-correlation can be estimated from two single realizations, $x(t)$ and $y(t)$, using the time average cross-correlation function, $r_{xy}(\Delta t)$:

$$r_{xy}(\Delta t) = \frac{1}{2T} \int_{-T}^{T} x^*(t) \cdot y(t + \Delta t) dt, \tag{2.53}$$

[4]We assume, in general, complex-valued processes, $X(t) = A(t) + jB(t)$, being $A(t)$ and $B(t)$ two real stochastic processes. The complex process $X(t)$ is specified in terms of the joint statistics of the real processes, $A(t)$ and $B(t)$.
Wide-sense stationarity (WSS) of the random process $X(t)$ is assumed. This implies that its mean is constant, $E[X(t)] = \eta$, and its autocorrelation, $R_{xx}(t_1, t_2)$, depends only on the lag, $\Delta t = t_1 - t_2$, and not on the particular time instants, i.e., $R_{xx}(t_1, t_2) = R_{xx}(\Delta t)$.

[5]A random process is said to be ergodic if its statistical properties can be deduced from a single, sufficiently long, random sample of the process.

which is an unbiased estimator of $R_{XY}(\Delta t)$, since its mean value tends to the cross-correlation function, $R_{XY}(\Delta t)$; the variance of this estimator tends to 0 as $T \to \infty$.

Let us assume now that the continuous signals $x(t)$ and $y(t)$ have been sampled according to the Nyquist-Shannon theorem delivering the corresponding discrete-time signals, $x[n]$ and $y[n]$. The cross-correlation of both is given by (Proakis and Manolakis, 1996, Oppenheim and Schafer, 2007):

$$r_{xy}[l] = \sum_{k=-\infty}^{\infty} x^*[k] \cdot y[k+l], \tag{2.54}$$

where l is commonly known as the shift or *lag* parameter and the subscript xy indicate the signals being correlated. The cross-correlation function presents following property: $r_{xy}[l] = r^*_{yx}[-l]$.

When performing the cross-correlation between both signals, a finite number of samples from both is extracted. Assuming that their duration is N, we obtain following signals:

$$v[n] = \begin{cases} x[n], & 0 \leq n < N \\ 0, & \text{otherwise} \end{cases} \qquad w[n] = \begin{cases} y[n], & 0 \leq n < N \\ 0, & \text{otherwise} \end{cases} \tag{2.55}$$

We assume in the following that the sampled duration-limited signals, $v[n]$ and $w[n]$ have been normalized to have unitary power:

$$\sum_{k=0}^{N-1} |v[k]|^2 = \sum_{k=0}^{N-1} |w[k]|^2 = 1 \tag{2.56}$$

Considering the finite duration of the signals $v[n]$ and $w[n]$, the following estimator can be considered:

$$\widetilde{r}_{xy}[l] = \frac{1}{N} r_{vw}[l] = \begin{cases} \dfrac{1}{N} \displaystyle\sum_{k=0}^{N-l-1} x^*[k] \cdot y[k+l], & 0 \leq l < N \\ \dfrac{1}{N} \displaystyle\sum_{k=-l}^{N-1} x^*[k] \cdot y[k+l], & -N < l < 0 \\ 0, & |l| \geq N \end{cases} \tag{2.57}$$

To determine the properties of $\widehat{r}_{xy}[l]$, we can calculate its mean, which can be written as:

$$E\{\widetilde{r}_{xy}[l]\} = \begin{cases} \dfrac{N-|l|}{N} r_{xy}[l] & |l| < N \\ 0, & |l| \geq N \end{cases} \tag{2.58}$$

The estimator presented in (2.57) presents a (lag-dependent) bias, which is small for $|l| \ll N$, however should not be ignored. The unbiased estimator of the cross-correlation function can be written as:

$$\widehat{r}_{xy}[l] = \frac{1}{N-|l|} r_{vw}[l] = \begin{cases} \dfrac{1}{N-|l|} \displaystyle\sum_{k=0}^{N-l-1} x^*[k] \cdot y[k+l], & 0 \leq l < N \\ \dfrac{1}{N-|l|} \displaystyle\sum_{k=-l}^{N-1} x^*[k] \cdot y[k+l], & -N < l < 0 \\ 0, & |l| \geq N \end{cases} \tag{2.59}$$

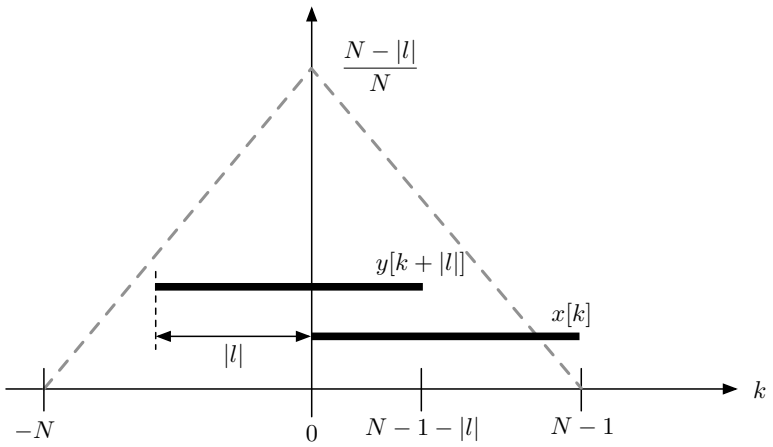

FIGURE 2.21: Normalized overlapping between the signals $x[n]$ and $y[n]$ for a certain lag, l.

To summarize, two estimators of the cross-correlation function for finite-duration signals have been presented: a biased (2.57) and an unbiased (2.59). The only difference between both estimators lies on their normalization factor. The unbiased estimator considers the actual overlapping between sequences, $N-|l|$, for each lag, l. The biased estimator does not account for this, and normalizes by the total number of samples, N. Fig. 2.21 depicts the effective overlapping between the signals $x[n]$ and $y[n]$ for each lag, l. The relationship between both estimators is given by:

$$\widetilde{r}_{xy}[l] = \frac{N-|l|}{N}\widehat{r}_{xy}[l], \tag{2.60}$$

i.e., the biased estimator is the result of multiplying the unbiased estimator by a triangular window.

The lag for which the modulo of the cross-correlation function attains its maximum value corresponds to the shift between both signals. In order to obtain the position of the maximum of the correlation functions with sub-sample accuracy, the functions can be interpolated by convolution with a sinc function. Depending on which cross-correlation estimator is used, two lag estimates can be obtained:

$$\widehat{l} = \arg\max_{l}\{\left|\widehat{r}_{xy}[l]\right|\} \qquad\qquad \widetilde{l} = \arg\max_{l}\{\left|\widetilde{r}_{xy}[l]\right|\} \tag{2.61}$$

It is important to note that both lag estimates provide, in general, different values (except in case the true lag, l, is 0). This is due to the modulation effect originated by the triangular window on the cross-correlation function, which introduces an asymmetry on the cross-correlation peak, shifting effectively its maximum position. This effect is depicted in Fig. 2.22 with simulated data. The left part of the figure shows the unbiased cross-correlation function (black curve). The effect of multiplying the latter by a linear function (green curve) corresponds to the biased function (red curve), which presents an assymetry, as it can be appreciated. The right part of the figure shows the detail around the maximum position. Aside from biasing the correlation function, the maximum position suffers also a displacement.

For practical applications, the preferred estimator is the unbiased estimator, which can be calculated in time-domain from (2.59). However more efficient implementations in the frequency domain provide the biased version of the estimator. For this reason, (2.60) allows easily to obtain the unbiased estimator. Next section provides the details for an efficient computation.

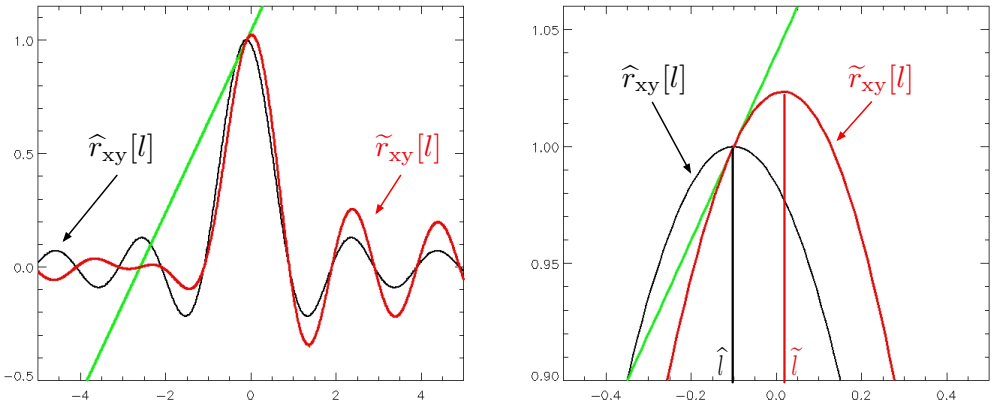

(a) (b)

FIGURE 2.22: Effect of the triangular window modulation on the peak position of the cross-correlation function. The horizontal axis corresponds to the lag, whereas the vertical axis corresponds to the magnitude of the correlation function.

2.4.1.1 Efficient implementation in the frequency domain

It is interesting to note that the cross-correlation operation is very similar to a linear convolution, being the latter given by:

$$x[n] * y[n] = \sum_{k=-\infty}^{\infty} y[k] \cdot x[n-k], \tag{2.62}$$

where $*$ denotes linear convolution. By inspecting (2.54) and (2.62), we can see that by time-reversing and conjugating one of the signals, the cross-correlation can be calculated through linear convolution. Therefore we can write:

$$r_{xy,\mathrm{C}}[m] = x^*[-m] * y[m] \tag{2.63}$$

The subscript $_{\mathrm{C}}$ refers to the coherent correlation, i.e., the correlation of the complex-valued data.

The convolution operation can be performed efficiently in the frequency domain using the (circular) convolution theorem (Oppenheim and Schafer, 2007), which states that the Fourier transform of a convolution of two signals is the pointwise product of their Fourier transforms. Therefore, taking the duration-limited signals, $v[n]$ and $w[n]$, according to (2.55) we obtain:

$$v[n] \circledast w[n] = \mathcal{F}^{-1}\{\mathcal{F}\{v[n]\} \cdot \mathcal{F}\{w[n]\}\}, \tag{2.64}$$

where $\mathcal{F}$ indicates Discrete Fourier transform (DFT) and $\circledast$ circular convolution. A circular convolution operation can be easily converted into a linear convolution by performing a zero-padding operation to the time-domain signals:

$$v_{\mathrm{ZP}}[n] = \begin{cases} v[n], & 0 \le n < N \\ 0, & N \le n < 2N \end{cases} \qquad w_{\mathrm{ZP}}[n] = \begin{cases} w[n], & 0 \le n < N \\ 0, & N \le n < 2N, \end{cases} \tag{2.65}$$

where the subscript ZP indicates that the time-domain signal has been zero-padded by a factor of two, i.e. reaching a duration double than the original signal.

When cross-correlating complex SAR signals, a compensation for systematic differential phase contributions is necessary, in order to align the complex vectors of both signals. The most relevant phase contribution is due to the flat Earth phase (2.41) and the topography (2.42), and we might refer to the contribution of both as the geometric phase, $\phi_{\text{geo}} = \Delta\phi_{\text{flat Earth}} + \Delta\phi_{\text{topography}}$. Fig. 2.23 summarizes the operations to compute the coherent cross-correlation. In the first place both signals are limited in time by multiplying them by a rectangular signal. The geometric (differential) phase can be compensated by multiplying one of the signals by $e^{-j\phi_{\text{geo}}}$. Afterwards a zero-padding (by a factor 2) is applied in the time domain to both signals, so that the convolution, implemented through FFTs, becomes linear. The debiasing of the cross-correlation function can be afterwards performed.

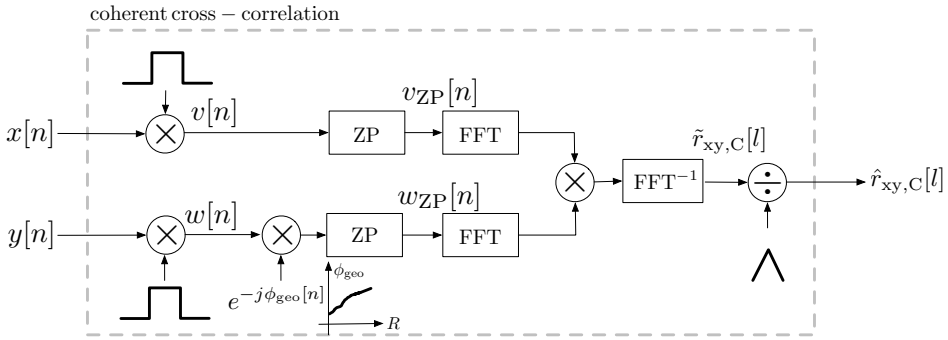

FIGURE 2.23: Block diagram of an efficient computation of the coherent cross-correlation function.

The biased estimator of the coherent cross-correlation, $\tilde{r}_{xy}$, can therefore be calculated in the frequency domain according to:

$$\tilde{r}_{xy,C}[l] = v[n] * w[n] = \mathcal{F}^{-1}\{\mathcal{F}\{v_{ZP}[n]\} \cdot \mathcal{F}\{w_{ZP}[n] \cdot e^{-j\phi_{\text{geo}}[n]}\}\}, \tag{2.66}$$

where the DFT can be efficiently performed through Fast Fourier Transform (FFT). The unbiased estimator, $\hat{r}_{xy,C}[l]$, can be obtained substituting (2.66) in (2.60).

The mutual shift, $\hat{l}$, can be found as the position of the maximum of the modulo of the cross-correlation function, $\left|\hat{r}_{xy,C}[l]\right|$ [6].

2.4.1.2 Incoherent cross-correlation

The incoherent version of the cross-correlation operation correlates the intensities or magnitudes between signals, discarding the phase information. This operation is also known as speckle tracking. Before the incoherent cross-correlation can be applied, the signals have to be detected: each signal has to be oversampled by a factor 2 in order to accommodate the resulting bandwidth after taking the absolute value. This operation can be efficiently performed by zero padding the signal spectrum, as illustrated in Fig. 2.25

The unbiased estimator of the incoherent cross-correlation can be written as:

$$\hat{r}_{xy,I}[l] = \begin{cases} \dfrac{1}{2N-|l|} \displaystyle\sum_{k=0}^{2N-l-1} v'[k] \cdot w'[k+l], & 0 \le l < 2N \\ \dfrac{1}{2N-|l|} \displaystyle\sum_{k=-l}^{2N-1} v'[k] \cdot w'[k+l], & -2N < l < 0 \\ 0, & |l| \ge N \end{cases} \tag{2.67}$$

[6] Note that the obtained shift has to be divided by two, due to the applied temporal zero padding for the linear convolution computation.

The subscript $_{\mathrm{I}}$ refers to the incoherent correlation, i.e., correlation of the real-valued data after a detection has been performed.

Fig. 2.24 shows the procedure to carry out an incoherent cross-correlation efficiently in the frequency domain. In this case, since the phase information has been discarded at the detection stage, no compensation of the phase, e.g., due to the topography, is needed, in contrast to the coherent case.

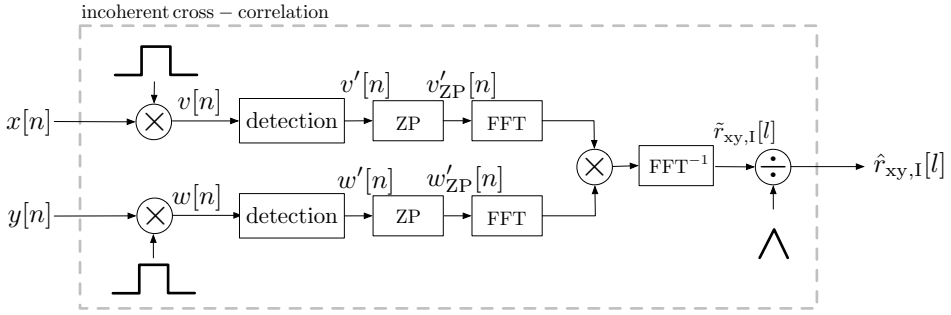

FIGURE 2.24: Block diagram of an efficient computation of the incoherent cross-correlation function.

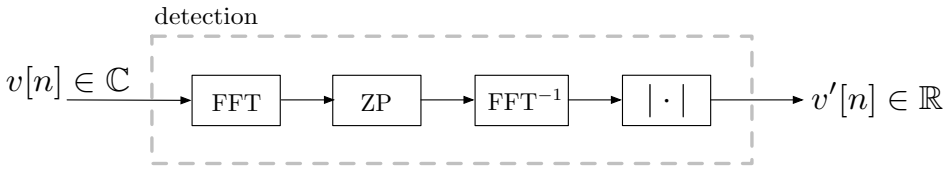

FIGURE 2.25: Block diagram for the detection of a complex signal

The biased estimator of the incoherent cross-correlation, $\tilde{r}_{xy}$, can therefore be calculated in the frequency domain according to:

$$\tilde{r}_{xy,\mathrm{I}}[l] = v'[n] * w'[n] = \mathcal{F}^{-1}\{\mathcal{F}\{v'_{\mathrm{ZP}}[n]\} \cdot \mathcal{F}\{w'_{\mathrm{ZP}}[n]\}\}, \tag{2.68}$$

where the DFT can be efficiently performed through FFT. The unbiased estimator, $\hat{r}_{xy,I}[l]$, can be obtained substituting (2.68) in (2.60).

The mutual shift, $\hat{l}$, can be found as the position of the maximum of the modulo of the cross-correlation function, $\left|\hat{r}_{xy,\mathrm{I}}[l]\right|$ [7].

It is worth mentioning that correlating detected signals induces a bias of the cross-correlation function, due to correlating positive real numbers. This results in a overestimation of the correlation coefficient (maximum value of the correlation function). In the case of homogeneous patches, where every resolution cell corresponds to distributed scatterers, the correlation coefficient can be approximated, for high coherent values, by (Yague-Martinez et al., 2010):

$$\widetilde{\gamma} \approx \frac{3}{4} + \frac{|\gamma|^2}{4}, \tag{2.69}$$

where γ is the true value of the correlation coefficient and $\widetilde{\gamma}$ is obtained from incoherent cross correlation.

[7] Note that the obtained shift has to be divided by four, due to (i) the applied temporal zero padding for the linear convolution computation and (ii) the spectral zero padding for the detection.

2.4.1.3 Examples with TerraSAR-X data

Some experimental results with TerraSAR-X data are provided. Figure 2.26 shows two 128 pixel $\times$ 128 pixel master and slave patches corresponding to an homogeneous area (a) and inhomogeneous area (b). After correlating both homogeneous patches, the modulo of the coherent cross-correlation function is shown in (c). The modulo of the incoherent cross-correlation function of the inhomogeneous patches is shown in (d). In order to obtain sub-pixel accuracy, the correlation functions are oversampled in the region surrounding the maximum, the modulo of the oversampled functions is shown in (e) and (f), for the coherent and incoherent correlation, respectively.

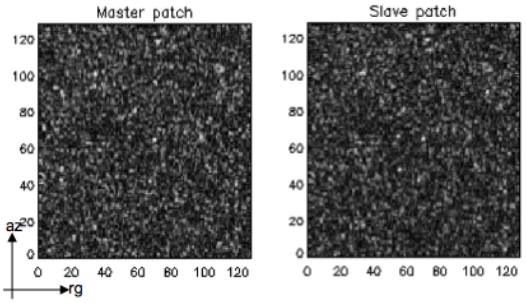

(a) Amplitude of master and slave patches over an homogeneous area

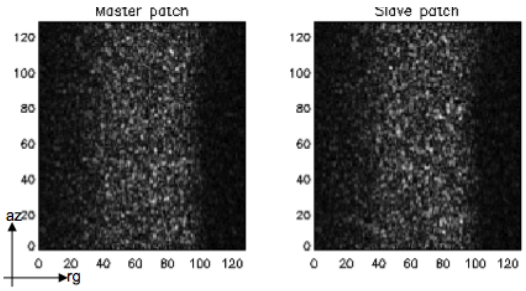

(b) Amplitude of master and slave patches covering a feature invariant in azimuth direction

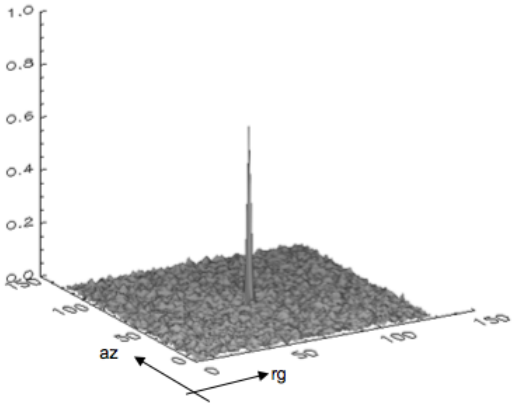

(c) Modulo of the coherent cross-correlation function

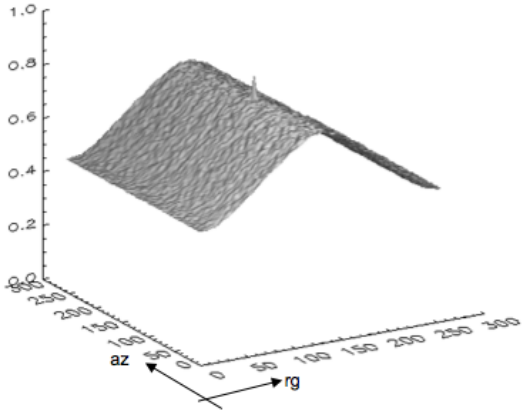

(d) Modulo of the incoherent cross-correlation function. The function presents invariance in azimuth direction

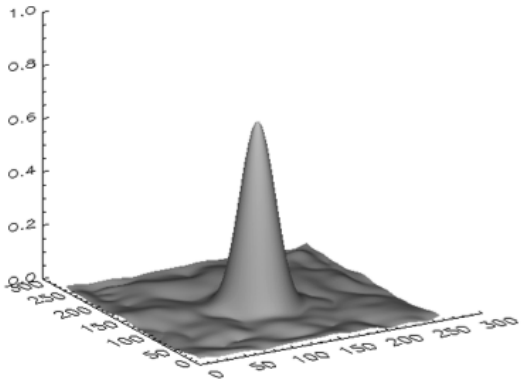

(e) Modulo of the oversampled coherent cross-correlation function in the surroundings of the peak.

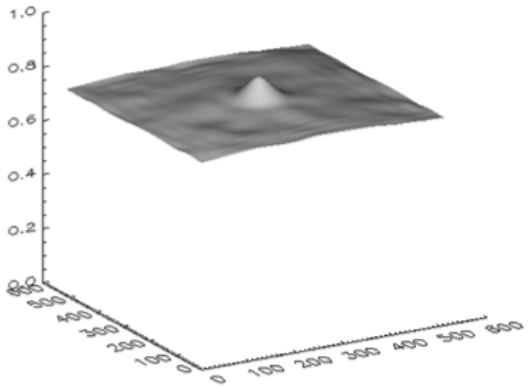

(f) Modulo of the oversampled incoherent cross-correlation function in the surroundings of the peak. Note the bias.

FIGURE 2.26: Coherent and incoherent cross-correlation examples with TerraSAR-X. Source: Yague-Martinez et al., 2010

2.4.1.4 Shift estimation accuracy

The optimum estimator (Maximum Likelihood Estimator) of the mutual shift between partially correlated stationary circular Gaussian signals is the coherent cross-correlation (Bamler, 2000). The incoherent cross-correlation, i.e., cross-correlating the signal intensities, appears as a sub-optimum, however practical for many implementations. In Bamler, 2000 and De Zan, 2014, the derivation of the accuracy that can be achieved with both versions of the cross-correlation estimation can be found, respectively. The procedure to obtain the uncertainty of the lag that maximizes the modulo of the cross-correlation function depends on the curvature of the correlation peak, i.e., the variance of $\left|r_{xy}(l)\right|'$ and on the average slope of $\left|r_{xy}(l)\right|'$ at the (true) position of the maximum, l_0 (Bamler, 2000 and De Zan, 2014):

$$\sigma_{\hat{l}}^2 = \frac{Var\{\left|r_{xy}(l_0)\right|'\}}{E\{\left|r_{xy}(\tilde{l})\right|''\}^2}, \tag{2.70}$$

where $'$ and $''$ denote the first and second derivative, respectively. Eq. (2.70) can be understood as the variance of the zero-crossing position of $\left|r_{xy}(l)\right|'$.

Assuming a large number of samples of the correlation estimation window, N, the standard deviation of the coherent cross-correlation corresponds to the Cramér Rao bound and is given by (Bamler and Eineder, 2005):

$$\sigma_{l,C} = \sqrt{\frac{3}{2N}}\frac{\sqrt{1-\gamma^2}}{\pi\gamma}, \tag{2.71}$$

with γ being the interferometric coherence.

The standard deviation of the incoherent cross-correlation, also for large N, is given by (De Zan, 2014):

$$\sigma_{l,I} = \sqrt{\frac{3}{10N}}\frac{\sqrt{2+5\gamma^2-7\gamma^4}}{\pi\gamma^2}. \tag{2.72}$$

Eqs. (2.71) and (2.72) provide the accuracy of the mutual shift in units of resolution elements. A multiplication by the resolution provides the estimate in metrical units. In case of working with oversampled data, by a factor osf, the shift in units of samples can be obtained by multiplying the standard deviations by osf and dividing the number of samples in the estimation window by osf. Effectively, this results in multiplying eqs. (2.71) and (2.72) by $\text{osf}^{3/2}$.

Combining (2.36) and (2.47), we obtain that the achievable accuracy in the retrieval of the range shift, Δr, using interferometry is given by:

$$\sigma_{\Delta r}^{\text{InSAR}} = \frac{\lambda}{4\pi}\sigma_{\Delta\phi} = \frac{\lambda}{4\pi}\frac{1}{\sqrt{2N}}\frac{\sqrt{1-\gamma^2}}{\gamma}. \tag{2.73}$$

Defining the relative variance between (coherent) cross-correlation in the line of sight and interferometry as the quotient between the variance of the cross-correlation, $\sigma_{\Delta r,\text{CCC}}^2$, and the variance of the interferometric phase, $\sigma_{\Delta r,\text{InSAR}}^2$, i.e.:

$$\rho = 10\cdot\log_{10}\left\{\frac{\sigma_{\Delta r,\text{CCC}}^2}{\sigma_{\Delta r,\text{InSAR}}^2}\right\} = 10\cdot\log_{10}\left\{48\cdot\frac{\rho_r^2}{\lambda^2}\right\}, \tag{2.74}$$

we obtain that, in case of TerraSAR-X, with $\lambda = 3.1$cm, and a range resolution, ρ_r =1.2m, the performance of the coherent cross-correlation is 48.5 dB worse than the one of interferometry.

The use of cross-correlation is not just restricted to the line-of-sight direction but can be also applied in the azimuth direction. Fig. 2.27 shows the normalized accuracies ($\sigma_l\sqrt{N}$) that can be achieved in the line of sight (ρ_r =1.2 m) and azimuth (ρ_a =2.5 m) employing coherent cross-correlation and incoherent cross-correlation with the TerraSAR-X system, including the accuracy of the shift estimation with interferometry for reference purposes. Fig. 2.27 (bottom) shows the relative variance of the coherent and incoherent cross-correlation with respect to InSAR.

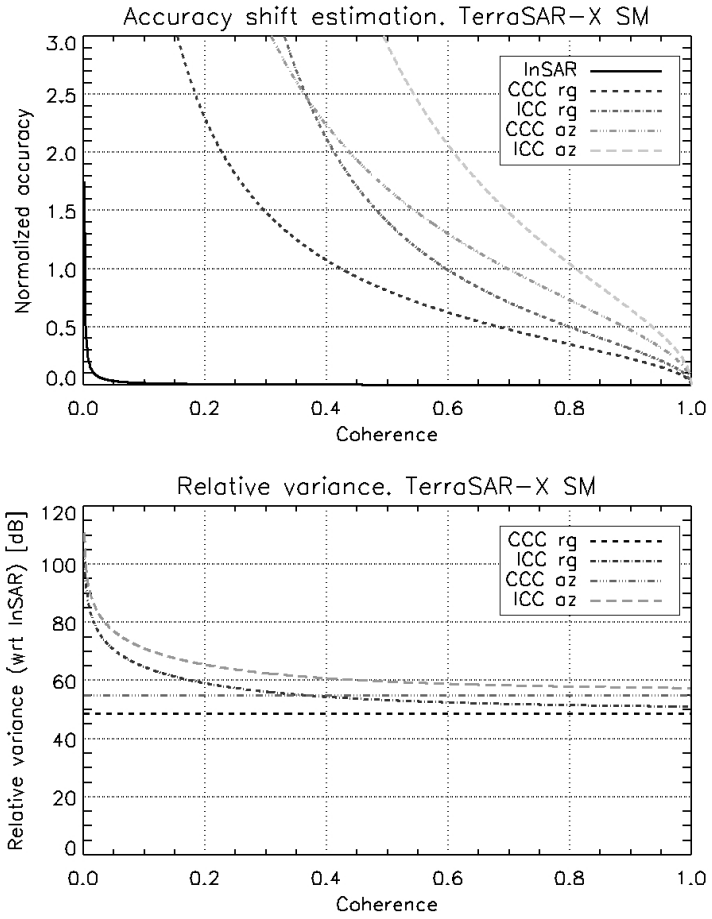

FIGURE 2.27: (Top) normalized accuracy ($\sigma_l\sqrt{N}$) of the shift estimation using interferometry and correlation techniques in range and azimuth directions. (Bottom) Relative variance of correlation techniques with respect to interferometry.

The achievable accuracy through correlation has been provided in terms of resolution elements units. Its accuracy in metrical units will depend on the system resolution. In practical cases, we can state that for ground deformation estimation, interferometry is preferred over correlation in the range direction, due to its better accuracy (for the same product resolution). However cross-correlation in range is a very powerful tool that can complement interferometry in the sense of providing absolute measurements, for, e.g., the determination of the absolute offset or deformation estimates which are not affected by wrapping, therefore very adequate for the study of coseismic events, where large displacements are expected that might make useless the interferometric phase. Cross-correlation in the azimuth direction provides an unique opportunity to estimate 2-D deformation, overcoming this way the intrinsically "blindness" of radar to along-track motion. In case of using mid-resolution acquisition modes, as e.g., ScanSAR or TOPS (Section 2.2.3.1) or TOPS (Section 2.2.3.2), the azimuth sensitivity is expected to be degraded with respect to modes acquiring during the

whole synthetic aperture (StripMap). Next section tackles the mutual shift estimation from another perspective based on combining different separated parts of the spectrum.

2.4.2 Split-bandwidth interferometry (SBI) / Spectral diversity (SD) / Multiple aperture interferometry (MAI)

A second approach for the measurement of mutual shifts between SAR acquisitions consists in splitting the available bandwidth into sub-bands and calculating the differential interferogram between the interferograms of both. The phase of the later is proportional to the shift between both acquisitions. This technique can be applied in range and/or azimuth. The approach can be found in the literature as split-bandwidth interferometry (SBI), spectral diversity (SD) or multiple aperture interferometry (MAI) and is conceptually the same, where the problem has been tackled from different points of view.

The technique of splitting the spectrum in sub-bands was originally introduced for the purpose of retrieving the absolute phase offset of interferograms (Madsen and Zebker, 1992, Madsen et al., 1993) and is briefly summarized in the following.

From the acquisition geometry in Fig. 2.18, due to the range difference, Δr, between the first and the second acquisition, we obtain an additional delay given by:

$$\Delta\tau = \frac{2\Delta r}{c_0} \tag{2.75}$$

The signals received for each acquisition (omitting the pulse modulation) are given by:

$$\begin{aligned} s_1(\tau) &= e^{j2\pi f_0 \tau} \\ s_2(\tau) &= e^{j2\pi f_0(\tau-\Delta\tau)}, \end{aligned} \tag{2.76}$$

where f_0 is the carrier frequency. At reception, the signals are down converted by the local oscillator frequency, f_{LO}, and the baseband signals become:

$$\begin{aligned} c_1(\tau) &= e^{j2\pi f'\tau} \\ c_2(\tau) &= e^{j2\pi f'(\tau-\Delta\tau)-j2\pi f_{\text{L0}}\Delta\tau}, \end{aligned} \tag{2.77}$$

where $f' = f_0 - f_{\text{LO}}$ is the baseband frequency. If we assume that the envelopes of $s_1(\tau)$ and $s_2(\tau)$ overlap, the interferogram can be directly formed by computing the conjugated complex product between the base band signals:

$$\begin{aligned} w(\tau) &= c_1(\tau)\cdot c_2^*(\tau) \\ &= e^{j2\pi f'\Delta\tau + j2\pi f_{\text{L0}}\Delta\tau} \end{aligned} \tag{2.78}$$

Processing a symmetric bandwidth between $\pm B/2$ delivers an interferometric phase $\phi = 2\pi f_0 \Delta\tau$. Substituting (2.75), the interferometric phase becomes $\phi = \frac{4\pi}{\lambda}\Delta r$.

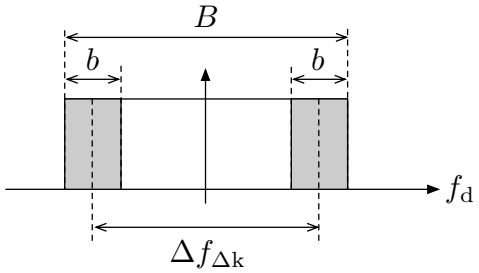

FIGURE 2.28: Split-bandwidth Interferometry: the available bandwidth, B, is splitted into two sub-bands with bandwidth b. The spectral separation is given by $\Delta f_{\Delta\text{k}}$.

When processing two sub-bands at different center frequencies, f'_u and f'_l, with a certain bandwidth b, the phases become:

$$\begin{aligned} \phi_+ &= 2\pi f'_u \Delta\tau + 2\pi f_{L0}\Delta\tau \\ \phi_- &= 2\pi f'_l \Delta\tau + 2\pi f_{L0}\Delta\tau \end{aligned} \tag{2.79}$$

The phase difference can be calculated as:

$$\begin{aligned} \phi_{\Delta k} &= \phi_u - \phi_l \\ &= 2\pi \Delta f_{\Delta k} \Delta\tau \end{aligned} \tag{2.80}$$

where $\Delta f_{\Delta k} = f'_u - f'_l$. The terminology Δk (Bamler and Eineder, 2005) refers to the fact that two separated parts of the range spectrum are combined, being conceptually equivalent to having two systems with two different wavenumber frequencies, $k = 2\pi/\lambda$.

The unknown differential delay between both signals, $\Delta\tau$, can be obtained from the phase of the differential interferogram between both sub-bands:

$$\Delta\tau = \frac{\phi_{\Delta k}}{2\pi \Delta f_{\Delta k}} \tag{2.81}$$

An analysis of the impulse response functions, obtained by the matched filter approach (Scheiber and Moreira, 2000), leads to the same conclusions and is applicable also in azimuth direction by splitting the Doppler spectrum into sub-bands. This procedure, known as spectral diversity, was originally proposed to accurately coregister burst-mode SAR acquisitions in the azimuth direction.

The estimation can be enhanced by averaging N samples of the differential interferogram. Assuming a large number of averaged samples and circular complex Gaussian signals, the standard deviation of the split bandwidth method in the retrieval of the mutual shift l, in resolution elements units, is given by (Bamler and Eineder, 2005):

$$\sigma_{l,SBI} = \frac{1}{2}\frac{B}{B-b}\sqrt{\frac{B}{b}}\frac{1}{\sqrt{N}}\frac{\sqrt{1-\gamma^2}}{\pi\gamma} \tag{2.82}$$

Note that the spectral separation, $\Delta f_{\Delta k} = B - b$, as it can be observed in Fig. 2.28. The accuracy of the split bandwidth method reaches the accuracy of the coherent cross-correlation (Cramér Rao bound) for $b = B/3$ (Eq. 2.71) (Bamler and Eineder, 2005). Some consideration on the multilooking of the sub-bands interferograms and the differential interferogram has to be taken into account in order to reach the Cramér Rao bound (De Zan et al., 2015), specifically the need for an early and late multilooking, respectively. If only multilooking of the differential interferogram is performed, the accuracy tends to the incoherent cross-correlation.

Unlike the correlation estimate, the split bandwidth estimate is ambiguous by $\Delta\tau_{amb} = \frac{1}{\Delta f_{\Delta k}}$. In terms of distance, the shift is ambiguous by $\Delta r_{amb} = \frac{c_0}{2\Delta f_{\Delta k}}$. Assuming chirp signals with 100 MHz bandwidth, the shift can be obtained with an ambiguity of 2.2 m (assuming $b = B/3$, $\Delta f_{\Delta k} = 2/3B$), which is much greater than the ambiguity band of the interferometric phase ($\lambda/2$). The ambiguity band can be easily increased by taking additional sub-bands with smaller spectral separation.

It is important to mention that the split bandwidth techniques can not only be applied for accurate coregistration purposes, but also for the retrieval of geophysical displacements. The multiple aperture interferometry (MAI) technique (Bechor and Zebker, 2006) demonstrated its potential for the derivation of along-track shift of the 1999 Hector Mine earthquake. The rationale of MAI follows a geometrical point of view, in which the synthetic aperture is splitted into two sub-apertures, resulting in the ability to measure displacement

with two slightly different lines of sight. This results in a sensitivity to azimuth displacement.

In this section it has been assumed that the available bandwidth is splitted into subbands. This limitation can, however, be removed assuming that the design of an acquisition mode that records slices of the spectrum with larger frequency separation is possible. Thus the apparent restriction that the azimuth sensitivity is limited by the system resolution can be also eliminated. This opens the door to the design of mid-resolution modes with high azimuth sensitivity, as the proposed 2-look TOPS mode in Chapter 6 and its associated paper in Appendix D.

Chapter 3

2-D ground deformation estimation through correlation techniques

In this chapter, correlation techniques are employed in order to derive 2-D ground deformation maps from TerraSAR-X StripMap images. Geophysical corrections due to the turbulent troposphere, using numerical weather model data, and solid Earth tides are performed in order to validate the measurements against GPS data.

The study case corresponds to the 2011 Tohoku-Oki Earthquake, Japan. A total of nine co-seismic interferometric acquisitions in StripMap mode (covering 30 km x 50 km) have been used. The extension of these images is too small to study wide area deformation phenomena. Therefore post-seismic acquisitions have been acquired sparsely spread over the Japan archipelago, according to pre-seismic available data. The temporal baseline of the InSAR pairs for this dataset is typically 100-140 days and many acquisitions correspond to vegetated areas, therefore with strongly degraded coherence due to temporal decorrelation effects at X-band. The validation against GPS data provides a standard deviation of about 15 cm in slant-range and azimuth directions.

The associated paper provides the methodology to apply correlation techniques, compensate the turbulent troposphere from European Centre for Medium-Range Weather Forecasts (ECMWF) Interim data and to compensate for solid Earth tidal effects.

3.1 Motivation

The use of interferometric techniques with SAR systems allows to derive the ground displacement in the radar line of sight (1-D measurement). This contribution shows the potential of correlation techniques to estimate 2-D ground deformation fields – in the radar line of sight and in the azimuth direction. Moreover the unambiguous nature of cross-correlation allows to obtain absolute measurements, with no need for phase unwrapping. Correlation techniques present, under the same circumstances, poorer performance than interferometry, thus the intention is not to substitute interferometry but to complement it. Correlation techniques are of great interest for geophysical applications, as the study of active tectonics,

This chapter presents an overview of the paper in Appendix A (Yague-Martinez et al., 2012):
N. Yague-Martinez, M. Eineder, X. Y. Cong, and C. Minet (2012). "Ground Displacement Measurement by TerraSAR-X Image Correlation: The 2011 Tohoku-Oki Earthquake". In: *IEEE Geoscience and Remote Sensing Letters* 9.4, pp. 539–543. ISSN: 1545-598X. DOI: 10.1109/LGRS.2012.2196020

Earthquakes or landslides, where the deformation is not only in the vertical direction (as it is the case for urban scenarios), but also in the horizontal direction. Moreover, in the case of strong seismic events, the interferometric phase can be difficult to use if phase wrapping has occurred. The use of correlation is also widely applied for glacier tracking to derive 2-D displacement fields.

3.2 Expected performance

The large temporal baseline between pre- and post-seismic acquisitions (more than hundred days) results in a low coherence. Therefore correlating intensities is more suitable than correlating complex signals, since the former is more robust. The unbiased estimator for the incoherent cross-correlation has been provided in Section 2.4.1.2 for 1-D signals, being its extension to 2-D signals immediate. Details about the expected performance have been provided in Section 2.4.1.4.

Incoherent cross correlation is applied over a grid of patches distributed regularly over the images. Patches of 128 pixel $\times$ 128 pixel ($\sim$ 190 m $\times$ 250 m) whose centers are separated by 64 pixels ($\sim$ 100 m) have been used. Fig. 3.1 shows the achievable accuracy in range and azimuth together with the accuracy of the interferometric phase. A multilooking of 11 $\times$ 11 pixels ($\sim$ 13 m $\times$ 27 m) has been assumed for the phase.

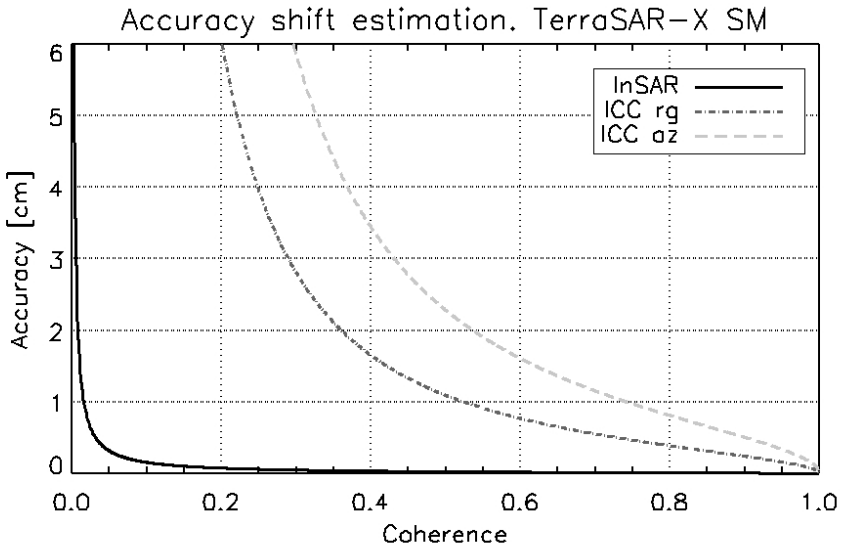

FIGURE 3.1: Performance of the interferometric phase and incoherent cross-correlation. Patches of 128 $\times$ 128 pixels ($\sim$ 190 m $\times$ 250 m) are assumed for cross-correlation. A multilooking of 11 $\times$ 11 pixels has been applied to the phase.

3.3 Interferometry vs Correlation

A comparison between the line-of-sight displacement employing interferometric techniques and cross-correlation is provided. The interferometric pair corresponds to an acquisition on 12.03.2011, one day after the major event, and an acquisition 55 days earlier. Fig. 3.2 shows the interferometric phase, once the topographic phase from a digital elevation model has been subtracted (left) and the shifts from cross-correlation after compensating for the parallax effect (right). Each fringe cycle corresponds to $\lambda/2 = 1.55$ cm.

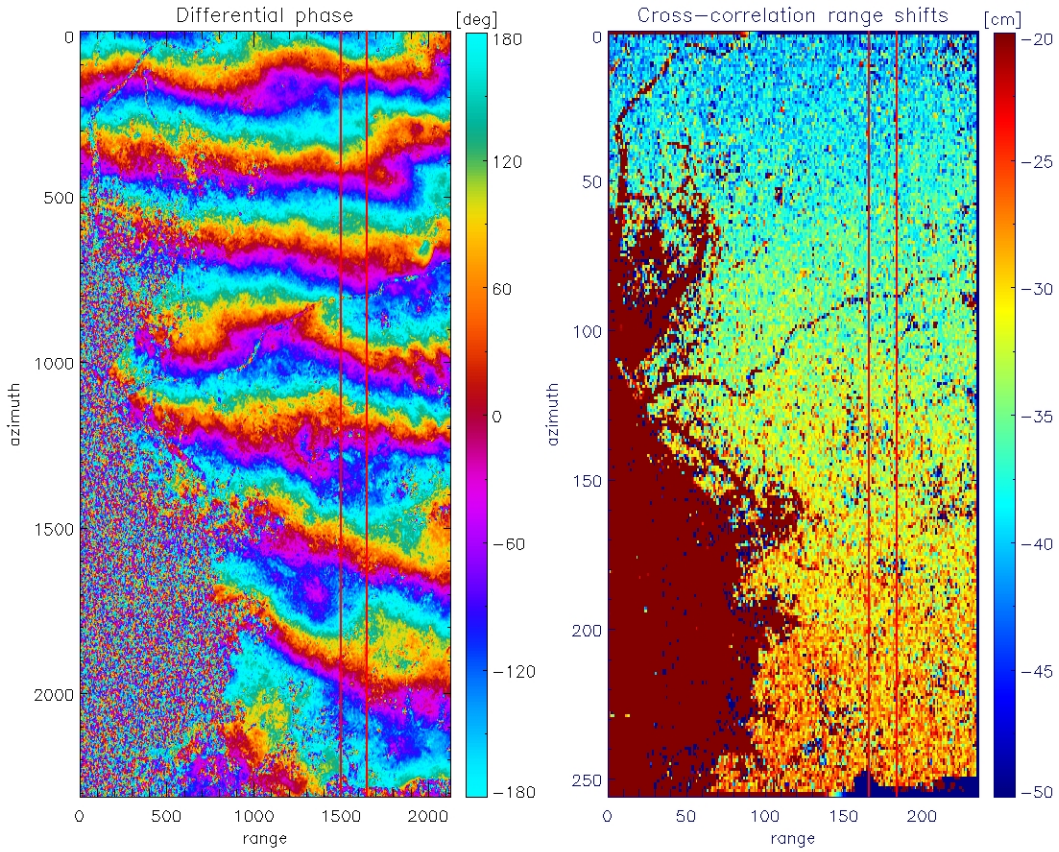

FIGURE 3.2: Results over Tokyo site. Differential interferometric phase (left). Range shifts from cross-correlation (right)

Fig. 3.3 shows an averaged profile over azimuth dimension for the shifts from the differential phase (black) and incoherent cross-correlation (red stars). Observe that the shifts from interferometry are wrapped between $\pm\lambda/4$. The 1-D unwrapped differential phase is also displayed (blue), where the absolute shift has been determined from cross-correlation. It can be observed that the cross-correlation shifts are comprised in the range of 5 cm around the shifts obtained from the unwrapped differential phase. (A more recent computation has provided a 3σ of the differences of 2.75 cm). The potential to retrieve the absolute shift from cross-correlation and its support to phase unwrapping is evident.

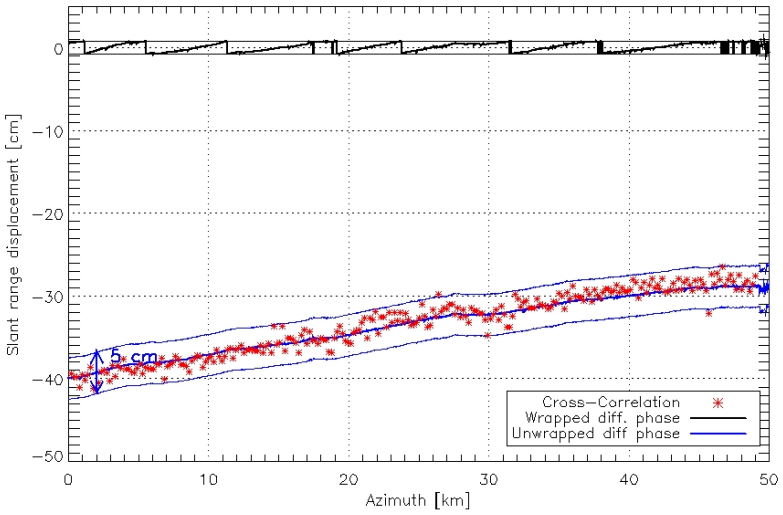

FIGURE 3.3: Profiles of the displacement in the line of sight. A total of 150 multilooked pixels over range have been averaged for the displacement from the differential phase. The phase has been multilooked with a 11 × 11 boxcar window. In the case of the range shifts from cross-correlation, a total of 18 estimates are averaged over range. Each estimate has been computed by correlating patches of 128 pixel × 128 pixel separated by 64 pixels.

Fig. 3.4 shows the scatter plot of the profiles of the displacement in the line of sight from both estimates, being the Pearson correlation coefficient (PCC)[1] equal to 0.98.

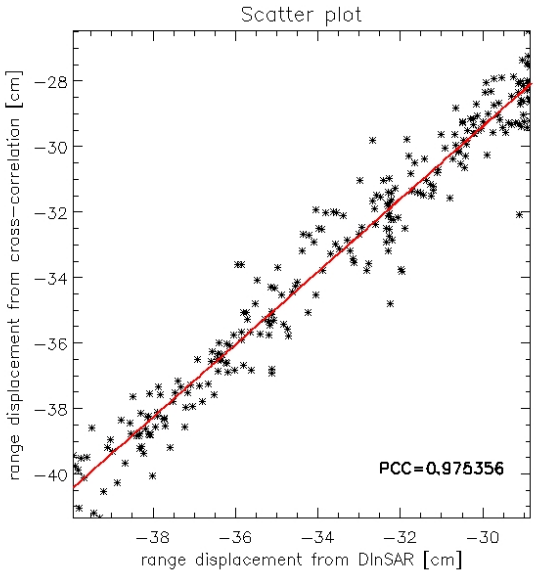

FIGURE 3.4: Scatter plot of the line of sight displacement profiles. The red line corresponds to the linear fit.

[1] The Pearson correlation coefficient is a measure of the linear correlation between two variables. It is defined as:

$$PCC = \frac{cov(\Delta r_{\text{DInSAR}}, \Delta r_{\text{xcorr}})}{\sigma_{\text{DInSAR}} \sigma_{\text{xcorr}}}, \tag{3.1}$$

where cov and σ denote covariance and standard deviation, respectively. Δr_{DInSAR} and Δr_{xcorr} are the line of sight displacements computed from interferometry and cross-correlation techniques, respectively.

3.4 2-D displacement fields

Fig. 3.5 shows an overlay of the slant range/azimuth displacement vector field over the SAR amplitude for Sendai (left) and Tokyo sites (right). Every arrow averages 16×16 correlation estimates. This supposes at most 256 averaged values since an outlier rejection procedure has been carried out.

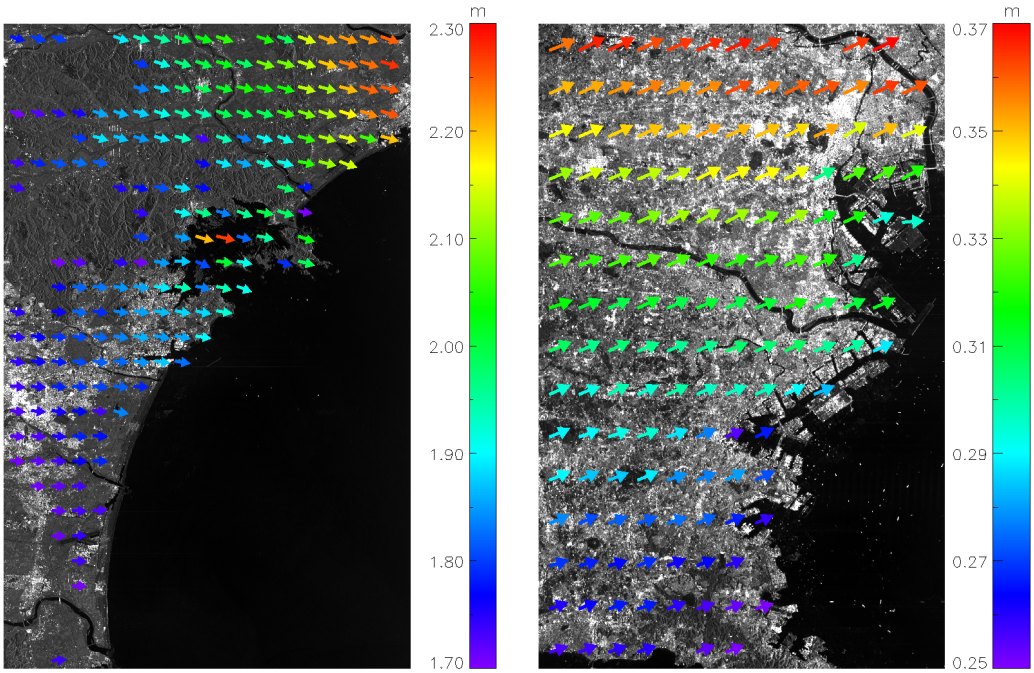

FIGURE 3.5: 2-D vector displacement maps (slant range / azimuth) over SAR amplitude for Sendai site (left) and Tokyo site (right). The color of each arrow of the vector field indicates the magnitude of the absolute displacement. Range is horizontal and azimuth is vertical.

3.5 Geophysical corrections

In order to obtain an accurate absolute deformation measurement in the centimeter range, the atmospheric delay effect needs to be considered. In our work, global weather model data are used to estimate the atmospheric path delay. The numerical weather model data from the European Centre for Medium-Range Weather Forecasts (ECMWF) Interim have been chosen. The weather data are available four times per day (at 0, 6, 12, and 18 h) with a grid resolution of about 80 km and stratified in 60 levels.

An additional effect to consider are the solid Earth tides, which are due to the response of the Earth to lunisolar gravitational attraction. The deformation of the Earth's crust can reach up to 40 cm for the radial component and several centimeters for the horizontal components.

3.6 Summary of results

A total of nine InSAR pairs have been acquired over the Japanese archipelago, covering the M_w9.0 megathrust Earthquake on March 11, 2011. For each of them, cross-correlation has been applied to calculate the 2-D ground displacements, the mentioned geophysical corrections applied and a 2-D vector obtained. Table 3.1 summarizes the obtained results. The

dataset presents mainly large temporal baselines, corresponding the majority of the acquisitions to rural vegetated areas (indicated by R), providing therefore a low coherence at X band. Three acquisitions correspond to two sites over urban areas (indicated by U), presenting a higher coherence. A validation has been performed with GPS data, and the differences are provided in the last column. Regarding the range differences, errors below approximately 15 cm, except for site 4, have been achieved. Reasons for large differences can be due to fast changes in the turbulent troposphere between the availability of the weather data (each 6 h) and the acquisition time. Note that the acquisitions present a (worst case) acquisition time, since there are approximately 3 h time difference. In addition, one should take into account that TerraSAR-X orbits present a 3-D accuracy of 4.2 cm for the so-called science orbit products (Yoon et al., 2009). This implies an accuracy in the geometric shift prediction in the line of sight of about 8.5 cm, according to simulations. Regarding the azimuth shifts, differences of a few centimeters are achieved for the majority of cases, except for sites 2, 5 and 9, which very likely correspond to outliers. Discarding site 2, the computation of the standard deviations provide 14 cm and 13 cm for range and azimuth respectively. These values are worse than obtained for corner reflectors or incoherent cross-correlation over urban areas with one cycle temporal baseline (Eineder et al., 2011) applying a correction of the atmospheric delay effect using the GPS zenith-path delay (with zero time delay with respect to the acquisition time), which represents a more ideal scenario.

TABLE 3.1: Cross-correlation results from TerraSAR-X dataset

Site	Coordinates (lat, lon)	UTC Acquisition time postseismic acq.	Temporal baseline [days]	Error wrt GPS (rg,az) [cm]
1(U)	38.27°, 141.06°	12.03.2011; 20:43:07	143	2 ; 0
2(U)	38.24°, 140.86°	17.03.2011; 20:51:41	143	2 ; -71
3(U)	35.53°, 139.66°	12.03.2011; 20:43:52	55	-14; 2
4(R)	44.16°, 145.81°	24.03.2011; 20:24:20	121	30; -6
5(R)	43.27°, 145.60°	24.03.2011; 20:24:35	121	11;-27
6(R)	43.82°, 144.18°	18.03.2011; 20:33:03	132	5 ; 5
7(R)	35.05°, 136.86°	02.04.2011; 21:01:12	121	-11; -4
8(R)	31.95°, 130.85°	01.04.2011; 21:19:18	110	-17; 6
9(R)	28.28°, 129.45°	28.03.2011; 09:17:45	121	7 ; 20
Standard deviation				14; 13

3.7 Conclusions

Cross-correlation techniques allow to derive 2-D ground displacement maps with accuracies in the range of a few centimeter, that are adequate for geophysical applications, e.g., study of strong Earthquakes. The use of cross-correlation overcomes some limitations of DInSAR, as e.g., the insensitivity of the latter to the azimuth direction or the estimation of unambiguous and absolute estimates, being a phase unwrapping procedure not necessary. The use of multiple scenes of TerraSAR-X allows the generation of a wide area displacement map through the use of correlation techniques and geophysical corrections. A comparison between dInSAR and correlation in the line-of-sight direction shows good agreement. The results compare in general well with GPS measurements with a standard deviation of the differences about 15 centimeters. For datasets with lower temporal baseline and higher coherence better results are expected. The reduced coverage provided by the StripMap mode

and the heterogeneity of the acquisition surveys dates justify further investigation of acquisition modes for large-scale mapping, able moreover to reduce the temporal sampling between acquisitions.

Chapter 4

Sentinel-1 TOPS InSAR processing

The terrain observation by progressive scans (TOPS) acquisition mode was introduced in the literature in 2006 (De Zan and Monti Guarnieri, 2006). The TOPS mode achieves wide coverage by switching the elevation beam in order to acquire several subswaths, following a similar procedure as ScanSAR (Tomiyasu, 1981). TOPS performs additionally a steering of the antenna beam in azimuth in order to illuminate each target with the complete antenna pattern, overcoming this way the limitations of ScanSAR, namely azimuth-variant SNR and azimuth ambiguities due to the scalloping effect. TOPS represents an evolved ScanSAR mode, which is able to obtain wide coverage at the expense of azimuth resolution (typically in the order of 20 m).

The Sentinel-1 mission (Torres et al., 2012) employs a constellation of two identical satellites (launched in April 2014 and April 2016), whose acquisition baseline over land consists in the use of the Interferometric Wideswath (IW) mode, which is a TOPS mode with three subswaths. The IW mode provides a range coverage of 250 km at 20 m azimuth resolution. The coverage capacity of Sentinel-1 allows to map systematically the entire Earth in 12 days, employing one satellite, orbiting at a height of approximately 690 km. The use of both Sentinel units allows to reduce the repetition cycle to just 6 days, since both units are orbiting in the same orbit but with a mean anomaly delta of 180 degree (ESA, 2018). The reduced repetition cycle of Sentinel-1 together with the free, full and open data policy, turn it into the main instrument for measuring small-scale crustal deformation over large areas exploiting interferometric techniques (Elliott et al., 2016). This is a significant advancement since short-period interferograms keep a higher coherence and can map time-dependent deformation, as well as provide a greater number of sampling observations for the exploitation of time-series (Ferretti et al., 2001 Hooper et al., 2004, Berardino et al., 2002).

Similarly as ScanSAR, the TOPS acquisition takes place by acquiring bursts of echoes, i.e., each target is illuminated during a time interval smaller than the StripMap one. This results in azimuth-variant spectral characteristics of the SAR signal, which needs to be accounted for during the interferometric processing. Several aspects related to the interferometric processing of ScanSAR data, as azimuth scanning pattern synchronization, spectral

This chapter presents an overview of the paper in Appendix B (Yague-Martinez et al., 2016b):
N. Yague-Martinez, P. Prats-Iraola, F. Rodriguez Gonzalez, R. Brcic, R. Shau, D. Geudtner, M. Eineder, and R. Bamler (2016b). "Interferometric Processing of Sentinel-1 TOPS Data". In: *IEEE Transactions on Geoscience and Remote Sensing* 54.4, pp. 2220–2234. ISSN: 0196-2892. DOI: 10.1109/TGRS.2015.2497902

shift filtering in the presence of high squint, Doppler centroid estimation, interferogram formation, etc. have been provided in Holzner and Bamler, 2002.

The associated paper provides the methodology for the interferometric processing of Sentinel-1 TOPS data. Specifically, the spectral characteristics, taking into account the azimuth antenna steering, the use of deramping functions, burst synchronization requirements, coregistration aspects, spectral shift filtering, interferogram formation and first interferometric results. This chapter focuses on the stringent azimuth coregistration aspects and the methodology to be applied to Sentinel-1 data.

4.1 Spectral properties of TOPS data

The non-stationarity of the squint angle during the TOPS acquisition produces a linear variation of the Doppler centroid frequency in the SAR data. Fig. 4.1 shows the (unfolded) time-frequency diagram of two raw bursts (of the same subswath) of duration T_{B}. Observe that the azimuth resolution is controlled by the dwell time, T_{dwell}, (integration time for a point target), resulting in a target bandwidth $B_T = |k_a| \cdot T_{\mathrm{dwell}}$, with k_a being the Doppler rate. The Doppler rate introduced by the antenna steering is given by:

$$k_{\mathrm{rot}} \approx \frac{2v_s}{\lambda}\omega_r, \tag{4.1}$$

being v_s the satellite velocity, λ the radar wavelength and ω_r the antenna steering rate in radians per second.

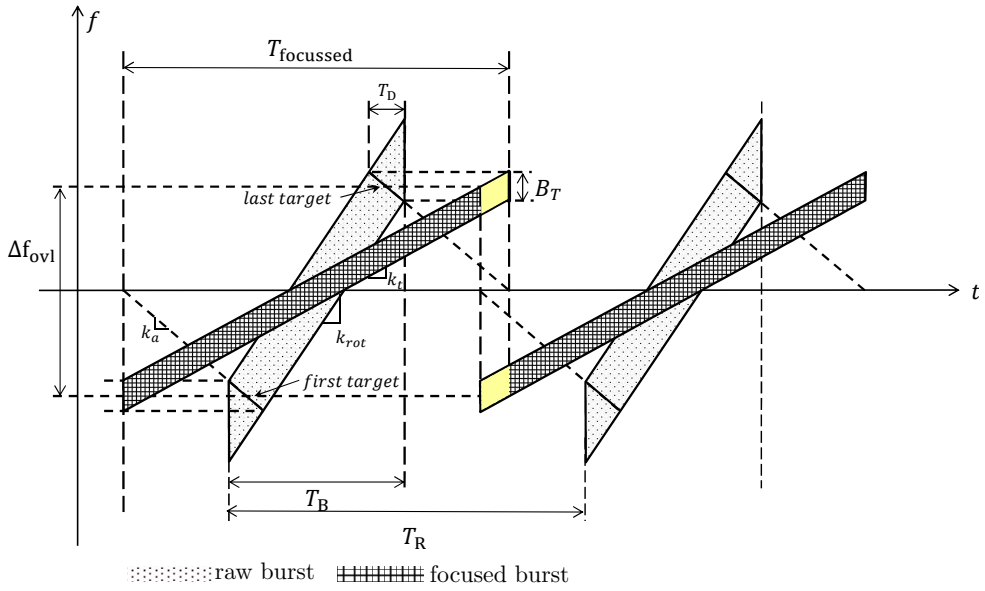

FIGURE 4.1: Time-frequency diagram of a TOPS system, which shows two bursts of the same subswath at a certain range. Each target presents a Doppler rate, k_{a}. The antenna is rotated in the azimuth direction originating a linear frequency variation of the burst, of duration T_{B}, at a rate k_{rot}. The SAR processing at zero-Doppler geometry causes that the focused burst, of duration T_{focused}, presents also a linear frequency variation, with rate k_{t}. The dwell time, T_{D}, is the time interval in which a target on ground is illuminated with the main lobe, and results on a bandwidth B_{T}. The cycle time or interburst time, T_{R}, is the elapsed time between bursts of the same subswath. The resulting overlap in time between consecutive bursts (yellow area) results in a spectral separation given by Δf_{ovl}.

After the burst raw data have been focused to SLC bursts in zero-Doppler geometry, a linear Doppler centroid frequency variation is present in the azimuth direction. The range-dependent Doppler rate at image level $k_t(r)$ can be calculated as:

$$k_t(r) = \frac{k_a(r) \cdot k_{\text{rot}}}{k_a(r) - k_{\text{rot}}}, \tag{4.2}$$

being $k_a(r)$ the range-dependent target Doppler rate. Assuming that the Doppler frequency is f_c[1] at the burst center, t_c, the Doppler frequency variation over azimuth can be written, neglecting the range dependence, as:

$$f(t) = f_c + k_t \cdot (t - t_c) \tag{4.3}$$

The impulse response function (IRF) in azimuth for a target located at the zero Doppler time, t_0, and observed under a certain squint, is given by (Bara et al., 2000, Fornaro et al., 2002):

$$\begin{aligned} s(t) = C \cdot s_a(t) \cdot & e^{-j\frac{4\pi}{\lambda}r_0} \\ & \cdot e^{j2\pi \cdot f(t) \cdot (t - t_0)}, \end{aligned} \tag{4.4}$$

being C a complex constant, $s_a(t)$ the azimuth envelope of the compressed target and r_0 its range of closest approach.

When computing the interferogram between a pair of acquisitions, we obtain that the phase is given by:

$$\begin{aligned} \phi_{\text{int}}(t) = & -\frac{4\pi}{\lambda} \cdot \Delta r \\ & + 2\pi \cdot f_c \cdot \Delta t \\ & + 2\pi \cdot k_t \cdot t \cdot \Delta t, \end{aligned} \tag{4.5}$$

where the same mean Doppler centroid and same steering rates have been assumed for both acquisitions; Δr is the differential range to the target between both acquisitions and Δt is the the time difference between the common target observed for both acquisitions, i.e., the azimuth misregistration. The first term of the equation (4.5) corresponds to the desired interferometric phase. The second term is a constant offset and therefore negligible. The third term, however, results in a linear phase over the burst in azimuth, whose slope is proportional to the azimuth misregistration. A constant azimuth misregistration introduces therefore phase ramps in the interferograms as already discussed in Prats-Iraola et al., 2012.

4.2 Burst synchronization considerations

In order to be able to form an interferogram between a pair of acquisitions, it is necessary that the bursts are synchronized. This way common targets are observed with similar squint angles, or equivalently Doppler frequencies. A lack of spectral Doppler overlap leads to decorrelation. There are two contributions to the burst synchronization:

1. Timing mis-synchronization: related to the starting times of the acquisitions, or actually the along-track satellite positions. The acquisition has to be started at the same

[1]Spaceborne SAR systems employ usually a total zero Doppler steering (TZDS) law, therefore the Doppler centroid frequency due to the platform attitude is just a few Hz and can be neglected.

along-track positions for both passes. However, not only the accuracy of the synchronization at the beginning of the datatakes is relevant, the size of the orbital tube in the radial dimension affects synchronization during the datatake, i.e. Δt_{acq} varies during the acquisition (Prats-Iraola et al., 2015).

The Doppler shift due to a mismatch of the acquisitions starting times is given by:

$$\Delta f^{\text{TOPS}}_{\text{timing}}(r) = k_t(r) \cdot \Delta t_{\text{acq}} = \frac{k_a(r) \cdot k_{\text{rot}}}{k_a(r) - k_{\text{rot}}} \Delta t_{\text{acq}}, \tag{4.6}$$

where Δt_{acq} is the timing difference between both acquisitions (raw data).

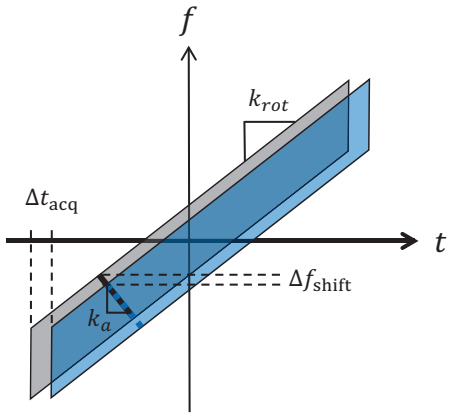

FIGURE 4.2: Time-frequency diagram of an interferometric pair of raw bursts to depict the burst mis-synchronization due to a timing error, Δt_{acq}. The plot depicts the case where the master (gray) burst observes the target before the slave (blue).

As it has been observed by Geudtner et al., 2015, TOPS is more robust than ScanSAR to timing synchronization errors, being the Doppler shift for the latter equal to $k_a(r) \cdot \Delta t_{\text{acq}}$.

2. Antenna mis-pointing: related to the difference of Doppler frequencies between both acquisition due to pointing errors. The Doppler shift due to antenna mis-pointing is given by (Geudtner et al., 2015):

$$\Delta f^{\text{TOPS}}_{\text{pointing}}(r) = \frac{\Delta f_{\text{dc}}}{k_a(r) - k_{\text{rot}}}, \tag{4.7}$$

where Δf_{dc} is the Doppler mismatch between both acquisitions. An antenna mis-pointing in TOPS mode supposes a smaller shift than in the equivalent ScanSAR mode.

The coherence loss can be calculated by substituting the total Doppler shift from equations (4.6) and (4.7) in (2.3.2.2 (ii)). The coherence loss can, however, be avoided if proper azimuth spectral shift filtering is performed, at the cost of a reduced azimuth resolution. More details can be found in the associated paper.

4.3 Coregistration approach for the Sentinel-1 IW mode

The steering angles of the Sentinel-1 IW mode are comprised between $\pm 0.6°$. This corresponds to a maximum Doppler frequency of about 5.2 kHz. In order to limit the phase ramp to e.g. 1/100 cycle ($= 3.6°$), a coregistration accuracy of approximately 0.0009 pixels at a

typical azimuth sampling frequency, $f_{az} = 486$ Hz would be required, which is equivalent to approximately 1.3 cm.

An adequate approach for the coregistration of TOPS data consists of a two stages procedure. In first place a geometrical coregistration, employing precise orbital information and an external DEM, is performed (Sansosti et al., 2006). This allows obtaining a coregistration accuracy whose error is mainly due to timing/orbital reasons, for scenes not affected by ground displacement.

Regarding the azimuth shifts, a refinement is needed to correct for a rigid shift. The overlap areas between bursts can be employed exploiting the enhanced spectral diversity (ESD) technique (Prats-Iraola et al., 2012).

ESD is based on the spectral diversity technique (Scheiber and Moreira, 2000), which performs the differential interferogram between sublooks interferograms. ESD takes advantage of the large spectral separation at the overlap areas between bursts. The phase of the differential interferogram is proportional to the misregistration, Δt, and the spectral separation, according to:

$$\phi_{\text{ESD}} = 2\pi\Delta f_{\text{ovl}}\Delta t, \tag{4.8}$$

where Δf_{ovl} is the spectral separation at the overlapping area between focused bursts (see Fig. 4.1).

The ESD phase can be calculated for every pixel of each overlap area as follows:

$$\phi_{\text{ESD}} = arg\{(m_i \cdot s_i^*) \cdot (m_{i+1} \cdot s_{i+1}^*)^*\}, \tag{4.9}$$

where m_i, and s_i refer to the i^{th} master and slave complex bursts, and m_{i+1}, and s_{i+1} refer to the $(i+1)^{th}$ master and slave bursts. In the associated paper (Yague-Martinez et al., 2016b) an estimator for the calculation of the fine azimuth shift is proposed.

The standard deviation of the azimuth shift, Δx, expressed in meter units, can be obtained from (2.47) and (4.8) and is given by (Prats-Iraola et al., 2012):

$$\sigma_{\Delta x} = \frac{1}{2\pi\Delta f_{\text{ovl}}}\frac{1}{\sqrt{N}}\frac{\sqrt{1-\gamma^2}}{\gamma}v_g, \tag{4.10}$$

where N is the number of averaged samples, v_g is the beam ground velocity and γ is the interferometric coherence.

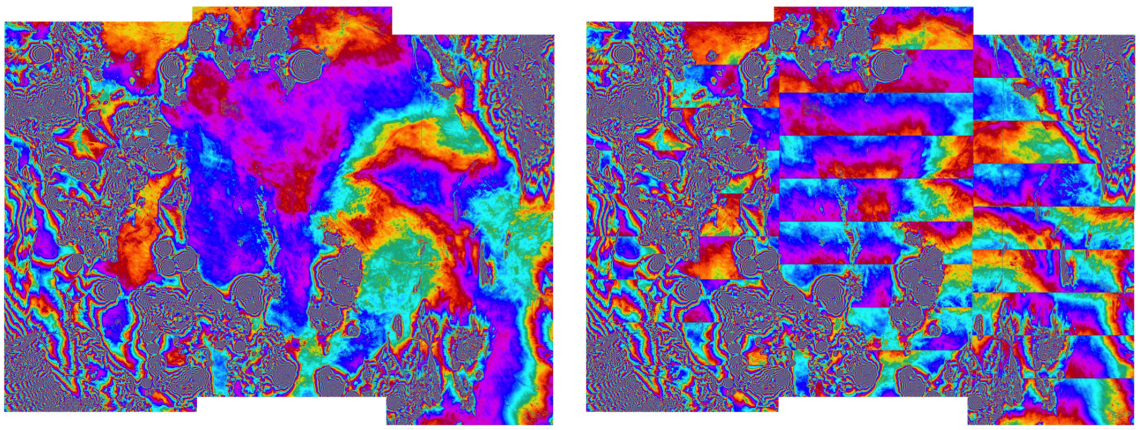

FIGURE 4.3: Sentinel-1 IW mode flattened phase over Salar de Uyuni, Bolivia. (Left) An accurate azimuth coregistration employing ESD has been applied, no significant phase discontinuities are present between bursts. (Right) An artificial azimuth misregistration of 0.05 samples (approx. 65 cm) has been introduced. This originates phase jumps at burst edges of approximately 190°. Range is horizontal and azimuth is vertical.

4.4 Conclusions

The wide-swath characteristics of the TOPS mode provides the Sentinel-1 mission the ability to map globally the Earth surface with an unprecedented temporal sampling of just 12 days with a single satellite and reduced to 6 days with two satellites. This is an unique opportunity for the measurement of small-scale crustal deformation over large areas. TOPS supposes an evolution with respect to the ScanSAR mode in the sense of overcoming the limitations of the latter, namely azimuth-variant SNR and azimuth ambiguities due to the scalloping effect.

The methodology to perform interferometry with Sentinel-1 TOPS data is provided in the associated paper. In this chapter the focus has been the analysis of the required azimuth coregistration for InSAR pairs and its methodology by means of the ESD technique. However, its performance dependence on the interferometric coherence, according to 4.10, makes necessary its extension for long time series, in order to obtain enough accuracy for stacks with very large temporal baselines. A joint approach exploiting all acquisitions of the stack is the focus of Chapter 5.

TOPS achieves a reduced temporal revisit thanks to its wide swath capability. However, its low azimuth resolution results in a poor performance for the application of correlation techniques to derive azimuth displacements, as demonstrated feasible with StripMap data in Chapter 3. For this reason further investigation of acquisition modes to enhance the accuracy of the azimuth estimates are necessary and will be covered in Chapter 6.

Chapter 5

Joint-coregistration of stacks of Sentinel-1 TOPS acquisitions

Chapter 4 presented the methodology for the coregistration of interferometric pairs, based on the ESD technique. The accuracy of this procedure depends on the interferometric coherence (eq. 4.10). Thus the performance in the retrieval of the azimuth shift worsens for low coherence values. In a real scenario, this occurs typically when the temporal baseline between acquisitions increases, being relevant when working with long time series.

5.1 Motivation

In order to illustrate the temporal decorrelation effect, a time-series of interferometric coherences of a set of Sentinel-1 (S1) Interferometric Wide (IW) acquisitions over Mexico is shown in Fig. 5.1. The coherences are chronologically arranged, being the master acquisition chosen at the beginning of the stack. The stack starts in November 2014 and spans approximately 18 months. The temporal baseline increases cumulatively by 12 days. The City of Mexico is located on the right side of the scenes and presents relatively high coherence through the time series due to the stability of the interferometric phase over urban areas. The rest of the scene corresponds mainly to rural areas, characterized by distributed scatterers. Note that the coherence decays rapidly over these regions.

The scatterer temporal decorrelation law can be modeled, as proposed by Rocca, 2007, according to a decreasing exponential law, including a long-term coherence term (Parizzi et al., 2009):

$$\gamma(t) = (\gamma_0 - \gamma_\infty) \cdot e^{\frac{-t}{\tau}} + \gamma_\infty \tag{5.1}$$

being τ the time constant, γ_0 the short-term coherence (0-day lag) and γ_∞ the long-term coherence.

This chapter presents an overview of the paper in Appendix C (Yague-Martinez et al., 2017):
N. Yague-Martinez, F. De Zan, and P. Prats-Iraola (2017). "Coregistration of Interferometric Stacks of Sentinel-1 TOPS Data". In: *IEEE Geoscience and Remote Sensing Letters* 14.7, pp. 1002–1006. ISSN: 1545-598X. DOI: 10.1109/LGRS.2017.2691398

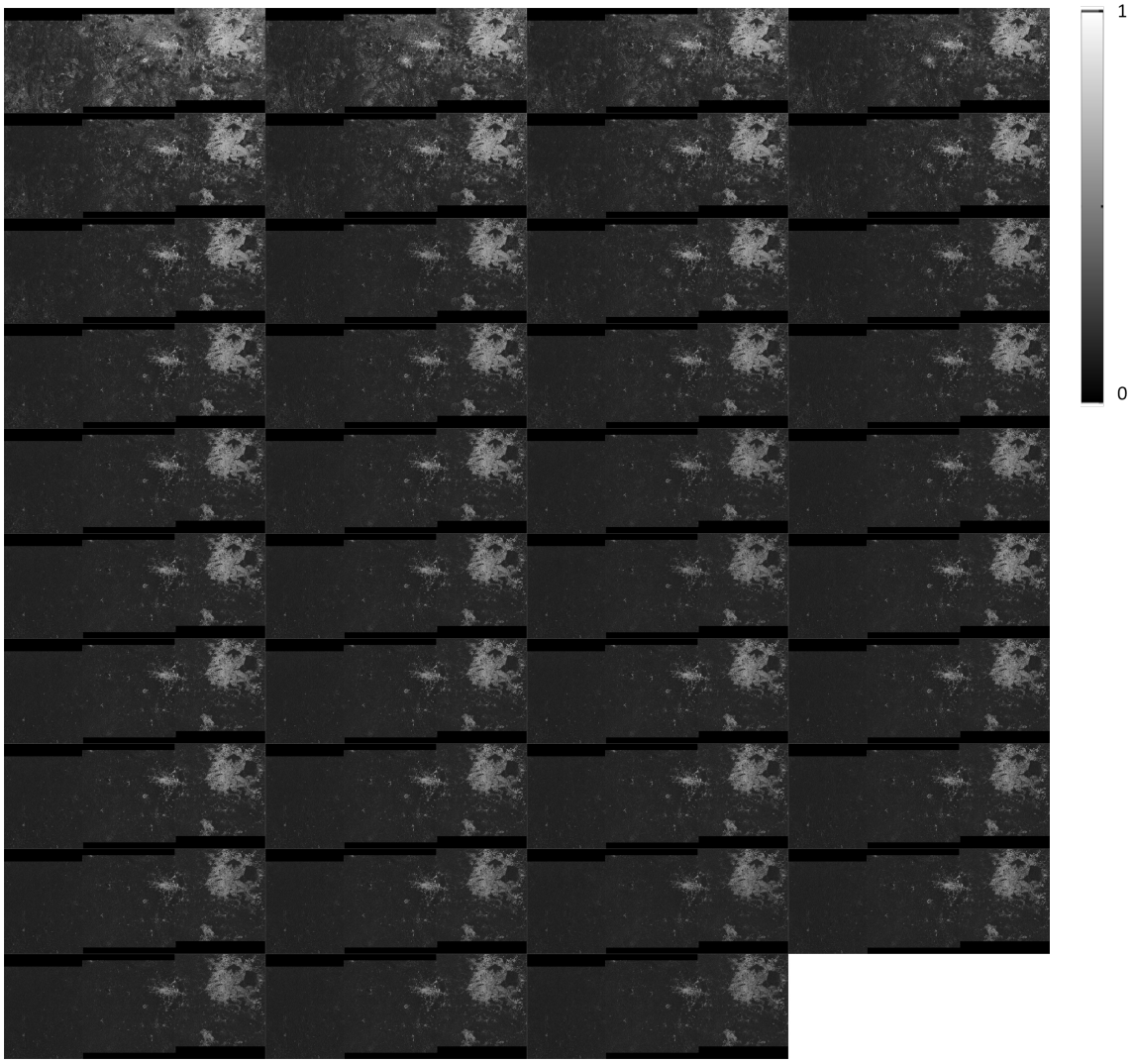

FIGURE 5.1: Time series of the coherence maps of a Sentinel-1 IW stack of images over Mexico City, covering 18 months, and acquired in ascending geometry. The master image has been selected at the beginning of the stack. The temporal baseline increases from top left towards bottom right.

Fig. 5.2 shows exemplary covariance matrices and the coherence time series for two patches with different decorrelation properties over the Mexico area. An exponential fitting according to (5.1) is also plotted, providing three parameters: initial coherence, i.e., coherence for 0-day lag, time constant, and long-term coherence. The top part of the figure corresponds to a patch over a rural area. The covariance matrix indicates some periodical effects/events. The exponential fitting presents a long-term coherence of 0.22 and a time constant of 35 days. On the contrary, the bottom part corresponds to a patch over an urban area, characterized by a long-term coherence of approx. 0.64.

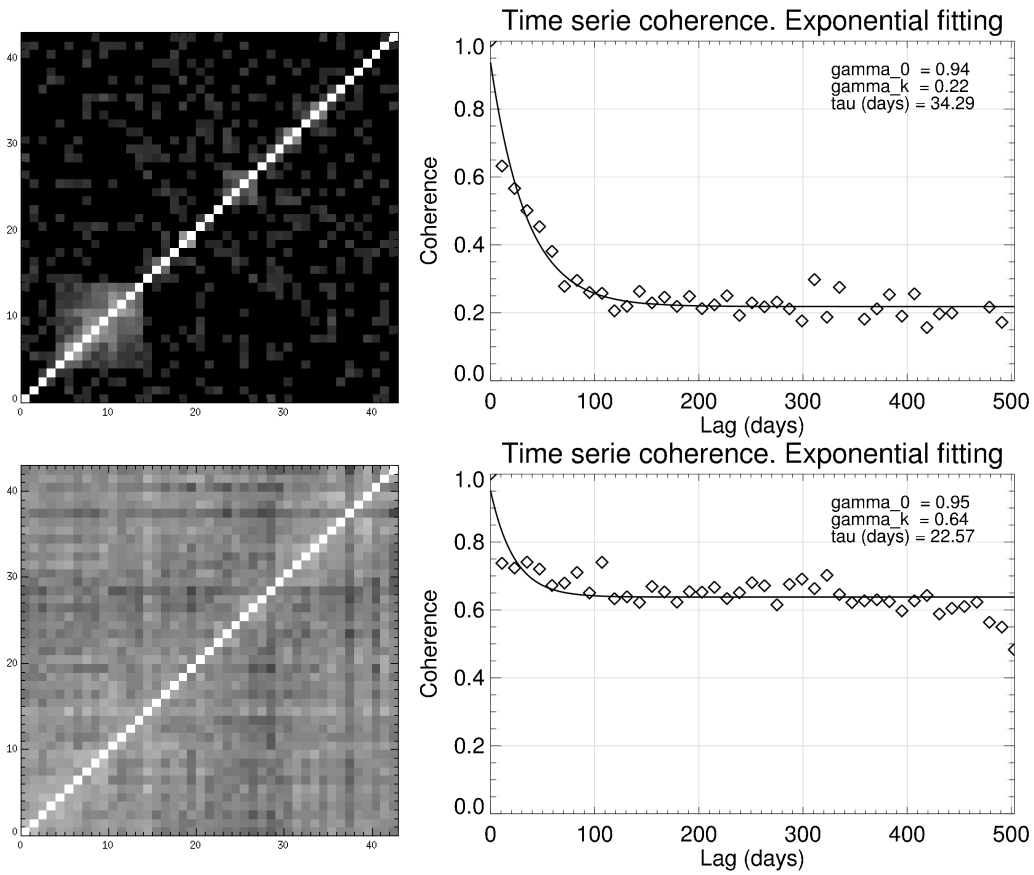

FIGURE 5.2: Covariance matrix (left) and time-series coherence (right). The top part corresponds to a patch located over land, whereas the bottom part to a patch located in an urban area.

From the previous results, it is clear that the achievement of accurate rigid azimuth coregistration can be an issue for scenes covering rural areas, if just the conventional ESD procedure is used.

The necessity of exploiting the burst overlap areas to retrieve the fine rigid azimuth shift has been discussed recently in international conferences with a group of scientist claiming to obtain accurate results with just a geometrical coregistration. Their argument is that the orbital accuracy is good enough. For instance, a phase error of 15° between bursts translates into a deformation error of just 1 mm. Moreover it has been suggested that in case some errors are present, a PSI processing could absorb them in the atmospheric phase screen (APS) estimation stage. The APS estimation presumes that the turbulent troposphere disturbance is uncorrelated in time and correlated in space. This is in general not true for the residual azimuth coregistration error if ESD is not applied. The left part of Fig. 5.3 depicts the phase error over azimuth for two bursts due to an azimuth misregistration (black curve). The phase bias ranges from -10° to 10° originating a discontinuity of 20° at the burst interface. The red curve is the result of a spatial filtering. The right part of the figure shows the residual phase after APS compensation, as it can be seen the spatial correlation requirement does not hold.

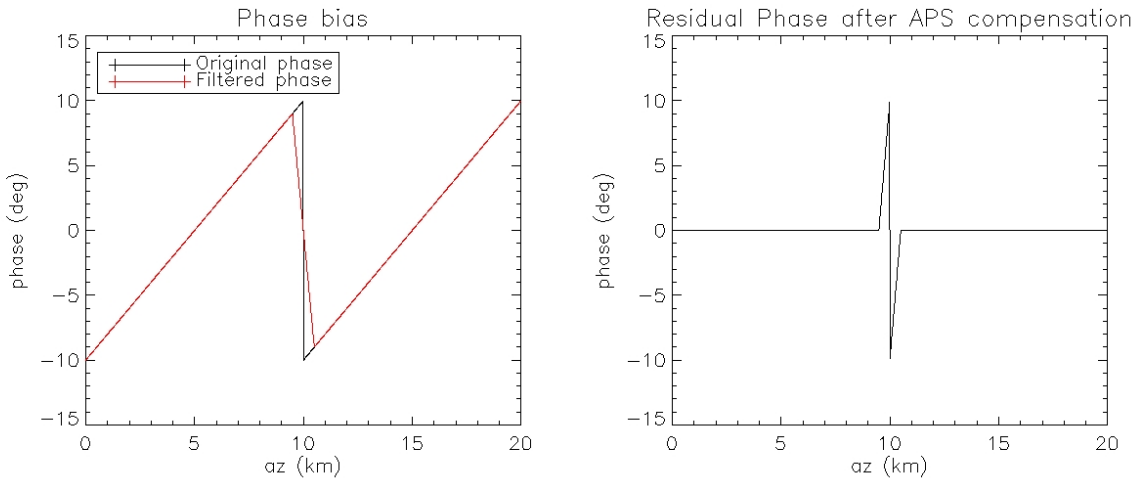

FIGURE 5.3: The left hand graph shows the phase bias over azimuth for two bursts due to an azimuth misregistration (black curve). The phase bias ranges from -10° to 10° originating a discontinuity of 20° at the burst interface. The red curve is the result of a spatial filtering. The residual phase after APS compensation is plotted on the right hand graph.

5.2 Joint approach

The coregistration problem consists in retrieving the azimuth shift of each image with respect to a common master image. The conventional single-master approach applies ESD between each image and the master image. The joint coregistration approach has been already addressed in the literature for the case of coherently correlating speckle signals (De Zan, 2011). The same principle can be applied when employing the ESD technique for azimuth coregistration of TOPS images. Another interesting option is to employ only point scatterers for the ESD estimation, which keep a high coherence over time. The performance of the estimation would, however, depend on the density of scatterers that are imaged in the overlap areas. Moreover, since the Sentinel-1 mission was devised to map wide areas, where for some cases no urban regions are present, a more general solution is required. The justification of the application of a joint coregistration approach might depend on the site: whether the overlap regions cover urban areas or long-term coherent scatterers. However, a joint approach will always provide better results since it represents the optimal solution.

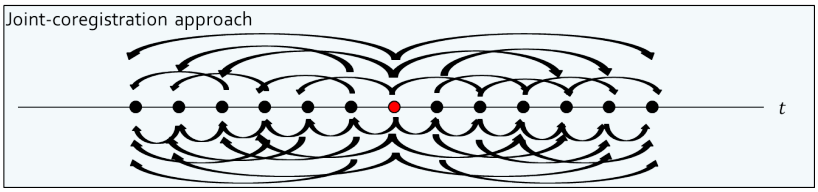

FIGURE 5.4: In the joint-coregistration procedure, the mutual shifts among all available pairs are calculated. This way the temporal decorrelation effect can be mitigated. In the standard single-master approach uniquely the shifts between each slave and a selected master, usually chosen in the middle of the stack, is performed. The joint approach supposes moreover additional flexibilities regarding the selection of the master image. The slave images are represented by a black circle whereas the master acquisition by a red circle.

In the first place, all images are coarsely coregistered to a common master using geometric information, as discussed in Section 4.3. Afterwards mutual ESD estimation can be

applied among all possible pairs, as shown in Figure 5.4. All samples of the overlapping areas are used in the ESD step, providing a robust estimation against phase wrapping effects (in the case of phase noise due to low coherence). Note that an outlier rejection procedure, e.g., based on the coherence, can be applied to avoid averaging pure noise samples.

The azimuth shifts, $\mathbf{m}_{L_2}$, of each image with respect to the master image can be calculated using:

$$\mathbf{m}_{L_2} = (\mathbf{G}^T\mathbf{W}\mathbf{G})^{-1}\mathbf{G}^T\mathbf{W}\mathbf{d} \tag{5.2}$$

where $\mathbf{G}$ is the system matrix defining the relations between the different measurements, $\mathbf{d}$ the data vector (pairwise ESD measurements). $\mathbf{W}$ is a diagonal matrix including the weights (inverse of the shift variance of the pairwise measurements, that can be computed from the estimated coherences). In Yague-Martinez et al., 2016a a detailed description of the system of equations can be found for the case where the master image is the first of the stack. A possibility to limit the computational burden when working with long time series is to exploit subsets of images of the stack, e.g., by setting a maximum time span (Fattahi et al., 2017). However, this strategy would not profit from distant high coherent images in the presence of seasonal effects or long-term coherence, and represents a sub-optimal solution in terms of performance.

5.3 Results with Sentinel-1

The data set consists of a total of 43 Sentinel-1A IW acquisitions over Mexico for the evaluation of the procedure. The city of Mexico is covered by one of the subswaths, whereas one of the remaining subswaths corresponds mainly to non-urban areas. This makes the scenario suitable to perform a validation of the method since long-term coherent as well as rapidly decorrelating scatterers can be found. The images were acquired between November 2014 and August 2016 in ascending geometry (track 78). The master image, acquired on November 4, 2014, has been chosen at the beginning of the stack in order to maximize temporal decorrelation effects.

A quantitative comparison between the shifts obtained with joint and single-master approaches is shown in first place. From Fig. 5.2, it can be seen that the targets over urban areas present long-term coherence whereas distributed scatterers have a faster decay of the coherence with time. Taking advantage of this fact, a mask for the urban areas can be generated by establishing a threshold to the coherence between the master image and the slave image with the largest temporal span. The estimation of the shifts applied to these areas can be performed using the joint and single-master approach. Fig. 5.5 shows the difference between direct ESD and the joint retrieved shifts for the urban areas. The deviation of the direct ESD shifts with respect to the joint solution is very small. This is an expected result since urban areas present long-term coherence properties and the single-master estimate already provides good results.

If the urban areas are masked out and only the areas with distributed scatterers are considered, the plot of Fig. 5.6 is obtained. Much larger differences between direct ESD and the joint retrieved shifts over the land areas can be observed. It is assumed that the joint estimates are the reference since they correspond to the optimal estimation. The required 0.0009 samples values have been depicted with blue dashed lines and it can be observed

that these limits are exceeded for some of the acquisitions, especially large when the temporal baseline increases. It should be expected to have interferometric phase errors of about 10° at the burst edges for some acquisitions, e.g., on 10/03/2016 or 02/06/2016[1].

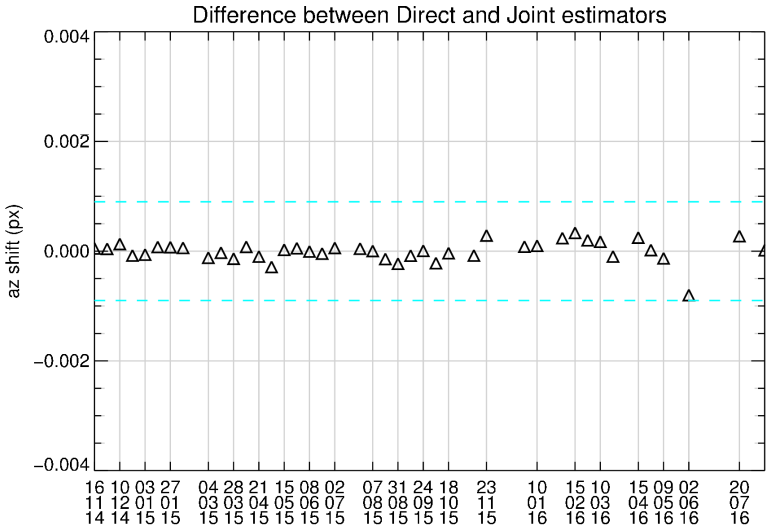

FIGURE 5.5: Comparison between the azimuth shifts retrieved with the joint coregistration approach and the single master approach over urban areas. The blue dashed lines correspond to the required 0.0009 samples accuracy.

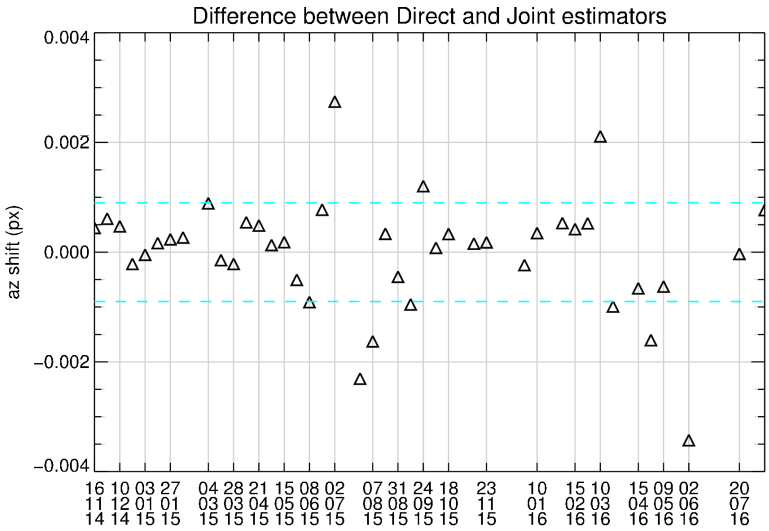

FIGURE 5.6: Comparison between the azimuth shifts retrieved with the joint coregistration approach and the single master approach over distributed targets (non-urban areas). The blue dashed lines correspond to the required 0.0009 samples accuracy.

From Fig. 5.6 it can be seen that the acquisitions on 10/03/2016 and 02/06/2016 present large deviations between both estimates. The residual ESD phase - measured in a direct way - over the urban area is evaluated. This area presents long-term coherence, being the direct estimation reliable. This measurement is performed for three different coregistered versions of the images: (i) only geometric coregistration, (ii) single-master approach and (iii) joint approach. For (ii) and (iii), the non-urban area was used to retrieve the azimuth shifts with

[1] According to $\phi_{\text{error}} \approx 2\pi\Delta f_{\text{DC}}\Delta t$, being Δf_{DC} the Doppler frequency span for each burst. The first subswath (IW1) has been assumed, with Δf_{DC}=5.2 kHz. Note that $\Delta t = \Delta y / f_{\text{az}}$, being Δy the azimuth shift and f_{az}=486.49 Hz the azimuth sampling frequency (see Table I from Yague-Martinez et al., 2016b)

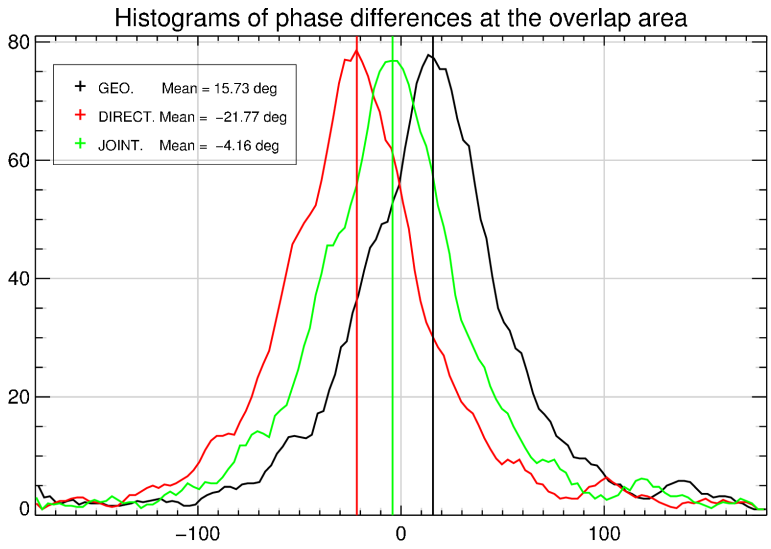

FIGURE 5.7: Histograms of the measured residual ESD phases for the three coregistration possibilities. The histogram of the residual ESD phase in case that only a geometric coregistration is performed is shown in black, presenting a mean value of 15.73°. The histogram in case that the azimuth shifts are calculated employing the single-master approach is shown in red, providing a residual ESD phase equal to -21.77°. The histogram of the residual ESD phase for the images coregistered jointly is shown in green. In this case the mean error is only -4.16° which is much closer to our established boundaries

respect to the master image. The results are summarised in Fig 5.7. The figure shows the histograms of the measured ESD phases for all three cases. The mean value of the ESD phase in case that only a geometric coregistration is performed is 15.73°, larger than the targeted 3.6°. This phase error is due to timing/orbital errors of both acquisitions. In case that the azimuth shifts are calculated employing the single-master approach an "overcorrection" takes place, delivering a residual ESD phase equal to -21.77°, which is even a larger error than the one corresponding to the orbital error. The joint estimate delivers a residual ESD phase of only -4.16° which is much closer to our established requirement.

5.4 Conclusions

The azimuth coregistration problem of interferometric stacks of TOPS images using S1 IW data has been adressed. The high coregistration requirements for TOPS data have been stressed, highlighting the necessity of sophisticated methods when coregistering long stacks of images. The joint coregistration idea has been applied to the retrieval of the (rigid) azimuth shifts applying a least squares estimate.

The better performance of the joint estimation has been demonstrated with a stack of 43 S1 images over Mexico. The best results are achieved when mapping land areas, where temporal decorrelation effects are important. A comparison of the joint estimation with the single-master approach has been done indicating that deviations of more than 0.0009 samples can occur if a joint approach is not used. These errors introduce biases in the interferometric phases, as shown for the analyzed stack, increasing the noise of the line-of-sight deformation measurements over time. The higher the density of persistent scatterers at the overlap areas is, the lower is the gain of the join estimator. However applying a joint estimation procedure provides, in general, a better estimation of the shifts.

In the case that local ground displacement in the along-track direction takes place, a phase linking (PL) (Monti Guarnieri and Tebaldini, 2008) procedure can be applied to the ESD phases at the overlapping areas in order to retrieve the maximum likelihood estimate

of the phases. PL with a small multilook window is used in order to be adaptive to local displacements, since the WLS approach averages all valid samples of all overlap areas. For each multilooked pixel, the ESD phases would contain two contributions: one due to the orbital error and one due to the ground displacement. The periodogram can be applied to obtain the mean azimuth deformation rate. Once the slope is retrieved, the values can be "de-trended" in order to isolate the orbital errors. An average of the "de-trended" values employing all multilooked samples for each pair would provide the corresponding azimuth shift due to an orbital error. Note that the result also corresponds to a joint estimate, since PL is applied to the ESD phases.

Chapter 6

A novel acquisition mode: the 2-look TOPS

Chapter 4 presented the interferometric processing techniques for the generation of wide-swath TOPS interferograms. The high azimuth coregistration requirements, due to the azimuth beam steering of TOPS, was highlighted, proposing the exploitation of spectral diversity (Section 2.4.2) at the overlapping areas between bursts to obtain fine azimuth accuracy (ESD technique, see Section 4.3). Chapter 5 presented an extension of the ESD method for coregistering stacks of TOPS acquisitions through a joint estimation approach. This way decorrelation effects for long time series can be mitigated. In this chapter the 2-look TOPS acquisition mode is proposed. Its high azimuth sensitivity (even better than StripMap) allows to retrieve ground deformation in the azimuth direction, making it possible to generate 2-D deformation maps, as done in chapter 3 through correlation techniques. The price to pay is a degradation of the resolution of the single-look complex (SLC) image by a factor of approximately two, a minor effect for interferometry, since after multilooking the phase the number of looks is the same as its equivalent (1-look) TOPS mode. The associated paper provides full details on the design of the mode, which proposes two modalities: TOPS2, a 2-look TOPS mode whose design is driven by the azimuth resolution and TOPS2+, a 2-look TOPS, whose design is based on the azimuth motion sensitivity by increasing the beam steering angles range. The expected performances are provided considering the effect of the turbulent troposphere. Moreover a demonstration with experimental TerraSAR-X acquisitions for pairs over Petermann glacier, Greenland, and two years of time series over Hoshab fault, Pakistan, demonstrate its capabilities. This chapter provides just a summary of the associated paper.

6.1 Motivation

Since radar systems measure distances in the line-of-sight direction, spaceborne SAR instruments in near-polar orbits are very sensitive to ground displacements in the East-West (E-W) and vertical directions. By combining different geometries, a 3-D deformation field can be

This chapter presents an overview of the paper in Appendix D (Yague-Martinez et al., 2019b):
N. Yague-Martinez, P. Prats-Iraola, S. Wollstadt, and A. Moreira (2019b). "The 2-Look TOPS Mode: Design and Demonstration With TerraSAR-X". in: *IEEE Transactions on Geoscience and Remote Sensing* 57.10, pp. 7682–7703. ISSN: 0196-2892. DOI: 10.1109/TGRS.2019.2915797

obtained (Rocca, 2003, Wright et al., 2004). However, the sensitivity to displacements in the North-South (N-S) direction remains low. A common procedure to enhance the sensitivity in along-track direction, and therefore to the N-S direction, is to apply correlation techniques.

The interest on SAR systems with short repetition cycle from the scientific community has fostered the use of wide-swath acquisition modes. The TOPS mode (De Zan and Monti Guarnieri, 2006) has been implemented as the baseline mode for acquisitions over land, offering a swath of 250 km at 20 m azimuth resolution. The degraded azimuth resolution impairs the accuracy of correlation techniques in this direction, since the sensitivity depends on the resolution cell size (Bamler and Eineder, 2005). This limitation can be overcome employing the ESD technique at the overlapping area between bursts, which provide measurements of the ground displacement (Hooper and Spaans, 2017, Yague-Martinez et al., 2019a). The latter approach provides unfortunately discontinuous measurements due to the limited coverage of the overlapping areas (10% in azimuth), and calls for a mode that provide continuous ground displacement.

The focus of this chapter lies on the design of *two-look* acquisition modes based on TOPS and its demonstration with TerraSAR-X. The achieved coverage is the same as the one provided by single look modes at the expense of a degradation of the azimuth resolution by a factor of two, maintaining however the number of looks for a given product resolution. The benefit of this strategy lies on the possibility to exploit spectral diversity techniques (Scheiber and Moreira, 2000, Bamler and Eineder, 2005), improving significantly the sensitivity to azimuth surface displacements. The mid-azimuth resolution of the proposed mode does not suppose a limitation for geophysical applications as, e.g., strain estimation.

6.2 The 2-look TOPS mode: concept and design

Fig. 6.1 illustrates the operation mode of a 2-look TOPS system compared to a 1-look TOPS system, henceforth referred as TOPS. The left part of the figure refers to a 1-look system, which depicts the acquisition of two bursts of the same subswath. Employing one look, each target on ground is observed with just one line of sight (except at the overlapping area between bursts). The right part of the figure corresponds to a 2-look system, in which the scanning timeline allows to illuminate each target with two different lines of sight.

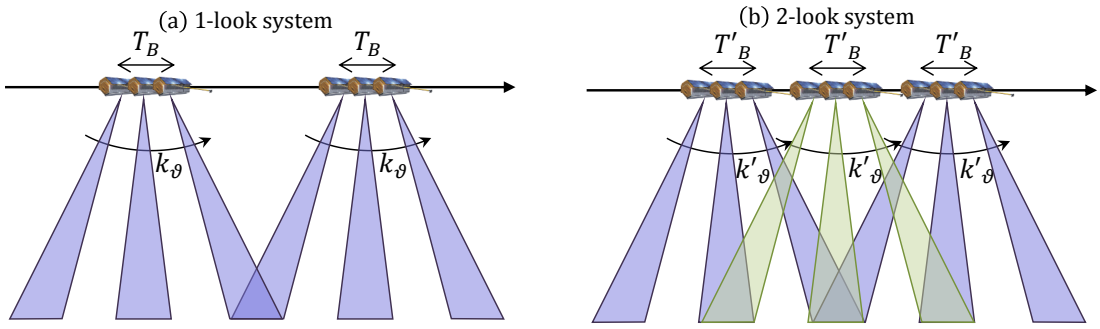

FIGURE 6.1: (a) Schematic operation of a TOPS system (1 look) and a (b) 2-look TOPS system. The antenna is steered in azimuth from backward to forward at a rate k_ϑ and k'_ϑ for TOPS and 2-look TOPS, respectively. In a 1-look system each target is observed only once (except eventually at the burst overlapping areas), a 2-look system allows illuminating each target with two different squint angles.

The 2-look TOPS mode obtains two *time-varying* lines of sight, however, the spatial diversity between both remains constant over the acquisition. This can be better understood by

comparing the time-frequency diagrams for TOPS and 2-look TOPS depicted in Fig. 6.2. The top part of the figure corresponds to the conventional 1-look system, which illustrates the acquisition of two consecutive bursts of the same subswath for a certain range, presenting each target a Doppler rate, k_a. The antenna is rotated in the azimuth direction originating a linear frequency variation of the burst, of duration T_B, at a rate k_{rot}. The SAR processing at zero-Doppler geometry causes that the focused burst, of duration $T_{focused}$, exhibits a linear frequency variation with a rate k_t. The cycle time or interburst time, T_R, is the elapsed time between bursts of the same subswath. Two targets, P_1 and P_2, are displayed at their zero-Doppler position indicating the portion of the (once) covered raw and focused data Doppler spectra. The bottom part of the figure refers to a 2-look system, where three bursts are depicted. The cycle time, T'_R, allows to map each target with two portions of the spectra, as can be seen for both depicted targets, P_1 and P_2.

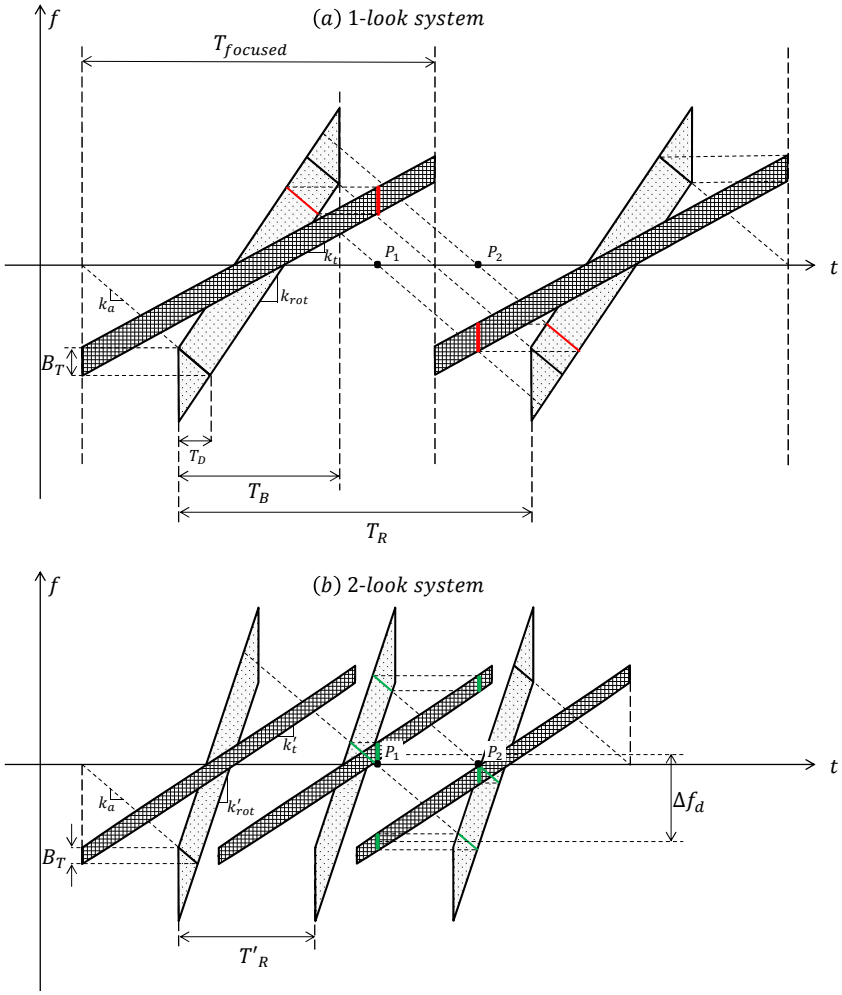

FIGURE 6.2: (a) Time-frequency diagram of a TOPS system, which shows two bursts of the same subswath at a certain range. Two targets, P_1 and P_2, are displayed at their zero-Doppler position indicating the portion of the (once) covered raw and focused data Doppler spectra. (b) Time-frequency diagram of a 2-look TOPS system. In this case the cycle time, T'_R, allows to map each target with two portions of the spectrum as can be seen for targets.

The spectral separation for a target on ground between two consecutive bursts (looks) can be exploited to retrieve an accurate estimation of the azimuthal motion according to:

$$\phi_{ESD}(r,x) = 2\pi \cdot \Delta f_d(r) \cdot \Delta t(r,x), \tag{6.1}$$

which is the same as (4.8), where the dependency of the local azimuth shift (in temporal units) with range, r, and azimuth, x, has been highlighted. $\Delta f_{\mathrm{d}}(r)$ is the spectral separation between looks, independent of the target's azimuth position.

The spectral separation, $\Delta f_{\mathrm{d}}(r)$, can be calculated according to (Prats-Iraola et al., 2012):

$$\Delta f_{\mathrm{d}}(r) = \left| \frac{k_{\mathrm{rot}} \cdot k_{\mathrm{a}}(r)}{k_{\mathrm{rot}} - k_{\mathrm{a}}(r)} \right| T_{\mathrm{R}}, \tag{6.2}$$

where $k_{\mathrm{rot}} \approx \frac{2 \cdot v_{\mathrm{s}}}{\lambda} k_{\vartheta}$ is the antenna Doppler rate due to the antenna rotation at a rate k_{ϑ}, v_{s} is the satellite velocity, k_{a} is the target Doppler rate, and T_{R} is the the cycle time or interburst time.

We will call, in general, 2-look TOPS a TOPS system that maps each target on ground with two separated Doppler sub-bands. Henceforth we employ the nomenclature TOPS2 for a 2-look system with a timeline design driven by the azimuth resolution. The timeline equations of the TOPS2 mode are provided in section 6.2.1. An optimization of the scanning timeline in terms of achieving a higher sensitivity to the azimuthal motion is moreover proposed; we refer in this case to a 2-look TOPS system with such a scanning timeline which selects the spectral separation between looks (usually larger than the one achievable by establishing the resolution) as TOPS2+. The design equations of TOPS2+ are presented in section 6.2.2.

6.2.1 Scanning timeline equations: TOPS2

Following the classical approach for the design of a SAR mode driven by the desired resolution, ρ_{az}, the steering parameters for each subswath, n, can be obtained using:

$$k_{\vartheta}^{(n)} = \left(\frac{2\rho_{\mathrm{a}} \vartheta_0^{(n)}}{\lambda} \frac{(v_{\mathrm{eff}}^{(n)})^2}{(v_{\mathrm{g}}^{(n)})^2} - 1 \right) \frac{v_{\mathrm{g}}^{(n)}}{r_0^{(n)}}, \tag{6.3}$$

where ρ_{a} is the desired azimuth resolution, ϑ_0 is the antenna azimuth bandwidth at -3 dB, v_{g} is the beam ground velocity, v_{eff} is the effective velocity, r_0 is the range of closest approach and λ is the radar wavelength.

Once the steering rate has been obtained, the global 2-look TOPS scanning timeline can be obtained setting a cycle time, T_{R}, that allows that the total bandwidth spanned in the burst duration is at least two times larger than the one spanned by a target in the interburst interval. This leads to the equations provided in De Zan and Monti Guarnieri, 2006 including a factor 2 multiplying the cycle time:

$$\left(k_{\vartheta}^{(n)} T_{\mathrm{B}}^{(n)} - \vartheta_0^{(n)} \right) r_0^{(n)} + v_{\mathrm{g}}^{(n)} T_{\mathrm{B}}^{(n)} \geq 2 \cdot v_{\mathrm{g}}^{(n)} T_{\mathrm{R}}. \tag{6.4}$$

As stated in De Zan and Monti Guarnieri, 2006 there is a bound on the azimuth resolution, ρ_{a}, for any subswath:

$$\rho_{\mathrm{a}} > 2 \cdot \sum_{n=0}^{N_{\mathrm{ss}}-1} \rho_{\mathrm{a}}^{\mathrm{SM}\ (n)}, \tag{6.5}$$

being $\rho_{\mathrm{az}}^{\mathrm{SM}\ (n)}$ the resolution of an equivalent StripMap acquisition for each subswath, n, and N_{ss} the number of subswaths. The factor 2 is again due to the mapping of two looks.

A 2-look system has a degraded resolution by a factor of two with respect to its equivalent 1-look system. Since our interest is to combine the looks at the *interferometric processing* stage, in order to apply spectral diversity techniques, the strategy is to focus each burst (look) separately.

A second consequence of degrading the resolution by a factor of two is that, according to (6.3), the steering rate is increased by a factor slightly larger than two. Provided that (6.5) is fulfilled, choosing a finer resolution results in a lower steering rate. This implies that the bursts become longer, spanning the antenna beam larger maximum steering angles. This fact can be exploited to maximize the spectral separation, as discussed in the next section.

6.2.2 Alternative scanning timeline equations for azimuth sensitivity enhancement: TOPS2+

From (6.2), it can be observed that the spectral separation is proportional to the cycle time, T_{R}. Longer cycle times can be obtained either by enhancing the resolution or by imposing a larger maximum steering angle, equivalently. The design of the timeline based on the maximum steering angle is appropriate for systems employing phased-array antennas, since it allows to control the maximum level of the grating lobe and therefore the level of the azimuth ambiguities.

Once the desired maximum steering angle, β_{max}, has been set, the following relation can be written:

$$k_{\vartheta}^{(n)} = \frac{\Delta\beta}{T_{\mathrm{B}}^{(n)}}, \tag{6.6}$$

where $\Delta\beta = 2 \cdot \beta_{\mathrm{max}}$. Substituting (6.6) in (6.4) we obtain the TOPS2+ set of equations:

$$\left(\Delta\beta - \vartheta_0^{(n)}\right) r_0^{(n)} + v_{\mathrm{g}}^{(n)} T_B^{(n)} \geq 2 \cdot v_{\mathrm{g}}^{(n)} T_{\mathrm{R}}. \tag{6.7}$$

By solving this system of equations, the burst durations, $T_{\mathrm{B}}^{(n)}$, are obtained, which establish the steering rates for each subswath, $k_{\vartheta}^{(n)}$ according to (6.6). The resulting azimuth resolution is given by:

$$\rho_{\mathrm{a}}^{(n)} = \frac{v_{\mathrm{g}}^{(n)}}{B_{\mathrm{T}}^{(n)}}, \tag{6.8}$$

being $B_{\mathrm{T}}^{(n)} = k_{\mathrm{a}}^{(n)} \cdot T_{\mathrm{D}}^{(n)}$ the target bandwidth for the $(n)^{th}$ subswath. $T_{\mathrm{D}}^{(n)}$ is its corresponding dwell time, given by:

$$T_{\mathrm{D}}^{(n)} \approx \frac{r_0^{(n)} \cdot \vartheta_0^{(n)}}{\alpha^{(n)} \cdot v_{\mathrm{g}}^{(n)}}. \tag{6.9}$$

The maximum steering angle cannot be set arbitrarily, since the azimuth ambiguity level increases with it. The associated paper provides a detailed performance analysis (see Appendix D.III).

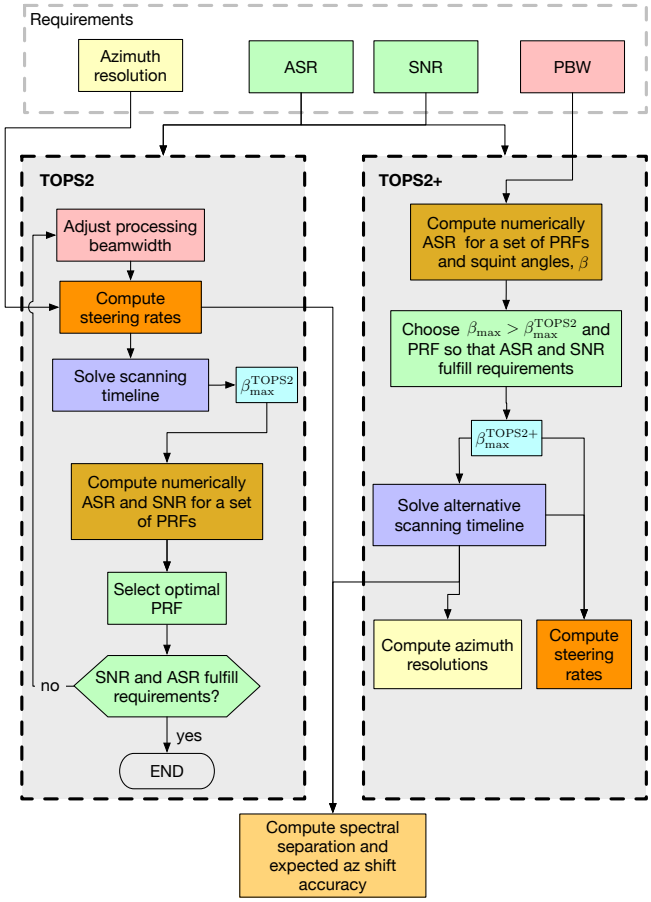

FIGURE 6.3: Flow diagram for the design of the TOPS2 and TOPS2+ modes.

Fig. 6.3 provides the flow diagram for the design of TOPS2 and TOPS2+. Note that the obtained PRF might be modified according to the timing constraints imposed for the transmission of pulses and reception of echoes, and nadir returns, provided in Section 2.2.2.

A coverage of approximately 100 km can be achieved with the TerraSAR-X system employing two wide beams (Steinbrecher et al., 2014). Establishing a single look complex (SLC) azimuth resolution equal to 16.6 m for TOPS2 and applying (6.3) and (6.4) the scanning timeline parameters detailed in Table 6.1 are obtained, where a maximum steering angle, $\beta_{\max}$, of approximately 0.55° is obtained. The maximum steering angle for TOPS2+ is established, as a matter of example, to approximately twice that of the TOPS2 mode, i.e., 1.1°. The TOPS2+ timeline parameters are obtained by applying (6.6) and (6.7). The parameters for TOPS, assuming 8.3 m resolution, and StripMap are also included for reference. For the latter modes, the spectral diversity technique, i.e., the split of the Doppler bandwidth into two sub-looks can be applied in order to obtain the azimuth shifts. The optimal sub-look bandwidths correspond to $b_{\text{SD}} = B_{\text{T}}/3$ (Bamler and Eineder, 2005), which deliver a spectral separation of $\Delta f_d = 2/3B_{\text{T}}$.

TABLE 6.1: Scanning timeline parameters for the TOPS, TOPS2 and TOPS2+ modes, using two subswaths. The mid-range position of the subswaths have been assumed. The values in bold indicate the design criteria to determine the acquisition timeline parameters. An additional overlap between odd/even bursts of 10% has been considered for the design. The achievable values for StripMap are included for reference. The parameter b_{SD} indicates the bandwidth that can be obtained by splitting the Doppler spectrum into two sub-looks for StripMap and TOPS in order to apply the spectral diversity technique to measure the azimuth shift. For TOPS2 and TOPS2+ there is no need to split the spectrum. The TerraSAR-X system parameters have been used.

	SM	TOPS	TOPS2	TOPS2+
ρ_{az} [m]	3.3	**8.3**	**16.6**	13.38/15.11
β_{max} [deg]	-	0.501/0.487	0.547/0.532	**1.1**
T_B [s]	-	0.834/0.840	0.355/0.358	0.936/0.832
T_R [s]	-	1.675	0.71	1.77
k_ϑ [rad/s]	-	0.021/0.020	0.054/0.052	0.041/0.046
Δf_d [Hz]	1843	664	3420/3297	8028/7994
B_T [Hz]	2765	996	498	618/547
b_{SD} [Hz]	921.67	332	-	-
Amb. band [m]	$\approx \pm 2$	$\approx \pm 5$	$\approx \pm 1$	$\approx \pm 0.5$

The estimation error of the azimuth shift, Δx, (in meter units) can be written combining (4.8) and the standard deviation of the differential phase between the interferograms of both looks, $\sigma_{\phi_{ESD}}$, which can be assumed to be $\sqrt{2}$ times the standard deviation of the interferometric phase, given by (2.47). assuming that the number of independent samples, N, is large, obtaining:

$$\sigma_{\Delta x} = \frac{\sigma_{\phi_{ESD}}}{2\pi\Delta f_d} v_g = \frac{1}{2\pi\Delta f_d \sqrt{N}} \frac{\sqrt{1-\gamma^2}}{\gamma} v_g, \tag{6.10}$$

where γ is the interferometric coherence.

The plot of the accuracies in the retrieval of the azimuth mutual shift between two images, for TOPS, TOPS2 and TOPS2+ with a maximum steering angle of 1.1°, is shown in Fig. 6.4, as a function of the coherence. The curves have been generated taking into account the spectral separation between looks, bandwidths, and establishing an output product resolution of 100 m $\times$ 100 m.

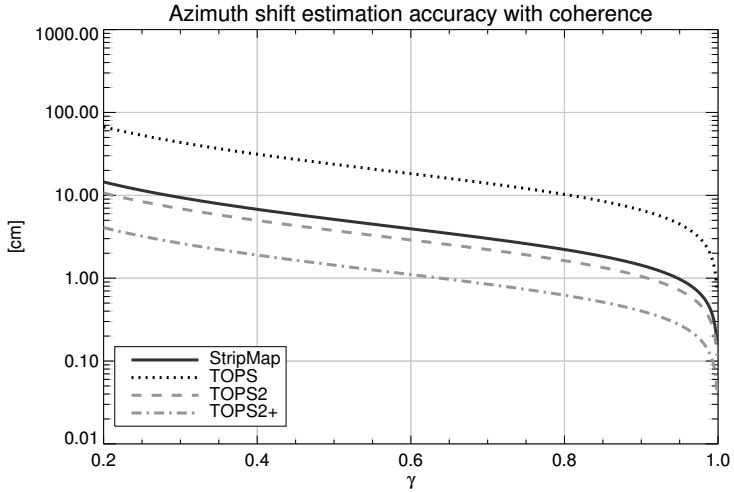

FIGURE 6.4: Azimuth shift standard deviation for a StripMap, TOPS, TOPS2 and TOPS2+ system as a function of the coherence. The output product resolution has been set to 100 m $\times$ 100 m

The standard deviation of a TOPS mode is 4.6 times worse than for Stripmap. Regarding TOPS2 and TOPS2+, the standard deviations are 0.73 and 0.28 times the StripMap one, respectively. The standard deviation of the TOPS2+ mode with respect to conventional TOPS is 16.5 times smaller.

The interferometric coherence diverges among the modes, since each mode is unequally affected by ambiguities and SNR losses. In the associated paper additional plots of the accuracy are provided as a function of the backscattering coefficient.

The 2-D performances for TOPS2 and TOPS2+ are provided in the associated paper, which has made use of the Hybrid Cramér-Rao Bound (HCRB) for the crustal displacement field estimator provided (Monti Guarnieri and Tebaldini, 2007) and has modeled the turbulent troposphere according to Prats-Iraola et al., 2017. The 3-D achievable performances combining ascending and descending geometries are as well provided.

6.3 Consideration of ionospheric effects

The interferometric compensation of ionospheric disturbances for burst-mode acquisitions has been tackled in Gomba et al., 2017, where a modification of the (range) split-spectrum method is proposed and applied to ScanSAR and TOPS data. For TOPS systems, gaps of the ionospheric phase screen appear in the azimuth direction due to the burst-mode acquisition nature and the high altitude of the ionosphere. In the following the continuity of the phase screen for 2-look TOPS systems is analyzed.

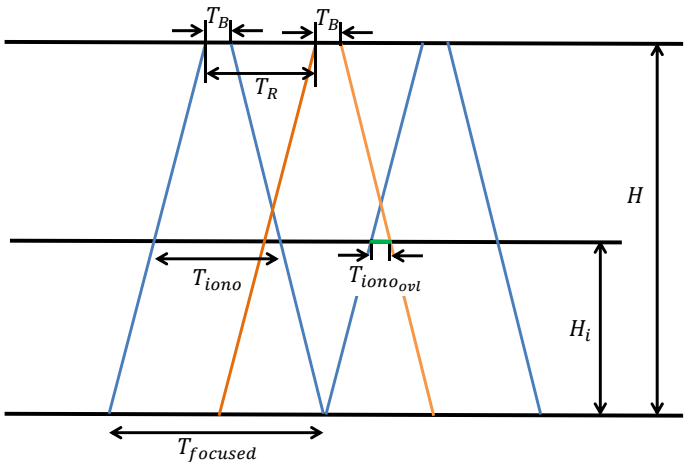

FIGURE 6.5: Scheme depicting the extension of the imaged ionosphere, T_{iono}, for an assumed certain height, H_{i}, when focusing the data at zero-Doppler geometry. The height of the sensor is H, T_{B} is the burst duration, T_{R} the cycle time and T_{focused} the duration of the focused burst.

Once the ionospheric piercing-point, i.e., the intersection between the radar line of sight and the (modeled as single-layer shell) ionosphere, is established at an assumed height, H_{i}, the covered duration of the burst at the ionospheric height, T_{iono}, is given by:

$$T_{\text{iono}} = T_{\text{B}} + \frac{H_{\text{i}}}{H} \cdot \frac{T_{\text{B}} k_{\text{rot}} - B_{\text{a}}}{|k_{\text{a}}|}, \tag{6.11}$$

where H is the satellite height. Fig. 6.5 depicts the involved timing parameters according to the corresponding heights.

Taking the TOPS timelines parameters summarized in Table 6.1, we obtain the indicated overlaps in Table 6.2 at different ionospheric heights for TOPS, TOPS2 and TOPS2+ modes. The typical ionosphere height, H_{i}, is about 300 km (Davies, 1990).

TABLE 6.2: Overlap between bursts for different ionospheric heights, H_{i}. The values indicate the overlap, $T_{\text{iono}_{\text{ovl}}}$, between consecutive bursts of the first subswath at the assumed ionospheric height, H_{i}. The overlap percentage ($T_{\text{iono}_{\text{ovl}}} / T_{\text{iono}}$) is indicated between brackets. Negative values indicate gaps between bursts and positive values overlap. The timeline from table 6.1 has been assumed.

H_{i}	TOPS	TOPS2	TOPS2+
200 km	-0.22 s (-15%)	0.34 s (32%)	0.86 s (33%)
250 km	-0.32 s (-24%)	0.23 s (24%)	0.59 s (25%)
300 km	-0.42 s (-34%)	0.12 s (14%)	0.32 s (15%)
350 km	-0.52 s (-45%)	0.01 s (1%)	0.05 s (3%)
400 km	-0.62 s (-58%)	-0.10 s (-17%)	-0.21 s (-14%)

It can be observed that a 1-look system with two subswaths presents gaps (negative values) between bursts for the given ionosphere heights, H_{i}, whereas the 2-look modes achieve overlap between bursts up to a ionosphere height of about 350 km. A higher ionosphere presents marginal gaps, when compared to TOPS. A gap-free mapping of the ionosphere allows a better smoothing of the phase screen, since edge effects are avoided, and is specially relevant in the case where high frequency variations are present.

The split-spectrum technique is able to recover the ionospheric phase screen. However, the estimation noise imposes limitations to the achievable spatial resolution, allowing only

to retrieve large-scale ionospheric variations. A powerful technique, which allows to estimate the gradient of the ionospheric differential delay along azimuth, consists in calculating the mutual azimuth shifts between the interferometric images, as suggested in Meyer et al., 2006. Since the 2-look TOPS modes provide an enhanced sensitivity to the azimuth shift, small-scale variations along azimuth can be retrieved.

It can be concluded that the use of 2-look TOPS modes allows applying joint estimations from split-spectrum and azimuth shifts, without any limitation (in terms of data gaps or degraded sensitivity), as proposed by Gomba and De Zan, 2017 and applied to StripMap acquisitions. This represents an additional advantage with respect to the conventional TOPS mode.

6.4 Demonstration with TerraSAR-X

Experimental TOPS2 acquisitions have been performed over different sites to demonstrate the applicability of the mode for the retrieval of large azimuth displacements employing pairs of images, and of mean deformation velocities by exploiting time series. The first example, with pairs of images, corresponds to the retrieval of the local azimuth shifts on the Petermann glacier which allows to remove phase discontinuities due to azimuth displacement. The second example, employing time-series, corresponds to the estimation of post-seismic ground deformation after the 2013 Balochistan earthquake in Pakistan.

6.4.1 InSAR pairs

A pair of TerraSAR-X TOPS2 images have been acquired on 16/10/2015 and 27/10/2015 over the Petermann glacier. The data takes are composed by four subswaths and 122 bursts (with a length of approx. 10 km each). The range coverage is 100 km, with a total scene length of 500 km, being the azimuth resolution 40 m. Fig. 6.6 shows an overview of the obtained results, the horizontal direction corresponds to along-track. From the reflectivity (a), it can be seen that the ice flows from left to right, where the ice tongue can be distinguished. After a geometric coregistration has been performed, the coherence (b), and InSAR phase (c) can be obtained. It can be observed that due to the high glacier velocity, the coherence is low on the ice tongue, as in this case the shifts are larger than the resolution cell and no adaptive coregistration was applied. Our focus is outside these areas, since even if there were enough coherence, there is no justification to apply interferometry due to very high fringe frequency. For such areas, amplitude-based techniques, e.g. cross-correlation, immune to wrapping effects are more adequate. The parts of the glacier with a slower displacement rate present an acceptable coherence and moderate velocities. A Greenland DEM (Howat et al., 2014) has been employed to subtract topographic fringes. On the left part of the InSAR phase (c), phase discontinuities due to glacier displacement can be observed. The aim is to remove the phase discontinuities by applying an accurate local azimuth coregistration by exploiting both looks, as expounded in the associated paper (section V.A). The combination of the InSAR phases from both looks allows the computation of the ESD phase. The spectral separation between looks is approximately 3000 Hz, corresponding the ambiguity band of the shift estimate to be around 1 m. Since larger movements in the azimuth direction are expected, the ESD phase (d) has to be unwrapped. A smoother ESD phase would be expected, however, phase discontinuities are to be found at the burst interfaces indicating that there are ionospheric perturbations due to the high solar activity occurred in 2015, strong enough to be sensed at X band. An estimation of the ionospheric contribution employing, e.g., split bandwidth techniques (Gomba et al., 2017) in order to separate displacement from ionospheric disturbances is, however, out of the scope of this contribution.

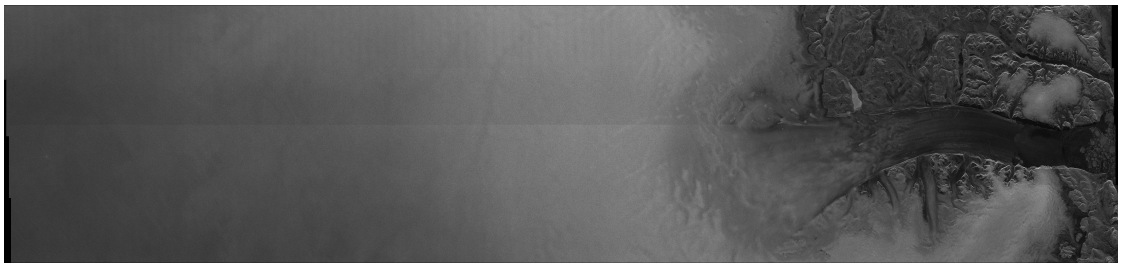

(a)

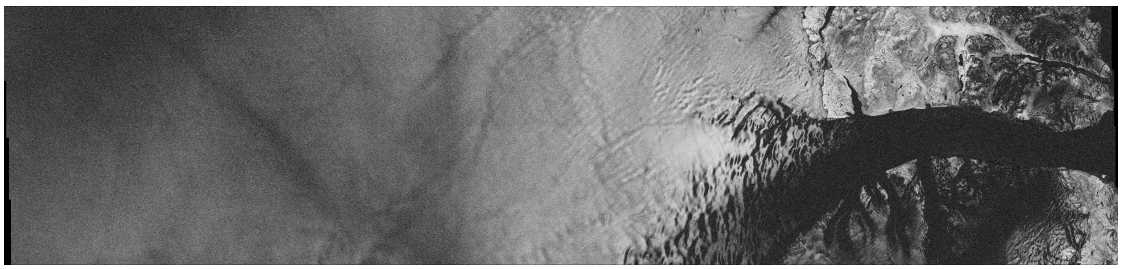

(b)

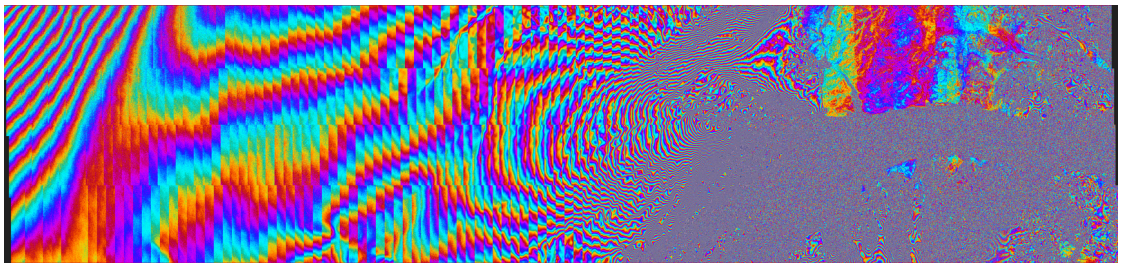

(c)

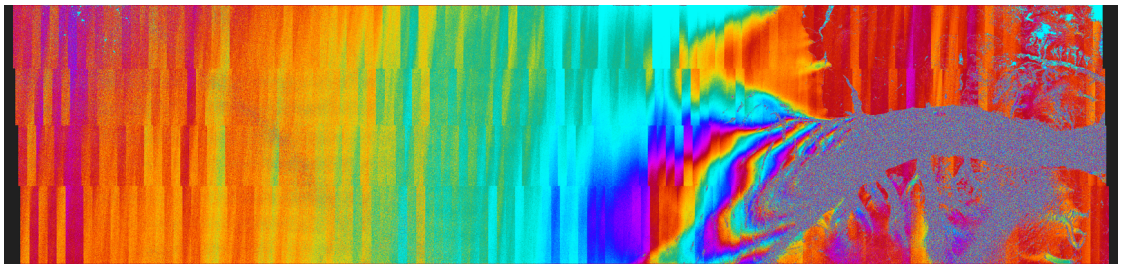

(d)

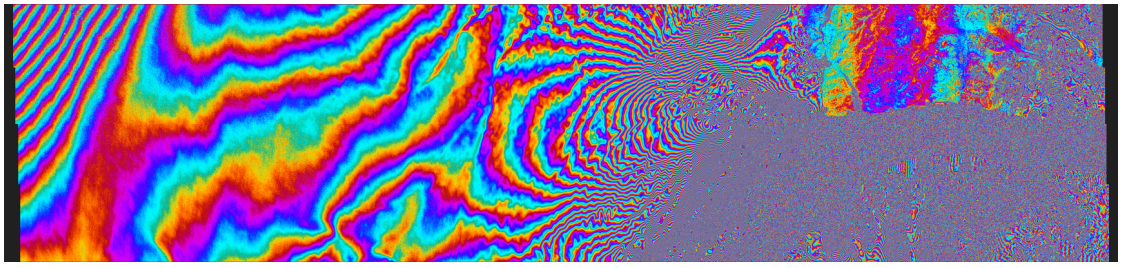

(e)

FIGURE 6.6: Interferometric TOPS2 results over Petermann site corresponding to the pair 16/10/2015-27/10/2015. The acquisition covers an area of 100 km $\times$ 500 km and employs four subswaths with an azimuth resolution of 40 m. (a) Reflectivity, (b) coherence, (c) interferometric phase after removing the topography, (d) ESD phase proportional to the along-track motion, and (e) interferometric phase obtained after removing the along-track component of the motion by exploiting the 2 looks. The Greenland Ice Mapping Project (GIMP) DEM (Howat et al., 2014) has been used to remove the topography contribution to the phase. The phases are scaled between $\pm 180^{\circ}$. Range is vertical and azimuth is horizontal.

6.4.2 Time series. Post-seismic deformation over the Hoshab Fault

The Chaman fault system, between Pakistan and Afghanistan, demarks the western boundary of the Indian plate, which is the locus of many catastrophic earthquakes (Riaz et al., 2019). The 2013 earthquake (Jolivet et al., 2014, Avouac et al., 2014, Barnhart et al., 2014) with magnitude M_w7.7 occurred on the Hoshab Fault. The tectonics of southern and central Pakistan reflect a complex plate boundary where the India plate slides northward relative to the Eurasia plate in the east, and the Arabia plate subducts northward beneath the Eurasia plate in the Makran. These motions typically result in N-S to Northeast-Southwest strike-slip motion. After the 2013 shocks, post-seismic deformation close to the 2013 epicenter location is expected, with displacements in N-S to North East-South West.

Two stacks of experimental TerraSAR-X TOPS2 acquisitions, in ascending and descending geometry, have been acquired from April 2016 until April 2018. The acquisitions have two subswaths and cover an extension of 85 km $\times$ 265 km with 17 m azimuth resolution. The spectral separations for each subswaths are 3334 Hz and 3218 Hz, which correspond to ambiguity bands of $\pm$1.06 m and $\pm$1.1 m, respectively.

The mean azimuth velocity can be estimated applying the periodogram operator, as described in the associated paper (Section V.B), to the multilooked ESD phases of the stack. An output resolution for the mean azimuth velocity of 100 m $\times$ 100 m results roughly in an equivalent number of looks of 1000.

The middle part of Fig. 6.7 shows the estimated mean azimuth velocity and temporal coherence for the ascending (a) and descending (b) geometries. Two rectangles over homogeneous areas have been selected to compute the histograms and the mean and the standard deviation of the estimated mean deformation velocity. The bottom part of the same figure shows the resulting histograms and Gaussian fitting for each rectangle. Points with a temporal coherence greater than 0.5 have been considered. In the ascending geometry we obtain standard deviations of about 2.9 to 3.5 mm/month, whereas the expected standard deviation for 53 images is approximately 2.2 mm/month according to the TOPS2 theoretical curves provided in the associated paper. For the descending geometry the obtained standard deviation is below 2.5 mm/month, whereas 1.7 mm/month is expected in case of having 67 images, according to the theoretical curves. The differences between expected and measured standard deviations are very likely due to a mismatch of the decorrelation model used for the calculation of the expected performance, as well as due to the inherent assumptions of the HCRB not occurring in a real scenario.

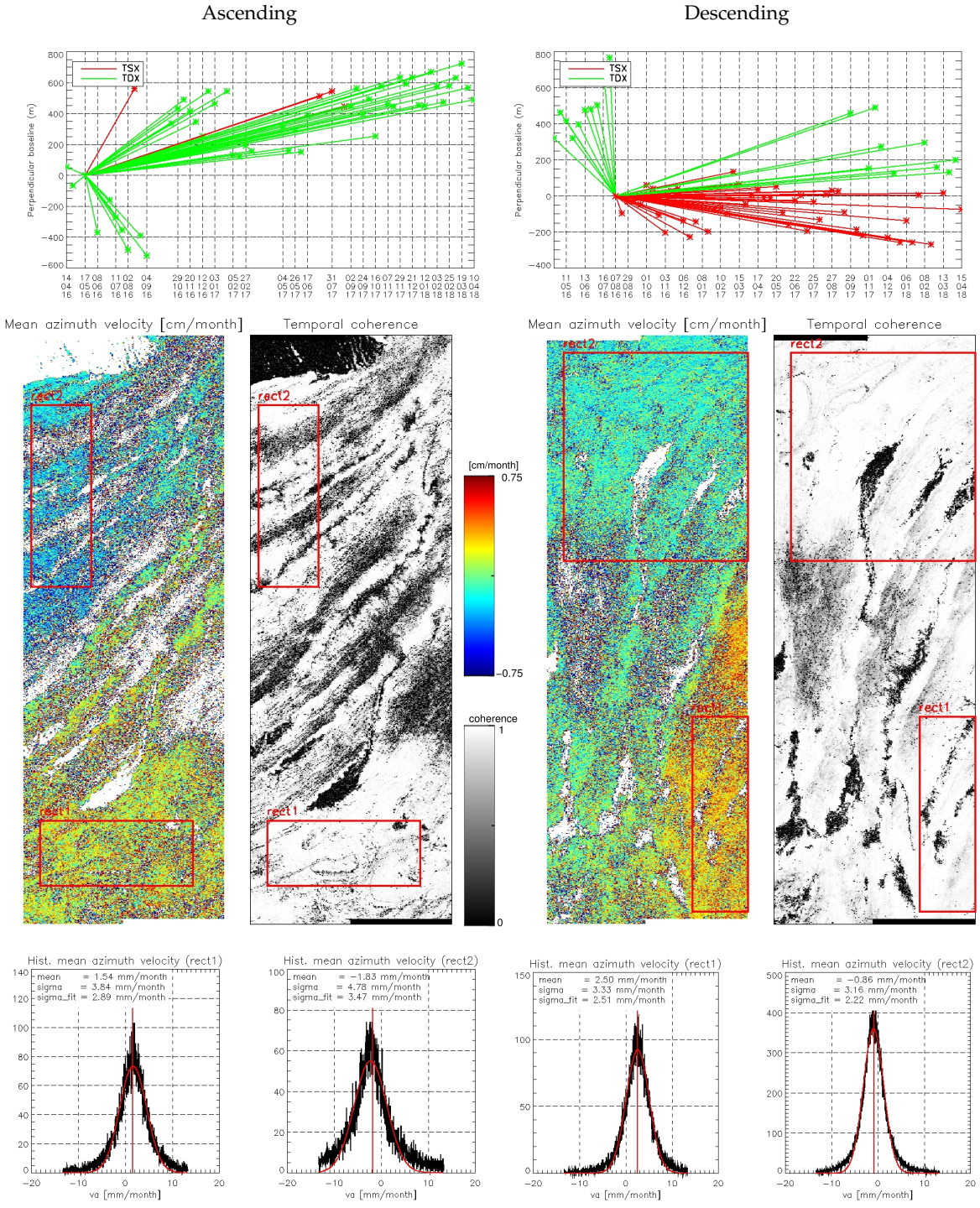

FIGURE 6.7: Time-series TOPS2 results over Balochistan site corresponding to the time frame April 2016 to April 2018. The left part corresponds to the ascending geometry, with a total of 53 images, whereas the right part to the descending geometry, having a total of 67 images. The top part shows the distribution of the perpendicular and temporal baselines for both geometries. The middle part of the figure shows the retrieved mean azimuth velocity map and the temporal coherence, indicating the areas covered by two rectangles for statistics analysis. Range is horizontal and azimuth is vertical. The bottom part shows the histograms of the mean velocity, where a Gaussian fitting (red line) has been performed. The average mean velocity and the standard deviation are provided, as well as the standard deviation result from the Gaussian fit.

6.5 Conclusions

Burst-mode acquisitions have been traditionally employed to map large areas by employing different range subswaths. There have been multiple radar missions which have operated in ScanSAR mode. The design of the modes has been done usually employing multiple looks due to SNR reasons. This way the dependence of the azimuth target position observed by the antenna pattern could be moderately mitigated. The TOPS mode solved the scalloping and associated effects, making the use of multiple looks not necessary. However, if we compare modes recording bursts of echoes to full aperture modes (StripMap), the sensitivity to the along-track direction is degraded in the former case due to its lower azimuth resolution. The 2-look TOPS concept overcomes this limitation. It achieves the same coverage as a single-look TOPS mode at the expense of a degradation of the azimuth resolution by a factor of two, maintaining however the number of looks for a given product resolution.

Two different design principles have been presented, the first one, TOPS2, follows a design based on resolution and achieves very similar azimuth sensitivity to StripMap. The second one, TOPS2+, consists in an optimization of the 2-look TOPS mode, which achieves an enhanced azimuth sensitivity. The design is based on selecting larger antenna beam steering angles and is mainly limited by azimuth ambiguities.

The looks can be combined at the interferometric processing stage reducing this way the residual scalloping. In the case of TOPS2, the resulting residual scalloping is 0.07 dB, whereas for TOPS2+ it amounts 0.4 dB (similar to TOPS, i.e., 0.36 dB). An additional benefit is that ionospheric perturbations can be estimated with continuous coverage (in contrast to TOPS).

Experimental TerraSAR-X data have been acquired over two different scenarios: fast deformation (glacier flow) and slow deformation (post-seismic ground displacement). In the first case, the high potential of the exploitation of 2-look modes to perform a local coregistration has been shown, which allows to remove phase discontinuities due to azimuth displacement. The second case demonstrates the retrieval of a post-seismic signal in along-track direction employing time series, with a 2-year stack, delivering accuracies in the mean along-track velocity of a few mm/month.

The 2-look concept employing burst modes is not only restricted to TOPS operation but can also be employed with ScanSAR (Prats-Iraola et al., 2016). In this case a design based on the azimuth sensitivity, as done for TOPS2+, is not possible, since the maximum Doppler span is linked solely to the antenna beamwidth. However, in spite of achieving a lower sensitivity than its equivalent TOPS mode, spectral diversity techniques can be also applied.

The benefits and high potential of the 2-look TOPS concept have been demonstrated, specially of interest for geophysical applications, where high azimuth resolution is not required.

Chapter 7

Conclusion and Outlook

The monitoring of geophysical dynamic processes of the Earth with interferometric SAR techniques demands short satellite repetition cycles in order to be able to capture single events, as, e.g., earthquakes or volcano eruptions, and to have enough acquisitions over a certain time period in order to perform multi-temporal analyses with data stacks. The satellite repetition cycle can be reduced by adjusting the orbital design and/or employing multiple platforms orbiting in such a configuration that the repetition cycle is reduced. In addition, it would be required to have global coverage over land within the repetition cycle. For this sake, a wide-swath SAR acquisition mode becomes necessary. The mid-resolution TOPS acquisition mode appears as a suitable solution to cope with this problem and a significant part of this dissertation is related to its processing and the proposal of a novel acquisition mode that enhances its capabilities in terms of deformation monitoring.

In the first place, it has been demonstrated with TerraSAR-X data that it is possible to obtain accurate 2-D ground deformation estimates using correlation techniques. Cross-correlation overcomes some limitations of DInSAR, as, e.g., its insensitivity to the azimuth direction, and it provides an absolute measurement in the line of sight direction, i.e., no reference point and phase unwrapping are needed. The correction of geophysical effects, namely, the induced delay by the signal propagation through the turbulent troposphere, with numerical weather data, and the solid Earth tides provide results that compare well with GPS measurements. The standard deviation of the differences is below 15 centimeters for the 2011 Tohoku-Oki Earthquake case study. The StripMap dataset covered many vegetated areas with temporal baselines of typically 100 days. Better results are therefore expected in lower bands (C or L - more appropriate for geophysical applications) with systems acquiring systematically with a short repetition cycle, as Sentinel-1 (12 or even 6 days).

The processing of data acquired in TOPS mode requires special care during the interferometric processing in order to account for the azimuth variance of the spectrum. The consolidation of the interferometric algorithms has been the second contribution of this work, particularly for the Interferometric Wideswath mode of Sentinel-1 (a 3-subswath TOPS mode). One of the critical points when forming interferograms is the stringent azimuth coregistration requirement. The enhanced spectral diversity (ESD) technique has been successfully employed, which delivers high quality interferograms. The dependence of the accuracy of this estimator with the interferometric coherence calls for more sophisticated approaches when working with long time series.

The azimuth coregistration of stacks of Sentinel-1 data has been the focus of the third contribution. A joint-coregistration approach based on ESD overcomes the limitations of the single-master procedure, whose performance might be affected by degraded coherence

for long temporal baselines. The exploitation of ESD together with a weighted least squares approach applied to Sentinel-1 data indicates better performance than applying just ESD, specially for land areas, characterized by distributed scatterers, and profoundly affected by temporal decorrelation effects.

The medium resolution of the TOPS mode impairs the application of correlation techniques in the azimuth direction for shift measurement. A way to overcome this limitation is addressed in the last contribution of this dissertation: the proposal of a novel wide-swath acquisition mode, the 2-look TOPS, which exploits spectral diversity techniques in the azimuth direction. The proposed mode achieves the same coverage as conventional TOPS at the expense of a degradation of the azimuth resolution by a factor of two, maintaining however the number of looks for a given product resolution. Two design principles have been presented, based on the desired azimuth resolution (TOPS2), and based on the desired azimuth sensitivity - implemented by selecting the maximum steering angle (TOPS2+) to be used during the acquisition. TOPS2 provides an azimuth sensitivity slightly better than StripMap, whereas TOPS2+ overperforms TOPS2 when selecting larger maximum steering angles. A limit to the maximum steering angle is however set by the level of azimuth ambiguities, which can be relaxed for geophysical applications, characterized by the presence of distributed scatterers. The 2-D and 3-D performances have been provided in the associated paper indicating that for time series analyses 30 TOPS2 images or 13 TOPS2+ images (with a maximum steering angle of 1.1°) would be necessary to reach a mean azimuth velocity of 4 mm/month under the same decorrelation circumstances. Moreover the 2-look concept aids a local azimuth coregistration, eliminating this way possible phase discontinuities between bursts due to ground displacement. Experimental TerraSAR-X acquisitions have demonstrated its capabilities for two scenarios: fast deformation (glacier flow) and slow deformation (post-seismic ground displacement). In the first case, a local coregistration for a pair of acquisitions has allowed to remove phase discontinuities due to azimuth displacement. The second case demonstrates the retrieval of a post-seismic signal in along-track direction employing time series, with a 2-year stack, delivering accuracies in the mean along-track velocity of a few mm/month.

Burst-mode acquisitions, and specifically TOPS, represent an adequate baseline for tectonic monitoring. High-resolution wide-swath (HRWS) concepts, which are currently being investigated by several space agencies for the next generation of spaceborne SAR systems, can cover a major range of applications, however there are also some drawbacks related to the higher complexity of the system to acquire a continuous swath, due, for instance, to the existence of blind ranges or nadir returns. Moreover, HRWS modes require greater downlink capacity due to the higher data rate. Burst modes might not be optimal solutions for some applications which require high resolution, for instance, volcano monitoring, but for this cases wide-swath capabilities are not strictly necessary, being a possibility the switching to StripMap acquisitions for these cases. The proposed 2-look TOPS mode, able to be implemented in current systems with no hardware modifications, e.g., for Sentinel-1 expands the capabilities of quasi-polar orbiting satellite systems to retrieve ground displacements in the N-S direction keeping a short temporal sampling. It might be considered as a transition mode before forthcoming advanced technologies arrive, or even serve as a hybrid solution.

Appendix A

Ground Displacement Measurement by TerraSAR-X Image Correlation: The 2011 Tohoku-Oki Earthquake

Journal: IEEE Geoscience and Remote Sensing Letters
Authors: Nestor Yague-Martinez, Michael Eineder, Xiao Ying Cong and Christian Minet
Impact Factor: 3.57 (2017)

N. Yague-Martinez, M. Eineder, X. Y. Cong, and C. Minet (2012). "Ground Displacement Measurement by TerraSAR-X Image Correlation: The 2011 Tohoku-Oki Earthquake". In: *IEEE Geoscience and Remote Sensing Letters* 9.4, pp. 539–543. ISSN: 1545-598X. DOI: 10.1109/LGRS.2012.2196020

Ground Displacement Measurement by TerraSAR-X Image Correlation: The 2011 Tohoku-Oki Earthquake

Nestor Yague-Martinez, Michael Eineder, *Member, IEEE*, Xiao Ying Cong, and Christian Minet

***Abstract*—Japan was struck by an M9.0 megathrust earthquake on March 11, 2011. Synthetic aperture radar (SAR) images from the TerraSAR-X satellite have been used to generate a ground motion map by means of correlation techniques. Geophysical corrections due to solid Earth tide and atmospheric path delay effects have been applied. These corrections can reach up to 20 cm in the radar line of sight. Using this approach, absolute displacements in the radar line of sight and in the satellite flight direction are determined. This letter shows the potential of correlation techniques for ground motion monitoring and a comparison with the interferometric technique. Using multiple scenes, a wide area displacement map is generated and quantitatively compared with GPS data, showing a divergence of about 15 cm.**

***Index Terms*—Differential synthetic aperture radar (SAR) interferometry (DInSAR), earthquakes, image correlation, SAR, speckle tracking.**

I. Introduction

DIFFERENTIAL synthetic aperture radar (SAR) interferometry (DInSAR) has been widely used to measure ground displacements. However, DInSAR presents some limitations: It provides measurements in only one dimension, the radar line of sight (LOS). This dimension is mainly representative of east/west displacements, due to the quasi-polar orbit configuration of the current Earth observation satellites. The vertical component of the displacement is partially included in this measure depending on the looking angle, whereas the north/south component is almost not detected. Moreover, DInSAR presents the problem of the phase ambiguity. Phase unwrapping techniques can be used to remove it. This process is technically feasible when the ground displacement is small (few wavelengths), whereas it leads to useless results in case of very large displacement gradients. Furthermore, DInSAR provides only spatially relative measurements; thus, ground control points are often necessary.

On the other hand, correlation techniques overcome some of the previously enumerated drawbacks. They provide unambiguous 2-D measurements, in the radar LOS and in the azimuth direction. Moreover, correlation techniques provide absolute displacements, being the measurement independent of *in situ* information. The disadvantage of cross-correlation with respect to DInSAR is its lower accuracy [1], [2]. However, the accuracy is sufficient for a wide range of applications, e.g., the measurement of the deformation caused by strong earthquakes.

Correlation techniques have been already applied to SAR images, e.g., Michel *et al.* [3] have shown the possibility of measuring coseismic ground displacements using the amplitude of SAR images. In this letter, we apply the correlation technique for the study of the Tohoku-Oki Earthquake on TerraSAR-X images.

The TerraSAR-X [4] satellite has acquired high-resolution SAR data at X-band since June 2007. Every scene acquired in StripMap mode covers an area of about 30 km $\times$ 50 km, which is too small to study wide area deformation phenomena. Since the sensor capacity is not big enough for gapless global mapping, a way to overcome this limitation is the acquisition of data sparsely spread over the whole area of interest.

Before the earthquake, nine suitable images acquired in StripMap mode and distributed over the Japanese archipelago with different geometries were available as reference data. After the earthquake, the corresponding scenes were ordered. Because of the large time span between pre- and postseismic acquisitions (ranging from two to six months), a quality assessment of the displacement maps is of fundamental importance and has been performed. The displacement maps are corrected for solid Earth tides and atmospheric path delays.

II. Tohoku-Oki Earthquake

Japan was struck by an M9.0 megathrust earthquake on March 11, 2011, at 05:46 Universal Time Coordinated (UTC). The epicenter was located at the coordinates 38.322° N, 142.369° E, approximately 72 km east off Sendai coast, and the hypocenter was at a depth of about 32 km. The whole archipelago has been affected. Disastrous tsunami waves were triggered by the event. More than 19 000 people died or are still missing. The economic losses are still incalculable but expected to range up to US$300 billion [5]. Ozawa *et al.* [6] have already shown coseismic and postseismic displacement maps using the GPS Earth Observation Network (GEONET).

III. Methodology

The method used in this letter is outlined in Fig. 1. Cross-correlation is performed with image patches distributed over the TerraSAR-X single-look slant-range complex (SSC) pairs. This technique allows measuring local shifts between master and slave SSCs in both slant range and azimuth directions with an accuracy of several centimeters for TerraSAR-X. Since the images are taken from different positions in space, the topography produces an additional range shift (parallax). A geometric

Manuscript received November 9, 2011; revised March 3, 2012; accepted March 30, 2012. Date of publication May 11, 2012; date of current version June 15, 2012.

N. Yague-Martinez was with the Department of SAR Signal Processing, Remote Sensing Technology Institute, Deutsches Zentrum für Luft- und Raumfahrt, 82234 Wessling, Germany. He is now with the Space Engineering Consulting Division, Starlab Barcelona SL., 08022 Barcelona, Spain (e-mail: nestor.yague@gmail.com).

M. Eineder is with the Department of SAR Signal Processing, Remote Sensing Technology Institute, Deutsches Zentrum für Luft- und Raumfahrt, 82234 Wessling, Germany, and also with Technische Universität München, 80333 München, Germany (e-mail: michael.eineder@dlr.de).

X. Y. Cong is with the Technische Universität München, 80333 München, Germany (e-mail: Xiao.Cong@dlr.de).

C. Minet is with the Deutsches Zentrum für Luft- und Raumfahrt, 82234 Wessling, Germany (e-mail: christian.minet@dlr.de).

Digital Object Identifier 10.1109/LGRS.2012.2196020

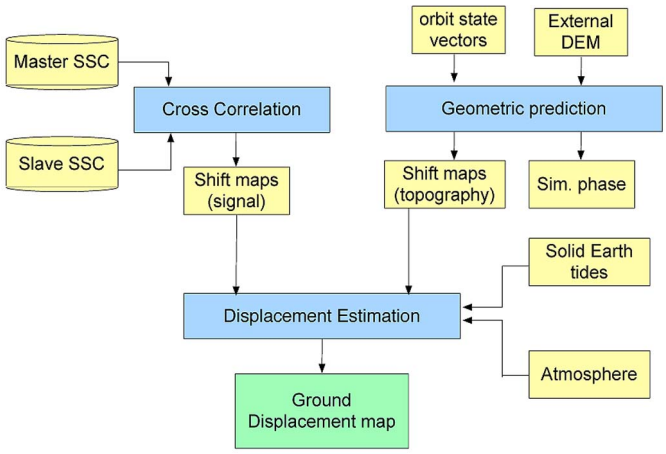

Fig. 1. Methodology block diagram.

prediction is carried out to correct for these additional shifts. TerraSAR-X precise orbit state vectors and an external digital elevation model (DEM) from the Shuttle Radar Topographic Mission are used for this purpose. Differential atmospheric path delay [7] and solid Earth tide [8] effects are taken into account to finally obtain the ground displacement map.

A. Image Correlation Technique

The cross-correlation, $R_{x_1x_2}$ of the two discrete 2-D complex signals x_1 and x_2, of duration $N \times M$ is given by [9]

$$R_{x_1x_2}[n,m] = \sum_{u=0}^{N}\sum_{v=0}^{M} x_1^*[u,v]x_2[u+n,v+m] = x_1^*[-n,-m] * x_2[n,m] \quad (1)$$

being equivalent to a convolution operation (denoted by $*$), in which the first signal has been time reversed and complex conjugated.

The cross-correlation can then be calculated efficiently in the frequency domain using the convolution theorem

$$R_{x_1x_2}[n,m] = \mathcal{F}^{-1}\left\{X_1^*[\mu,\nu]\cdot X_2[\mu,\nu]\right\} \quad (2)$$

where X_1 and X_2 are the Fourier transforms of the signals x_1 and x_2, respectively. The signals x_1 and x_2 have been, prior to the Fourier transformation, zero padded in the time domain in order that the convolution operation is linear.

The position of the maximum of the correlation function provides the shift between both signals. It can be obtained with subpixel accuracy by iterative interpolations of the correlation function with a cardinal sine.

Due to the low coherence of the acquisition pairs of our data set, only the amplitude of the complex data has been used for correlation. An oversampling of the complex data has been done prior the detection in order to avoid aliasing.

Cross-correlation is applied on patches distributed regularly over the images. Patches of 128 $\times$ 128 pixels ($\sim$190 m $\times$ 250 m) whose centers are separated by 64 pixels ($\sim$100 m) have been used. This means that a 50% patch overlap has been achieved. TerraSAR-X orbits present a 3-D accuracy of 4.2 cm for the so-called *science orbit products* [10]. This implies an accuracy in the geometric shift prediction of about 8.5 cm, according to simulations performed by the authors.

An outlier rejection stage based on mean and standard deviation is applied in order to eliminate unreliable estimates. A sliding window of 15 $\times$ 15 estimates has been used, and an empirical threshold of 0.2 has been set for the standard deviation.

B. Atmospheric Path Delay Correction

In order to obtain an accurate absolute deformation measurement in the centimeter range, the atmospheric delay effect needs to be considered. In fact, if we consider the stratified atmosphere in winter and in summer, a difference of up to 35 cm can be observed. In [8], a method to compensate the atmospheric delay effect by using the GPS zenith-path-delay measurements from the Reference Frame Sub Comission for Europe (EUREF) Permanent Network (EPN) has been described. In our work, global weather model data are used instead to estimate the atmospheric path delay. Since the weather model data are available in 3-D, the atmospheric path delay can be estimated directly in the radar LOS direction. Equation (3) obtains the path delay by integrating the atmospheric parameters provided from weather model data [7]

$$L_s = 10^{-6}\int_{r_0}^{r_n}\left(k_1\frac{P}{T} + (k_2-k_1)\frac{e}{T} + k_3\frac{e}{T^2}\right)dr \quad (3)$$

with P being the total atmospheric pressure in pascals, T being the temperature in kelvin, e being the partial pressure of water vapor in pascals, and r being the slant range vector. The constants are $k_1 = 0.776$ KPa^{-1}, $k_2 = 0.716$ KPa^{-1}, and $k_3 = 3.75 \cdot 10^3$ K^{2}Pa^{-1}.

The numerical weather model data from the European Centre for Medium-Range Weather Forecasts Interim are chosen because they include the global 3-D weather data from 1989 to the present with, at most, a three-month delay. The weather data are available four times per day (at 0, 6, 12, and 18 h) with a grid resolution of about 80 km and stratified in 60 levels. The weather data closest to the SAR image acquisition time are collected. The weather parameters are interpolated or extrapolated in the vertical direction at the actual terrain height and in the azimuth–range plane to fit with the correlation grid. The atmospheric delay map is then integrated for the preseismic and the postseismic SAR images. The differential path delay can then be obtained, and a correction is finally applied to the correlation shift maps. The time difference between the meteorological data and the SAR acquisition might be up to 3 h. This does no represent a major limitation since fast temporal variations of the atmosphere would imply an error in the order of 10–15 mm. This can be neglected because the cross-correlation technique presents an accuracy in the centimeter range.

C. Solid Earth Tide Corrections

The gravitational forces exerted by the Moon and the Sun produce a deformation of the Earth's crust. The height variation can reach up to 40 cm for the radial component and several centimeters for the horizontal components.

The slant range contribution in the radar LOS direction can be approximated using the following expression [8]:

$$\delta_{\text{ground}} = -\delta_{\text{Up}}cos\theta + \delta_{\text{East}}sin\theta cos\beta - \delta_{\text{North}}sin\theta sin\beta \quad (4)$$

where δ_{Up}, δ_{East}, and δ_{North} are the solid Earth tide corrections in the vertical, east, and north directions for the center of the scene, θ is the radar looking angle, and β is the heading angle,

TABLE I
TERRASAR-X ACQUISITION PARAMETERS

Site	Geographical coordinates (lat / lon)		Post-seismic scene acquisition time	Temp. baseline (days)	Look angle
1	38.27°	141.06°	12.03.2011; 20:43:07	143	37.34°
2	38.24°	140.86°	17.03.2011; 20:51:41	143	21.56°
3	35.53°	139.66°	12.03.2011; 20:43:52	55	42.84°
4	44.16°	145.81°	24.03.2011; 20:24:20	121	42.86°
5	43.27°	145.60°	24.03.2011; 20:24:35	121	42.87°
6	43.82°	144.18°	18.03.2011; 20:33:03	132	39.27°
7	35.05°	136.86°	02.04.2011; 21:01:12	121	31.08°
8	31.95°	130.85°	01.04.2011; 21:19:18	110	39.22°
9	28.28°	129.45°	28.03.2011; 09:17:45	121	26.48°

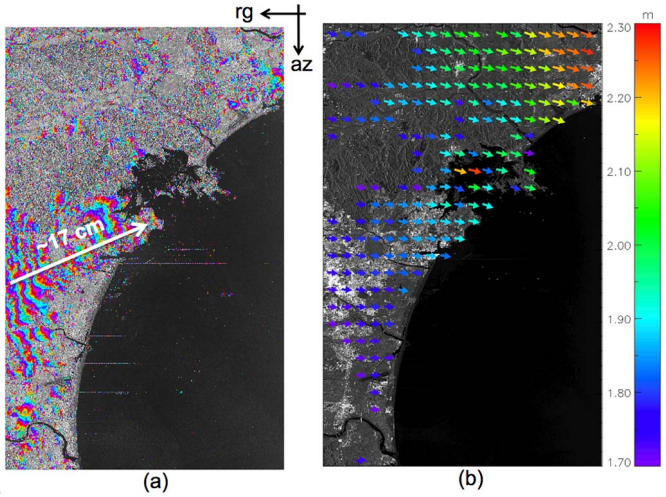

Fig. 2. (a) Sendai (Site 1) interferometric phase after topographic compensation and (b) 2-D vector displacement map (slant range/azimuth) over SAR amplitude. The color of each arrow of the vector field indicates the magnitude of the absolute displacement.

i.e., the clockwise angle between the north and the ground track of the beam. The algorithm for the calculation of the solid Earth tide has been done using the program solid [11] according to the International Earth Rotation and Reference Systems Service (IERS) conventions [12].

In this letter, we use only the recommended model for the solid Earth tide and neglect other influences such as atmospheric loading and ocean tide loading. Even if ocean tide loading may cause additional displacements, it can be concluded from [13] that its influence is less than 4 cm per scene.

IV. TERRASAR-X DATA SET

Nine descending coseismic pairs have been acquired, distributed over the archipelago with different look angles. Every scene has been acquired in StripMap mode and covers an area of about 30 km $\times$ 50 km. Unfortunately, there are no crossed orbit data, and thus, it is not possible to derive 3-D deformation maps.

In Table I, the TerraSAR-X scene geographical coordinates, the acquisition times after the main earthquake, the temporal baselines, and the look angles for every site are detailed.

In the following two sections, the acquisitions over Sendai (Site 1) and Tokyo (Site 3) will be analyzed in more detail.

A. Sendai (Site 1)

Fig. 2(a) shows an overlay of the differential interferometric phase over the SAR amplitude (at low coherent areas). Note that the interferogram suffers of high temporal decorrelation. Nevertheless, the urban area presents good coherence. The effective baseline is 48.05 m, and a multilooking of 11 $\times$ 11 pixels has been applied to the interferogram. A relative displacement in the LOS of approximately 17 cm can be measured along the plotted arrow.

Fig. 2(b) shows an overlay of the slant range/azimuth displacement vector field over the SAR amplitude. Every arrow averages 16 $\times$ 16 correlation estimates in order to get a more accurate and robust estimate. This would suppose at most 256 averaged values since, as mentioned previously outlier rejection procedure has been carried out in the quality assessment stage.

Fig. 3 shows the differential atmospheric path delay map in the slant range direction between both acquisitions.

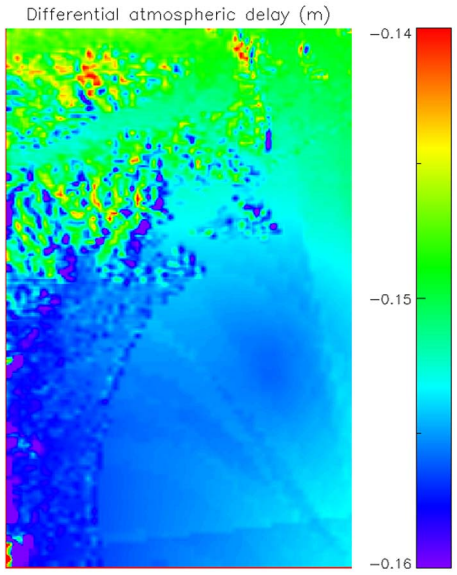

Fig. 3. Sendai (Site 1) differential atmospheric path delay between the acquisitions on 23.11.2010 and on 12.03.2011.

B. Tokyo (Site 3)

Fig. 4 is analogous to Fig. 2 for the Tokyo acquisition. The same processing parameters have been applied. The effective baseline is 116.36 m. A relative displacement in the radar LOS direction of approximately 11 cm can be measured from late to early azimuth.

C. Comparison Between DInSAR and Correlation Techniques

In this section, a comparison between both techniques, DInSAR and cross-correlation, is done. The Tokyo interferogram has been chosen. From the differential interferogram of Fig. 4(a), it can be seen that a fringe pattern over azimuth appears. That means that the LOS displacements are about 11 cm larger in early azimuth than in late azimuth. Fig. 5 shows the profiles of these displacements derived from the differential phase, after it has been unwrapped, and from the cross-correlation estimates. For visualization purposes, an offset has been added to the displacement profile derived from DInSAR using information from cross-correlation.

TABLE II
GPS AND CROSS-CORRELATION MOTION COMPONENTS IN SLANT RANGE AND AZIMUTH DIRECTIONS. THE RANGE CROSS-CORRELATION ESTIMATES ARE GIVEN WITHOUT GEOPHYSICAL CORRECTIONS AND CORRECTED. ATMOSPHERIC SOLID EARTH TIDE CORRECTIONS AND OUTLIER REJECTION RATE ARE PROVIDED

Site	GPS		Cross-corr. (rg without corrections / corrected / azimuth)			Differences (rg without corrections / corrected / azimuth)			Atm [m]	SET [m]	Outlier reject rate
	Rg[m]	Az[m]	Rg[m]	Rg[m]	Az[m]	Rg[m]	Rg[m]	Az[m]	Rg[m]	Rg[m]	
1	-1.72	0.03	-1.89	-1.71	0.03	-0.16	0.02	0.00	-0.15	-0.025	12.57%
2	-0.81	-0.13	-0.87	-0.79	-0.84	-0.07	0.02	-0.71	-0.13	0.038	26.69%
3	-0.15	-0.10	-0.28	-0.30	-0.08	-0.13	-0.14	0.02	0.06	-0.046	19.56%
4	0.02	-0.02	0.31	0.31	-0.08	0.30	0.30	-0.06	-0.01	0.005	35.59%
5	0.02	-0.02	0.12	0.13	-0.29	0.11	0.11	-0.27	-0.01	0.003	33.43%
6	-0.02	-0.02	-0.05	0.03	0.03	-0.03	0.05	0.05	-0.06	-0.018	33.78%
7	0.17	-0.05	0.09	0.06	-0.09	-0.08	-0.11	-0.04	-0.19	0.218	21.94%
8	0.10	-0.02	0.03	-0.07	0.03	-0.07	-0.17	0.06	-0.01	0.115	33.84%
9	-0.11	0.01	-0.36	-0.05	0.20	-0.24	0.07	0.20	-0.18	-0.128	34.35%
Standard deviation						**0.16**	**0.14**	**0.13**			

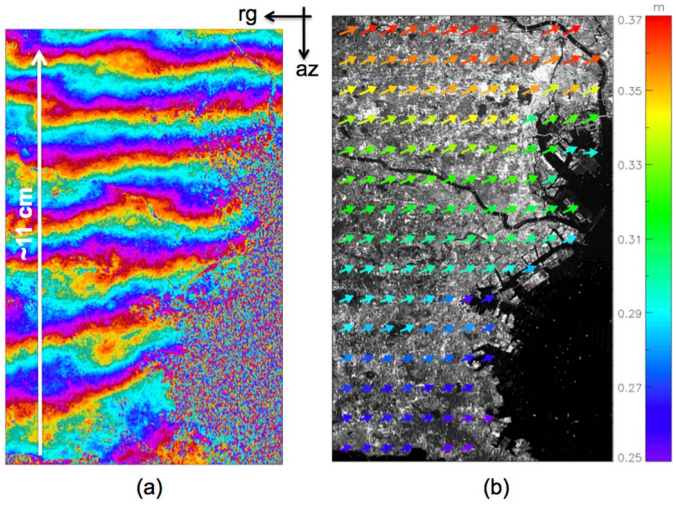

Fig. 4. (a) Tokyo (Site 3) interferometric phase after topographic compensation and (b) 2-D vector displacement map (slant range/azimuth) over SAR amplitude. The color of each arrow of the vector field indicates the magnitude of the absolute displacement.

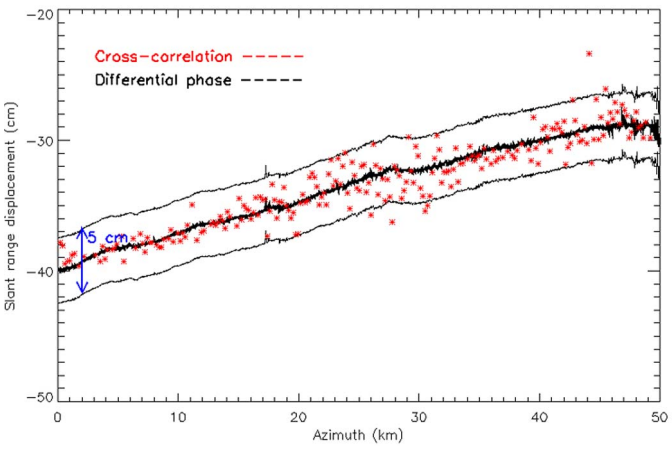

Fig. 5. Slant range displacement profile over azimuth for the Tokyo scene.

D. Comparison to GPS Measurements

A quantitative validation of our displacement vectors in slant range and azimuth directions could be performed with data from the GPS network of the Geospatial Information Authority of Japan. For the validation of each TerraSAR-X scene, the closest GPS station to the scene center is selected. From this station, the position is extracted at the days of the SAR acquisitions, and the 3-D coseismic displacement vector is calculated. This vector is then projected into the SAR range–azimuth plane and compared with the SAR displacement vector. An average of maximum 16×16 cross-correlation estimates has been done around the GPS station location. The GPS station coordinates are free of solid Earth tides. Table II contains the GPS and cross-correlation motion components in the slant range and azimuth directions, the differences between GPS and cross-correlation, the atmospheric path delay and solid Earth tide corrections, and the outlier reject rate. Both techniques differ in general in the order of a few centimeters. Observe that the geophysical corrections reduce in general the divergence to the GPS measurements. In the azimuth direction, there are some large discrepancies, e.g., Site 2 (71-cm difference in azimuth), and we consider this value as an outlier. Observe that sites 4, 5, 6, and 8 present noticeable deviations from GPS measurements due to the very high temporal decorrelation (vegetated areas). The standard deviation of the differences is also provided and is about 15 cm (Note: Site 2 has not been included for the standard deviation computation).

E. Wide Area Deformation Map

Fig. 6 shows the wide area displacement map obtained combining several TerraSAR-X images. A single arrow indicating horizontal displacement amplitude and direction has been assigned to every site. It is known from the GPS coseismic measurements by GEONET that the vertical displacements are by a factor of 6 smaller than the horizontal displacements [6]. Taking advantage of this fact, a projection on the ground of the measured slant range displacements has been applied for the wide area deformation map.

V. CONCLUSION

We have shown that, using multiple scenes of TerraSAR-X, a wide area displacement map can be generated using correlation techniques and geophysical corrections. A comparison between DInSAR and correlation shows good agreement in the relative

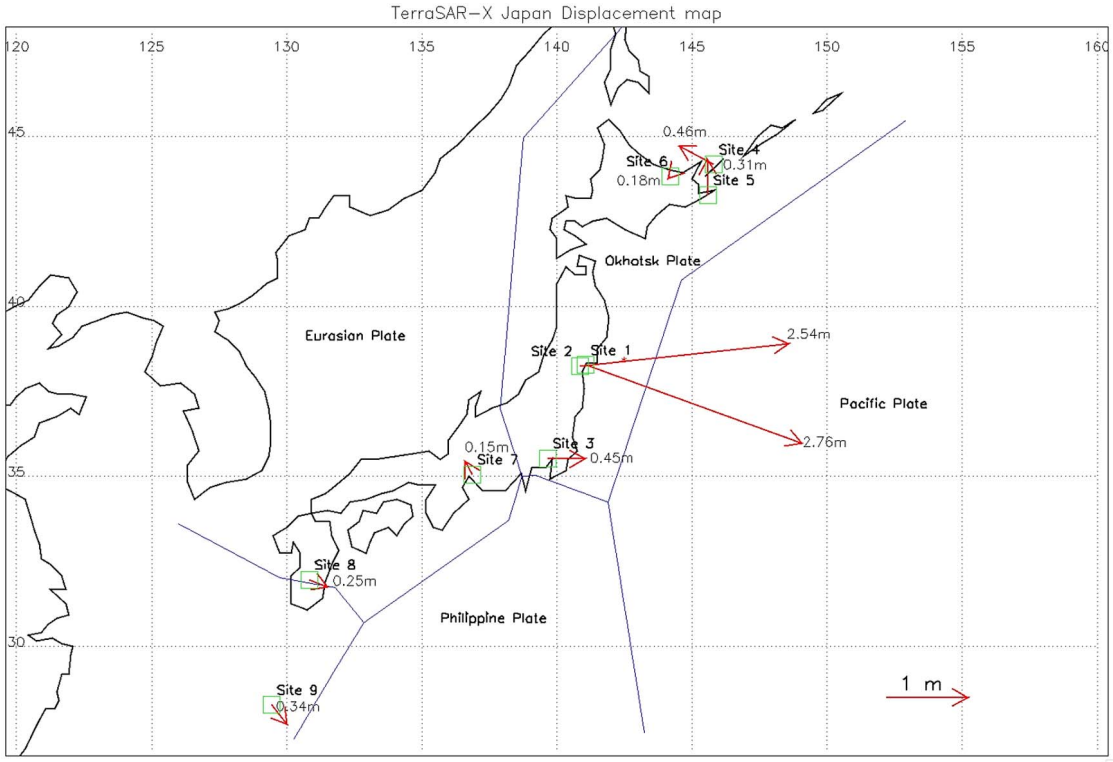

Fig. 6. TerraSAR-X horizontal displacement map, including schematic continent outlines and plate boundaries.

measurements. The results compare, in general, well with GPS measurements with a standard deviation of about 15 cm. Due to the high temporal decorrelation of our data set, deviations of the expected accuracy stated in [8] can be found for some scenes. Our analysis is based on 2-D comparison, but this can be extended by combining image pairs from ascending and descending passes.

ACKNOWLEDGMENT

The authors would like to thank B. Schättler from Deutsches Zentrum für Luft- und Raumfahrt (DLR) for her support to this work and the Geospatial Information Authority of Japan for providing GPS data to DLR. The authors would also like to thank Prof. Hashimoto and the Tohoku supersite [14]. The authors would like to thank the anonymous reviewers for their valuable comments and suggestions.

REFERENCES

[1] D. Just and R. Bamler, "Phase statistics of interferograms with applications to synthetic aperture radar," *Appl. Opt.*, vol. 33, no. 20, pp. 4361–4368, Jul. 1994.

[2] R. Bamler and M. Eineder, "Accuracy of differential shift estimation by correlation and split-bandwidth interferometry for wideband and Delta-κ SAR systems," *IEEE Geosci. Remote Sens. Lett.*, vol. 2, no. 2, pp. 151–155, Apr. 2005.

[3] R. Michel, J. P. Avouac, and J. Taboury, "Measuring ground displacements from SAR amplitude images: Application to the Landers earthquake," *Geophys. Res. Lett.*, vol. 26, no. 7, pp. 875–878, Apr. 1, 1999.

[4] R. Werninghaus and S. Buckreuss, "The TerraSAR-X mission and system design," *IEEE Trans. Geosci. Remote Sens.*, vol. 48, no. 2, pp. 606–614, Feb. 2010.

[5] National Police Agency of Japan. [Online]. Available: http://www.npa.go.jp/archive/keibi/biki/higaijokyo_e.pdf

[6] S. Ozawa, T. Nishimura, H. Suito, T. Kobayashi, M. Tobita, and T. Imakiire, "Coseismic and postseismic slip of the 2011 magnitude-9 Tohoku-Oki earthquake," *Nature*, vol. 475, no. 7356, pp. 373–377, Jul. 2011.

[7] X. Cong, U. Balss, M. Eineder, and T. Fritz, "Imaging Geodesy—Centimeter-level ranging accuracy with TerraSAR-X: An update," *IEEE Geosci. Remote Sens. Lett.*, vol. 9, no. 5, Sep. 2012, to be published.

[8] M. Eineder, C. Minet, P. Steigenberger, X. Cong, and T. Fritz, "Imaging Geodesy—Toward centimeter-level ranging accuracy with TerraSAR-X," *IEEE Trans. Geosci. Remote Sens.*, vol. 49, no. 2, pp. 661–671, Feb. 2011.

[9] A. Papoulis, *The Fourier Integral and Its Applications*. New York: McGraw-Hill, 1962.

[10] Y. Yoon, M. Eineder, N. Yague-Martinez, and O. Montenbruck, "TerraSAR-X precise trajectory estimation and quality assessment," *IEEE Trans. Geosci. Remote Sens.*, vol. 47, no. 6, pp. 1859–1868, Jun. 2009.

[11] D. Milbert, Author of the Solid Program Written in Fortran (as of March 2011). [Online]. Available: http://home.comcast.net/~dmilbert/softs/solid.htm

[12] D. D. McCarthy and G. Petit, "Verlag des Bundesamts für Kartographie und Geodäsie," in *Proc. IERS Conv.*, Frankfurt, Germany, 2004, IERS Tech. Note No. 32.

[13] C. Urschl, R. Dach, U. Hugentobler, S. Schaer, and G. Beutler, "Validating ocean tide loading models using GPS," *J. Geodesy*, vol. 78, no. 10, pp. 616–625, 2005.

[14] Tohoku Supersite, Co-Seismic Displacements Map From GPS by GEONET. [Online]. Available: http://supersites.earthobservations.org/sendai.php

Appendix B

Interferometric Processing of Sentinel-1 TOPS data

Journal: IEEE Transactions on Geoscience and Remote Sensing
Authors: Nestor Yague-Martinez, Pau Prats-Iraola, Fernando Rodriguez Gonzalez, Ramon Brcic, Robert Shau, Dirk Geudtner, Michael Eineder and Richard Bamler
Impact Factor: 5.84 (2017)

N. Yague-Martinez, P. Prats-Iraola, F. Rodriguez Gonzalez, R. Brcic, R. Shau, D. Geudtner, M. Eineder, and R. Bamler (2016b). "Interferometric Processing of Sentinel-1 TOPS Data". In: *IEEE Transactions on Geoscience and Remote Sensing* 54.4, pp. 2220–2234. ISSN: 0196-2892. DOI: 10.1109/TGRS.2015.2497902

Interferometric Processing of Sentinel-1 TOPS Data

Nestor Yague-Martinez, Pau Prats-Iraola, *Senior Member, IEEE*, Fernando Rodriguez Gonzalez, Ramon Brcic, *Member, IEEE*, Robert Shau, *Senior Member, IEEE*, Dirk Geudtner, Michael Eineder, *Senior Member, IEEE*, and Richard Bamler, *Fellow, IEEE*

***Abstract*—Sentinel-1 (S-1) has an unparalleled mapping capacity. In interferometric wide swath (IW) mode, three subswaths imaged in the novel Terrain Observation by Progressive Scans (TOPS) SAR mode result in a total swath width of 250 km. S-1 has become the European workhorse for large area mapping and interferometric monitoring at medium resolution. The interferometric processing of TOPS data however requires special consideration of the signal properties, resulting from the ScanSAR-type burst imaging and the antenna beam steering in azimuth. The high Doppler rate in azimuth sets very stringent coregistration requirements, making the use of enhanced spectral diversity (ESD) necessary to obtain the required fine azimuth coregistration accuracy. Other unique aspects of processing IW data, such as azimuth spectral filtering, image resampling, and data deramping and reramping, are reviewed, giving a recipe-like description that enables the user community to use S-1 IW mode repeat-pass SAR data. Interferometric results from S-1A are provided, demonstrating the mapping capacity of the S-1 system and its interferometric suitability for geophysical applications. An interferometric evaluation of a coherent interferometric pair over Salar de Uyuni, Bolivia, is provided, where several aspects related to coregistration, deramping, and synchronization are analyzed. Additionally, a spatiotemporal evaluation of the along-track shifts, which are directly related to the orbital/instrument timing error, measured from the SAR data is shown, which justifies the necessity to refine the azimuth shifts with ESD. The spatial evaluation indicates high stability of the azimuth shifts for several slices of a datatake.**

***Index Terms*—Coregistration, Interferometric SAR (InSAR), Sentinel-1 (S-1), synthetic aperture radar (SAR), Terrain Observation by Progressive Scans (TOPS).**

Manuscript received April 24, 2015; revised October 2, 2015; accepted October 7, 2015. Date of publication January 22, 2016; date of current version March 9, 2016. This work was supported in part by the European Space Agency under Contract 4000111074/14/NL/MP/lf, Contract 4000109669/13/I-AM, Contract 4000106082/12/NL/MP, and Contract 4000110587/14/I-BG and in part by the German Federal Ministry for Economics and Technology through the TanDEM-X Project under Förderkennzeichen 50 EE 1035.

N. Yague-Martinez was with the Remote Sensing Technology Institute, German Aerospace Center, 82234 Weßling, Germany. He is now with the Microwaves and Radar Institute, German Aerospace Center, 82234 Weßling, Germany (e-mail: nestor.yague@dlr.de).

P. Prats-Iraola is with the Microwaves and Radar Institute, German Aerospace Center, 82234 Weßling, Germany (e-mail: pau.prats@dlr.de).

F. Rodriguez Gonzalez, R. Brcic, R. Shau, M. Eineder, and R. Bamler are with the Remote Sensing Technology Institute, German Aerospace Center, 82234 Weßling, Germany (e-mail: Fernando.rodriguezgonzalez@dlr.de; ramon.brcic@dlr.de; robert.shau@dlr.de; michael.eineder@dlr.de; richard.bamler@dlr.de).

D. Geudtner is with the European Space and Technology Center, European Space Agency, 2201 AZ Noordwijk, The Netherlands (e-mail: dirk.geudtner@esa.int).

Color versions of one or more of the figures in this paper are available online at http://ieeexplore.ieee.org.

Digital Object Identifier 10.1109/TGRS.2015.2497902

I. Introduction

THE Sentinel-1 (S-1) mission is based on a constellation of identical C-band synthetic aperture radar (SAR) satellites, which are currently comprised of the A and B units, to provide data continuity to European Space Agency's (ESA) previous European Remote Sensing (ERS) and ENVISAT SAR missions.

The joint operation of both satellites will provide data sets for Copernicus Services [1] for the following areas: monitoring of sea ice zones and the arctic environment, surveillance of the marine environment, monitoring of land surface motion risks, mapping of land surfaces (forest, water, and soil), and mapping in support of humanitarian aid in crisis situations.

The S-1A unit was launched in April 2014, reaching its reference orbit on August 7, 2014. A second satellite (B unit) is scheduled for 2016.

The S-1 system was conceived to provide repeat-pass interferometric capabilities with unprecedented wide area coverage for medium-resolution applications [2]. The repeat cycle has been notably reduced from 35 days for ERS-1 and ERS-2 or 30/35 days for ENVISAT to 12 days for S-1A, and can still be reduced effectively to 6 days when both units are in space. The systematic data acquisition along with the exceptional temporal sampling allows a vast range of geophysical applications, such as the monitoring of cryosphere dynamics and the mapping of surface deformation, e.g., caused by tectonic processes, volcanic activities, landslides, and ground subsidence. In addition, the S-1 orbit maintenance strategy ensures a ground-track repeatability of 120 m resulting in small orbital InSAR baselines on the order of 150 m. The wide-swath coverage is achieved by employing the novel Terrain Observation by Progressive Scans (TOPS) [3] acquisition mode, which similarly to ScanSAR acquires images by recording subsets of echoes of the SAR aperture, which are called *bursts*.

The SAR instrument, operating at 5.405 GHz, supports four imaging modes providing different resolution and coverage: Interferometric Wide Swath Mode (IW), Extra Wide Swath Mode (EW), StripMap (SM), and Wave (WV). IW and EW modes are implemented as three and five subswath TOPS SAR modes, respectively. This is to provide large swath widths of 250 and 400 km at ground resolutions of 5 m $\times$ 20 m and 20 m $\times$ 40 m, respectively, with enhanced image performance as compared with the conventional ScanSAR mode [4]. The IW TOPS mode is the main mode of operations for the systematic monitoring of large land and coastal areas [2] and is the mode we will focus in this paper.

The original publication describing the TOPS principle by De Zan and Monti Guarnieri [3] covers all aspects of this

new SAR mode, including the requirements for interferometry. Further aspects were considered in [5]. The TOPS mode was first implemented as an experimental four-subswath mode on TerraSAR-X [6]–[8]. The feasibility of repeat-pass TOPS SAR for interferometry was demonstrated in [9] for stationary scenes and in [10] for nonstationary surface scenarios, such as glaciers.

Prior to the launch of S-1A, an experimental three-subswath TOPS mode was implemented on RADARSAT-2, operating at the same C-band frequency as S-1, to simulate S-1-like IW mode data products to support the development of processing and exploitation of S-1 IW TOPS data with a particular focus on SAR interferometry [11], [12].

Other publications concerned with efficient focusing of TOPS acquisitions have appeared in the last years [13]–[16], including experiments with an airborne SAR in [17].

In [18], the description of burst-mode interferometric signal properties is provided, covering, among other issues, azimuth scanning pattern synchronization, spectral shift filtering in the presence of high squint coregistration and subswath alignment, and ScanSAR interferogram formation.

This paper focuses on the interferometric processing of S-1 IW mode data acquired over stationary scenes and provides a recipe-like description of the required operations. We summarize the experience and results obtained with two independent InSAR processors developed at the DLR, which are the Integrated Wide Area Processor (IWAP) [19] and the experimental TanDEM-X interferometric processor (TAXI) [20]. In order to illustrate some important parameters and intermediate results of IW data, we have selected an S-1A IW mode InSAR data pair acquired over Salar de Uyuni, Bolivia.

This paper is structured as follows. Section II provides a description of the S-1 IW mode, including the burst spectral properties and the key parameters of the single-look complex (SLC) data product. Moreover, based on the IW mode burst spectral properties, we discuss the impact of burst mis-synchronization on azimuth spectral alignment and evaluate the required accuracy for azimuth coregistration of S-1A IW burst images. Section III provides a recipe for interferometric processing, covering coregistration, spectral shift filtering and consideration of the Doppler frequency variation. In Section IV S-1A interferometric results are provided. Finally, Section V presents an interferometric evaluation performed with S-1A data by using a stack of acquisitions over Mexico City. The along-track shifts are systematically analyzed using two types of orbits. In addition, the common Doppler bandwidth is evaluated. A spatial analysis of the along-track shift is provided using a datatake over Europe. In the Appendix, we briefly review the S-1 data product description and outline practical information on how to handle the IW SLC data format.

II. S-1 IW Mode

The TOPS SAR acquisition mode is capable of providing wide range swaths as with the ScanSAR technique, but it almost eliminates the associated problems of scalloping and azimuth varying signal-to-noise ratio, noise equivalent sigma zero, and azimuth ambiguities [3].

In addition to scanning in elevation in order to extend the range coverage, the antenna azimuth beam is steered electronically from aft to fore at a constant rate. The scan pattern is shown in Fig. 1. As a result and in contrary to ScanSAR, all targets on the ground are observed by the entire azimuth antenna pattern. The acquisition takes place by recording bursts of echoes, i.e., employing subapertures, at the expense of a lower azimuth resolution. S-1 employs three predefined subswaths in IW mode (IW1, IW2, and IW3), achieving a ground swath coverage of 250 km in the across-track direction.

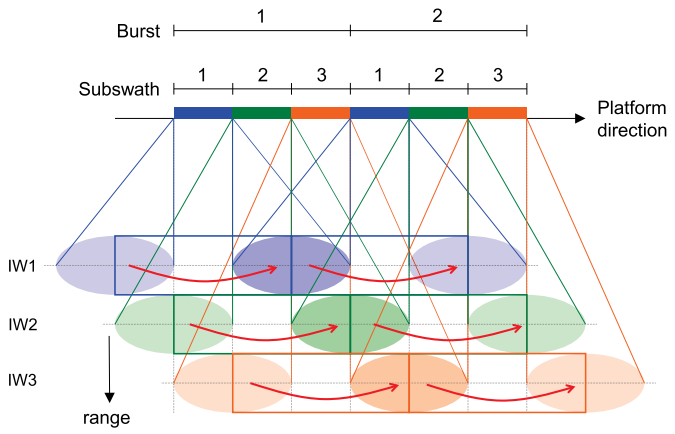

Fig. 1. TOPS Scan pattern for S-1 IW mode, composed of three subswaths. The acquisition starts with the first burst of the first subswath (blue) at top left with the beam steered along azimuth in the same direction as the platform moves (as depicted by the red arrows). Once this burst has been acquired, the antenna is switched in elevation, and the first burst of the second subswath (green) is acquired. Once the first of the third subswath (orange) is acquired, the beam is switched back to the first subswath, and the process is cyclically repeated.

S-1A is capable of operating up to 25 min per orbit [21]; thus, a slicing procedure has been defined for the generation of products. Regarding the L1 SLC products, each product slice is provided as a segment of approximately 25 s in length, which corresponds to about 170 km. An overlap area of about 7%–8% is present in the azimuth direction between consecutive focused bursts, as well as in range between adjacent subswaths. This assures that the images can be mosaicked without any gap. Moreover, as will be shown in Section III-D, these areas will be exploited to obtain the necessary coregistration accuracy for interferometric processing.

Table I lists the most relevant SLC product parameters of S-1 IW mode. The indicated incidence angles are approximate since a roll steering law is applied to the spacecraft to compensate for altitude variations [4].

A. Spectral Properties

The nonstationarity of the squint angle during the TOPS acquisition produces a linear variation of the Doppler centroid frequency in the SAR data. Fig. 2 shows the (unfolded) spectrum of a single raw burst of duration T_{burst}. Observe that the azimuth resolution is controlled by the dwell time T_{dwell} (integration time for a point target), resulting in a target bandwidth $B_T = |k_a| \cdot T_{\mathrm{dwell}}$, with k_a being the Doppler rate. The Doppler rate introduced by the antenna steering is given by

$$k_{\mathrm{rot}} \approx \frac{2v}{\lambda}\omega_r \tag{1}$$

TABLE I
S1 INTERFEROMETRIC WIDE SWATH MODE
SLC PRODUCT PARAMETERS

Beam id.	IW1	IW2	IW3
Incidence angles	32.9°	38.3°	43.1°
Slant range resolution	2.7 m	3.1 m	3.5 m
Range Bandwith	56.5 MHz	48.3 MHz	42.79 MHz
Azimuth resolution	22.5 m	22.7 m	22.6 m
Processing Bandwidth	327 Hz	313 Hz	314 Hz
Doppler Centroid span (Δf_{DC})	5.2 kHz	4.4 kHz	4.6 kHz
Slant range pixel spacing	2.3 m		
Range sampling frequency	64.35 MHz		
Azimuth pixel spacing	14.1 m		
Azimuth sampling frequency	486.49 Hz		
Azimuth steering angle	±0.6°		
Burst length (T_{focused})	2.75s / ≈ 20 km		
Ground Swath width	250 km		
Slice length	170 km		
Orbital Repeat Cycle	12 days		
Orbit height	698 - 726 km		
Wavelength	5.547 cm		
Polarization	Single (HH or VV) or Dual (HH+HV or VV+VH)		

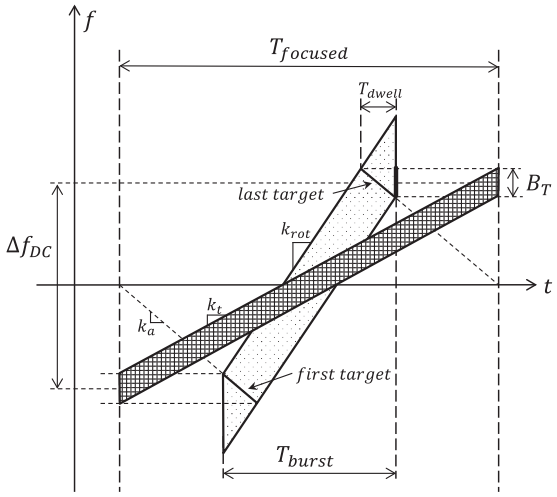

Fig. 2. Time–frequency diagram of a single TOPS burst. The raw burst (dotted pattern) of duration T_{burst} presents a linear Doppler variation due to the steering of the antenna. The zero-Doppler focused burst (hashed pattern) of duration T_{focused} also exhibits a linear Doppler variation. The first and last observed target Doppler histories are depicted with bold lines and have a slope given by the Doppler rate k_a. Their zero-crossing positions determine the length of the focused burst. The dwell time T_{dwell} controls the azimuth resolution, being the resulting target bandwidth B_T.

where v is the satellite velocity, λ is the radar wavelength, and ω_r is the antenna steering rate in radians per second.

After the burst raw data have been focused to SLC bursts in zero-Doppler geometry, a linear Doppler centroid frequency variation is present in the azimuth direction. The range-dependent Doppler rate at image level $k_t(r)$ can be calculated as

$$k_t(r) = \frac{k_a(r) \cdot k_{\mathrm{rot}}}{k_a(r) - k_{\mathrm{rot}}} \tag{2}$$

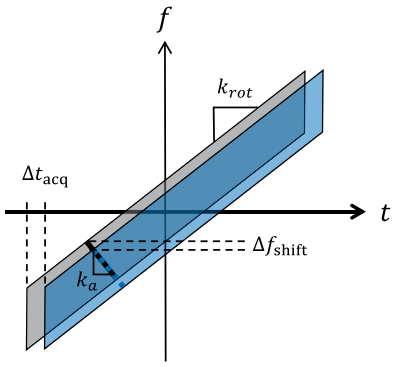

Fig. 3. Time–frequency diagram of a pair of raw bursts depicting the azimuth spectra in the presence of a timing error Δt_{acq}. The master burst is depicted in gray and the slave in blue. The plot depicts the case where the master datatake observes the target before the slave datatake. Note that the delay of observation of each target is shorter than the delay of the overall acquisition.

where $k_a(r)$ is the range-dependent target Doppler rate.

This Doppler variation has to be considered for further InSAR processing steps, including interpolation and spectral shift filtering, as will be discussed in Section III-B.

B. Burst Synchronization Aspects for Interferometry

Burst synchronization relates to the fact that the satellite must be at the same along-track position for both passes in order to observe the targets with the same squint angle. A lack of spectral overlap due to burst mis-synchronization leads to decorrelation. The need for burst synchronization puts requirements on commanding, namely on the accuracy of data acquisition timing, as depicted in Fig. 3. The Doppler shift is given by

$$\Delta f_{\mathrm{shift}}(r) = k_t(r) \cdot \Delta t_{\mathrm{acq}} \tag{3}$$

where Δt_{acq} is the timing difference between both acquisitions (raw data), and k_t is the Doppler rate at image level, which is given by (2).

However, not only the accuracy of the synchronization at the beginning of the datatakes is relevant, the size of the orbital tube in the radial dimension affects synchronization during the datatake, i.e., Δt_{acq} varies during the acquisition. This effect has been addressed in [22] in the frame of the S-1 mission.

The coherence loss can be avoided if proper azimuth spectral shift filtering is performed, at the cost of a reduced azimuth resolution. The calculation of the timing difference between both acquisitions and the final common Doppler bandwidth will be provided in Section III-E.

C. Coregistration Accuracy

For conventional nonsquinted stripmap acquisitions, misregistration does not introduce a phase bias but may increase the phase variance [23]. An accuracy of 0.1 pixels is usually sufficient to obtain high-quality interferograms. The coregistration requirements for TOPS mode are however much more demanding due to the significant Doppler frequency variation. In [24] and [25], an analysis of the phase error introduced by a

misregistration in the case of squinted acquisitions shows that the variation in squint angle over azimuth and, to a lesser extent, over range cause phase ramps in both azimuth and range if a misregistration is present. We focus on the azimuth misregistration error since the greater variation of the squint angle in this direction produces much more pronounced phase ramps in azimuth. Using a small-angle approximation, a misregistration of Δt seconds in azimuth between master and slave leads to an azimuth phase ramp over the burst of

$$\Delta\phi_{\mathrm{az}} = 2\pi\Delta f_{\mathrm{DC}}\Delta t = 2\pi\frac{2v}{\lambda}\Delta\beta\Delta t \ [\mathrm{rad}] \tag{4}$$

where Δf_{DC} is the change in Doppler centroid over azimuth, $\Delta\beta$ is the corresponding change in squint angle, and Δt is the misregistration.

Considering the maximum Δf_{DC} of 5.2 kHz, in order to limit the phase ramp to, for example, 1/100 cycle $(= 3.6^\circ)$, coregistration accuracy of approximately 0.0009 pixels at an azimuth sampling frequency f_{az} of 486 Hz would be required, which is equivalent to circa 1.9 μs or 1.3 cm.

The high accuracy requirement for the azimuth coregistration limits on the use of traditional methods as, for example, cross-correlation with small patches distributed over the scene, where each correlation estimate is taken directly as the shift for the center position of the patch. Section III-D addresses the coregistration approach.

III. InSAR Processing Flow

Here, the methodology for interferometric processing is provided. Some details on the importing of the SLC data are first discussed, and the processing chain at burst level is presented. The remaining part concentrates on specific algorithms, namely, deramping the focused bursts, coregistration, spectral shift filtering, and mosaicking of the bursts.

The data can be handled following a three-level hierarchical structure. The lowest level is the burst-level, at which interferometric processing is performed, e.g., signal interpolation and spectral shift filtering. The next higher level is the subswath where mosaics of the bursts are generated. The highest level corresponds to the slice, at which a mosaicking of all three subswaths can be performed.

The philosophy that we have adopted for the coregistration consists of performing a geometric coregistration using an external digital elevation model (DEM) and orbit information, followed by a correction of the residual shift in range and azimuth estimated from the SAR data. This residual shift can be due to orbit inaccuracies, timing errors, or physical effects (e.g., troposphere or solid Earth tides).

A. Data Importing and Preparation

The processing starts with the importing of the master and slave SLC data products; some details on the format of the products can be found in Appendix. The L1 SLC data are generated by the operational ESA Instrument Processing Facility (IPF). It is important to emphasize that all interferometric operations, e.g., spectral shift filtering or burst resampling, have to be done at burst-level, in order to properly consider the Doppler centroid frequency variation. Thus, the data reader should be able to extract the single SLC bursts with their associated annotation. Although not necessary if nominal slice framing has been applied by the IPF, it is good practice to find the corresponding master and slave burst-pairs. It is sufficient to perform this calculation once per subswath. The possible azimuth whole-burst offset can be retrieved by performing a geolocation of an arbitrary slant-range point included in each subswath, e.g., midpoint, using the master orbit to obtain the position on ground. Afterward, an inverse geolocation of this point using the slave orbit provides the slant-range coordinates for the slave point. With the azimuth burst length and the subswath timing information, the whole-burst offset can be easily obtained.

B. Deramping Function

The consideration of the Doppler centroid frequency of the focused burst is critical for interferometric processing. In [26], the procedure for calculating the deramping function for S-1 products is provided and will not be repeated here.

There are two possible approaches to correctly account for the Doppler centroid when performing interpolation and/or filtering operations on the bursts.

1) *Demodulate data:* The complex data are deramped in azimuth in order to obtain a low-pass signal. This approach is appropriate for spectral shift filtering and for resampling. The data have to be reramped after the filtering/resampling has been performed, where in the case of the resampling, one needs to resample also the reramping function before applying it to the data. Note that the deramping and the demodulation introduce a range spectral shift due to their slight range dependence. However, this shift can be neglected for the S-1 case.
2) *Modulate kernel:* The data are not demodulated, but the kernel is modulated in azimuth such that its spectrum follows the local Doppler centroid of the data. This approach can be more convenient when resampling the complex bursts and avoids the separate resampling of the complex data and the deramping function as in the previous case. However, one needs to consider the Doppler variation within the kernel's length to avoid aliasing. For S-1, this variation is about 4 Hz/sample, which, given the oversampling of the azimuth signal of 160 Hz (approximately 32%), does not impose a critical kernel length.

C. Burst-Level Interferometric Processing

Fig. 4 shows a simplified block diagram of the interferometric processing of every burst. The Enhanced Spectral Diversity (ESD) technique [9] is applied for the retrieval of the fine (rigid) azimuth shift. In the first iteration, a geometric coregistration is performed to ensure negligible coherence loss for interferogram formation and the calculation of the subsequent differential interferogram in the overlap area. An external DEM and precise orbit information is used for this coarse coregistration. Interpolation of the slave bursts is performed with a six-point cubic convolution kernel [27]. For each azimuth position, as

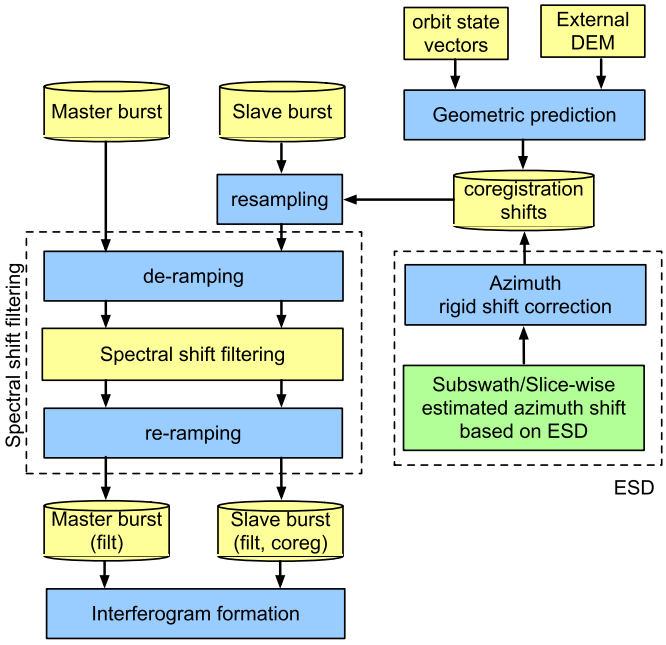

Fig. 4. Burst-level interferometric processing. Resampling, spectral shift filtering, in range and azimuth, and interferogram formation are computed at this level. A geometric coregistration is performed, which is corrected by using ESD.

with Spotlight data, the kernel is modulated in azimuth with a linear phase function so that its spectrum is centered at the local Doppler centroid frequency of the data. Spectral shift filtering is also performed in order to increase the coherence. The master and slave bursts are filtered to a common range and azimuth bandwidth. ESD can be applied by calculating the differential interferogram on the overlap areas between consecutive bursts (along the subswath). Section III-D will give more details on the estimation of the azimuth shift. Once the rigid shift has been retrieved, several possibilities arise for the second iteration. A first option is to repeat the procedure by correcting the coregistration shifts, resampling the slave, and filtering master and slave bursts to a common bandwidth. A second more efficient option is to apply the fine azimuth shift to the slave burst by multiplying its Doppler Spectrum by a linear phase term (not depicted in the figure).

D. Coregistration

First, a geometric coregistration, using an external DEM and orbit information, is performed. This state-of-the-art procedure is precisely described in [28] and not detailed here. There are however some interesting aspects to consider regarding the accuracy of the external DEM for the geometric azimuth coregistration in case of squinted acquisitions, which are covered in [22].

It is important to note that there are three orbit products available: the orbit information annotated in the SLC product, the restituted orbit, and the precise orbit. The last two are provided by ESA as independent products. The restituted orbit is available just a few hours after the acquisition and establishes an accuracy requirement of 10 cm 2-D 1-sigma, where 2-D means the along-track and cross-track directions. The precise orbit product, available 20 days after the acquisition, establishes an accuracy requirement of 5 cm 3-D 1-sigma [29].

From our experience, we do not recommend the use of the orbit information annotated in the SLC product for accurate calculations. However, ESA has confirmed that this issue is currently being addressed as enhanced orbit accuracy of the annotated orbit can be expected in the future.

The geometric coregistration is followed by a refinement of the shifts exploiting the SAR data. Regarding the range direction, cross-correlation can be applied to patches distributed over the master and slave SLCs and a linear correction of the shifts can be performed.

Regarding the azimuth direction, it is important to distinguish between two possible scenarios:

1) *Stationary:* No deformation is expected, or if present, there is no component in the azimuth direction. The azimuth correction to apply is, in essence, a rigid shift due to a possible timing error.
2) *Nonstationary:* The phase jumps that may appear at the interface between adjacent bursts in the case of ground deformation in the azimuth direction have already been addressed in [30]. The reason for the phase jumps is the different projection of the azimuth shift onto the (changing) line of sight. In [30], it is proposed not to perform a local azimuth coregistration if the displacement is sufficiently small such that there is sufficient coherence but to compensate solely for the timing error. At a latter stage, the differential phase should be correctly interpreted by taking into account the actual line-of-sight for each pixel.

We will focus on the stationary case. Several possibilities arise for the retrieval of the constant azimuth shift. A first possibility is to apply cross-correlation techniques [31]—in its coherent (CCC) or incoherent (ICC) versions—to patches distributed over the master and slave SLCs and afterward average the residual azimuth shift to correct for the rigid shift, as already proposed in [32]. Another possibility is to use the ESD technique [9], which exploits the large Doppler frequency difference in the overlap areas between adjacent bursts. The main advantage of correlation techniques over ESD is that they provide a nonambiguous measurement, whereas some care has to be taken when using ESD since it exploits the phase, meaning the retrieval of the correct ambiguity band may not be possible. If the performance of ICC [33] is compared with the performance of ESD, we see that ESD outperforms ICC by approximately one order of magnitude for the S-1 parameters. Fig. 5 compares the standard deviation of both estimators when using all bursts in a single subswath. The overlap regions between bursts within the subswath are assumed used for ESD and all pixels within the subswath for ICC. The exponential decorrelation model [34] with a decorrelation time of 35 days was used to predict the coherence after 1–6 12-day repeat-pass cycles.

We have chosen the ESD technique to obtain the fine azimuth coregistration accuracy; however, it is possible that for certain scenarios (e.g., islands, where the overlap areas correspond to water and therefore incoherent, or if the ambiguity band is not solved), ICC can be useful. A combination of both

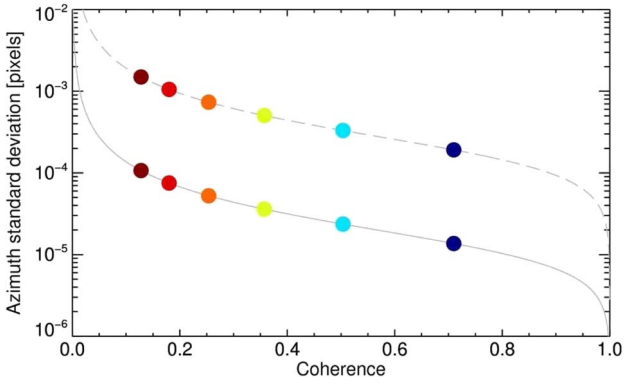

Fig. 5. Azimuth coregistration accuracy for IW2 using ICC (dashed) and ESD (solid). The circles (blue to red) correspond to the coherence after 1–6 12-day repeat-pass cycles, respectively, using the exponential decorrelation model with a decorrelation time of 35 days.

TABLE II
ESD AMBIGUITY BAND AND THREE-SIGMA (99.73%) VALUES OF THE EXPECTED ALONG-TRACK ACCURACY WHEN COMBINING TWO (MASTER AND SLAVE ACQUISITIONS) PRECISE OR RESTITUTED ORBITS

	IW1	IW2	IW3
$\langle \Delta f_{\mathrm{DC}}^{\mathrm{ovl}} \rangle$ [Hz]	4814.25	4044.80	4267.22
Ambiguity band [pix]	$\pm$ 0.051	$\pm$ 0.060	$\pm$ 0.057
Ambiguity band [m]	$\pm$ 0.71	$\pm$ 0.85	$\pm$ 0.80
Precise Orbit $3\sigma_{\mathrm{1D}}^{\mathrm{InSAR}}$ [m]	0.12		
Restituted Orbit $3\sigma_{\mathrm{1D}}^{\mathrm{InSAR}}$ [m]	0.30		

methods is also possible, where ICC is employed to determine the ambiguity band, applying afterward ESD to obtain a fine estimate of the shift. The approximate main ambiguity band is detailed in Table II for each subswath. The three-sigma values of the expected along-track accuracy when combining two (master and slave acquisitions) precise or restituted orbits are also provided, indicating that the ambiguity band is already solved if the geometric coregistration has been performed with precise or restituted orbits. An isotropic distribution of the error in the different components (along-track and cross-track for the restituted orbit and radial, and along-track and cross-track for the precise orbit), has been assumed for the calculation of the expected along-track accuracy, which, although generally not true, is sufficient to obtain an order of magnitude estimate of the expected accuracy. A systematic evaluation of the azimuth shifts with S-1A data in Section V confirms this.

ESD exploits the phase difference in the overlap area between adjacent bursts within a subswath and between adjacent bursts from subswath-to-subswath. We will focus our analysis on the exploitation of the overlap areas within a subswath. The overlap areas from subswath-to-subswath can also be employed, as proposed in [35]. Using these overlap areas improves the performance of the estimation and can also help to resolve the ambiguity band since the Doppler differences in these areas are smaller than in the overlap areas within each subswath, resulting in a larger ambiguity band.

The ESD phase can be calculated for every pixel of each overlap area as follows:

$$\phi_{\mathrm{ESD}} = \arg\left\{ (m_i \cdot s_i^*) \cdot \left(m_{i+1} \cdot s_{i+1}^*\right)^* \right\} \tag{5}$$

where m_i and s_i refer to the ith master and slave complex bursts, respectively; m_{i+1} and s_{i+1} refer to the $(i+1)$th master and slave bursts, respectively; and $\arg\{\cdot\}$ gives the phase of a complex number.

Rewriting (4), an azimuth coregistration error of Δy pixels for pixel p causes an interferometric phase difference, in radians, of [9], [25]

$$\phi_{\mathrm{ESD},p} = 2\pi \Delta f_{\mathrm{DC},p}^{\mathrm{ovl}} \frac{\Delta y}{f_{\mathrm{az}}} \tag{6}$$

where $\Delta f_{\mathrm{DC},p}^{\mathrm{ovl}}$ is the Doppler centroid frequency difference in the overlap area for each burst, and f_{az} is the image azimuth sampling frequency.

A first approximation for the estimation of the shift would be to average the ESD phase and the Doppler centroid frequency differences, i.e.,

$$\widehat{\Delta y} = \frac{f_{\mathrm{az}}}{2\pi} \cdot \frac{\arg\left\{ \langle e^{j\phi_{\mathrm{ESD},p}} \rangle \right\}}{\left\langle \Delta f_{\mathrm{DC},p}^{\mathrm{ovl}} \right\rangle} \tag{7}$$

where $\langle \cdot \rangle$ indicates average value.

We propose to model the ESD phase at each pixel, induced by a constant azimuth shift within the overlap area, using the local Doppler centroid frequency difference.

The estimation of the azimuth coregistration shift Δy requires accounting not only for the local Doppler centroid frequency differences but also for the wrapped nature of the differential phase, $\phi_{\mathrm{ESD},p}$. It is not possible to divide the phase difference values by the local shift-to-phase conversion factor according to (6); otherwise, the estimation would be biased.

The following estimator is proposed:

$$\widehat{\Delta y} = \arg\min_{\Delta y} \left\{ \left| \arg \sum_p e^{j\left(\phi_{\mathrm{ESD},p} - 2\pi \Delta f_{\mathrm{DC},p}^{\mathrm{ovl}} \frac{\Delta y}{f_{\mathrm{az}}}\right)} \right| \right\}. \tag{8}$$

Another approach consists of maximizing the absolute value of the real part, as proposed in [36]. A weighted estimation using the coherence can also be considered, but this is not included in (8) for simplicity.

Its application is only valid for shifts smaller than the smallest of the ambiguity bands of the overlap areas used within the estimation. Thus, if multiple bands of ambiguity are present, as in the case of a combination of the overlap areas within one subswath but for all swaths jointly (IW1-IW1, IW2-IW2, and IW3-IW3), then the search should be restricted to the ambiguity band of IW1.

The value of the estimator for different shift values and the residual phase after compensation of the phase created by the estimated shift is depicted in Fig. 6. The parameters have been calculated for S-1A data in IW mode over Salar de Uyuni. Due to the small variation of the Doppler difference, the estimator is quasi-cyclic. Thus, the search space must be constrained to one ambiguity band according to (6).

As introduced in [37], some spatial multilooking of the interferograms in the overlap area prior to calculation of the differential interferogram (so-called early-multilooking) increases the estimation accuracy. The effect on the histogram of the residual differential phase for a scene-wise estimation (i.e., considering all overlap areas within each subswath) is depicted

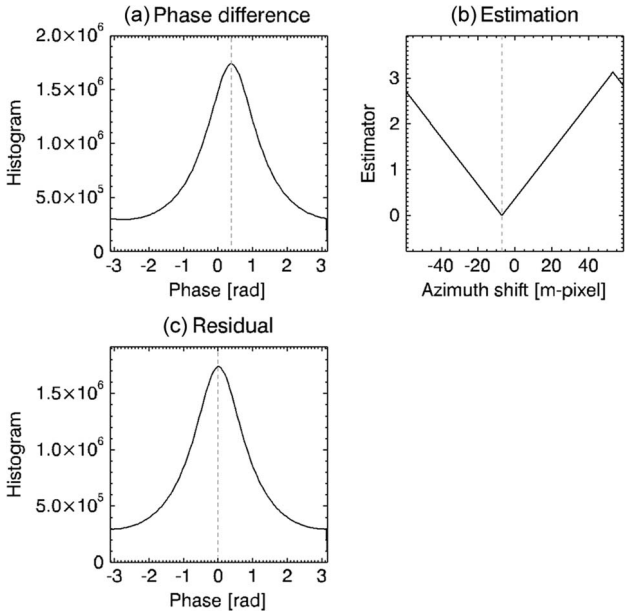

Fig. 6. Proposed shift estimator applied to subswath IW2. (a) Histogram of phase differences. (b) Evaluation of the estimator; estimate depicted by vertical dashed line. (c) Histogram of residual phase difference after compensation of the estimated azimuth shift. The plots are derived from the S-1A interferometric pair over Salar de Uyuni.

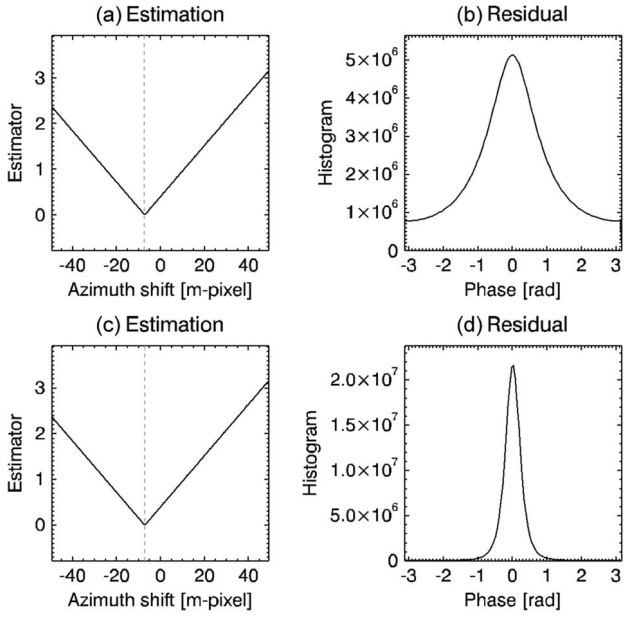

Fig. 7. Effect of burst multilooking in azimuth offset estimation. (a) and (b) Estimation and residual phase without burst multilooking. (c) and (d) Estimation and residual phase with burst multilooking (25 looks). The plots are derived from the S-1A interferometric pair over Salar de Uyuni.

in Fig. 7. (a) and (b) show the estimation result and the residual differential phase histogram if no-multilooking is performed, whereas (c) and (d) show the same results if a multilooking of 25 looks has been applied to the interferograms.

E. Spectral Shift Filtering

The different acquisition geometries for an interferometric pair introduce spectral decorrelation [38]. This effect can be avoided by filtering the master and slave bursts to a common bandwidth. Conventional range spectral filtering can be applied in TOPS mode as usual, but filtering in azimuth requires special care due to the time-variant Doppler change over azimuth. The principle of azimuth spectral filtering is the same as for Spotlight interferometry, i.e., deramping and reramping operations must be performed prior to and after filtering, as described in detail in [39].

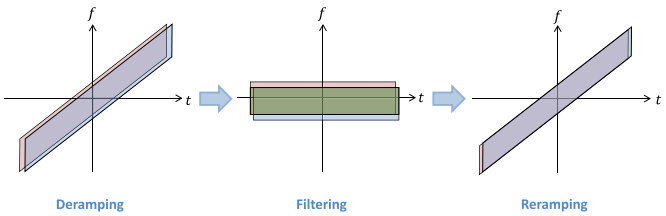

Fig. 8. Time–frequency diagrams at image level showing the rationale of the azimuth spectral filtering process. In the example, only the burst mis-synchronization is depicted, i.e., it is assumed that the Doppler centroid for both datatakes is 0 Hz and that there is no contribution due to the crossing orbits. The master is depicted in orange and the slave in blue. (Left) Original signals. (middle) After deramping with the master deramping function, where it can be observed that the burst mis-synchronization introduces spectral decorrelation. The green block represents the bandpass spectral filter. (Right) After reramping.

The calculation of the common Doppler bandwidth for each pixel p due to possible Doppler centroid differences and to the burst mis-synchronization can be calculated as

$$B_{\text{common},p} = B_a - \left| f_{\text{DC},p}^{\text{master}} - \left(f_{\text{DC},p}^{\text{slave\_resampled}} + \Delta f_{\text{orbit}} \right) \right| \quad (9)$$

where B_a is the azimuth bandwidth, Δf_{orbit} is the spectral shift due to the nonparallel orbits, $f_{\text{DC},p}^{\text{master}}$ is the Doppler centroid of the master burst for each pixel, and $f_{\text{DC},p}^{\text{slave\_resampled}}$ is the Doppler centroid of the slave burst mapped to the master burst geometry. The rationale of azimuth spectral filtering is depicted in Fig. 8.

As for all the steps in burst interferometric processing, the parameters must be independently determined for each of the bursts. Fig. 9(a), (c), and (e) shows the Doppler centroid frequency over range of IW1, IW2, and IW3 for an interferometric pair over Salar de Uyuni after a deramping has been applied. Note that the Doppler centroid frequencies are close to zero for both channels, the difference in Doppler frequency being only a few Hertz. The Doppler centroid frequency rate varies considerably over range, as shown in Fig. 9(b), (d), and (f) for IW1, IW2, and IW3, respectively. As a consequence, the deramping and reramping operators must be adapted to the local Doppler centroid rate for each range bin.

The range spectral filtering does not require an update for TOPS interferometry. Fig. 10 displays the range fringe frequency considering flat Earth for all three subswaths. The plots show the local fringe frequency and a constant fringe frequency calculated at mid burst. As it can be observed, the local fringe frequency varies over range, being this variation more significant for subswath IW1. In any case, note that, due to the small orbital tube of S-1 (kept to a radius of less than 100 m) and the large range bandwidth (given in Table I), the range spectral filter will seldom be necessary.

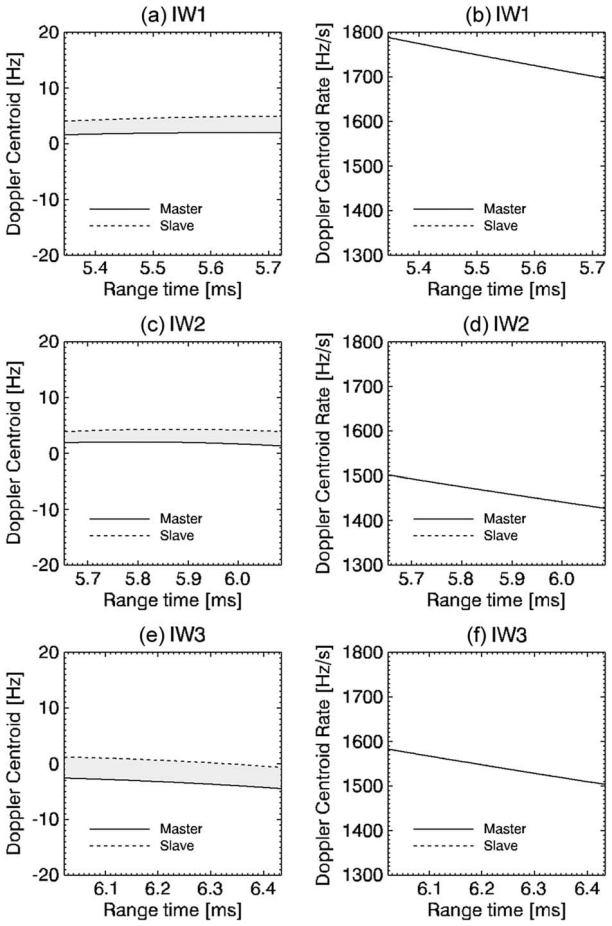

Fig. 9. Master and slave azimuth parameters for spectral shift filtering (after deramping has been applied). (a),(c), and (e) Doppler centroid frequency in range at azimuth center of burst. (b), (d), and (f) Doppler centroid frequency rate at the azimuth center of bursts. Slave parameters have been coregistered to master time. The parameters have been extracted from a S-1A interferometric pair over Salar de Uyuni.

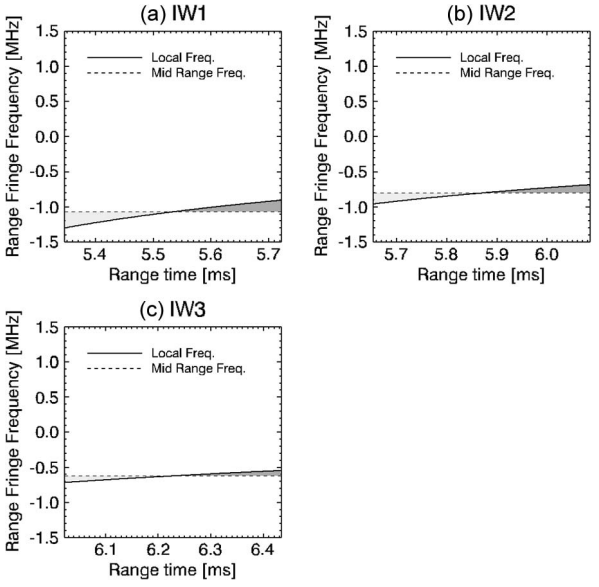

Fig. 10. Range fringe frequency (considering flat earth) for all three subswaths. The plots indicate the local fringe frequency (continuous line) and a constant fringe frequency, calculated at mid burst. The parameters have been extracted from a S-1A interferometric pair over Salar de Uyuni, which presents an effective baseline of 108 m.

F. Mosaicking of Bursts Within a Slice

After the slave bursts have been resampled, the burst interferograms can be computed, and the coherence can be estimated. At this stage, it is important to account for the pixel validity, whose information can be extracted from the L1 products. The general approach is to mosaic the full-resolution interferogram (pixelwise by definition) first, followed by phase flattening and multilooking operations.

There are some minor points to consider with respect to mosaicking the bursts to produce subswath or scene-level interferograms. Three approaches to mosaicking appear possible.

1) Join at a certain azimuth or range line such as the azimuth midpoint of the overlap area between bursts within a subswath or the range midpoint of the overlap area between subswaths.
2) Loop over all bursts, with the current burst overwriting the mosaic but only when the burst pixel is valid as determined from the burst's valid pixel mask.
3) Perform a weighted average within the overlap area. This approach can quickly become complicated when considering the valid pixel masks and applying roll-off functions in both the range and azimuth directions within the overlap area to smooth the transition.

We do not recommend the third approach even if the phase quality can be enhanced by averaging both looks. By consistently cutting at fixed range and azimuth lines, it is easier to visually identify phase discontinuities between bursts due to residual misregistration, for quality analysis purposes or more interestingly in the case of scenarios with horizontal displacement in the azimuth direction.

The flat Earth phase can be subtracted once the mosaic of the interferogram has been generated and differential phase can be obtained by subtracting a DEM simulated phase. Finally, interferogram multilooking is performed.

IV. First Interferometric Results

The first IW InSAR pair was available in ascending geometry over the Gulf of Genoa, Italy, on August 19, 2014, 12 days after S-1A had reached its final orbit on August 7, 2014. This first TOPS pair was processed some hours later, demonstrating the readiness of the S-1 system (both in-orbit instrument and on-ground commanding and processing) for interferometric applications. Fig. 11 shows the interferometric phase and SAR amplitude overlay image of the mosaic of the first two slices over Italy. The image is composed of three subswaths and has a ground range extension of 250 km. The effective baseline is about 120 m. After flat Earth phase removal, one fringe color cycle corresponds to a height of ambiguity of about 129 m.

A further interferometric acquisition over Italy in ascending geometry was available from August 9 and 21. A mosaic of the interferometric phase, having removed a simulated phase from a DEM from the Shuttle Radar Topography Mission (SRTM), overlaid with the SAR amplitude (left) and coherence (right) of the datatake, is shown in Fig. 12. The acquisition extends from Sicily to the Alps demonstrating the high mapping capabilities

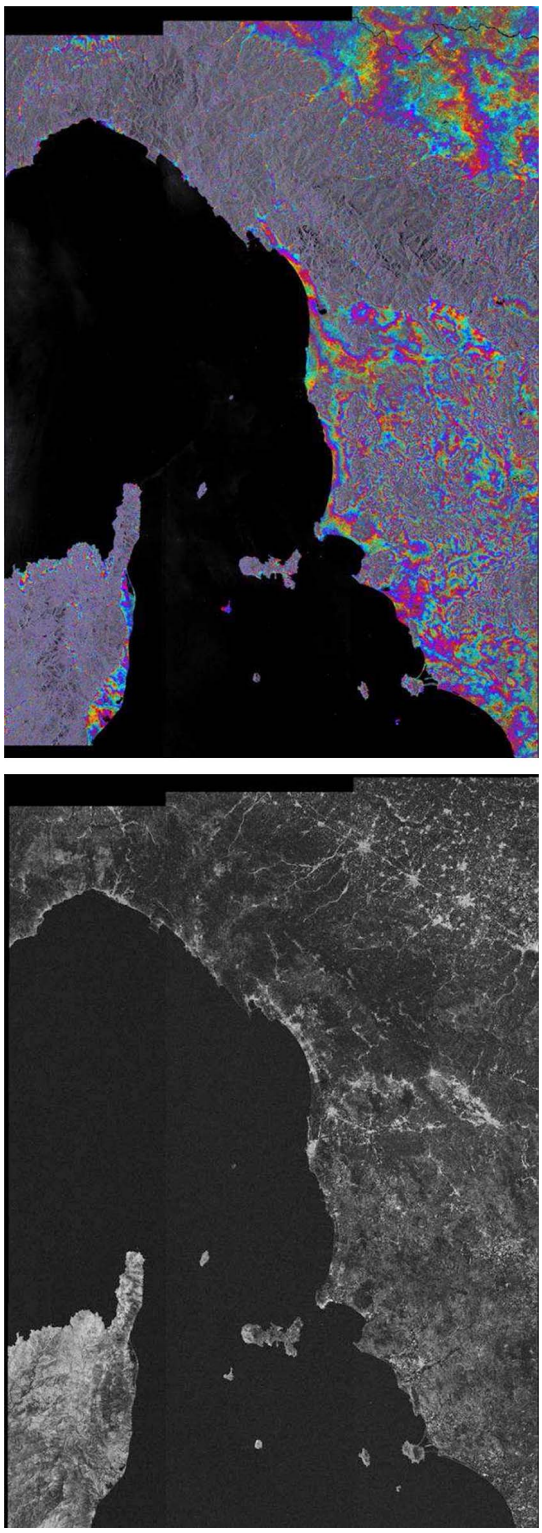

Fig. 11. Mosaic of the first S-1A TOPS interferogram (two slices) in IW mode around the Gulf of Genoa, Italy, acquired on August 7 and 19. Interferometric phase overlaid with the SAR amplitude (top) and coherence (bottom). Range in horizontal direction. Range extension, 250 km; azimuth extension, 340 km.

of the S-1 mission. A total of seven slices has been used for the mosaic, which corresponds to approximately 30 ERS full scenes. The residual fringes that can be observed are probably due to atmospheric disturbances.

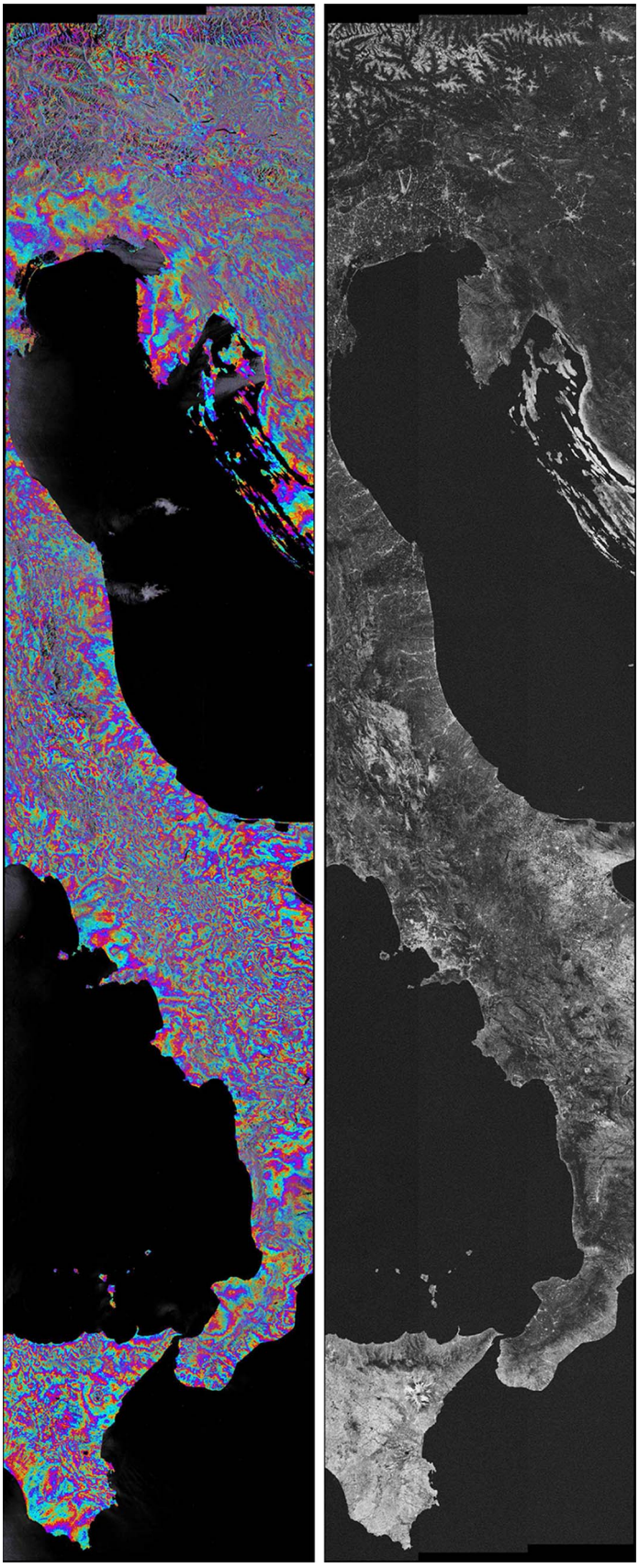

Fig. 12. Mosaic of seven IW slice interferograms in IW mode acquired on August 9 and 21. Interferometric phase, after a simulated phase from a SRTM DEM has been removed, overlaid with the SAR amplitude (left) and coherence (right). Range in horizontal direction. Range extension 250 km; Azimuth extension 1200 km.

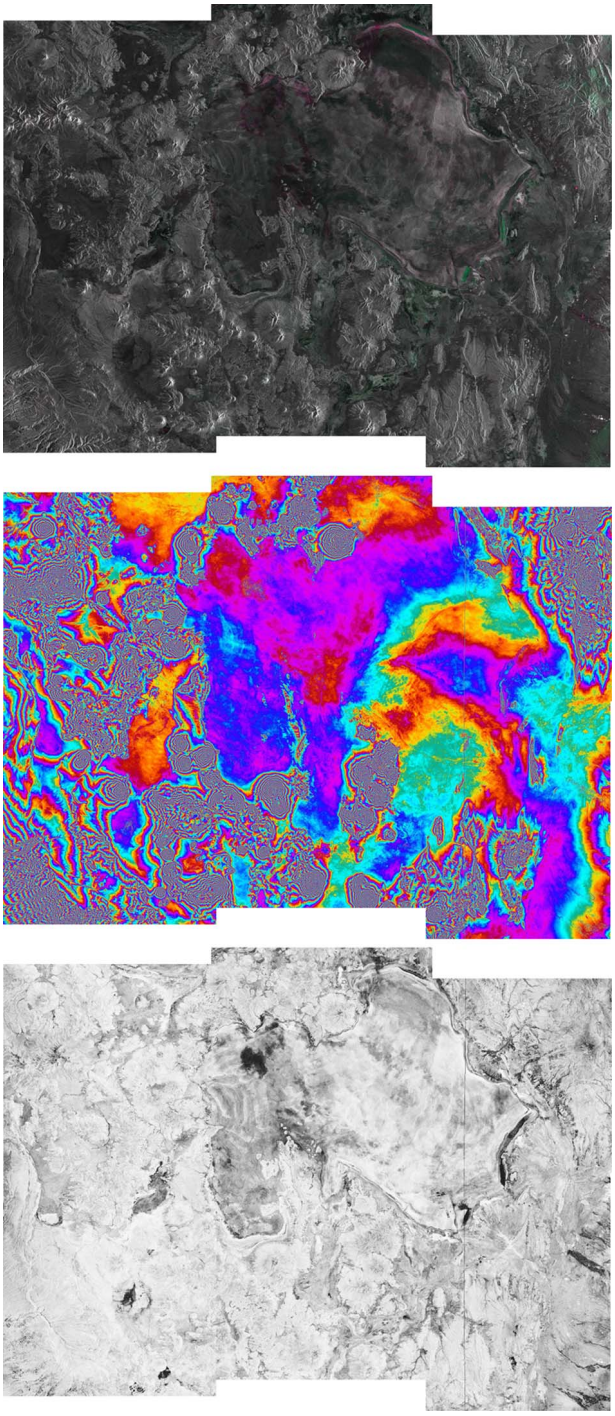

Fig. 13. Interferometric acquisitions in IW mode, descending geometry on December 3 and 27 over Salar de Uyuni, Bolivia. The effective baseline is 108 m, corresponding to a phase cycle of 146 m. Interferometric phase (top), differential phase—SRTM phase subtracted (middle), and coherence (bottom). Range in horizontal direction, increasing to the left. Range extension 250 km, azimuth extension 170 km. The images are in slant-range coordinates but oriented geographically.

V. Interferometric Evaluation

Here, an interferometric evaluation of S-1A data is carried out. A highly coherent interferometric pair in IW mode covering Salar de Uyuni, Bolivia, is first analyzed in terms of Doppler spectrum (deramping), burst synchronization, and coregistration. The spectral shift was already analyzed in Section III-E.

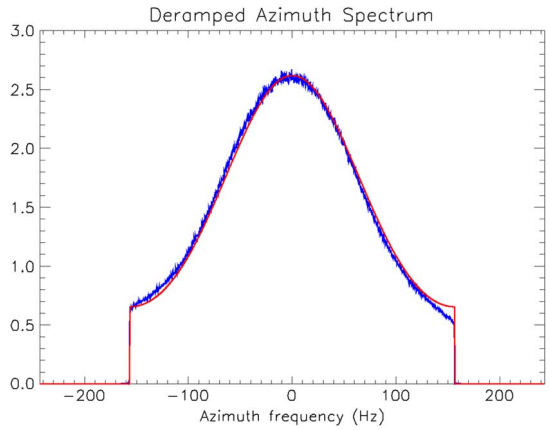

Fig. 14. Deramped Doppler spectrum averaged over range for an S-1A acquisition over Bolivia on December 3, 2014. The blue curve results from a data-based estimate, whereas the red curve corresponds to the annotated Hamming weighting window. The fourth burst of the IW2 subswath was selected.

Later, an evaluation of the along-track shifts employing two types of orbits, i.e., precise and restituted, is provided.

The Uyuni salt lake is the world's largest salt flat covering 10 582 km^2 (4086 mi^2). It is located in Potosí, near the crest of the Andes, at an elevation of 3656 m above mean sea level. The Salar is covered by a few meters of salt crust, which has an extraordinary flatness. The datatakes were acquired in descending geometry on December 3 and 27, 2014, with VV polarization. The L1 products were generated with Processor version IPFV241. The effective baseline is about 108 m, corresponding to a phase cycle of approximately 146 m. Fig. 13 shows a multitemporal composite of the amplitudes, the interferometric phase, and the coherence. The observed slow variation of the interferometric phase over the salt flat is possibly due to atmospheric effects.

A. Deramping

To illustrate the spectral properties of the S-1 bursts, a plot of the deramped Doppler spectrum of a burst from IW2 is provided in Fig. 14. The deramping function has been applied to the burst, and an azimuth fast Fourier transform performed followed by an averaging over range. The plot demonstrates that, after deramping, the spectrum is confined within the expected 313 Hz bandwidth of IW2. The blue curve corresponds to the estimated Doppler spectrum, whereas the red curve indicates the theoretical Hamming weighting window applied by the SAR processor.

B. Burst Synchronization

Regarding burst synchronization, the along-track position mismatching in the middle of the scene is 0.12 ms, equivalent to 0.82 m on the ground. The platform Doppler centroids in the middle of the scene were approximately 2 and 4 Hz for the first and second acquisitions, respectively, indicating excellent burst synchronization characteristics. Fig. 9(a), (c), and (e) shows the variation in range of the Doppler centroid frequencies for all three subswaths.

TABLE III
RETRIEVED AZIMUTH SHIFTS, IN PIXELS AND CENTIMETERS, FOR EACH SUBSWATH OF THE ACQUISITION OVER SALAR DE UYUNI

az. retrieved shift	IW1	IW2	IW3
az. shift (pix)	-0.00730	-0.00704	-0.00713
az. shift (cm)	-10.2677	-9.9108	-10.0274

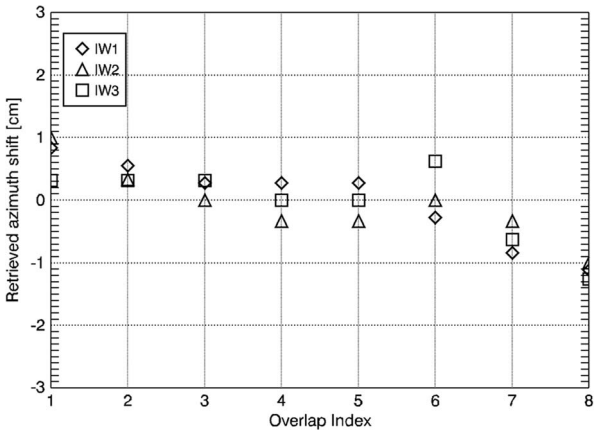

Fig. 15. Residual azimuth shift measured in the overlap areas within each subswath of the slice.

C. Coregistration Analysis

The consistency of the retrieved azimuth shift for each overlap area within every subswath is analyzed here. Precise orbits were used for interferometric processing. ESD was used to retrieve the fine residual azimuth shift of approximately −10 cm. The estimation of the residual azimuth shift was carried out independently for each subswath in order to check the consistency between all three subswaths. Table III summarizes the retrieved shift for each subswath showing differences of a few millimeters, which are negligible. This indicates that a global azimuth shift can be estimated by considering all overlap areas of all three subswaths.

We can also check for the consistency of the residual azimuth shift within each subswath by reestimating the azimuth shift per overlap region after correction of the azimuth shifts given in Table III. Fig. 15 shows this residual azimuth shift for all three subswaths. Observe that the curves are centered around zero. The standard deviation of the shifts for each subswath is 6.8 mm for IW1, 5.8 mm for IW2, and 6.2 mm for IW3.

The reader should keep in mind that an azimuth shift error of 1.2 cm corresponds to a phase variation along the burst of approx 3.6°. With the plot of Fig. 15, it can be concluded that the remaining phase error is below this value.

D. Common Doppler Bandwidth

The common Doppler bandwidth is evaluated here with a stack of acquisitions over Mexico City in descending geometry. The images were acquired between October 3, 2014 and January 1, 2015. The acquisition on December 2, 2014, has been selected as the master. Fig 16 shows the common Doppler bandwidth for each acquisition pair for each subswath. The available Doppler bandwidth is indicated with a horizontal line for each subswath. The common bandwidth is above 95% of the

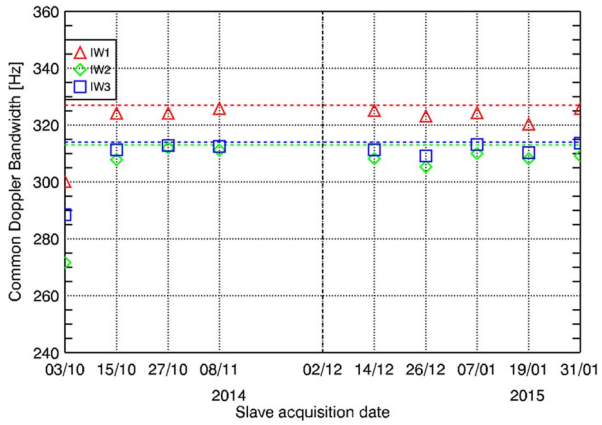

Fig. 16. Assessment of the common Doppler bandwidth. A stack of a total of 10 acquisitions over Mexico City in IW mode has been analyzed. The acquisition on December 2, 2014, has been chosen as master (dashed vertical line). The available Doppler bandwidth is indicated with a horizontal line. The common Doppler bandwidth for each acquisition pair for each subswath is shown.

available bandwidth for all pairs, except for the first acquisition, which was acquired in an early phase, and an issue with the attitude steering was still not solved. This analysis indicates excellent burst synchronization and attitude steering of the system, concluding that the azimuth spectral shift filtering could be skipped without having a significant coherence drop.

E. Along-Track Shifts

Since very sensitive measurements in the along-track direction can be performed with TOPS acquisitions, we can very accurately evaluate the performance of the precise and restituted orbits in this direction. The analysis can be done in time, by analyzing the differential azimuth orbital error for a stack of images, and in space, by analyzing the consistency of the differential azimuth orbital error for consecutive slices within a datatake. The ESD technique is exploited for this purpose, which measures the differential azimuth shift in the burst overlap areas between the slave image(s) and the master image.

1) Temporal Consistency: The same data set of ten S-1A slices acquired over Mexico is analyzed here. The residual along-track shift has been measured employing ESD technique, which not only accounts for the orbital timing error but also for timing error of the SAR instrument, SAR processing effects, ionospheric effects, and geodynamic effects. We considered the gravitational effects exerted by the Moon and the Sun on the Earth's crust (solid Earth tides), which can reach a few centimeters in the horizontal direction [40].

Fig. 17 shows the retrieved differential orbit error in the along-track direction for the precise and restituted orbits, on the order of a few centimeters. We have to be careful when drawing conclusions from this plot. The retrieved azimuth shift is *differential* between the slave acquisitions with respect to the master acquisition. This means that a possible bias in the along-track shift cannot be determined since the along-track orbital error of the master acquisition is also a realization of the same process. We are interested in the dispersion of the values and provide the standard deviation, which is 4.42 cm for the precise orbit and 2.52 cm for the restituted orbit. From

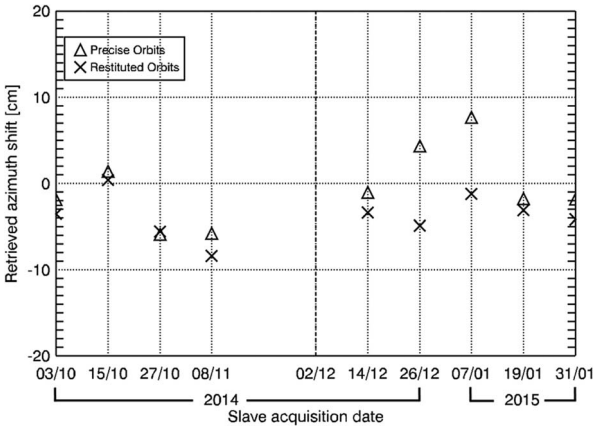

Fig. 17. Assessment of the differential along-track accuracy of the precise and restituted orbits over time. A stack of a total of ten acquisitions over Mexico City in IW mode has been analyzed. The acquisition on December 2, 2014 has been chosen as master (dashed line). The standard deviation of the precise orbit is 4.42 and 2.51 cm for the restituted orbit. The overlap areas within IW2 have been used for the measurement. The differential solid Earth tides were considered.

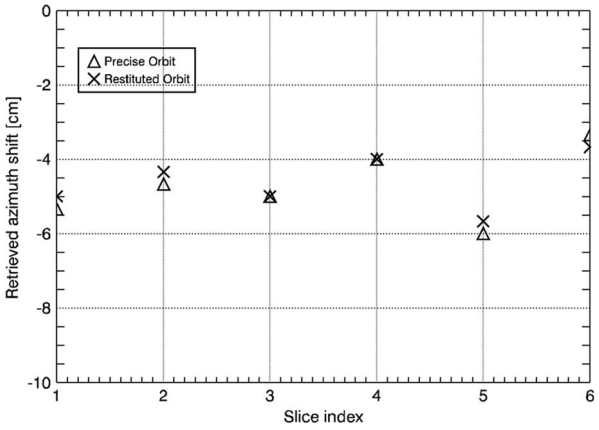

Fig. 18. Assessment of the differential along-track accuracy of the precise and restituted orbits along a datatake. Six slices of a datatake over Germany in IW mode have been employed. The acquisitions were made on December 21, 2014 and January 2, 2015. The standard deviation of the precise orbit is 9.5 and 7.4 mm for the restituted orbit. The overlap areas within IW2 have been used for the measurement.

the specifications, the nominal (1-D) standard deviation of the azimuth orbital error – assuming an isotropic distribution of the error in the different components (along-track and cross-track for the restituted orbit; radial, along-track and cross-track for the precise orbit) – would be 2.88 cm for the precise orbit, and 7.07 cm for the restituted orbit (assuming that the standard deviation is the same for each direction). We conclude that the measured standard deviation of the precise orbit is very similar to the expected one from the specifications. However, we observe that the measured standard deviation of the restituted orbit is surprisingly better than nominal and paradoxically even better than the one obtained with the precise orbits in this particular data set.

2) Spatial Consistency: We have selected a datatake pair acquired over Europe in descending geometry, composed of six slices. The datatakes were acquired on December 21, 2014 and January 2, 2015 and include the area from Hamburg, Germany to Genoa, Italy. Fig. 18 shows the estimated differential orbit error in the along-track direction for the precise and the restituted orbits, to be around -4.7 cm when using precise orbits, and -4.6 cm when using restituted orbits. The standard deviation of the differential orbit error in the along-track direction retrieved with the precise orbit is 9.5 mm and 7.4 mm for the restituted orbit. The spatial stability of the differential orbit error for both types of orbits is below 1 cm. This information is of valuable interest when working with scenarios that present deformation in the along-track direction. The shift to be corrected can be retrieved from a slice not affected by deformation and applied to the slice(s), experiencing deformation.

VI. Conclusion

In this paper, a guideline on how to process interferometric S-1 data in TOPS mode has been provided. The analysis has been performed for IW mode, i.e., the standard mode over land. A brief description of the S-1 IW TOPS mode, including spectral properties, burst synchronization aspects, and needed coregistration requirements, has been provided. The central part of this paper focused on interferometric processing, where aspects such spectral shift filtering, interpolation, and coregistration were discussed. The adopted strategy for coregistration is based on a geometric prediction of the shifts employing orbit information and an external DEM, followed by a refinement of the azimuth shifts using ESD [9] and a refinement of the range shifts using incoherent cross-correlation. We have proposed a pixelwise estimation of the azimuth shift, considering the shift and the local Doppler centroid frequency differences for each pixel in the overlap area. Other aspects such as data importing, preparation, and mosaicking of interferometric results have been also discussed. First S-1A interferograms in IW TOPS mode acquired during the commissioning phase have been shown, including an interferogram of a datatake over Italy, reaching from Sicily to the Alps that demonstrates the high mapping capabilities of the S-1 mission. An interferometric evaluation with highly coherent data over Salar de Uyuni has been provided, where a quality analysis of the azimuth shifts, both within and between subswaths, indicates high phase stability. We conclude that the azimuth shift can be retrieved globally by employing the overlap areas of all three subswaths. An evaluation of a stack of acquisitions over Mexico City has shown that the common Doppler bandwidth is above 95% of the available bandwidth, indicating very good burst synchronization and attitude steering of the system. An evaluation of the along-track shifts employing ESD shows that the precise and restituted orbits provide similar accuracy in the along-track direction. Moreover, by compensating solid Earth tides, an assessment of the performance of both types of orbits has been provided. The spatial stability of the azimuth shifts for several slices of a datatake has also been provided, showing that the retrieved differential orbital error possesses high spatial stability.

Appendix
L1B Product Description Format (XML, TIFF, etc.)

Focused S-1 SAR data products are available in the so-called "SAFE" container format comprising the binary raster

data as Tagged Image File Format (TIFF) files and various annotation information in eXtensible Markup Language (XML) files. Combinations of transmit/receive polarizations are termed "channels". For the TOPS modes, i.e., IW and EW, both the subswath index and polarization are considered channels. The channels of a product are delivered as separate sets within a SAFE container consisting of a TIFF file with its corresponding XML files. This information effectively provides a mask for the valid/invalid samples (pixels) in the SLC data product. Technically, the TIFF files are actually GeoTIFF files containing specific geo-information tags, and the TIFF file sizes commonly exceed 4 GB, thus requiring the Big[Geo]TIFF format. Handling of classic TIFF and BigTIFF files, as well as automatic conversion between binary formats of different hardware platforms, is accomplished by the open-source libTIFF library (4.0.3). Within these (Big) GeoTIFF files, the binary raster data are stored pixel-interleaved with pixels from near range to far range in a line. Lines are stored from early azimuth to late azimuth. The complex-valued L1 data pixels consist of two 16-bit signed integers representing the real and imaginary parts. For the TOPS modes, the bursts are stored in the TIFF of a channel as a series of patches with the same number of lines per burst that can be obtained from the XML annotation. For every such line in every burst, there is also an indication given in the XML annotation for the offset of the first and of the last valid sample or whether all samples in the line are valid. The XML files contain general information about the acquisition parameters and data-specific information for SAR signal processing in the form of polynomial coefficients. Orbital state vectors of the sensor platform that can be used for quicklook purposes are already included in the SAFE containers. Restituted orbital state vector products are available soon after the acquisition. Precise orbit data are available 20 days after the acquisition. The restituted and precise orbit products can be downloaded as separate products in XML format from the S-1 Quality Control webpage [41].

ACKNOWLEDGMENT

The authors would like to thank N. Miranda from the European Space Agency for his support.

REFERENCES

[1] Copernicus Programme. [Online]. Available: http://www.copernicus.eu
[2] R. Torres *et al.*, "GMES Sentinel-1 mission," *Remote Sens. Environ.*, vol. 120, pp. 9–24, May 2012.
[3] F. De Zan and A. Monti Guarnieri, "TOPSAR: Terrain observation by progressive scans," *IEEE Trans. Geosci. Remote Sens.*, vol. 44, no. 9, pp. 2352–2360, Sep. 2006.
[4] D. Geudtner, R. Torres, P. Snoeij, M. Davidson, and B. Rommen, "Sentinel-1 system capabilities and applications," in *Proc. IEEE IGARSS*, Jul. 2014, pp. 1457–1460.
[5] F. De Zan, A. M. Guarnieri, F. Rocca, and S. Tebaldini, "Sentinel-1 radar interferometry applications," in *Proc. 7th EUSAR*, Jun. 2008, pp. 1–4.
[6] A. Meta, J. Mittermayer, P. Prats, R. Scheiber, and U. Steinbrecher, "TOPS imaging with TerraSAR-X: Mode design and performance analysis," *IEEE Trans. Geosci. Remote Sens.*, vol. 48, no. 2, pp. 759–769, Feb. 2010.
[7] R. Scheiber *et al.*, "Sentinel-1 imaging performance verification with TerraSAR-X," in *Proc. 8th EUSAR*, Jun. 2010, pp. 1–4.
[8] J. Mittermayer *et al.*, "TOPS Sentinel-1 and TerraSAR-X processor comparison based on simulated data," in *Proc. 8th EUSAR*, Jun. 2010, pp. 1–4.
[9] P. Prats-Iraola, R. Scheiber, L. Marotti, S. Wollstadt, and A. Reigber, "TOPS interferometry with TerraSAR-X," *IEEE Trans. Geosci. Remote Sens.*, vol. 50, no. 8, pp. 3179–3188, Aug. 2012.
[10] R. Scheiber, M. Jäger, P. Prats-Iraola, F. De Zan,and D. Geudtner, "Speckle tracking and interferometric processing of TerraSAR-X TOPS data for mapping nonstationary scenarios," *IEEE J. Sel. Topics Appl. Earth Observ. Remote Sens.*, vol. 8, no. 4, pp. 1709–1720, Apr. 2014.
[11] G. Davidson, V. Mantle, B. Rabus, D. Williams, and D. Geudtner, "Implementation of TOPS mode on RADARSAT-2 in support of the Sentinel-1 mission," presented at the ESA Living Planet Symp., Edinburgh, U.K., Sep. 2013.
[12] D. Geudtner, "Implementation of the TOPS mode on RADARSAT-2 in support of the Copernicus Sentinel-1 mission: RADARSAT-2 TOPS SAR Interferometry (InSAR) scene pair data acquisitions," European Space Agency, Paris, France, Tech. Rep. ESA-S1-TN-ESA-SY-0452, 2014.
[13] P. Prats, R. Scheiber, J. Mittermayer, A. Meta, and A. Moreira, "Processing of sliding spotlight and TOPS SAR data using baseband azimuth scaling," *IEEE Trans. Geosci. Remote Sens.*, vol. 48, no. 2, pp. 770–780, Feb. 2010.
[14] M. Rodriguez-Cassola *et al.*, "Doppler-related distortions in TOPS SAR images," *IEEE Trans. Geosci. Remote Sens.*, vol. 53, no. 1, pp. 25–35, Jan. 2015.
[15] W. Xu, P. Huang, Y. Deng, J. Sun, and X. Shang, "An efficient approach with scaling factors for TOPS-Mode SAR data focusing," *IEEE Geosci. Remote Sens. Lett.*, vol. 8, no. 5, pp. 929–933, Sep. 2011.
[16] G. Engen and Y. Larsen, "Efficient full aperture processing of TOPS mode data using the moving band chirp Z-transform," *IEEE Trans. Geosci. Remote Sens.*, vol. 49, no. 10, pp. 3688–3693, Oct. 2011.
[17] G. Sun *et al.*, "Sliding spotlight and TOPS SAR data processing without subaperture," *IEEE Geosci. Remote Sens. Lett.*, vol. 8, no. 6, pp. 1036–1040, Nov. 2011.
[18] J. Holzner and R. Bamler, "Burst-mode and ScanSAR interferometry," *IEEE Trans. Geosci. Remote Sens.*, vol. 40, no. 9, pp. 1917–1934, Sep. 2002.
[19] F. Rodriguez Gonzalez, N. Adam, A. Parizzi, and R. Brcic, "The Integrated Wide Area Processor (IWAP): A processor for wide area persistent scatterer interferometry," in *Proc. ESA Living Planet*, Sep. 2013, p. 353.
[20] P. Prats *et al.*, "TAXI: A versatile processing chain for experimental TanDEM-X product evaluation," in *Proc. IEEE IGARSS*, Honolulu, HI, USA, Jul. 25–30, 2010, pp. 4059–4062.
[21] C. Herbert, C. Thain, D. Ramsbottom, P. Lim, and T. Wong, "Sentinel-1 product definition," Macdonald, Dettwiler Assoc. Ltd., Richmond, BC, Canada, Tech. Rep. MDA S1-RS-MDA-52-7440, Mar. 28, 2014.
[22] P. Prats-Iraola *et al.*, "Role of the orbital tube in interferometric spaceborne SAR missions," *IEEE Geosci. Remote Sens. Lett.*, vol. 12, no. 7, pp. 1486–1490, Jul. 2015.
[23] R. Bamler and D. Just, "Phase statistics of interferograms with application to synthetic aperture radar," *Appl. Opt.*, vol. 33, no. 20, pp. 4361–4368, Jul. 1994.
[24] M. Bara, R. Scheiber, and A. Broquetas, "Interferometric SAR signal analysis in the presence of squint," in *Proc. IEEE IGARSS*, 1999, vol. 1, pp. 257–259.
[25] R. Scheiber and A. Moreira, "Coregistration of interferometric SAR images using spectral diversity," *IEEE Trans. Geosci. Remote Sens.*, vol. 38, no. 5, pp. 2179–2191, Sep. 2000.
[26] N. Miranda, "Definition of the TOPS SLC deramping function for products generated by the S-1 IPF," Eur. Space Agency, Paris, France, Tech. Rep., 2014.
[27] R. Hanssen and R. Bamler, "Evaluation of interpolation kernels for SAR interferometry," *IEEE Trans. Geosci. Remote Sens.*, vol. 37, no. 1, pp. 318–321, Jan. 1999.
[28] E. Sansosti, P. Berardino, M. Manunta, F. Serafino, and G. Fornaro, "Geometrical SAR image registration," *IEEE Trans. Geosci. Remote Sens.*, vol. 44, no. 10, pp. 2861–2870, Oct. 2006.
[29] Sentinels POD team, "Sentinels POD service file format specifications," European Space Agency, Paris, France, Tech. Rep. GMES-GSEG-EOPG-FS-10-0075, 2013.
[30] F. De Zan, P. Prats-Iraola, R. Scheiber, and A. Rucci, "Interferometry with TOPS: Coregistration and azimuth shifts," in *Proc. 10th EUSAR*, Jun. 2014, pp. 1–4.
[31] R. Bamler and M. Eineder, "Accuracy of differential shift estimation by correlation and split-bandwidth interferometry for wideband and delta-k SAR systems," *IEEE Geosci. Remote Sens. Lett.*, vol. 2, no. 2, pp. 151–155, Apr. 2005.
[32] N. Yague-Martinez, F. Rodriguez-Gonzalez, U. Balss, H. Breit, and T. Fritz, "TerraSAR-X TOPS, ScanSAR and WideScanSAR interferometric processing," in *Proc. 10th EUSAR*, Jun. 2014, pp. 1–4.

[33] F. De Zan, "Accuracy of incoherent speckle tracking for circular Gaussian Signals," *IEEE Geosci. Remote Sens. Lett.*, vol. 11, no. 1, pp. 264–267, Jan. 2014.
[34] A. Parizzi, X. Y. Cong, and M. Eineder, "First results from multi-frequency interferometry. A comparison of different decorrelation time constants at L, C and X band," in *Proc. Fringe Workshop*, 2009, pp. 2–6.
[35] N. Sakar, R. Brcic, F. Rodriguez-Gonzalez, and N. Yague-Martinez, "Advanced co-registration method for TOPSAR mode," in *Proc. IEEE IGARSS*, Jul. 2015, pp. 5240–5243.
[36] S. Mancon, A. Monti Guarnieri, and S. Tebaldini, "Sentinel-1 precise orbit calibration and validation," in *Proc. FRINGE*, Jun. 2015, pp. 1–4.
[37] F. De Zan, P. Prats-Iraola, and M. Rodriguez-Cassola, "On the dependence of delta-k efficiency on multilooking," *IEEE Trans. Geosci. Remote Sens.*, vol. 12, no. 8, pp. 1745–1749, Aug. 2015.
[38] R. Bamler and P. Hartl, "Synthetic aperture radar interferometry," *Inv. Prob.*, vol. 14, pp. R1–R54, 1998.
[39] M. Eineder, N. Adam, R. Bamler, N. Yague-Martinez, and H. Breit, "Spaceborne spotlight SAR interferometry with TerraSAR-X," *IEEE Trans. Geosci. Remote Sens.*, vol. 47, no. 5, pp. 1524–1535, May 2009.
[40] M. Eineder, C. Minet, P. Steigenberger, Xiaoying Cong, and T. Fritz, "Imaging geodesy—Toward centimeter-level ranging accuracy with TerraSAR-X," *IEEE Trans. Geosci. Remote Sens.*, vol. 49, no. 2, pp. 661–671, Feb. 2011.
[41] Sentinel-1 Quality Control. [Online]. Available: https://qc.sentinel1.eo.esa.int/

Néstor Yagüe-Martínez received the Ingeniero degree in telecommunications engineering from Universitat Politècnica de València (UPV), Valencia, Spain, in 2004.

From 2006 to 2015 he was with the Chair for Remote Sensing Technology, Technische Universität München (TUM), Munich, Germany, and also with the Remote Sensing Technology Institute, German Aerospace Center (DLR), Oberpfaffenhofen, Germany, where he worked in the development of the operational interferometric processor of the TanDEM-X mission. He spent a year from 2011 to 2012 at Starlab Barcelona S.L. working on along-track Interferometry for ocean surface currents retrieval. In 2015 he joined the Multimodal Algorithms Group, Microwaves and Radar Institute, DLR, Oberpfaffenhofen. His research interests include SAR processing, SAR interferometry, and differential SAR interferometry.

Pau Prats-Iraola (S'03–M'06–SM'13) was born in Madrid, Spain, in 1977. He received the Ingeniero degree and Ph.D. degree in telecommunications engineering from Universitat Politècnica de Catalunya (UPC), Barcelona, Spain, in 2001 and 2006, respectively.

In 2001, he was a Research Assistant with the Institute of Geomatics, Barcelona. In 2002, he was with the Department of Signal Theory and Communications, UPC, where he worked in the field of airborne repeat-pass interferometry and airborne differential SAR interferometry. From December 2002 to August 2006, he was an Assistant Professor with the Department of Telecommunications and Systems Engineering, Universitat Autònoma de Barcelona, Barcelona. In 2006, he joined the Microwaves and Radar Institute, German Aerospace Center (DLR), Wessling, Germany, where, since 2009, he has been the Head of the Multimodal Algorithms Group. His research interests include high-resolution airborne/spaceborne SAR processing and SAR interferometry.

Dr. Prats-Iraola received the First Prize in the Student Paper Competition of the 2005 IEEE International Geoscience and Remote Sensing Symposium held in Seoul, Korea, and the DLR Science Award in 2012.

Fernando Rodríguez González received the Ingeniero degree in telecommunications engineering from Universidad Politécnica de Madrid (UPM), Madrid, Spain, and the Diplôme de l'École Polytechnique from École Polytechnique, Palaiseau, France, in 2009.

From 2009 to 2010, he worked at the Chair of Remote Sensing Technology with Technische Universität München, Munich, Germany. In 2010, he joined the Department of SAR Signal Processing, Remote Sensing Technology Institute, German Aerospace Center (DLR), Wessling, Germany. He has worked in the development of the operational interferometric processor of the TanDEM-X mission. His research interests include SAR interferometry, persistent scatterer interferometry, and SAR stereo radargrammetry.

Ramon Brcic (M'03) received the B.Eng. (Hons. 1) degree in aerospace avionics from the Queensland University of Technology, Brisbane, Australia, in 1998 and the Ph.D. degree in electrical engineering from Curtin University of Technology, Perth, Australia, in 2003.

From 2003 to 2007, he was a Research Associate with the Signal Processing Group, Technische Universität Darmstadt, Darmstadt, Germany. Since 2008, he has been with the Department of SAR Signal Processing, Remote Sensing Technology Institute, German Aerospace Center (DLR), Wessling, Germany, as a Research Scientist. His current research interests include interferometric SAR and persistent scatterer interferometry.

Robert Shau (M'01–SM'13) received the Diploma and the Doctorate degrees in physics in the field of semiconductor laser diodes from Technische Universität München (TUM), Munich, Germany, in 1998 and 2005, respectively.

From 1998 to 2003, he worked at TUM on the development of optical gain material, device structure, and fabrication, and on prototyping, characterization, and application development, of vertical-cavity surface-emitting laser diodes based on indium phosphide in the near infrared. From 2002 to 2010, he worked at a spin-off company cofounded by him on the commercialization of these devices and invented a design for tunable laser applications with low fringe noise. He continued working as a Technology Consultant. Since 2013, he has been with German Aerospace Center, Wessling, Germany and is currently working in the field of persistent scatterer interferometry.

Dirk Geudtner received the M.S. degree in geophysics from Freiberg University of Mining and Technology, Freiberg, Germany, in 1991 and the Ph.D. degree in InSAR from the University of Stuttgart, Stuttgart, Germany, in 1995.

In 1991, he joined the DLR, where he worked as a SAR Scientist on the development of new methods for satellite InSAR data processing and analysis. In 1994, he joined the German Research Center for Geosciences and became responsible for the development of geoscientific applications of satellite InSAR techniques. From 1995 to 1997, he was a Visiting Scientist with the Canada Centre for Remote Sensing (CCRS), working on differential InSAR for monitoring glacier and ice motion. In 1997, he joined the Microwaves and Radar Institute, DLR, where he developed InSAR calibration concepts for the X-SAR system on the Space Shuttle Radar Topography Mission (SRTM). During SRTM operations, he was the Lead Engineer for the in-orbit X-SAR interferometric antenna beam alignment at the NASA Payload Operations Control Center, Houston, TX, USA. From 2000 and 2002, with a Research Grant from the German Humboldt Foundation. He was a Visiting Scientist at CCRS, working on new methods for the interferometric processing of Canada's RADARSAT-1 data and for the polarimetric calibration of RADARSAT-2 data. From 2002 and 2008, during a six-year assignment to the Canadian Space Agency, he worked as key SAR Scientist/Engineer on feasibility studies for future satellite SAR missions focusing particularly on CSA's RADARSAT Constellation Mission. For the RCM project, he was entrusted to lead the external Canadian SAR expert Image Quality and Science Advisory Group. After returning back to DLR in 2008, he significantly contributed to the TerraSAR-X2 feasibility study and the analysis of methods for orbital baseline calibration for the TanDEM-X mission. From 2009 to 2011, he worked as a Scientific Advisor (Seconded National Expert) at the European Commission's Global Monitoring for Environment and Security (GMES) Bureau, where he supported the analysis of the GMES space component and was also responsible for the implementation of the GMES marine and climate change monitoring services. Since March 2011, he has been the Head of the Sentinel-1 Mission and Systems Section at the European Space Agency. In this role, he is responsible for the compliance of the SAR system performance with user/science requirements, the end-to-end SAR system calibration, and the initiation and technical supervision of SAR system and related application studies.

Michael Eineder (SM'01) received the Diploma degree in electrical engineering from Technische Universität München (TUM), Munich, Germany, in 1990 and the Dr. rer. Nat. degree from the University of Innsbruck, Innsbruck, Germany, in 2004.

Since 1990, he has been with German Aerospace Center (DLR), Wessling, Germany, where he has worked on a variety of international missions including SIR-C/X-SAR, SRTM/X-SAR in cooperation with NASA, ERS-1 (ESA), TerraSAR-X, and TanDEM-X (Germany). Since 2013, he has been an Honorary Professor with TUM. He is currently the Head of the Department of SAR Signal Processing, Remote Sensing Technology Institute, DLR. His responsibilities encompass the development of SAR and InSAR processing systems for current and future radar missions. Furthermore, he is a Part-Time Lecturer for remote sensing at TUM. His current research interests include future SAR missions and imaging geodesy, an absolute positioning technique exploiting high-resolution SAR.

Richard Bamler (M'95–SM'00–F'05) received the Diploma degree in electrical engineering, the Doctorate degree in Engineering, and the Habilitation in signal and systems theory from the Technische Universität München (TUM), Munich, Germany, in 1980, 1986, and 1988, respectively.

From 1981 to 1989, he worked with TUM on optical signal processing, holography, wave propagation, and tomography. Since 1989, he has been with the German Aerospace Center (DLR), Wessling, Germany, where he is currently the Director of the Remote Sensing Technology Institute. In early 1994, he was a Visiting Scientist with Jet Propulsion Laboratory, in preparation of the SIC-C/X-SAR missions. In 1996, he was a Guest Professor with the University of Innsbruck, Innsbruck, Germany. Since 2003, he has been a Full Professor of remote sensing technology with TUM as a double appointment with his DLR position. His teaching activities include university lectures and courses on signal processing, estimation theory, and SAR. He, his team, and his institute have been working on SAR and optical remote sensing, image analysis and understanding, stereo reconstruction, computer vision, ocean color, passive and active atmospheric sounding, and laboratory spectrometry. They were and are responsible for the development of the operational processors for SIR-C/X-SAR, SRTM, TerraSAR-X, TanDEM-X, Tandem-L, ERS-2/GOME, ENVISAT/SCIAMACHY, MetOp/GOME-2, Sentinel 5p, EnMAP, etc. He has devised several high-precision algorithms for monostatic and bistatic SAR processing, SAR calibration and product validation, ground moving target indication for traffic monitoring, SAR interferometry, phase unwrapping, persistent scatterer interferometry, differential SAR tomography, and data fusion. His research interests include algorithms for optimum information extraction from remote sensing data with emphasis on SAR, which involves new estimation algorithms, such as sparse reconstruction and compressive sensing.

Appendix C

Coregistration of Interferometric Stacks of Sentinel-1 TOPS Data

Journal: IEEE Geoscience and Remote Sensing Letters
Authors: Nestor Yague-Martinez, Francesco de Zan, Pau Prats-Iraola
Impact Factor: 3.57 (2017)
N. Yague-Martinez, F. De Zan, and P. Prats-Iraola (2017). "Coregistration of Interferometric Stacks of Sentinel-1 TOPS Data". In: *IEEE Geoscience and Remote Sensing Letters* 14.7, pp. 1002–1006. ISSN: 1545-598X. DOI: 10.1109/LGRS.2017.2691398

Coregistration of Interferometric Stacks of Sentinel-1 TOPS Data

Nestor Yague-Martinez, Francesco De Zan, and Pau Prats-Iraola, *Senior Member, IEEE*

***Abstract*— The coregistration of synthetic aperture radar images is of fundamental importance for the generation of interferograms. The high azimuth coregistration requirements imposed by the TOPS acquisition mode imply that an advanced approach for the coregistration of stacked time series images is needed due to temporal decorrelation effects. In some scenarios, the conventional approach of estimating the shifts pairwise with respect to the same master might result insufficient. Therefore, a joint estimation is proposed here, which exploits jointly all interferograms in order to retrieve more accurate results. Simulated data and Sentinel-1A images acquired in IW mode are used to validate this procedure, demonstrating the better performance of the joint approach when compared to the standard single-master approach.**

***Index Terms*— Coregistration, interferometric synthetic aperture radar (InSAR), Sentinel-1, Terrain Observation by Progressive Scans (TOPS).**

I. Introduction

THE European Sentinel-1A (S1A) and Sentinel-1B satellites were launched in April 2014 and April 2016, respectively. This constellation of synthetic aperture radar (SAR) satellites was conceived to provide repeat-pass interferometric capabilities with unprecedented wide area coverage for medium-resolution applications [1]. The SAR instrument, operating at 5.405 GHz, employs the interferometric wide (IW) swath mode for the systematic monitoring of large land and coastal areas. The IW mode is implemented as a three subswath Terrain Observation by Progressive Scans (TOPS) [2] SAR mode providing large swath widths of 250 km with a spatial resolution of 5 m $\times$ 20 m in the range and azimuth dimensions, respectively.

The necessary high azimuth coregistration requirements for TOPS data due to the nature of the burst-mode acquisition and the azimuth antenna steering have already been pointed out [3], [4]. In [5] details on the interferometric processing of Sentinel-1 TOPS SAR image pairs are provided indicating that a coregistration accuracy of approximately 0.0009 samples (equivalent to ca. 1.9 μs or 1.3 cm) is required to limit the interferometric synthetic aperture radar (InSAR) phase error to 1/100 cycle. The established method to achieve the necessary azimuth coregistration accuracy is based on enhanced spectral diversity (ESD) [4], which exploits the spectral separation of the data in the overlapping areas between adjacent bursts.

Manuscript received January 24, 2017; revised March 14, 2017 and March 29, 2017; accepted March 30, 2017. Date of publication May 12, 2017; date of current version June 22, 2017. This work was supported by the European Space Agency's SEOM Programme under Contract 4000110587/14/I-BG. *(Corresponding author: Nestor Yague-Martinez.)*

The authors are with the German Aerospace Center (DLR), D-82234 Oberpfaffenhofen, Germany (e-mail: nestor.yague@dlr.de).

Color versions of one or more of the figures in this letter are available online at http://ieeexplore.ieee.org.

Digital Object Identifier 10.1109/LGRS.2017.2691398

When applying advanced techniques for displacement measurement, such as persistent scatterers interferometry, it is necessary to have the images of the stack coregistered to a common master image. The state-of-the-art procedure consists in performing first a geometrical coregistration between all slaves and the master image using precise (PREC) orbit information and an external digital elevation model. Afterward, baseline errors or orbital/instrument timing errors can be determined by exploiting the SAR data.

In this letter, we will focus on the determination of the (rigid) along-track shifts for S1 TOPS images stacks. The coregistration problem consists in retrieving the azimuth shift of each image with respect to a common master image. The single-master approach applies ESD between each image and the master image. Since the ESD performance depends on the coherence, it is expected that the performance of the estimation drops with the temporal baseline. A joint coregistration approach appears to be the optimal solution when working with long stacks. This approach has been already addressed in the literature for the case of coherently correlating speckle signals [6]. The same principle can be applied when employing the ESD technique for azimuth coregistration of TOPS images [7]–[9]. This letter is an extended and updated version of the work presented in [8]. A similar procedure employing subsets of the total number of images of the stack has been proposed recently in [10]. Another interesting option is to employ only point scatterers for the ESD estimation, which keep a high coherence over time. The performance of the estimation would, however, depend on the density of scatterers that are imaged in the overlap areas. Moreover, since the Sentinel-1 mission was devised to map wide areas, where for some cases no urban regions are present, a more general solution is required.

This letter is structured as follows. Section II provides the methodology to perform a joint coregistration by exploiting ESD together with a weighted least squares (WLS) approach. Section III evaluates the performance of this estimator and compares it to the phase linking (PL) algorithm by employing Monte-Carlo simulations. In Section IV, results with a stack of S1A data over Mexico are provided. In Section IV-A, the performance of the joint coregistration approach over the single master approach in terms of retrieved shifts variance is exposed. Section IV-B makes a quantitative comparison of the shifts obtained between the direct and joint approaches. In Section IV-C, a validation is performed exploiting the long-term coherence properties at urban areas. After having validated the method with S1A data not presenting ground displacements in the north–south direction, in Section V, a suitable solution for scenarios presenting

ground displacements is briefly discussed. The conclusions are drawn in Section VI.

II. Methodology

In Section II-A the ESD estimator is introduced. Section II-B introduces the joint coregistration approach based on WLS.

A. Enhanced Spectral Diversity

ESD [4] exploits the phase difference in the overlap area between adjacent bursts. The ESD phase can be calculated for every sample, p, of each overlap area as follows:

$$\phi_{\mathrm{ESD,p}} = \arg\left\{\left(m_i \cdot s_i^*\right) \cdot \left(m_{i+1} \cdot s_{i+1}^*\right)^*\right\} \tag{1}$$

where m_i and s_i refer to the ith master and slave complex bursts, and m_{i+1}, and s_{i+1} refer to the $(i+1)th$ master and slave bursts; $\arg\{\cdot\}$ gives the phase of a complex number.

The azimuth shift can be retrieved by exploting following periodogram, equivalently as in [5]

$$\widehat{\Delta y} = \arg\max_{\Delta y}\left\{\Re\left(\sum_p e^{j\left(\phi_{\mathrm{ESD,p}} - 2\pi\,\Delta f_{\mathrm{DC,p}}^{\mathrm{ovl}}\frac{\Delta y}{f_{\mathrm{az}}}\right)}\right)\right\} \tag{2}$$

where $\arg\max_{\Delta y}\{\cdot\}$ stands for the argument of the maximum (azimuth shift, Δy, for which the function attains its largest value). $\Delta f_{\mathrm{DC,p}}^{\mathrm{ovl}}$ is the Doppler centroid frequency difference in the overlap areas for each sample, p, and f_{az} is the image azimuth sampling frequency.

B. Joint Coregistration

Among the different possibilities to jointly estimate the azimuth shifts we can differentiate between methods working with the ESD interferograms (complex domain) or the derived shifts (real numbers). More precisely, the PL algorithm [11] provides a joint estimation of the phases whereas a WLS procedure works with retrieved shifts. PL is the maximum likelihood estimator of the phases in a stack, which exploits all possible interferogram combinations (N^2, having N acquisitions). PL requires the coherence matrix, which is estimated from the data.

In our case, shifts of only a few centimeters are expected, mainly coming from inaccuracies of the orbit product. Thus, having into account that the ESD ambiguity band is about ± 71 cm in the worst case [5], we could assume that the shifts from each pair are not affected by wrapping effects. The requirement for this implies that a certain coherence is available, which should be the case when working with real data. Moreover a sufficient number of samples have to be averaged in order to avoid wrapping effects due to phase noise. This is also fulfilled since we can employ all samples of all overlapping areas of the scene. This enables the use of WLS to jointly estimate the shifts of the stack. In Section V, we propose the use of PL for a scenario with ground deformation in the sensor along-track direction.

In the first place, all images are coarsely coregistered to a common master using geometric information. In order to achieve this, the use of PREC or restituted orbits is recommended since they provide an accuracy in the order of a few centimeters in the along-track dimension [5], which is within the main ambiguity band of ESD. Afterward mutual ESD estimation can be applied among all possible pairs, as shown in Fig. 1. All samples of the overlapping areas are used in the ESD step, providing a robust estimation against phase wrapping effects (in the case of phase noise due to low coherence). Note that an outlier rejection procedure, e.g., based on the coherence, can be applied to avoid averaging pure noise samples.

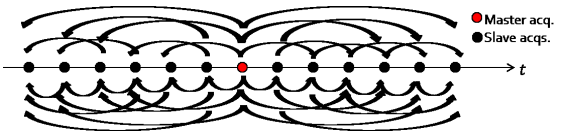

Fig. 1. In the joint coregistration procedure, the mutual shifts among all available pairs are calculated. This way the temporal decorrelation effect can be mitigated. In the standard single-master approach uniquely the shifts between each slave and a selected master, usually chosen in the middle of the stack, is performed. The joint approach supposes moreover additional flexibilities regarding the selection of the master image.

The azimuth shifts, $\mathbf{m}_{\mathrm{L}_2}$, of each image with respect to the master image can be calculated using

$$\mathbf{m}_{\mathrm{L}_2} = (\mathbf{G}^T\mathbf{W}\mathbf{G})^{-1}\mathbf{G}^T\mathbf{W}\mathbf{d} \tag{3}$$

where $\mathbf{G}$ is the system matrix defining the relations between the different measurements, $\mathbf{d}$ the data vector (pairwise ESD measurements). $\mathbf{W}$ is a diagonal matrix including the weights (inverse of the shift variance of the pairwise measurements, that can be computed from the estimated coherences). In [8], a detailed description of the system of equations can be found for the case where the master image is the first of the stack. A possibility to limit the computational burden when working with long time series is to exploit subsets of images of the stack, e.g., by setting a maximum time span. However, this strategy would not profit from distant high coherent images in the presence of seasonal effects or long-term coherence, and represents a suboptimal solution in terms of performance.

The WLS method has been described so far. However, being rigorous, the correlation between shift estimates should be considered as well. The covariance between shifts (in s) can be computed as [12]

$$E\{d_{n,k}d_{h,l}\} = \frac{\gamma_{\mathrm{nh}}\gamma_{\mathrm{kl}} - \gamma_{\mathrm{nl}}\gamma_{\mathrm{kh}}}{L\gamma_{\mathrm{nk}}\gamma_{\mathrm{hl}}\left(2\pi\,\Delta f_{\mathrm{DC}}^{\mathrm{ovl}}\right)^2} \tag{4}$$

where L is the effective number of looks of the estimation window and γ_{ij} is the interferometric coherence between image i and image j.

The weight matrix, $\mathbf{W}$, should then be filled with the corresponding covariance values and would become a variance–covariance matrix. The inversion problem employing the variance–covariance matrix becomes a generalized least squares (GLS) one. A feasible GLS (FGLS) solution can be obtained using the Prais-Winsten or Cochrane-Orcutt estimator [13]. This is, however, out of the scope in this letter.

It is interesting to note that if the stack is large enough, the mean of all estimated shifts corresponds to the along-track geolocation error of the master image, which occurs mainly due to the error in the master orbit. Therefore, in such cases

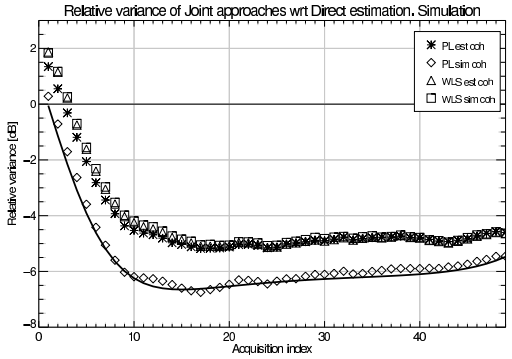

Fig. 2. Relative variance, in dB, of Phase Linking and Weighted Least Squares estimators with respect to the direct estimation employing simulated data. A Monte-Carlo simulation was done assuming an exponential decorrelation model with a constant time of 40 days and a long-term coherence of 0.2 for a stack of 50 images acquired consecutively with a repetition cycle of 12 days. The master image is chosen at the beginning of the time-series (index 0). The solid red line corresponds to the relative variance of the Cramér-Rao lower bound of the joint estimator over the direct estimator. The relative variance decreases linearly with the number of images until a certain number where it almost saturates. Negative values of the plot mean a reduction of the standard deviation of the joint approaches in comparison to the single-master estimator. The actual point in which the behavior changes is related to the particular relationship between the decorrelation constant time and the repetition cycle of the system.

one can also use this joint-estimator to evaluate the quality of the orbit products (at least in the along-track direction).

III. Joint Coregistration Approaches and Achievable Performance With Simulated Data

In order to evaluate the performance of the WLS estimator, a Monte-Carlo simulation for a stack of 50 images has been carried out. The master image corresponds to the first acquisition. For the simulation, an exponential decorrelation model [14] with a time constant of 40 days and a long-term coherence of 0.2 was assumed. Fig. 2 shows the gain of the joint approach employing WLS and PL with respect to the direct estimation. The solid red line corresponds to the Cramér–Rao bound [11]. Note that the estimation results employing two sources of coherences for the covariance matrix have been used: the one estimated from the simulated data (est coh) and the theoretical one used to generate the simulated data (sim coh). We can see that in the case of using PL, the curve approaches the bound if the theoretical coherence is used. If the estimated coherence is used, there is a gain loss. In the case of WLS, we cannot appreciate significant differences employing one or the other and, moreover, the performance is very similar to the one achieved by PL with the estimated coherence. We conclude that employing WLS represents a good solution for the retrieval of the azimuth shifts.

IV. Application to S1 Data

We have selected a data set of a total of 43 S1A IW acquisitions over Mexico for the evaluation of the procedure. The City of Mexico is covered by one of the subswaths, whereas one of the remaining subswaths corresponds mainly to nonurban areas. This makes the scenario suitable to perform a validation of the method since long-term coherent as well as rapidly decorrelating scatterers can be found. The images were acquired between November 2014 and August 2016 in ascending geometry (track 78). The master image, acquired on November 4, 2014, has been chosen at the beginning of the stack in order to maximize temporal decorrelation effects.

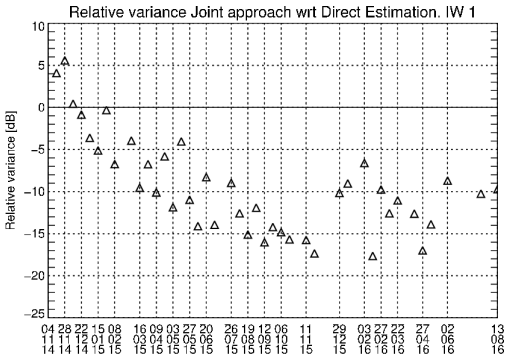

Fig. 3. Relative variance, in dB, of the joint estimator over the single-master estimator for the IW1 subswath over Mexico site (distributed scatterers). Negative values of the plot mean a reduction of the standard deviation of the joint estimator in comparison to the single-master estimator. The gain of the joint estimation raises as the temporal baseline increases.

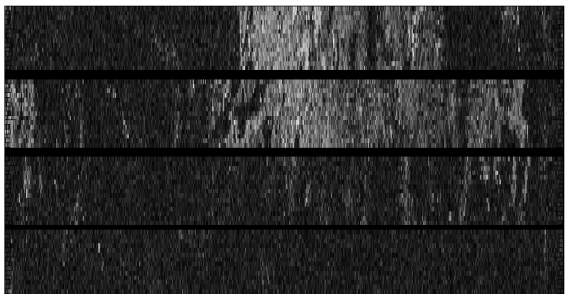

Fig. 4. Coherence of the forward look at the overlap areas of IW3 for the pair November 4, 2014–August 13, 2016, corresponding to a temporal baseline of 504 days. We focus on the third overlap area, which cover the City of Mexico, where long-term coherence properties can be appreciated.

A. Joint Estimator Performance Evaluation

The first assessment that we present corresponds to the comparison of the standard deviation of the estimated shifts with the single-master and joint approaches. We focus on the IW1 subswath, which covers nonurban areas. Each overlap area of the subswath is divided into blocks and the joint estimator is applied to each block. The performance of the estimation is calculated as the quotient between the standard deviation of the joint estimation and the one of the single-master approach. Fig. 3 shows the relative variance, in dB, of the joint estimator over the single-master estimator for areas affected by temporal decorrelation. Negative values of the plot mean a reduction of the standard deviation of the joint estimator in comparison to the single-master estimator. It can be observed that the gain of the joint approach raises as the temporal baseline increases for this kind of scatterers.

B. Comparison Between Joint Coregistration and Single-Master Approaches

A quantitative comparison between the shifts obtained with joint and single-master approaches is shown in the following.

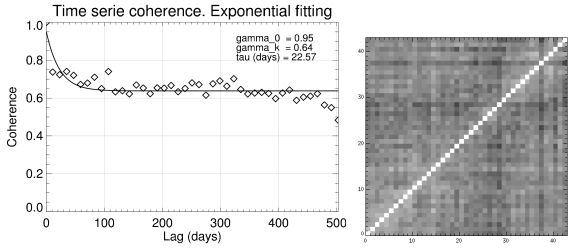

Fig. 5. Modeling of the temporal decorrelation for an urban target.

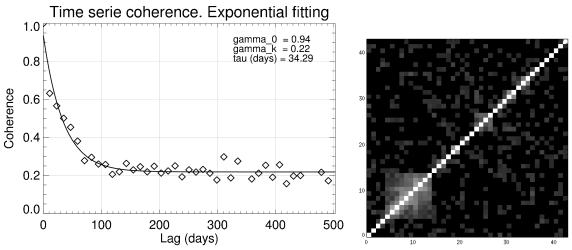

Fig. 6. Modeling of the temporal decorrelation for a target over land area.

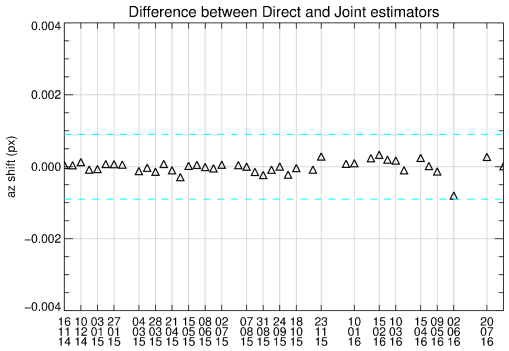

Fig. 7. Comparison between the azimuth shifts retrieved with the joint coregistration approach and the single master approach over urban areas. The blue dashed lines correspond to the required 0.0009 samples accuracy.

We focus now on the IW3 subswath, which covers urban and nonurban areas. Fig. 4 shows the coherence at the overlapping areas of this subswath for the largest temporal baseline of the stack (504 days). It can be appreciated that the third overlap contains urban (City of Mexico) and nonurban areas making it convenient for a validation of the joint method in terms of retrieved shift values. Figs. 5 and 6 show the exponential fitting that has been performed together with the covariance matrices for exemplary targets located in urban area and over land, respectively. The decorrelation model proposed in [14] has been used, which provides three parameters: initial coherence, i.e., coherence for 0 days lag, time constant, and long-term coherence.

It can be seen that the targets over urban areas present long-term coherence whereas distributed scatterers have a faster decay of the coherence with time. Taking advantage of this fact, we generate a mask for the urban areas (establishing a threshold to the coherence between the master image and the slave image with the largest temporal span) and estimate the shifts using the joint and single-master approach. Fig. 7 shows the difference between direct ESD and the joint retrieved shifts for the urban area. The deviation of the direct ESD shifts with

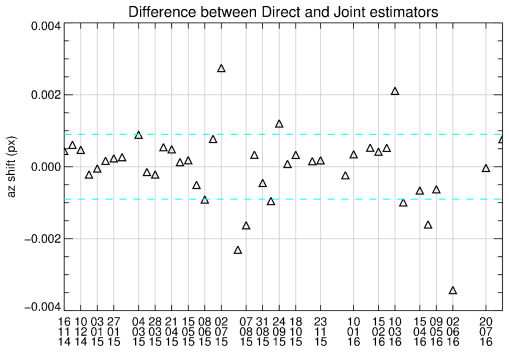

Fig. 8. Comparison between the azimuth shifts retrieved with the joint coregistration approach and the single master approach over distributed targets (nonurban areas). The blue dashed lines correspond to the required 0.0009 samples accuracy.

respect to the joint solution is very small. This is an expected result since urban areas present long-term coherence properties and the single-master estimate already provides good results.

If we mask out the urban areas and consider only the areas with distributed scatterers, we obtain the plot in Fig. 8 showing much larger differences between direct ESD and the joint retrieved shifts over the land areas. We assume that the joint estimates are the reference since they correspond to the optimal estimation. The required 0.0009 sample values have been depicted with blue dashed lines and it can be observed that these limits are exceeded for some of the acquisitions, being especially large when the temporal baseline increases. It should be expected to have interferometric phase errors of about 10 degrees for some acquisitions, e.g., on March 10, 2016 or June 2, 2016. These two acquisitions will be further analyzed in the next section.

We have compared the shift for two scenarios: 1) urban area and 2) nonurban area. The gain of the joint estimation is evident for nonurban areas. In the case of sites which present long-term coherence properties, it is also a matter of "luck" if these regions are mapped by the burst overlap areas. The estimation of the decorrelation parameters, specifically the long-term coherence agree with the obtained results.

C. Validation—Interferogram of a Selected Pair

We can make more evident the phase error that we would have in the case that we generate the interferogram of a selected pair, e.g., in an SBAS scenario, for the different coregistration approaches. From Fig. 8, we can see that the acquisitions on March 10, 2016 and June 2, 2016 present large deviations between both estimates. We evaluate in the following the residual ESD phase—measured in a direct way—over the urban area. This area presents long-term coherence, as shown in Fig. 5, being the direct estimation reliable. We perform this measurement for three different coregistered versions of the images: 1) only geometric coregistration; 2) single-master approach; and 3) joint approach. For 2) and 3) the nonurban area was used to retrieve the azimuth shifts with respect to the master image. The results are summarized in Fig. 9. The figure shows the histograms of the measured ESD phases for all three cases. The mean value of the ESD phase in the case that only a geometric coregistration

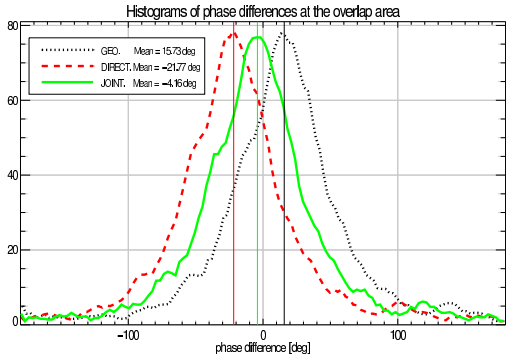

Fig. 9. Histograms of the measured residual ESD phases for the three coregistration possibilities. The histogram of the residual ESD phase in case that only a geometric coregistration is performed is shown with a black dotted line, presenting a mean value of 15.73°. The histogram in case that the azimuth shifts are calculated employing the single-master approach is shown with a red dashed line, providing a residual ESD phase equal to −21.77°. The histogram of the residual ESD phase for the images coregistered jointly is shown with a green solid line. In this case the mean error is only −4.16° which is much closer to our established boundaries

is performed is 15.73°, larger than the targeted 3.6°. This phase error is due to timing/orbital errors of both acquisitions. In case that the azimuth shifts are calculated employing the single-master approach an "overcorrection" takes place, delivering a residual ESD phase equal to −21.77°, which is even a larger error than the one corresponding to the orbital error. The joint estimate delivers a residual ESD phase of only −4.16° which is much closer to our established boundaries.

V. Discussion

We have assumed so far that in the scene no local displacement in the along-track direction occurs. However, this is, in general, not realistic, since time-series analyses are usually intended to monitor displacements. As the temporal baseline increases, these displacements can become important and cannot just be attributed to orbital errors. Our proposal to cope with this situation performing simultaneously a joint coregistration is now briefly described. A PLinking procedure can be applied to the ESD phases at the overlapping areas in order to retrieve the maximum likelihood estimate of the phases. PL with a small multilook window is used in order to be adaptive to local displacements, since it is noted that the WLS approach averages all valid samples of all overlap areas. For each multilooked pixel, the ESD phases would contain two contributions: one due to the orbital error and one due to the ground displacement. The periodogram can be applied to obtain the mean azimuth deformation rate. Once the slope is retrieved, the values can be detrended in order to isolate the orbital errors. An average of the "detrended" values employing all multilooked samples for each pair would provide the corresponding azimuth shift due to an orbital error. Note that the result also corresponds to a joint estimate, since we applied PL to the ESD phases.

VI. Conclusion

In this letter, we addressed the azimuth coregistration problem of interferometric stacks of TOPS images using S1 IW data. The high coregistration requirements for TOPS data have been stressed, highlighting the necessity of sophisticated methods when coregistering long stacks of images. The joint coregistration idea has been applied to the retrieval of the (rigid) azimuth shifts applying a least squares estimate. Results with Monte-Carlo simulations show that for the retrieval of the rigid azimuth shifts the least squares estimate provides very similar performance to PL.

The better performance of the joint estimation has been demonstrated with a stack of 43 S1A images over Mexico. The best results are achieved when mapping land areas, where temporal decorrelation effects are important. A comparison of the joint estimation with the single-master approach has been done indicating that deviations of more than 0.0009 samples can occur if a joint approach is not used. These errors introduce biases in the interferometric phases, as shown for the analyzed stack, increasing the noise of the line-of-sight deformation measurements over time. The higher the density of persistent scatterers at the overlap areas is, the lower is the gain of the join estimator. However, applying a joint estimation procedure provides, in general, a better estimation of the shifts.

References

[1] R. Torres *et al.*, "GMES Sentinel-1 mission," *Remote Sens. Environ.*, vol. 120, pp. 9–24, 2012. [Online]. Available: http://www.sciencedirect.com/science/article/pii/S0034425712000600

[2] F. D. Zan and A. M. M. Guarnieri, "TOPSAR: Terrain observation by progressive scans," *IEEE Trans. Geosci. Remote Sens.*, vol. 44, no. 9, pp. 2352–2360, Sep. 2006.

[3] R. Scheiber and A. Moreira, "Coregistration of interferometric SAR images using spectral diversity," *IEEE Trans. Geosci. Remote Sens.*, vol. 38, no. 5, pp. 2179–2191, Sep. 2000.

[4] P. Prats-Iraola, R. Scheiber, L. Marotti, S. Wollstadt, and A. Reigber, "TOPS interferometry with TerraSAR-X," *IEEE Trans. Geosci. Remote Sens.*, vol. 50, no. 8, pp. 3179–3188, Aug. 2012.

[5] N. Yagüe-Martínez *et al.*, "Interferometric processing of Sentinel-1 TOPS data," *IEEE Trans. Geosci. Remote Sens.*, vol. 54, no. 4, pp. 2220–2234, Apr. 2016.

[6] F. De Zan, "Coherent shift estimation for stacks of SAR images," *IEEE Geosci. Remote Sens. Lett.*, vol. 8, no. 6, pp. 1095–1099, Nov. 2011.

[7] F. De Zan and P. Prats-Iraola, "Joint coregistration of SAR images with an application to TerraSAR-X TOPS mode datasets," in *Proc. Living Planet Symp.*, Edinburgh, U.K., 2013.

[8] N. Yagüe-Martínez, P. Prats-Iraola, and F. De Zan, "Coregistration of interferometric stacks of Sentinel-1A TOPS data," in *Proc. 11th Eur. Conf. Synth. Aperture Radar (EUSAR)*, Jun. 2016, pp. 1–6.

[9] M. Nannini, P. Prats-Iraola, F. De Zan, and D. Geudtner, "TOPS time series performance assessment with TerraSAR-X data," *IEEE J. Sel. Topics Appl. Earth Observ. Remote Sens.*, vol. 9, no. 8, pp. 3832–3848, Aug. 2016.

[10] H. Fattahi, P. Agram, and M. Simons, "A network-based enhanced spectral diversity approach for TOPS time-series analysis," *IEEE Trans. Geosci. Remote Sens.*, vol. 55, no. 2, pp. 777–786, Feb. 2017.

[11] A. M. Guarnieri and S. Tebaldini, "On the exploitation of target statistics for SAR interferometry applications," *IEEE Trans. Geosci. Remote Sens.*, vol. 46, no. 11, pp. 3436–3443, Nov. 2008.

[12] F. De Zan, M. Zonno, and P. López-Dekker, "Phase inconsistencies and multiple scattering in SAR interferometry," *IEEE Trans. Geosci. Remote Sens.*, vol. 53, no. 12, pp. 6608–6616, Dec. 2015.

[13] C.-M. Kuan, *Generalized Least Squares Theory*. 2004. [Online]. Available: http://homepage.ntu.edu.tw/~ckuan/pdf/et01/et_Ch4.pdf

[14] F. Rocca, "Modeling interferogram stacks," *IEEE Trans. Geosci. Remote Sens.*, vol. 45, no. 10, pp. 3289–3299, Oct. 2007.

Appendix D

The 2-look TOPS Mode: Design and Demonstration with TerraSAR-X

Journal: IEEE Transactions on Geoscience and Remote Sensing
Authors: Nestor Yague-Martinez, Pau Prats-Iraola, Steffen Wollstadt and Alberto Moreira
Impact Factor: 5.84 (2017)

N. Yague-Martinez, P. Prats-Iraola, S. Wollstadt, and A. Moreira (2019b). "The 2-Look TOPS Mode: Design and Demonstration With TerraSAR-X". in: *IEEE Transactions on Geoscience and Remote Sensing* 57.10, pp. 7682–7703. ISSN: 0196-2892. DOI: 10.1109/TGRS.2019.2915797

The 2-Look TOPS Mode: Design and Demonstration With TerraSAR-X

Nestor Yague-Martinez, Pau Prats-Iraola, *Senior Member, IEEE*, Steffen Wollstadt, and Alberto Moreira, *Fellow, IEEE*

***Abstract*— Burst-mode acquisition schemes achieve wide coverage at the expense of a degraded azimuth resolution, reducing, therefore, the performance on the retrieval of ground displacements in the azimuth direction, when interferometric acquisitions are combined. Moreover, the azimuth varying line of sight can induce discontinuities in the interferometric phase when local azimuth displacements are present, e.g., due to ground deformation. In this contribution, we propose the interferometric 2-look terrain observation by progressive scans (TOPS) mode, a sustaining innovation, which records bursts of radar echoes of two separated slices of the Doppler spectrum. The spectral separation allows to exploit spectral diversity techniques, achieving sensitivities to azimuth displacements better than with StripMap and eliminating discontinuities in the interferometric phase. Moreover, some limitations of the TOPS mode to compensate ionospheric perturbations, in terms of data gaps or restricted sensitivity to azimuth shifts, are overcome. The design of 2-look TOPS acquisitions will be provided, taking the TerraSAR-X system as reference to derive achievable performances. The methodology for the retrieval of the azimuth displacement is exposed for the case of using pairs of images, as well as for the calculation of mean azimuth velocities when working with stacks. We include results with experimental TerraSAR-X acquisitions demonstrating its applicability for both scenarios.**

***Index Terms*— 2-look terrain observation by progressive scans (TOPS), burst-mode, synthetic aperture radar (SAR), SAR interferometry, TerraSAR-X, wide coverage.**

I. Introduction

CURRENT remote sensing satellites are operated following near-polar orbits. Since radar systems measure distances in the line-of-sight (LOS) direction, they are very sensitive to ground displacements in the east–west (E-W) and vertical directions. By combining different geometries, a 3-D deformation field can be obtained [1]; however, the sensitivity to displacements in the north–south (N-S) direction remains low. A common procedure to enhance the sensitivity in the along-track direction, and therefore to the N-S direction, is to apply correlation techniques exploiting the imaging capability of SAR. This has been done extensively with images acquired in the StripMap mode for different applications, as, e.g., tectonics [2] or the determination of glaciers ice flow [3].

With the high demand for wide-area coverage data from the scientific community, new SAR acquisition modes have been implemented on current systems or are under development. The ScanSAR mode [4] was the first to offer wide coverage by recording subsets of radar echoes over multiple subswaths. ScanSAR presents some limitations related to azimuth-dependent ambiguities and signal-to-noise ratio (SNR), and the so-called scalloping effect that has been overcome by the terrain observation by progressive scans (TOPS) mode [5]. However, both of them present a reduced azimuth resolution due to the burst-mode acquisition nature, impairing the accuracy of correlation techniques in this direction, since the sensitivity depends on the resolution cell size [6]. In order to solve this paradox, two strategies are possible: the first one consists in achieving a wide swath keeping high azimuth resolution. This can be fulfilled by employing multichannel systems such as the proposed high resolution wide swath (HRWS) SAR mode [7]. In the last years, an important number of concepts and techniques have been developed following this philosophy. Several works have been published which deal with the use of digital beamforming techniques [8], the use of multiple azimuth channels [9], [10], and the staggered SAR concept [11], which employs nonconstant acquisition pulse repetition intervals to avoid blind ranges when digital beamforming techniques are applied in elevation.

A second option, which is the focus of this paper, consists in employing conventional wide swath burst modes acquiring *two looks*. The achieved coverage is the same as the one provided by single-look modes at the expense of a degradation of the azimuth resolution by a factor of two, maintaining, however, the number of looks for a given product resolution. The benefit of this strategy lies on the possibility to exploit spectral diversity techniques [6], [12], improving significantly the sensitivity to azimuth surface displacements. This approach can also be understood from a geometrical point of view in that two LOSs are almost simultaneously obtained [13] using a single platform. The concept of this innovative acquisition mode, which exploits a single phased-array antenna to record two separated slices of the spectrum, was demonstrated with TerraSAR-X in 2015 employing ScanSAR [14] and in 2016 with TOPS [15]. The focus of this contribution is set on the 2-look TOPS mode, which, besides the known benefits over ScanSAR, allows tuning the sensitivity to the azimuth

Manuscript received December 14, 2018; revised March 6, 2019 and May 2, 2019; accepted May 3, 2019. Date of publication June 13, 2019; date of current version September 25, 2019. TerraSAR-X is supported in part by the German Federal Ministry for Economics and Technology and realized in a public-private partnership between the German Aerospace Center (DLR) and Astrium GmbH. *(Corresponding author: Nestor Yague-Martinez.)*

The authors are with the German Aerospace Center, D-82234 Oberpfaffenhofen, Germany (e-mail: nestor.yague@dlr.de).

Color versions of one or more of the figures in this article are available online at http://ieeexplore.ieee.org.

Digital Object Identifier 10.1109/TGRS.2019.2915797

displacements. In opposition to HRWS techniques, the 2-look mode keeps a low resolution in the azimuth direction, which does not suppose a limitation for geophysical applications, where high spatial resolution is not required.

This paper is structured as follows. Section II introduces the 2-look TOPS mode, illustrating its spectral properties and providing the timeline equations. Two designs are presented: the first, TOPS2, based on the desired azimuth resolution, and the second, TOPS2+, based on a design driven by the azimuth sensitivity. In Section III, the evaluation of the performance of the mode is provided, including the effects of the antenna sweeping, ambiguities, residual scalloping, and interferometric performance. Section IV focuses on the sensitivity that can be achieved for pairs of images and for time series, considering the effect of the troposphere. Some comments related to the ionospheric phase screen are, as well, provided. In Section V, the methodology for the generation of 2-look interferograms, the retrieval of azimuth local displacement for pairs, and the retrieval of the mean azimuth velocity for time series is exposed. Section VI provides experimental results with TerraSAR-X: in the first place, an interferometric pair of acquisitions over the Petermann glacier, Greenland, shows the high potential of the 2-look mode to eliminate phase discontinuities of the InSAR phase for fast-moving sites. The second scenario corresponds to a slow-deforming area over Balochistan, Pakistan. The evaluation of approximately two years of acquisitions demonstrates the capability of the mode to retrieve a postseismic signal with accuracies for the mean azimuth velocity of just a few mm/month.

II. The 2-Look TOPS Mode

The TOPS mode has been designed to illuminate each target by the entire azimuth antenna pattern performing an azimuth scanning. The acquisition takes place by recording bursts of echoes, which correspond to a portion of the synthetic aperture. The beam is switched cyclically in elevation in order to map multiple subswaths and to obtain wide coverage. TOPS overcomes this way the space-varying properties of the azimuth antenna pattern in ScanSAR, which leads to a periodical modulation of the amplitude of the SAR signal (scalloping effect), i.e., the resolution, ambiguity ratio, and noise equivalent sigma zero (NESZ) [5]. In Section II-A, the fundamental reasons for choosing a 2-look mode are provided. In Sections II-B and II-C, the design equations of such approach are provided.

A. Rationale

In order to be able to retrieve a 2-D ground deformation field, at least two LOSs are needed, as proposed in the dual-beam interferometer [16]. This concept achieves sensitivity in the across- and along-track directions by employing two antennas: one mechanically oriented with a certain squint forward and a second one oriented backward. The squint angles of the resulting LOSs are chosen usually symmetric around the zero-Doppler plane. When moving to a classical spaceborne system in which a single phased-array antenna is available, the rotation of the antenna of the TOPS mode can be used, not only to illuminate each target with the whole antenna pattern but also to record each target observed by two separated Doppler frequencies, which corresponds to observe each target on ground with two (varying) LOSs.

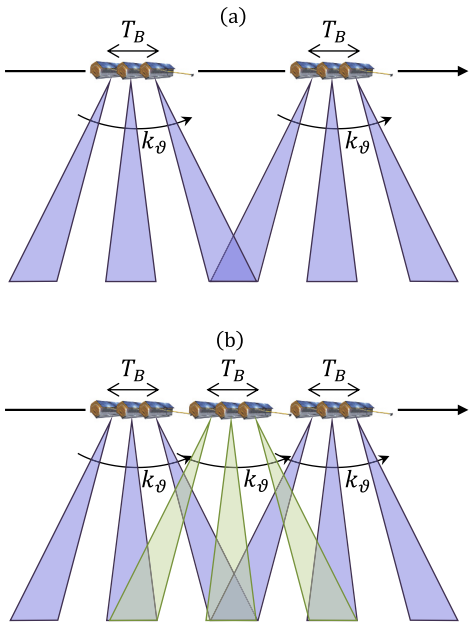

Fig. 1. Schematic operation of a (a) (1-look) TOPS system and a (b) 2-look TOPS system. The antenna is steered in azimuth from backward to forward at a rate k_ϑ. In a 1-look system, each target is observed only once (except eventually at the burst overlapping areas), and a 2-look system allows illuminating each target with two different squint angles.

The combination of the two previous ideas with the TOPS operation mode can be fulfilled by designing the scanning timeline for a 2-look system that achieves two quasi-simultaneous LOSs with spatial diversity. In this section, we restrict the 2-look concept explanation to one subswath, being the extension for several subswaths immediate. Fig. 1 shows the operation mode of a 2-look TOPS system compared with a 1-look TOPS system, henceforth referred as TOPS. In Fig. 1(a), the acquisition of two bursts for a TOPS system is depicted. Employing one look, each target on ground is observed with just one LOS. Fig. 1(b) corresponds to a 2-look system, in which the scanning timeline allows to illuminate each target with two different LOSs.

Unlike the dual-beam interferometer, the 2-look TOPS mode obtains two *time-varying* LOSs; however, the spatial diversity between both remains constant over the acquisition. This can be better understood by comparing the time–frequency diagrams for TOPS and 2-look TOPS shown in Fig. 2. Fig. 2(a) corresponds to the conventional 1-look system, which illustrates the acquisition of two consecutive bursts of the same subswath for a certain range, presenting each target a Doppler rate, k_a. The antenna is rotated in the azimuth direction originating a linear frequency variation of the burst, of duration T_B, at a rate k_{rot}. The SAR processing at zero-Doppler geometry causes that the focused burst, of duration T_{focused}, exhibits a linear frequency variation with a rate k_{t}. The cycle time or interburst time, T_R, is the elapsed time between bursts of

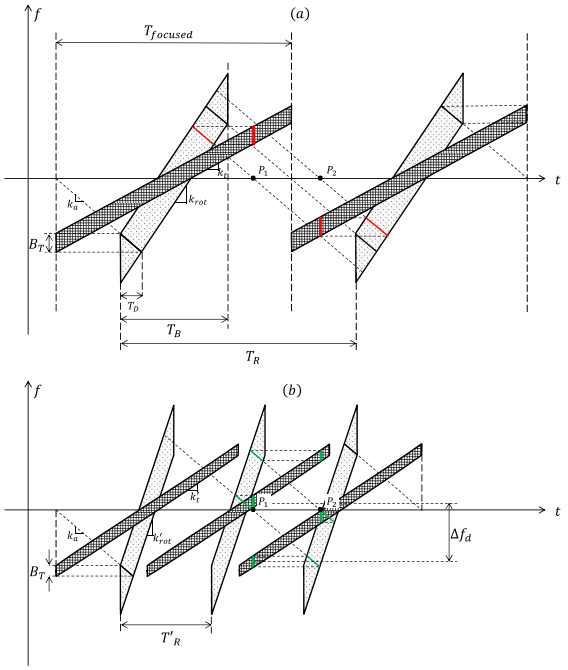

Fig. 2. (a) Time–frequency diagram of a TOPS system, which shows two bursts of the same subswath at a certain range. Each target presents a Doppler rate, k_a. The antenna is rotated in the azimuth direction originating a linear frequency variation of the burst, of duration T_B, at a rate k_{rot}. The SAR processing at zero-Doppler geometry causes that the focused burst, of duration T_{focused}, presents also a linear frequency variation, with rate k_t. The dwell time, T_D, is the time interval in which a target on ground is illuminated with the main lobe and results on a bandwidth B_T. The cycle time or interburst time, T_R, is the elapsed time between bursts of the same subswath. Two targets, P_1 and P_2, are displayed at their zero-Doppler position indicating the portion of the (once) covered raw and focused data Doppler spectra. (b) Time–frequency diagram of a 2-look TOPS system. In this case, the cycle time, T'_R, allows to map each target with two portions of the spectrum as can be seen for both targets.

the same subswath. Two targets, P_1 and P_2, are displayed at their zero-Doppler position indicating the portion of the (once) covered raw and focused data Doppler spectra. Fig. 2(b)refers to a 2-look system, where three bursts are acquired. The cycle time, T'_R, allows to map each target with two portions of the spectra, as can be seen for both depicted targets, P_1 and P_2. Note that a 2-look system records two separated slices of the Doppler spectrum, whose central frequency is azimuth-dependent; however, the spectral separation between looks, Δf_d, is constant over azimuth.

According to the signal processing rationale, the spectral separation for a target on ground between two consecutive bursts (looks) can be exploited to retrieve an accurate estimation of the azimuthal motion. From an interferometric pair, two 1-look interferograms can be generated, which when combined, result in a differential interferogram whose phase is given by [12]

$$\phi_{\text{ESD}}(r,x) = 2\pi \cdot \Delta f_d(r) \cdot \Delta t(r,x) \tag{1}$$

where $\Delta f_d(r)$ is the spectral separation between looks for a given range, r. Note that the spectral separation is independent of the target's azimuth position. $\Delta t(r,x)$ is the local misregistration (in temporal units) intended to be measured. The subscript ESD stands for enhanced spectral diversity and the spectral separation, $\Delta f_d(r)$, can be calculated according to [17]

$$\Delta f_d(r) = \left| \frac{k_{\text{rot}} \cdot k_a(r)}{k_{\text{rot}} - k_a(r)} \right| T_R \tag{2}$$

with $k_a(r)$ being the Doppler rate of a target, located at range r, and $k_{\text{rot}} = \frac{2v_s}{\lambda} k_\theta$ the antenna Doppler rate, where v_s is the platform velocity, λ the wavelength, and k_ϑ the antenna rotation rate. Since $\Delta f_d(r)$ is significantly larger than the spectral separation achievable by taking sublooks of the available bandwidth of a 1-look system (by a factor between 5 and 12 as will be shown in Section IV), the exploitation of both looks allows the retrieval of $\Delta t(r,x)$ with a higher accuracy. We will call, in general, 2-look TOPS to a TOPS system that maps each target on ground with two separated Doppler frequencies. Henceforth, we employ the nomenclature TOPS2 to a 2-look system with a timeline design driven by the azimuth resolution. The timeline equations of the TOPS2 mode are provided in Section II-B. We also propose an optimization of the scanning timeline in terms of achieving a higher sensitivity to the azimuthal motion; we then refer to a 2-look TOPS system with such a scanning timeline, which selects the spectral separation between looks (usually larger than the one achievable by establishing the resolution) as TOPS2+. The design equations of TOPS2+ are presented in Section II-C.

A second issue that can be addressed with the 2-look acquisition concept is related to the burst-mode acquisition nature and its application for the mapping of nonstationary scenarios. The azimuth-varying LOS during the acquisition experiments an abrupt change at the interface between bursts, which originate phase discontinuities in the presence of azimuth misregistration due to, e.g., ground motion. These discontinuities are not to be considered as artifacts but as the result of a different projection of the (same) ground displacement onto the radar LOSs of each look [18]. However, this effect can induce some problems for the later interferometric processing steps, e.g., in case a spatial phase unwrapping is to be performed, and thus it is interesting to perform an accurate local azimuth coregistration exploiting both looks. More details will be given in Sections IV-B and V-A.

B. Scanning Timeline Equations: TOPS2

In the first place, it is convenient to recall the dependence of the TOPS image azimuth resolution with the antenna rotation rate, k_ϑ. The azimuth pattern observed by a point target can be approximated by a sinc function and is given by [5]

$$G_T(\vartheta(t)) \approx G_0 \operatorname{sinc}^2\left(\frac{L v_g t}{\lambda R_0} \cdot \left(1 + \frac{R_0 k_\vartheta}{v_g}\right)\right) \tag{3}$$

where G_0 is a constant, $\vartheta(t)$ is the antenna rotation angle as a function of the time, t, L is the physical azimuth antenna length, v_g is the beam ground velocity, and R_0 is the range of the closest approach.

In the following, we extend our analyses to multisubswath systems indicating with the superscript (n) the n^{th} subswath.

The resulting azimuth resolution, ρ_{az}, is reduced with respect to the StripMap resolution by a factor

$$\alpha^{(n)} = 1 + \frac{R_0^{(n)} k_\vartheta^{(n)}}{v_g^{(n)}} \tag{4}$$

which leads to the azimuth resolution of the TOPS mode

$$\rho_{\text{az}} = \rho_{\text{az}}^{\text{SM}} \cdot \alpha^{(n)} = \frac{\lambda}{2\vartheta_0^{(n)}} \cdot \frac{\left(v_g^{(n)}\right)^2}{\left(v_{\text{eff}}^{(n)}\right)^2} \cdot \left(1 + \frac{R_0^{(n)} k_\vartheta^{(n)}}{v_g^{(n)}}\right) \tag{5}$$

where $\vartheta_0^{(n)}$ is the antenna azimuth bandwidth at -3 dB and $v_{\text{eff}}^{(n)}$ refers to the effective velocity. The superscript SM indicates StripMap mode.

Following the classical approach for the design of an SAR mode driven by the desired resolution, ρ_{az}, the steering parameters for each subswath, n, can be obtained using:

$$k_\vartheta^{(n)} = \left(\frac{2\rho_{\text{az}}\vartheta_0^{(n)}}{\lambda} \frac{\left(v_{\text{eff}}^{(n)}\right)^2}{\left(v_g^{(n)}\right)^2} - 1\right) \frac{v_g^{(n)}}{R_0^{(n)}}. \tag{6}$$

Once the steering rate has been calculated, the global 2-look TOPS scanning timeline can be obtained setting a cycle time, T_R, that allows that the total bandwidth spanned in the burst duration is at least two times larger than the one spanned by a target in the interburst interval. This leads to the equations provided in [5] including a factor 2 multiplying the cycle time

$$\left(k_\vartheta^{(n)} T_B^{(n)} - \vartheta_0^{(n)}\right) R_0^{(n)} + v_g^{(n)} T_B^{(n)} \geq 2 \cdot v_g^{(n)} T_R. \tag{7}$$

As stated in [5], there is a bound on the azimuth resolution, ρ_{az}

$$\rho_{\text{az}} > 2 \cdot \sum_i \rho_{\text{az}}^{\text{SM}\ (i)} \tag{8}$$

with $\rho_{\text{az}}^{\text{SM}\ (n)}$ being the resolution of an equivalent StripMap acquisition for each subswath, n. The factor 2 is again due to the mapping of two looks.

We can see that a 2-look system has a degraded resolution by a factor of two with respect to its equivalent 1-look system. This seems to be a contradiction considering that the looks could be combined at the *SAR processing* stage, following a *full-aperture* processing approach [19] for multilook systems. The impulse response function provided by the latter approach is, however, strongly degraded due to the interference of both looks. Moreover, since our interest, when designing a 2-look system, is to combine the looks at the *interferometric processing* stage, in order to apply spectral diversity techniques, the strategy is to focus each burst (look) separately.

A second consequence of degrading the resolution by a factor of two is that, according to (6), the steering rate is increased by a factor slightly larger than two. Provided that (8) is fulfilled, choosing a finer resolution results in a lower steering rate. This implies that the bursts become longer, spanning the antenna beam to larger maximum steering angles. This fact can be exploited to maximize the spectral separation, as discussed in Section II-C.

C. Alternative Scanning Timeline Equations for Azimuth Sensitivity Enhancement: TOPS2+

The original TOPS mode scanning timeline is obtained by setting the desired azimuth resolution, as usually done. We can, however, modify the design criterion in order to increase the azimuth sensitivity by maximizing the spectral separation, Δf_d, between looks. The latter is achieved by increasing the cycle time, T_R, according to (2). Longer cycle times can be obtained either by enhancing the resolution or by imposing a larger maximum steering angle, equivalently. The design of the timeline based on the maximum steering angle is appropriate for systems employing phased-array antennas, since it allows to control the maximum level of the grating lobe and therefore the level of the azimuth ambiguities.

Once the desired maximum steering angle, $\beta_{\max}$, has been set, we can write the following relation:

$$k_\vartheta^{(n)} = \frac{\Delta\beta}{T_B^{(n)}} \tag{9}$$

where $\Delta\beta = 2 \cdot \beta_{\max}$. Substituting (9) in (7), we obtain the TOPS2+ set of equations

$$\left(\Delta\beta - \vartheta_0^{(n)}\right) R_0^{(n)} + v_g^{(n)} T_B^{(n)} \geq 2 \cdot v_g^{(n)} T_R. \tag{10}$$

By solving this system of equations, the burst durations, $T_B^{(n)}$, are obtained, which establish the steering rates for each subswath, $k_\vartheta^{(n)}$, according to (9). The resulting azimuth resolution is given by

$$\rho_{\text{az}}^{(n)} = \frac{v_g^{(n)}}{B_T^{(n)}} \tag{11}$$

with $B_T^{(n)} = k_a^{(n)} \cdot T_D^{(n)}$ being the target bandwidth for the n^{th} subswath. $T_D^{(n)}$ is its corresponding dwell time given by

$$T_D^{(n)} \approx \frac{R_0^{(n)} \cdot \vartheta_0^{(n)}}{\alpha^{(n)} \cdot v_g^{(n)}}. \tag{12}$$

The maximum steering angle cannot be set arbitrarily, since the azimuth ambiguity level increases with it. Section III provides performance analyses with the two design approaches, considering the effects of sweeping the antenna beam to large steering angles.

III. Mode Performance

This section provides a quantitative analysis of the performance of the 2-look TOPS modes regarding the level of azimuth and range ambiguities, residual scalloping effect, effects of sweeping the antenna to large steering angles, and achievable interferometric performance when combining both looks.

The TerraSAR-X system has been taken as reference, employing two wide beams [20], which achieve a coverage of approximately 100 km. Establishing an SLC azimuth resolution equal to 16.6 m for TOPS2 and applying (6) and (7), we obtain the scanning timeline parameters detailed in Table I, where a maximum steering angle, $\beta_{\max}$, of approximately 0.55° is obtained. We establish, as a matter of example, our maximum steering angle for TOPS2+ to approximately twice

TABLE I
SCANNING TIMELINE PARAMETERS FOR THE TOPS, TOPS2, AND TOPS2+ MODES, USING TWO SUBSWATHS. THE MIDRANGE POSITION OF THE SUBSWATHS HAS BEEN ASSUMED. THE VALUES IN BOLD INDICATE THE DESIGN CRITERIA TO DETERMINE THE ACQUISITION TIMELINE PARAMETERS. AN ADDITIONAL OVERLAP BETWEEN ODD/EVEN BURSTS OF 10% HAS BEEN CONSIDERED FOR THE DESIGN. THE ACHIEVABLE VALUES FOR STRIPMAP ARE INCLUDED FOR REFERENCE. THE PARAMETER b_{SD} INDICATES THE BANDWIDTH THAT CAN BE OBTAINED BY SPLITTING THE DOPPLER SPECTRUM INTO TWO SUBLOOKS FOR STRIPMAP AND TOPS IN ORDER TO APPLY THE SPECTRAL DIVERSITY TECHNIQUE TO MEASURE THE AZIMUTH SHIFT. FOR TOPS2 AND TOPS2+, THERE IS NO NEED TO SPLIT THE SPECTRUM. THE LAST ROW INDICATES THE AMBIGUITY BAND OF THE AZIMUTH SHIFT. THE TERRASAR-X SYSTEM PARAMETERS HAVE BEEN USED

	SM	TOPS	TOPS2	TOPS2+
ρ_{az} [m]	3.3	**8.3**	**16.6**	13.38/15.11
$\beta_{\max}$ [deg]	-	0.501/0.487	0.547/0.532	**1.1**
T_{B} [s]	-	0.834/0.840	0.355/0.358	0.936/0.832
T_{R} [s]	-	1.675	0.71	1.77
k_ϑ [rad/s]	-	0.021/0.020	0.054/0.052	0.041/0.046
Δf_{d} [Hz]	1843	664	3420/3297	8028/7994
B_{T} [Hz]	2765	996	498	618/547
b_{SD} [Hz]	921.67	332	-	-
Amb. band [m]	$\approx \pm 2$	$\approx \pm 5$	$\approx \pm 1$	$\approx \pm 0.5$

that of the TOPS2 mode, i.e., 1.1°. The TOPS2+ timeline parameters are obtained by applying (9) and (10). The parameters for TOPS, assuming 8.3-m resolution, and StripMap are also included for reference. For the latter modes, the spectral diversity technique, i.e., the split of the Doppler bandwidth into two sublooks, can be applied in order to obtain the azimuth shifts. The optimal sublook bandwidths correspond to $b_{\mathrm{SD}} = B_T/3$ [6], which deliver a spectral separation of $\Delta f_d = 2B_T/3$. The corresponding values are included in the table for convenience purposes, since an intermode comparison will be provided in the sensitivity analysis in Section IV.

By comparing the 1-look with the 2-look system parameters from the table, we can extract the following conclusions:

1) The antenna steering rate, k_ϑ, for TOPS2 is a factor slightly larger than two with respect to TOPS due to the (2×) coarser resolution.
2) The fact of steering to larger maximum squint angles (TOPS2+) does not have a negative impact on the SLC resolution as long as the condition imposed by (8) is fulfilled. The antenna steering rate becomes smaller than for TOPS2 due to the fact that the bursts become longer when steering the antenna beam to larger maximum squint angles.
3) The unambiguous range of the azimuth shifts that can be retrieved is given by $\pm v_g/(2\Delta f_d)$, in meter units. Due to the higher sensitivity of TOPS2+, the ambiguity band is smaller, as indicated in the last row of Table I, so that ϕ_{ESD} might be wrapped if the motion gradient is large.

A. Effects of Sweeping the Antenna Beam to Large Steering Angles

When working with phased-array antennas, the maximum steering angle cannot be set arbitrarily large since the level of the azimuth ambiguities increases [21], [22]. The largest contribution to the azimuth ambiguities' level is due to the so-called grating lobes, which are the periodic repetitions of the main lobe. The sinc modulation effect of the antenna element pattern (EP) tapers the level of the grating lobes, making significant only the first one.

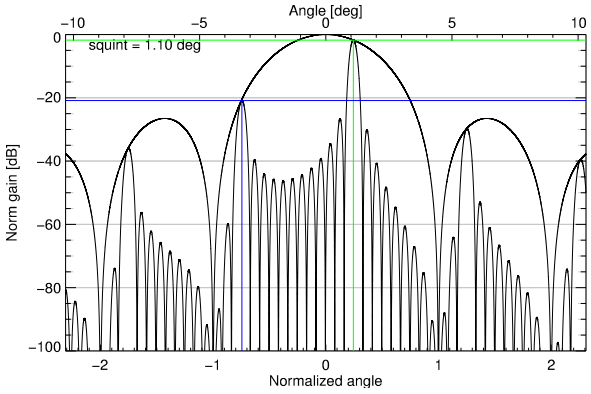

Fig. 3. EP and DP for a steering angle of 0.246 (normalized to the first null position of the EP) equivalent to 1.1° using the TerraSAR-X antenna panel.

In order to illustrate the relationship between main and grating lobes when introducing a steering angle, Fig. 3 shows the directivity pattern (DP) and EP for a squint angle of 1.1°, equivalent to a normalized (to the first null position of the EP) angle equal to 0.246. The plot has been generated by means of a numerical simulation employing the sinus cardinalis function according to the TerraSAR-X antenna dimensions, the number of elements, and wavelength, as detailed in Table II. We can see that for this squint, the level of the grating lobe is higher than that of the first sidelobe. The limiting parameter for setting the maximum steering angle will be given by the requirement value for the ambiguity-to-signal ratio (ASR). Sections III-B and III-C provide a discussion on the maximum steering angle and optimal pulse repetition frequency (PRF) selection.

The larger steering excursion of TOPS2+ with respect to TOPS or TOPS2 has some additional consequences related to the modulation effect of the EP of the antenna. The first one is related to a stronger SNR variability over azimuth. This effect is further analyzed in Section III-D and is taken into account for the performance evaluation in Section IV.

The second effect of the EP modulation is the (squint-dependent) shift introduced to the position of the main lobe of the DP in the azimuth direction. This has a (small) impact on the actual pointing direction and consequently, on the spectral separation between looks. The larger the squint angle, the larger the Doppler shift. In Fig. 4, a numerical evaluation of the pointing shift is shown for the range of squint angles of TOPS2+. The maximum pointing shift is equal to 0.008° and corresponds to the maximum squint of 1.1°, or equivalently 68-Hz Doppler shift for a Doppler of about 9.4 kHz. For comparison, in case of TOPS2, the maximum squint angle is about 0.55°, equivalent to a maximum Doppler of 4.7 kHz, and the maximum mispointing is approximately 0.004°, equivalent to about 32 Hz. The Doppler shift relative

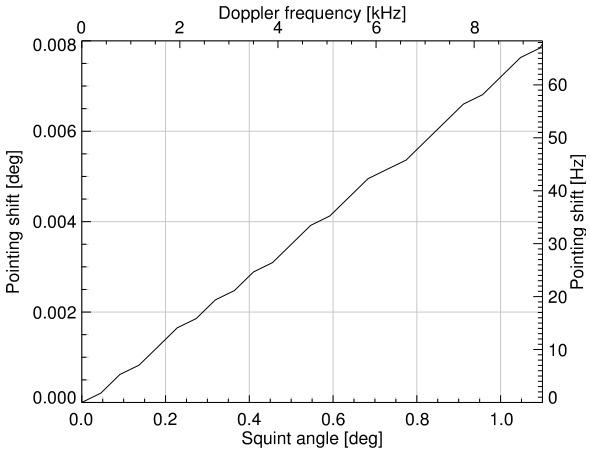

Fig. 4. Pointing shift due to the EP modulation effect for the TerraSAR-X system.

TABLE II
TERRASAR-X PARAMETERS

Wavelength (λ)	0.031 m
Orbit height	514 km
Orbital repeat cycle	11 days
Antenna dimension in azimuth (L)	4.784 m
Number of elements in azimuth	12
Number of azimuth beams	249
StripMap bandwidth (PBW_0)	2765 Hz

to the Doppler frequency is approximately 0.7%. Although the impact is small for interferometric applications, an effective antenna Doppler rate, $k_{\mathrm{rot}}^{\mathrm{eff}}$, can be easily computed and employed during the SAR Processing.

B. Azimuth Ambiguities, Maximum Steering Angle, and PRF Selection

The limiting factor to the largest steering is due to the level of the azimuth ambiguities, as a consequence of sampling the Doppler spectrum at a frequency PRF. The largest contribution to the azimuth ambiguities level is due to the grating lobe; therefore, if we just consider it, the optimal PRF can be selected so that the digital frequency of the grating lobe is equal to 0.5, i.e., the edge of the Doppler band. Following this strategy, a significant part of the energy from the grating lobe will fall outside the processing bandwidth. This condition can be written as

$$\frac{f_{\mathrm{GL}}}{\mathrm{PRF}_k} = \frac{1}{2} + k, k \in \mathbb{N} \tag{13}$$

where f_{GL} is the Doppler frequency at which the maximum of the grating lobe is located and k accounts for the periodicity of the spectrum of the sampled signal. Since the angular separation between the main lobe and the first grating lobe can be approximated for relatively small angles by λ/d, where d is the distance between antenna elements in the azimuth direction, the frequency of the grating lobe can be written as

$$f_{\mathrm{GL}} \approx \frac{2v_s}{\lambda}\left(\sin(\beta) + \sin\left(\frac{\lambda}{d}\right)\right) \tag{14}$$

with β being the squint angle.

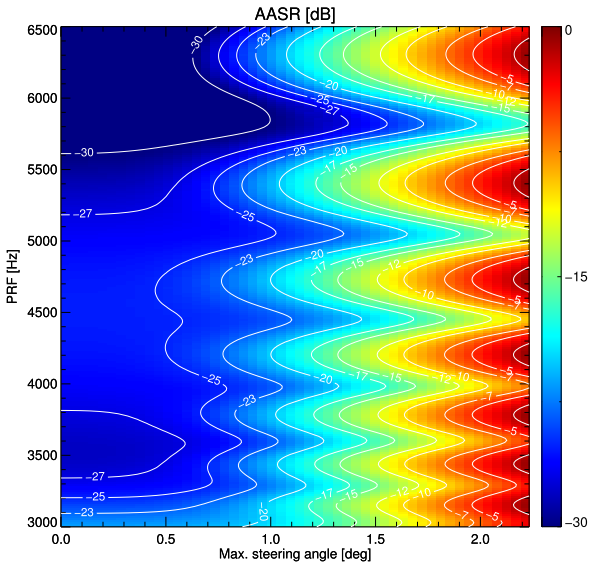

Fig. 5. AASR diagram for a set of PRFs and squint angles. It can be appreciated that, in general, the higher the squint angle, the higher the AASR level; however, the oscillating behavior of the AASR with the PRF indicates the possibility to select a set of optimal PRFs.

The set of PRFs which minimize the azimuth ambiguity from the first grating lobe is given by

$$\mathrm{PRF}_k = \frac{\frac{2v_s}{\lambda}\left(\sin(\beta_{\max}) + \sin\left(\frac{\lambda}{d}\right)\right)}{k + \frac{1}{2}}, \quad k \in \mathbb{N} \tag{15}$$

where note that the maximum squint angle, $\beta_{\max}$, is employed, since the grating lobe reaches its highest level for the maximum steering.

Equation (15) provides an approximation for the optimal PRF, since it only accounts for the first grating lobe and is also inaccurate when the maximum sweeping angles increase.

A more precise value for the optimal PRF can be obtained by numerically computing the integrated azimuth-ambiguity-to-signal ratio (AASR) according to the following expression:

$$\mathrm{AASR} \approx \frac{\sum_{\substack{k=-\infty \\ k\neq 0}}^{\infty} \int_{-B_a/2}^{B_a/2} W(f_d)\cdot G_a^2(f_d + k\cdot \mathrm{PRF})\cdot \mathrm{d}f_d}{\int_{-B_a/2}^{B_a/2} W(f_d)\cdot G_a^2(f_d)\cdot \mathrm{d}f_d} \tag{16}$$

where B_a is the azimuth processing bandwidth, $W(f_d)$ is the sidelobe suppression weighting function applied during processing, and $G_a^2(f_d)$ is the two-way far-field azimuth antenna power pattern. Fig. 5 shows the result of the computation presented as a 2-D map for a range of PRFs and squint angles. A processing bandwidth of 2765 Hz has been considered and a generalized Hamming tapering window with $\alpha = 0.6$ applied to the Doppler spectrum. Fig. 6 shows three profiles of the AASR for the case of no squint (StripMap-like), a squint $= 0.5°$ (TOPS or TOPS2), and a squint $= 1.1°$ (TOPS2+). There is an oscillating behavior of the AASR for TOPS2+ with the PRF, having several local minima in which the energy of the ambiguities is minimized. The selection

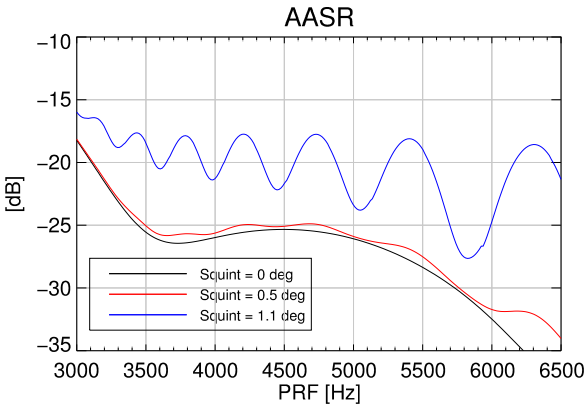

Fig. 6. AASR plot as a function of the PRF for the case of nonsquinted beam (StripMap), a squint of 0.5° (TOPS or TOPS2), and a squint of 1.1° (TOPS2+). The curves of StripMap and TOPS/TOPS2 present a very similar behavior and level, whereas the TOPS2+ curve presents a higher AASR and an oscillating behavior, having some minima for certain PRFs, in which the energy of the ambiguities is minimized. These sampling frequencies should be exploited for an optimal PRF selection.

of the PRF is, however, also restricted by the desired swath width $W_s < \frac{c_0}{2\text{PRF}}$ and the ASR. In order to account for these parameters, analyses, including the range ambiguities, are provided in Section III-C.

C. Range Ambiguities

A second constraint to limit the sampling of the Doppler spectrum with a high PRF is given by the range ambiguities [23]. The range-ambiguity-to-signal-ratio (RASR) can be obtained by considering the acquisition geometry, antenna pattern, and scattering models. The optimal PRF in terms of ambiguities will be given by the one which minimizes the ASR, result of combining RASR and AASR.

Fig. 7 shows the curves of the RASR, AASR, and ASR for the TerraSAR-X wide004 beam (look angle at midrange = 30.3°) in the case of using StripMap, TOPS2, and TOPS2+. The scatterer model for soil and rock from [24] has been used for this computation. The location of the ASR local minima is indicated along with the ASR level. The difference of the AASR between StripMap and TOPS2 is almost negligible. The ASR curve for the TOPS2+ mode shows larger deviations due to the oscillating behavior of the AASR with the PRF.

Table III summarizes the ambiguities' parameters for StripMap, TOPS2 and TOPS2+ for each TerraSAR-X wide beam. The ASR is indicated along with its corresponding PRF, which moreover establishes the largest coverage. The level of ASR is located, on average, at −25.66 dB for the TOPS2 mode and at −21.1 dB for TOPS2+. From these analyses, we conclude that TOPS2+ achieves a spectral separation, which is approximately twice as large as for TOPS2, at the expense of an ASR degradation of 4.5 dB. The maximum swath width for TOPS2+ is marginally narrower than that for TOPS2.

One option to reduce the azimuth ambiguities' level consists in processing a narrower Doppler bandwidth, B_a, at the

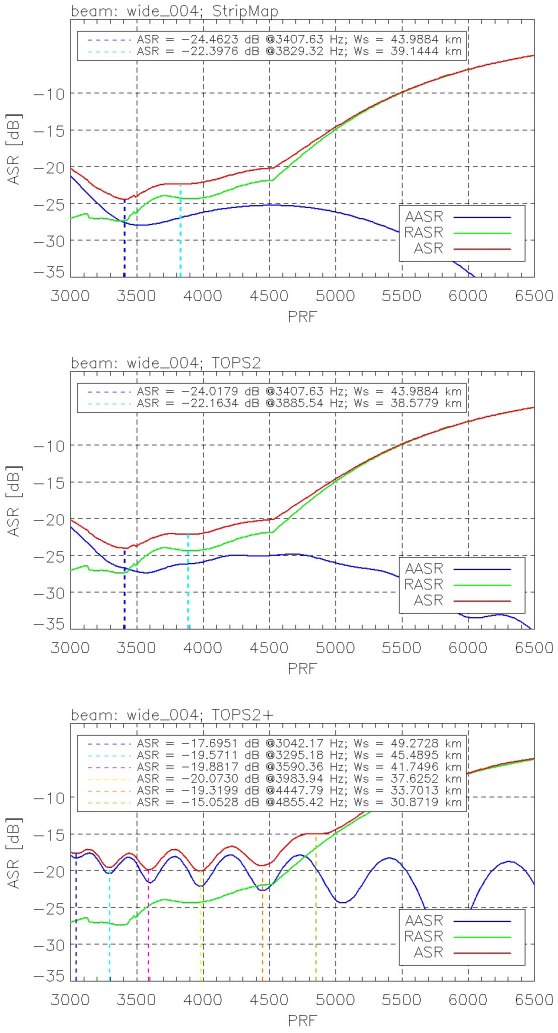

Fig. 7. AASR, RASR, and ASR as a function of the PRF for (Top) StripMap mode, (Middle) TOPS2 mode, and (Bottom) TOPS2+ mode. The TerraSAR-X beam wide004 (look angle at midrange = 30.3°) has been employed.

expense of azimuth resolution. For the sake of illustration, Table III includes the values of the ASR for the TOPS2+ mode when a 70% of the available bandwidth is processed, along with its gain with respect to a full processing bandwidth approach. The gain is, on average, around 1 dB. If stringent requirements on the ASR are to be fulfilled and/or the azimuth resolution shall not be degraded, the maximum squint angle of TOPS2+ can be relaxed.

D. Residual Scalloping Effect and Combination of Looks

The major aim of the TOPS mode is to solve the problem of scalloping and azimuth varying ambiguities present in ScanSAR [5]. However, due to the EP modulation effect, some residual scalloping is still present. The larger the squint angles, the larger the scalloping effect. Fig. 8 shows the evolution of the normalized intensity during the acquisition of one burst for TOPS2 and TOPS2+, according to the steering rates from Table I. The horizontal axis indicates the azimuth time.

TABLE III

ASR, PRF, AND MAXIMUM WIDE SWATH, $W_s^{\max}$, FOR STRIPMAP, TOPS2, TOPS2+, AND TOPS2+ PROCESSING 70% OF THE AVAILABLE DOPPLER BANDWIDTH. THE LAST COLUMN INDICATES THE GAIN IN THE ASR WHEN PROCESSING THE REDUCED BANDWIDTH WITH RESPECT TO THE FULL BANDWIDTH FOR THE TOPS2+ MODE. THE AZIMUTH RESOLUTION OF THE FIRST SUBSWATH, SS_1, IS INDICATED

Beam	StripMap $\rho_{\mathrm{az}} = 3.3m$			TOPS2 $\rho_{\mathrm{az}}^{SS_1} = 16.6m$			TOPS2+ $\rho_{\mathrm{az}}^{SS_1} = 13.38m$			TOPS2+ (PBW $= 0.7\mathrm{PBW}_0$) $\rho_{\mathrm{az}}^{SS_1} = 18.38m$			$\Delta\mathrm{ASR}_{\mathrm{TOPS2+}}^{\mathrm{PBW}}$
	ASR[dB]	PRF[Hz]	$W_s^{\max}$[km]	ASR[dB]	PRF[Hz]	$W_s^{\max}$[km]	ASR[dB]	PRF[Hz]	$W_s^{\max}$[km]	ASR[dB]	PRF[Hz]	$W_s^{\max}$[km]	[dB]
001	-27.91	3534.14	42.41	-27.31	3562.25	42.08	-21.59	3604.42	41.58	-22.91	3604.42	41.58	1.32
002	-27.70	3520.08	42.58	-27.11	3562.25	42.08	-21.54	3604.42	41.58	-22.84	3604.42	41.58	1.30
003	-27.91	3534.14	42.41	-27.31	3562.25	42.08	-21.59	3604.42	41.58	-22.91	3604.42	41.58	1.32
004	-24.46	3407.73	43.99	-24.02	3407.63	43.99	-20.07	3983.94	37.63	-21.07	3281.12	45.68	1.00
005	-24.36	3491.97	42.93	-24.02	3520.08	42.56	-20.36	3590.36	41.75	-21.33	3590.36	41.75	0.97
006	-27.59	3534.14	42.41	-26.99	3562.25	42.08	-22.02	3983.94	37.62	-22.89	3983.94	37.62	0.87
007	-27.53	3562.25	42.08	-26.99	3562.25	42.08	-21.85	3983.94	37.62	-22.78	3604.42	41.58	0.93
008	-24.42	3674.70	40.79	-24.15	3604.42	41.58	-21.11	3983.94	37.62	-21.81	3969.88	37.76	0.70
009	-24.79	3506.02	42.75	-24.41	3520.08	42.56	-20.55	3604.42	41.56	-21.58	3590.36	41.75	1.03
010	-24.79	3449.80	43.45	-24.32	3449.80	43.45	-19.83	3590.36	41.75	-21.34	3281.12	45.68	1.51

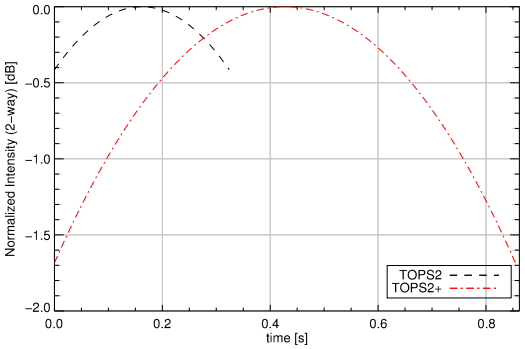

Fig. 8. Scalloping evaluation plot for TOPS2 and TOPS2+ modes. The normalized intensity is plotted during the acquisition of a single burst.

TOPS2 presents a maximum decay of 0.36 dB, whereas TOPS2+ has a decay of 1.76 dB.

We enumerate in the following the way to combine the looks. Since our case of interest corresponds to scenes over land, we assume a scenario characterized by distributed targets. The speckle noise can be modeled as a complex signal, whose in-phase and quadrature components are independent and identically distributed zero-mean Gaussian variables. The benefit of combining the looks is threefold.

1) On the one hand, the differential interferogram between the interferograms of the looks provides an enhanced measurement of the azimuth shift that can be considered a product by itself, but moreover aids to the across- and along-track decoupling procedure, supporting the spatial phase unwrapping of interferograms.
2) Second, the looks can be combined at the interferometric processing stage in order to obtain the 2-look interferogram, i.e., the coherent sum of the complex interferograms of each look. When performing this operation, the standard deviation of the interferometric phase is expected to be reduced by a factor $\sqrt{2}$.
3) The third benefit is the capability to reduce the speckle noise of the intensity image by applying an incoherent (spectral) multilooking, i.e., by averaging the intensities of each look.

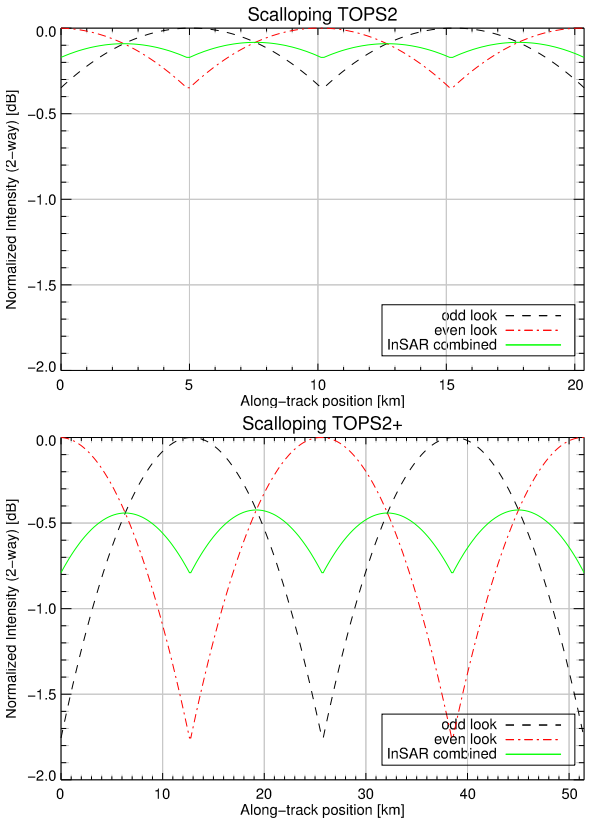

Fig. 9. Normalized intensity for the odd and even bursts and for the resulting interferogram when both looks are combined. (Top) Values for TOPS2. (Bottom) Values for TOPS2+.

Moreover, since the TOPS mode varies progressively the LOS, and considering that odd and even bursts are interleaved in the time–frequency domain, according to the acquisition timeline (see Fig. 2), there is an additional benefit when combining both looks since SNR losses and azimuth ambiguities present, for a given target, different levels for each look, resulting in an equalization of both parameters.

Fig. 9 shows this fact for the SNR losses. Fig. 9 (top) is related to the TOPS2 mode and shows the normalized intensity for two bursts of the odd looks and for two bursts

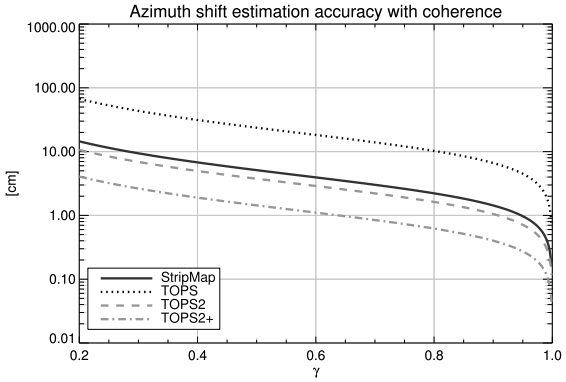

Fig. 10. Azimuth shift standard deviation for StripMap, TOPS, TOPS2, and TOPS2+ systems as a function of the coherence. The output product resolution has been set to 100 m × 100 m.

of the even looks according to their along-track ground position. If the interferograms of each look are averaged, the resulting interferogram experiments an equalization, being the scalloping reduced from 0.36 to 0.07 dB. Fig. 9 (bottom) corresponds to TOPS2+; in this case, the scalloping amplitude is reduced from 1.76 to 0.4 dB, which is very close to the TOPS case.

IV. Sensitivity Analysis

The accuracy that can be obtained with the 2-look TOPS modes to derive azimuth displacements is provided in Section IV-A and depends on several factors, being the spectral separation between looks, bandwidth, and interferometric coherence the most relevant. In order to compare the performance of different modes, other factors, such as SNR losses and ambiguities, have to be considered. The performance of the decoupling between along-track and LOS directions is provided in Section IV-B. Sections IV-C and IV-D include the consideration of tropospheric and ionospheric effects, respectively.

A. Azimuth Shift Accuracy

The estimation error of the azimuth shift, Δx, (in meter units) can be written combining (1) and the standard deviation of the differential phase between the interferograms of both looks, $\sigma_{\phi_{\text{ESD}}}$. Assuming that the number of independent samples, N, is large, we can make use of the asymptotic phase noise expression of [25], obtaining

$$\sigma_{\Delta x} = \frac{\sigma_{\phi_{\text{ESD}}}}{2\pi\,\Delta f_d} v_g = \frac{1}{2\pi\,\Delta f_d \sqrt{N}} \frac{\sqrt{1-\gamma^2}}{\gamma} v_g \tag{17}$$

where γ is the interferometric coherence.

The plot of the accuracies in the retrieval of the azimuth mutual shift between two images, for TOPS, TOPS2, and TOPS2+ with a maximum steering angle of 1.1°, is shown in Fig. 10, as a function of the coherence. The curves have been generated taking into account the spectral separation between looks, bandwidths, and establishing an output product resolution of 100 m × 100 m.

If we define the relative variance between each mode and the reference mode, and StripMap (SM) as

$$\rho = 10 \cdot \log_{10} \frac{\sigma^2_{\Delta x}}{\sigma^{\text{SM}\,2}_{\Delta \text{x}}} = 10 \cdot \log_{10} \frac{\left(\Delta f_d^{\text{SM}}\right)^2 \cdot B_T^{\text{SM}}}{\Delta f_d^2 \cdot B_T} \tag{18}$$

we obtain that the performance of TOPS is 13.3 dB worse than the StripMap one, whereas the TOPS2 mode is 2.7 dB better. In the case of TOPS2+, with a maximum steering angle of 1.1°, the gain becomes 11 dB. Since it can be very abstract for the reader to speak in terms of dB when comparing accuracies, we can equivalently say that the standard deviation of a TOPS mode is 4.6 times worse than that for Stripmap. Regarding TOPS2 and TOPS2+, the standard deviations are 0.73 and 0.28 times the StripMap one, respectively. The gain of the TOPS2+ mode with respect to conventional TOPS is 24.3 dB, which translates into a standard deviation 16.5 times smaller.

The interferometric coherence would, however, diverge among the modes, since each mode is unequally affected by ambiguities and SNR losses. In order to account for these effects, the accuracy analysis can be done as a function of the backscattering coefficient. Thus, we model the total coherence, γ, as follows:

$$\gamma = \gamma_{\text{temp}} \cdot \gamma_{\text{SNR}} \cdot \gamma_{\text{amb}} \tag{19}$$

where γ_{temp} is the temporal coherence and γ_{SNR} and γ_{amb} represent the error contribution due to a limited SNR and ambiguity ratio, respectively. The SNR can be written as

$$\text{SNR} = \frac{\sigma_0}{10^{\frac{(\text{NESZ}-\text{SNR}_{\text{loss}})}{10}}} \tag{20}$$

with σ_0 being the normalized backscattering coefficient, NESZ, in dB, and SNR_{loss} the maximum losses in the SNR due to the modulation effect of the antenna EP when introducing a steering, also in dB.

The limited SNR produces a coherence loss, being the resulting coherence [26]

$$\gamma_{\text{SNR}} = \frac{1}{1+\text{SNR}^{-1}}. \tag{21}$$

As detailed in Section III-D, the scalloping effect introduces a maximum SNR loss of 0.36 and 1.76 dB for TOPS2 and TOPS2+, respectively.

The error introduced by distributed ambiguities can be approximately modeled as Gaussian noise, whose contribution to the coherence loss is given by

$$\gamma_{\text{amb}} = \frac{1}{1+\text{AASR}} \cdot \frac{1}{1+\text{RASR}}. \tag{22}$$

The coherence penalization due to ambiguities will be different among the swaths, in average, $\gamma_{\text{amb}} > 0.996$ for TOPS2 and $\gamma_{\text{amb}} > 0.989$ for TOPS2+.

Taking into account the mentioned losses, we obtain the performance curves of Fig. 11 as a function of the backscattering coefficient, where a NESZ of −25 dB has been assumed. Since the dependence of the standard deviation with the coherence is not linear, we consider the case of high (0.8) and low (0.2) temporal coherences. For both cases, it can be

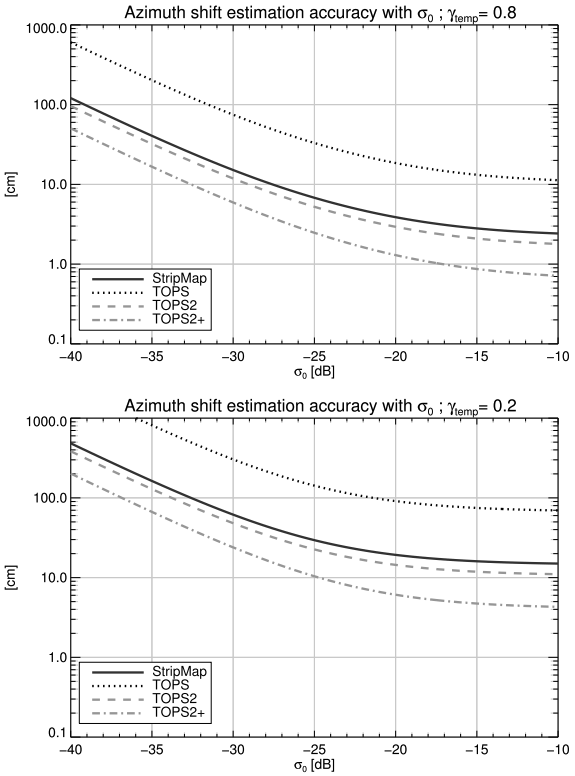

Fig. 11. Azimuth shift standard deviation for StripMap, TOPS, TOPS2, and TOPS2+ systems for a common output product resolution of 100 m × 100 m as a function of the backscattering coefficient. (Top) High temporal coherence (0.8). (Bottom) Low temporal coherence (0.2). A NESZ of −25 dB has been assumed.

appreciated that the StripMap and TOPS2 curves get closer due to the residual scalloping and slightly larger azimuth ambiguities of TOPS2; however, the latter is still better than StripMap. In spite of the larger SNR losses and greater azimuth ambiguities of TOPS2+, it still provides the best performance. When comparing the curves for high and low coherence, it can be concluded that the accuracy saturates with the backscattering coefficient more significantly for low temporal coherence than for high values. In Section IV-C, the effect of the turbulent troposphere is also taken into account, where the 2-D and 3-D achievable performances are, as well, provided.

B. Decoupling—Across-Track Phase Accuracy

The phase of the interferogram of each look, $\phi_{\text{look } i}$, contains, apart from the topographic phase, the contribution of the ground displacement vector, $\vec{g}$, measured in the LOS of each look, $\widehat{e}_{\text{los } i}$, which is given by [18]

$$\begin{aligned}\phi_{\text{look } i} &= \frac{4\pi}{\lambda} < \widehat{e}_{\text{los } i}, \vec{g} > \\ &= \phi_{\text{XT } i} + \phi_{\text{AT } i}, i = 1, 2\end{aligned} \tag{23}$$

where $\phi_{\text{XT } i} = \frac{4\pi}{\lambda}\Delta R_0$ is the contribution to the interferometric phase in the across-track direction, with ΔR_0 being the projection of the ground displacement on the zero-Doppler plane; and $\phi_{\text{AT } i}(t) = 2\pi \cdot f_{d\ i}(t) \cdot \Delta t$ is the additional phase due to the displacement in the along-track direction, Δt, with $f_{d\ i}(t)$ being the instantaneous Doppler frequency for each look, i.

A decoupling of the displacement in the across- and along-track directions can be carried out by combining the phases of both looks. In the following, we analyze the phase noise in the interferometric phase after removing the contribution of the along-track deformation estimated with ESD. The phase noise related to the azimuth component of the deformation is given by

$$\sigma_{\phi_{\text{AT}}}(t) = 2\pi \cdot f_d(t) \cdot \sigma_{\Delta t} \tag{24}$$

where $\sigma_{\Delta t}$ is given by (17), after dividing by v_g. The worst case corresponds to the largest Doppler centroid, given at the burst edges. For a 2-look system, this maximum is approximately equal to the spectral separation between looks, i.e., $f_d^{\max}(t) = \Delta f_d$. Therefore, from (17) and (24), the largest phase noise can be written as

$$\sigma_{\phi_{\text{AT}}} = \frac{1}{\sqrt{N_{\text{ESD}}}} \frac{\sqrt{1-\gamma^2}}{\gamma} \tag{25}$$

where N_{ESD} corresponds to the effective number of looks to estimate the ESD phase.

The standard deviation of the across-track phase for each look can be written as

$$\begin{aligned}\sigma_{\phi_{\text{XT } i}} &= \sqrt{\sigma^2_{\phi_{\text{look } i}} + \sigma^2_{\phi_{\text{AT } i}}} \\ &= \sqrt{\frac{1}{2N} + \frac{1}{N_{\text{ESD}}}} \frac{\sqrt{1-\gamma^2}}{\gamma}\end{aligned} \tag{26}$$

where N is the spatial multilooking factor of the interferograms of each look. After applying the same multilook to both looks and to the ESD phase, removing the along-track component from each look, and averaging them, the standard deviation of the final across-track phase results in

$$\sigma_{\phi_{\text{XT 2-look}}} = \frac{\sigma_{\phi_{\text{XT } i}}}{\sqrt{2}} = \sqrt{\frac{3}{2}}\sigma_{\phi_{\text{look } i}}. \tag{27}$$

By increasing the ESD multilooking by a factor 2, i.e., $N_{\text{ESD}} = 2N$, the standard deviation of the across-track phase results in the standard deviation of the phase of each look, i.e., $\sigma_{\phi_{\text{XT 2-look}}} = \sigma_{\phi_{\text{look } i}}$. Note that this extra multilook reduces the resolution of the along-track deformation product by this same factor when compared to the across-track one; however, this resolution loss does not play, in general, a big role.

C. 2-D and 3-D Performance—Consideration of Tropospheric Effects

In the following, the expected 2-D (LOS and azimuth) and 3-D (combining acquisitions in ascending and descending geometries) performances, including the influence of the turbulent troposphere, are presented.

The signal delay induced by the troposphere has been already characterized in the literature in the radar LOS, when employing interferometric techniques [27]. The effect of the

turbulent troposphere, also known as atmospheric phase screen (APS), can be modeled, in that direction, as a noise source of a certain power, $\sigma^2_{\text{tropo,LOS}}$. When 2-look data are exploited to obtain the displacement in the azimuth direction, two repeat-pass interferograms are available, containing each of them almost the same tropospheric delay because of the small temporal and spatial baseline between looks. This fact has already been observed in [13] in the case of splitting the Doppler spectrum of StripMap images. In [28], a quantitative analysis for the case of simultaneous squinted SAR acquisitions with two or more platforms can be found.

In our particular scenario, we have a single platform employing 2-look modes in repeat-pass configuration. Since the acquisition of both looks is not simultaneous, an effective along-track baseline is present. From Table I, we obtain a cycle time of 0.71 s for TOPS2 and 1.77 s for TOPS2+, which is equivalent to an effective along-track baseline (at the height of the satellite) of 5.48 and 13.95 km, respectively. However, the relevant baseline is the one located at the height of the atmospheric boundary layer, i.e., the portion of the troposphere responsible for the turbulence, which can be assumed to be at a height of approximately 1 km. At this height, the LOSs of each look are separated by 6.78 and 16.81 m, respectively. The slightly different tropospheric delays experienced by the signal in both LOSs are thus very small. The standard deviation of the tropospheric noise in the along-track direction (in meter units) is given by

$$\sigma_{\text{tropo,AT}} = \frac{2\sqrt{2\tilde{R}(\Delta l)}v_g}{\lambda \Delta f}\sigma_{\text{tropo,LOS}} \tag{28}$$

where $\tilde{R}(\Delta l)$ is the normalized autocorrelation function of the turbulent troposphere evaluated at the along-track baseline between the LOSs at the height of the turbulent troposphere, Δl. The autocorrelation function can be computed from the power spectrum of the turbulent troposphere, which can be modeled following Kolmogorov's power law [27], [28]. By evaluating the (conservative) autocorrelation function assumed in [28] for the along-track baselines corresponding to TOPS2 and TOPS2+ and considering a power of the turbulent troposphere in the LOS, $\sigma^2_{\text{tropo,LOS}} = 1\text{cm}^2$, we obtain that the standard deviation of the tropospheric noise in the along-track direction is 1.41 cm for TOPS2 and 1.35 cm for TOPS2+. There is no degradation, in terms of tropospheric perturbations, of TOPS2+ with respect to TOPS2 when retrieving azimuth shifts. The smaller correlation between LOSs of the latter is compensated with its larger spectral separation between looks, according to (28).

The effect of the turbulent troposphere in the along-track direction is, therefore, of similar order of magnitude than in the LOS (for the assumed conservative autocorrelation function). This is due to a noise upscaling effect, as a consequence of the small angular diversity between the two looks. The performance for retrieving azimuth shifts in a real scenario implies the consideration of temporal decorrelation effects, where we will be able to determine which effect, temporal decorrelation or tropospheric noise, prevails. We make use of the hybrid Cramér–Rao bound (HCRB) for the crustal displacement field estimator provided in [29] and model the turbulent troposphere according to [28] with a power, $\sigma^2_{\text{tropo,LOS}} = 1\ \text{cm}^2$.

In order to provide the performances that are achieved when working with pairs and stacks of images, we employ an exponential decorrelation model [30] with a time constant of 40 days and a long-term coherence of 0.1. The output product resolution has been set to 100 m $\times$ 100 m, which supposes 998 equivalent number of looks.

1) InSAR Pairs: Fig. 12 (top) shows the 2-D performance curves, i.e., across- and along-track, in case of using pairs of images according to the temporal baseline for the TOPS2 (left) and TOPS2+ (right) modes. The achievable accuracies are plotted including tropospheric effects and without its consideration. Fig. 12 (middle) shows the degradation of the accuracies due to the noise introduced by the troposphere. Regarding the performance in the along-track direction, we can see that for small temporal baselines (high coherence), the noise introduced by the troposphere dominates over temporal decorrelation effects. A few cycles later, the degradation introduced by the troposphere becomes negligible, as the quotient between the accuracies with and without troposphere tends to 1. From the plots of the degradation introduced by the troposphere, it seems that TOPS2+ is worse than TOPS2 in along track; however, it is a matter of the better sensitivity of TOPS2+ to displacements, which produces a larger ratio between tropospheric and temporal decorrelation effects. Observe that the final performance of TOPS2+ is better than TOPS2. Regarding the performance in across-track direction, the level of noise introduced by the troposphere is much greater than the noise due to temporal decorrelation effects. Fig. 12 (bottom) shows the 3-D performance when combining an ascending and a descending pair. Look angles of 30° have been assumed for both geometries with the orbit heading angles of 12° and 168°, respectively. The improvement in the N-S direction is evident for TOPS2+. Moreover, the performance in the vertical direction improves, benefited by the better estimation in along track. We can see that the sensitivity is, in general, better for the E-W and vertical directions; however, for small temporal baselines, the performances are closer for all three directions.

2) Time Series: In case of working with stacks of images, we are interested in obtaining the performance curves of the mean deformation velocities. Fig. 13 (top) shows the accuracies in range (across-track) and along-track directions as a function of the number of images employed, assuming that an image is acquired every repetition cycle (11 days). As for the cases of using pairs, the curves, including tropospheric effects and without its consideration, are provided. Fig. 13 (middle) shows the degradation of the accuracies due to the troposphere. Similar conclusions to the case of pairs of images can be drawn for the along-track direction: the noise introduced by the troposphere dominates over temporal decorrelation effects for very short stacks ($<$10 images). The effect of the troposphere becomes rapidly negligible when increasing the number of images (quotient $=$ 1). The tropospheric noise seems to be slightly larger for TOPS2+ than for TOPS2; this apparent behavior is not true, being the reason the better sensitivity of TOPS2+ to azimuth displacements, which produces that the

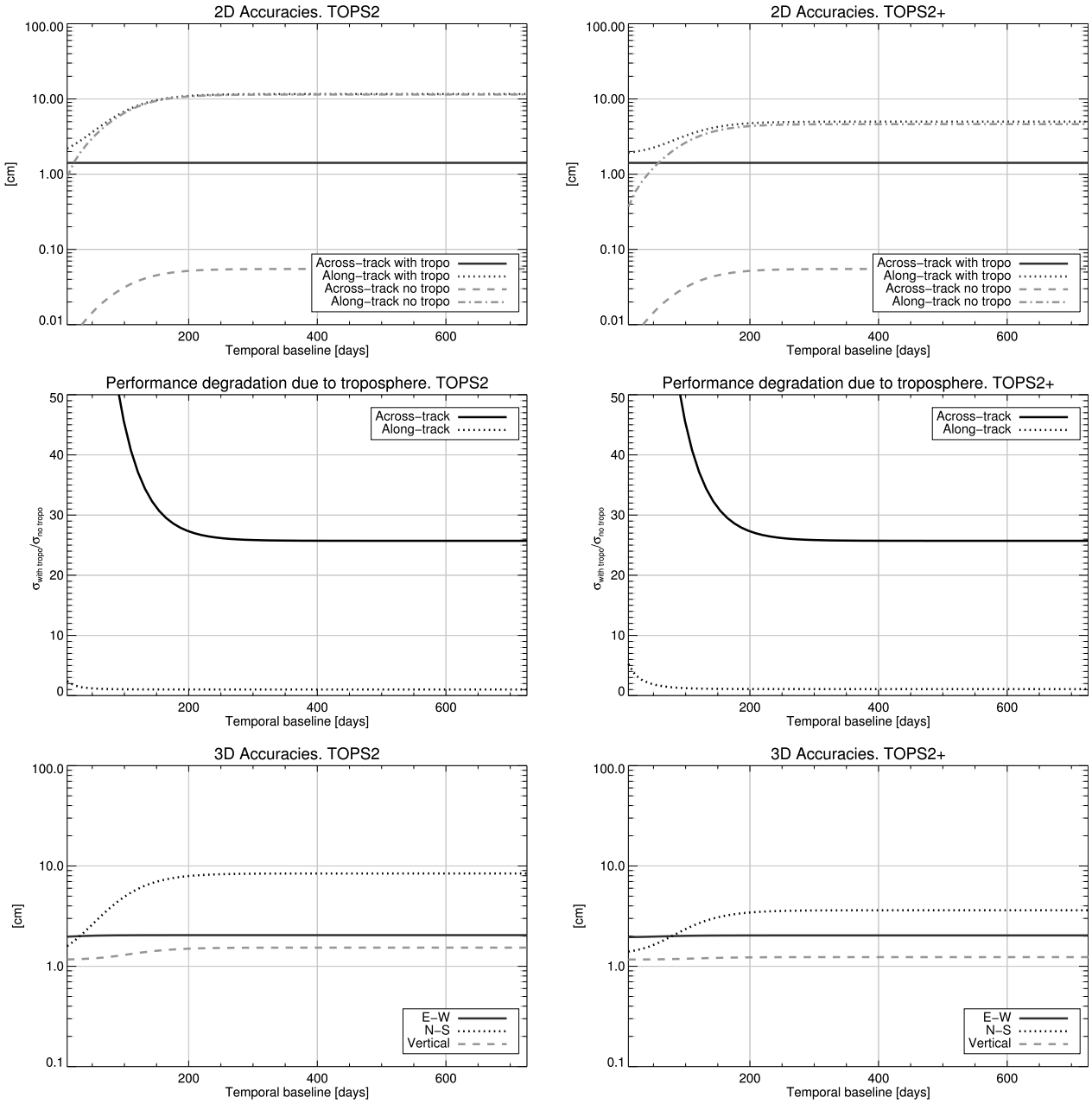

Fig. 12. (Top) Standard deviation of the shift measurement that can be retrieved in the LOS and in the azimuth direction with an interferometric pair as a function of the temporal baseline, with and without considering the turbulent troposphere. (Middle) Quotient of the accuracies in the retrieval of the shifts considering the troposphere and without its consideration. The effect of the troposphere is negligible in the along-track direction (quotient = 1), except for very high coherences (small temporal baseline) where the tropospheric noise dominates. The output product resolution has been set to 100 m × 100 m, resulting in an equivalent number of looks of 998. (Bottom) Expected 3-D performance when combining two interferometric pairs with ascending and descending geometries with the look angles of 30° and the orbit heading angles of 12° and 168°. (Left column) TOPS2. (Right column) TOPS2+.

tropospheric noise prevails slightly more over temporal decorrelation effects. Note that the final performance of TOPS2+ is better than TOPS2. For instance, TOPS2 achieves a standard deviation in the mean along-track velocity of 4 mm/month for a stack length of 30 images, whereas this can be achieved with just 13 images with TOPS2+. Fig. 13 (bottom) shows the 3-D performance when combining ascending and descending stacks. Look angles of 30° have been assumed for both geometries with orbit heading angles of 12° and 168°, respectively. As for the case of using pairs, TOPS2+ presents an evident improvement for the N-S direction, as well as in the vertical direction. The sensitivity is, in general, better for the E-W and vertical directions; however, for small stacks, the performances are closer for all three directions.

D. Consideration of Ionospheric Effects

The interferometric compensation of ionospheric disturbances for burst-mode acquisitions has been tackled in [31], where a modification of the (range) split-spectrum method is

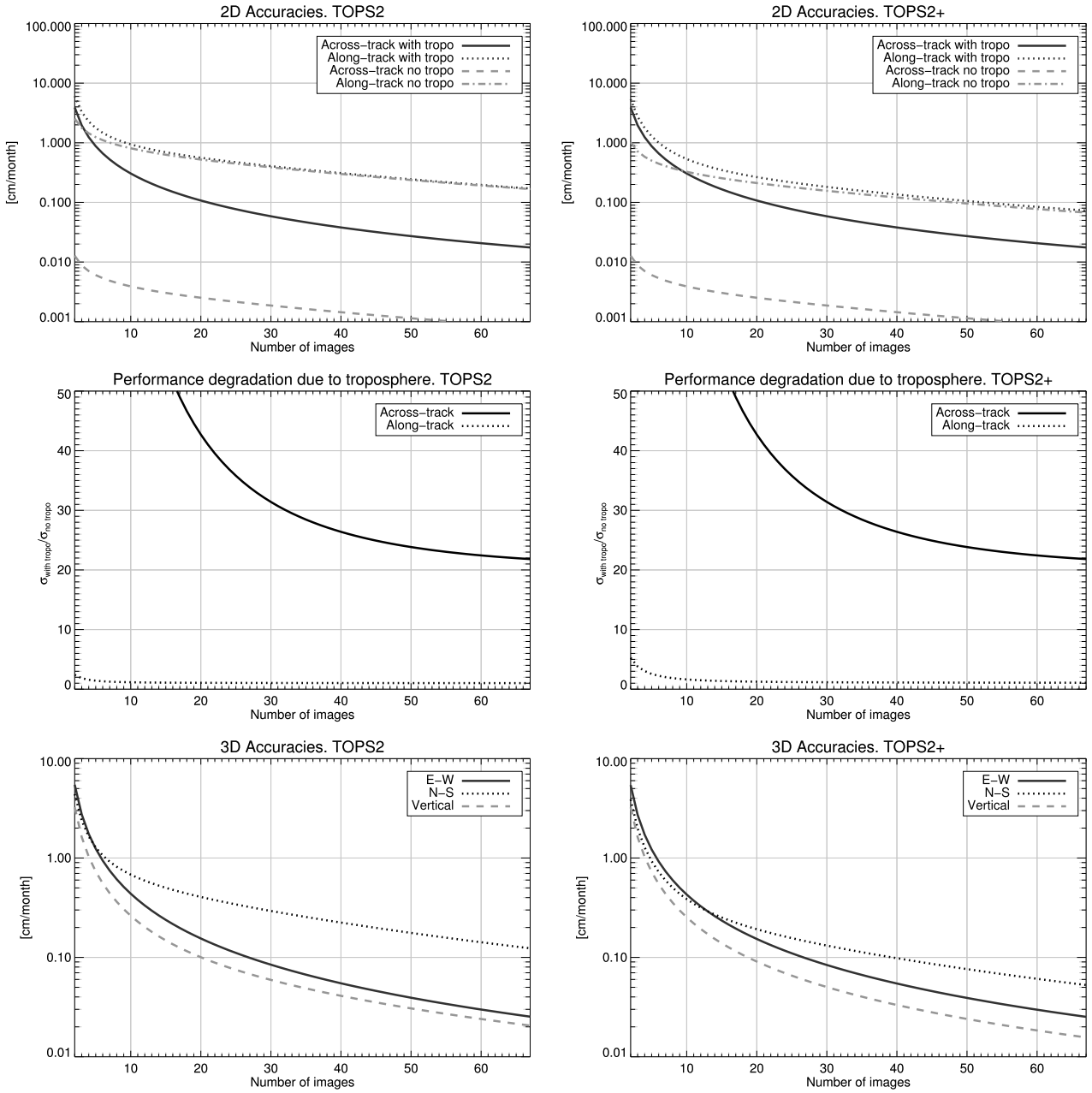

Fig. 13. (Top) Standard deviation of the shift measurement that can be retrieved in the LOS and in the azimuth direction with a stack of images as a function of the number of acquisitions with and without the consideration of the turbulent troposphere, assuming that an image is acquired every 11 days. (Middle) Degradation of the accuracies due to the troposphere. The tropospheric noise in the along-track direction is negligible (quotient = 1), except for very short stacks, where tropospheric effects dominate over temporal decorrelation. TOPS2 achieves a standard deviation in the mean along-track velocity of 4 mm/month for a stack length of 30 images, whereas this can be achieved with just 13 images with TOPS2+. (Bottom) 3-D performance when combining ascending and descending stacks. Look angles of 30° have been assumed for both geometries with the orbit heading angles of 12° and 168°, respectively. (Left column) TOPS2. (Right column) TOPS2+.

proposed and applied to ScanSAR and TOPS data. For TOPS systems, gaps of the ionospheric phase screen appear in the azimuth direction due to the burst-mode acquisition nature and the high altitude of the ionosphere. In contrast, 2-look systems enable to reduce noticeably and even remove the gaps, which allows to carry out a better smoothing of the phase screen, especially relevant if high-frequency variations are present.

The estimation noise of the split-spectrum technique imposes limitations to the achievable spatial resolution, allowing only to retrieve large-scale ionospheric variations. A powerful technique that enables the estimation of the gradient of the ionospheric differential delay along azimuth consists in calculating the mutual azimuth shifts between the interferometric images, as suggested in [32]. Since the 2-look TOPS modes provide an enhanced sensitivity to the azimuth shift, small-scale variations along azimuth can be retrieved. Therefore, joint estimations from split-spectrum and azimuth shifts are possible, without any limitation (in terms

of data gaps or degraded sensitivity), as, e.g., applied in [33] to StripMap acquisitions.

V. Methodology

In the following, the methodology for the interferometric processing and exploitation of 2-look data is provided. Section V-A focuses on the interferometric processing of pairs of images, combination of looks, and retrieval of azimuth shifts, whereas Section V-B provides the procedure to retrieve mean velocities with stacks.

A. InSAR Pairs

The interferometric processing algorithms for TOPS data can be found, for instance, in [17], [34], and [35], where a coregistration strategy based on a geometric approach followed by ESD applied at the bursts overlap areas can correct for constant azimuth misregistration due to orbital or timing errors. Additional processing aspects, as the necessity to perform deramping and reramping operations for the spectral shift filter and resampling operations, have been outlined. Fig. 14 shows the processing block diagram at burst level, where a geometrical coregistration is done using precise orbital information and an external DEM following the procedure described in [36]. Spectral shift filtering can be applied optionally afterward, especially important if large perpendicular baselines are expected.

The exploitation of both looks consists, in the first place, in calculating the map of local azimuth shifts by generating the differential interferogram between the interferograms of both looks (Int. look1 and Int. look2). The phase of the differential interferogram, ϕ_{ESD}, can, therefore, be written as

$$\phi_{\mathrm{ESD}} = \arg\left\{(m_i \cdot s_i^*) \cdot (m_{i+1} \cdot s_{i+1}^*)^*\right\} \tag{29}$$

where m_{i} and s_{i} refer to the i^{th} master and slave complex bursts, respectively, and $m_{\mathrm{i+1}}$ and $s_{\mathrm{i+1}}$ refer to the $(i+1)^{\mathrm{th}}$ master and slave bursts. Given a desired output product resolution, spatial multilooking can be applied to the InSAR phases/ESD phase. A small multilooking of the interferograms prior to the calculation of the differential interferogram (so-called early multilooking) increases the estimation efficiency [37].

As mentioned before, the differential phase between both looks is affected by wrapping effects. Thus, an unwrapping of the differential phase becomes, in general, mandatory, when working with pairs. The azimuth shifts' map, $\Delta t(r, x)$, can be retrieved according to

$$\Delta t(r, x) = \frac{\Gamma(\phi_{\mathrm{ESD}}(r, x))}{2\pi\, \Delta f_d(r)} \tag{30}$$

where $\Gamma(\cdot)$ is the phase unwrapping operator.

For the generation of the 2-look interferogram, we take advantage of the local azimuth shifts retrieved from the ESD phase. Its use makes possible the decoupling of the deformation in the across-track and along-track directions, as analyzed in Section IV-B. The removal of the phase due to azimuth displacement, ϕ_{AT}, consists in converting the ESD phase into azimuth shifts according to (30) and resampling again the slave bursts. If the azimuth shifts are small compared to the azimuth resolution, as a rule of thumb below $1/10^{\mathrm{th}}$ to avoid degrading the interferometric coherence [38], the phase due to the azimuth displacements can be directly subtracted from the interferograms of each look. This phase can be calculated as

$$\phi_{\mathrm{AT}}(r, x) = \frac{f_d(r, x)}{\Delta f_d(r)} \Gamma\left(\phi_{\mathrm{ESD}}(r, x)\right). \tag{31}$$

The result is two interferograms, Int. look1 (XT) and Int. look2 (XT), whose phases are sensitive to the across-track direction. The interferograms of each look can now be coherently averaged in order to obtain the 2-look (across-track) interferogram. An additional multilooking could be applied at this stage according to the desired product resolution.

The suggested approach for the decoupling relies on a correct phase unwrapping of the ESD phase. The ESD phase is neither affected by residual topography nor turbulent troposphere, and it suffers just from temporal decorrelation, which is, however, important for large temporal baselines and/or over vegetated areas.

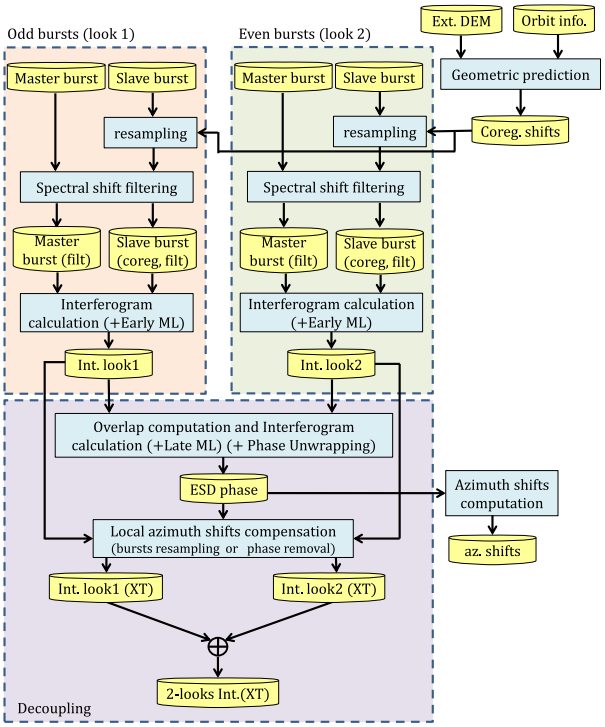

Fig. 14. Burst-level interferometric processing combining both looks. The slave bursts of both looks are, in first instance, coregistered employing precise orbital information and an external DEM. Resampling and spectral shift filtering are performed considering the signal spectral properties, i.e., deramping and reramping operations are necessary (not shown in diagram). Afterward, the interferograms corresponding to each look are generated. The contribution to the phase of these interferograms is due to the projection of the ground displacement onto the LOS of each look. The ESD phase can be computed by calculating the overlapping area between looks and forming the differential interferogram, applying the late multilooking; the ESD phase has to be unwrapped if shifts larger than the ambiguity band are expected. In order to obtain the 2-look interferogram, the ESD phase is used to decouple the displacement in the across- and along-track directions in order to obtain an interferogram which is sensitive to the displacement in the across-track direction (XT). The latter interferograms are averaged to obtain the 2-look across-track interferogram.

In case the decoupling is not performed, the effective LOS of the 2-look interferogram, resulting from the combination of the original interferograms of each look (Int. look1,2), presents a (time-varying) squint, $\beta_{2-\text{look}}(t)$, given by

$$\beta_{2-\text{look}}(t) = -\arcsin\left(\frac{\lambda}{4v_s}(f_d^{\text{look1}}(t) + f_d^{\text{look2}}(t))\right) \quad (32)$$

where $f_d^{\text{look1}}(t)$ and $f_d^{\text{look2}}(t)$ are the Doppler centroid frequencies of the first and second looks, respectively.

B. Time Series

Time-Series analysis of image stacks allows the retrieval of the temporal evolution of the deformation, where its mean velocity is usually obtained as a first step of the processing. In the case of 2-look systems, two equivalent approaches are possible in order to retrieve the along- and across-track deformation velocities, as expounded in the following.

From a geometrical point of view, we could retrieve the mean azimuth velocity by performing conventional independent time-series processings of each look, obtaining the mean velocities in the LOSs of each of them. The mean azimuth velocity, $\widehat{v_a}$, can be obtained by making the difference between the mean velocity for each look, $v_{\text{look1,2}}$, and scaling the result according to

$$\widehat{v_a} \approx \frac{2 \cdot v_g}{\lambda \cdot \Delta f_d} \cdot (v_{\text{look1}} - v_{\text{look2}}). \quad (33)$$

Since the estimation of the mean deformation velocity is performed independently for each look, the processing will have to cope with the presence of a higher noise due to the turbulent troposphere.

A second option consists in retrieving the azimuth mean velocity employing directly the ESD phases. The ESD phases can be computed from each pair of (looks) interferograms formed between a common selected master acquisition and the remaining slave images or jointly by calculating the ESD phases among all possible combination of acquisitions and using the phase linking algorithm [39]. The latter option provides a better estimation since the complete covariance matrix is exploited.

Provided that we have a stack of geometrically coregistered acquisitions to a common master image, we can compute the ESD phases between each slave image and master. The mean azimuth velocity can be retrieved for each multilooked pixel by exploiting the following periodogram:

$$\widehat{v_a} = \arg\max_{v_a}\left[\Re\left\{\sum_i e^{j\left(\phi_{\text{ESD}}[i] - 2\pi\,\Delta f_d v_a T[i] v_g[i]\right)}\right\}\right] \quad (34)$$

where $\arg\max_{v_a}\{\cdot\}$ stands for the argument of the maximum (mean azimuth velocity, v_a, for which the function attains its largest value). $\phi_{\text{ESD}}[i]$ is the temporal array of ESD phases of each (master–slave) interferogram, i, for each multilooked pixel and $T[i]$ are the temporal baselines of each interferogram. Note that the dependence of Δf_d and v_g with range has been omitted for simplicity.

Working with the ESD phases directly instead of with each look independently has a major advantage, namely, the phases are autocalibrated, i.e., systematic effects, such as residual topography, and most of the baseline errors and tropospheric noise cancel out, being not necessary to establish a reference point to align the ESD interferograms. In scenarios with low subsidence rates, it can also be assumed that the phases due to ground motion are also smaller than the ambiguity band. Therefore, (34) can be applied directly to each sample independently without having to exploit arcs between points as usually done when processing time series [40].

VI. Demonstration With TerraSAR-X: Experimental Results

Experimental TOPS2 acquisitions have been performed over different sites to demonstrate the applicability of the mode for the retrieval of large azimuth displacements employing pairs of images, and of mean deformation velocities by exploiting time series. The first example, with pairs of images, corresponds to the retrieval of the azimuth shifts on the Petermann glacier, located in northwest Greenland, with a main orientation to the N-S direction.

The second example, employing time series, corresponds to the monitoring of postseismic ground deformation after the 2013 Balochistan earthquake in Pakistan, covering the Hoshab fault.

A. Petermann Glacier

With its 80-km long and 16-km width, the Petermann glacier is the largest floating glacier in the Northern Hemisphere. It connects the Greenland ice sheet to the Arctic Ocean. Its study is of great interest among the glaciological community to determine how fast ice is being discharged to the seas. The Petermann glacier represents moreover a challenging scenario for our demonstration due to the heterogeneous motion gradient present [41]. A pair of TerraSAR-X TOPS2 images have been acquired on October 16, 2015 and October 27, 2015. The data takes are composed of four subswaths and 122 bursts (with a length of approximately 10 km each). The range coverage is 100 km, with a total scene length of 500 km, being the azimuth resolution 40 m. Fig. 15 shows an overview of the obtained results. From the reflectivity, it can be seen that the ice flows from left to right, where the ice tongue can be distinguished. After a coregistration has been performed, the coherence and InSAR phase can be obtained. It can be appreciated that due to the high glacier velocity, the coherence is low on the ice tongue. Our focus is outside these areas, since even if there were enough coherence, there is no justification to apply interferometry due to very high fringe frequency. For such areas, amplitude-based techniques, e.g., cross correlation, immune to wrapping effects are more adequate. The parts of the glacier with a slower displacement rate present an acceptable coherence and moderate velocities. A Greenland DEM obtained from the Ice Mapping Project (GIMP) [42] has been employed to subtract topographic fringes. On the left part of the InSAR phase, phase discontinuities due to glacier displacement can be observed. The aim is to remove the phase discontinuities by applying an accurate local azimuth coregistration by exploiting both looks, as expounded in

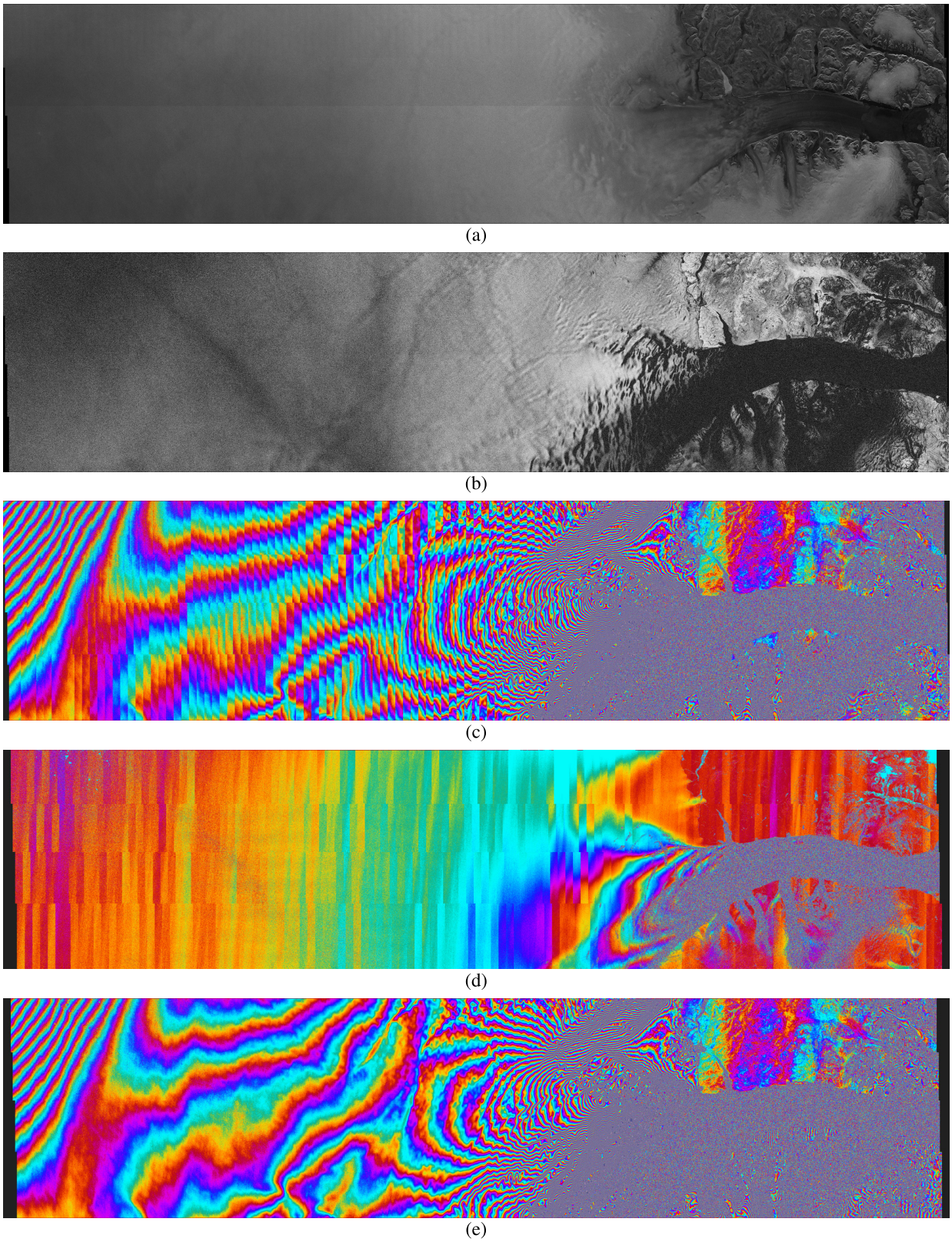

Fig. 15. Interferometric TOPS2 results over Petermann site corresponding to the pair October 16, 2015 to October 27, 2015. The acquisition covers an area of 100 km × 500 km and employs four subswaths with an azimuth resolution of 40 m. (a) Reflectivity, (b) coherence, (c) interferometric phase after removing the topography, (d) ESD phase proportional to the along-track motion, and (e) interferometric phase obtained after removing the along-track component of the motion by exploiting the two looks. The GIMP DEM has been used to remove the topography contribution from the phase. The phases are scaled between ±180°. Range is vertical and azimuth is horizontal.

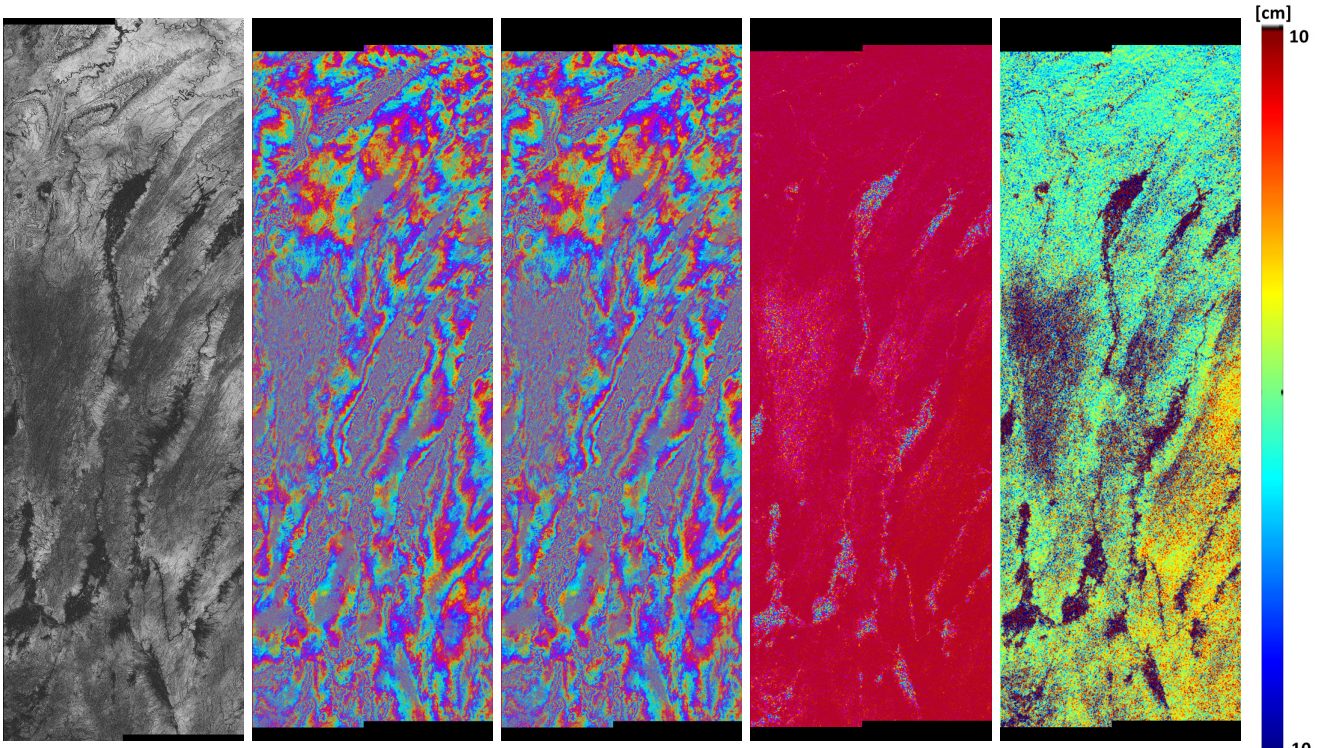

Fig. 16. Interferometric TOPS2 results over Balochistan site corresponding to the pair August 7, 2016 to May 20, 2017 (approximately 9.5 months), acquired in descending geometry. The acquisitions cover an area of 85 km × 265 km and employ two subswaths with an azimuth resolution of 17 m. (a) Interferometric coherence. Phase of (b) look 1 and (c) look 2 after topographic phase removal. (d) ESD phase. (e) Along-track shift map. The phases are scaled between ±180°. Range is horizontal and azimuth is vertical.

TABLE IV
MEAN DOPPLER FREQUENCY DIFFERENCES BETWEEN LOOKS AND THE CORRESPONDING ESD AMBIGUITY BAND. TOPS2 ACQUISITION WITH FOUR SUBSWATHS OVER PETERMANN GLACIER, GREENLAND

	SS1	SS2	SS3	SS4
$\langle \Delta f_{\mathrm{d}}^{\mathrm{ovl}} \rangle$ [Hz]	3182	3127	3039	2979
Ambiguity band [m]	± 1.11	± 1.13	± 1.16	± 1.18

TABLE V
MEAN DOPPLER FREQUENCY DIFFERENCES AT THE OVERLAP AREA AND CORRESPONDING ESD AMBIGUITY BANDS. TOPS2 ACQUISITION WITH TWO WIDE SUBSWATHS OVER PAKISTAN

	SS1	SS2
$\langle \Delta f_{\mathrm{d}}^{\mathrm{ovl}} \rangle$ [Hz]	3334	3218
Ambiguity band [m]	± 1.06	± 1.10

Section V-A. The combination of the InSAR phases from both looks allows the computation of the ESD phase. Table IV shows the spectral separation between looks and the ambiguity bands for each subswath, which is around 1 m. Since larger movements in the azimuth direction are expected, the ESD phase has to be unwrapped. We would expect to obtain a smoother ESD phase; however, phase discontinuities are to be found at the burst interfaces indicating that there are ionospheric perturbations due to the high solar activity occurred in 2015, strong enough to be sensed at the X-band. An estimation of the ionospheric contribution employing, e.g., split bandwidth techniques [31] in order to separate displacement from ionospheric disturbances is out of the scope of our evaluation.

Once the azimuth shifts have been estimated, they are removed from the interferograms of each look by using (31) in order to retrieve the across-track deformation for each look. The phase of the average of both interferograms is shown in Fig. 15(e), which is free of phase discontinuities.

B. Postseismic Deformation After the 2013 M_w7.7 Balochistan Earthquake

In late September 2013, two main Earthquakes took place in Balochistan, southwest of Pakistan. The main shock had a magnitude of 7.7, while an M_w6.8 aftershock occurred some days after. The coseismic events have been analyzed using ground surface deformation measured from subpixel correlation of Landsat-8 images, combined with backprojection and finite-source modeling of teleseismic waves [43]. Radar imagery was additionally used in [44]. The tectonics of southern and central Pakistan reflect a complex plate boundary, where the India plate slides northward relative to the Eurasia plate in the east, and the Arabia plate subducts northward beneath the Eurasia plate in the Makran. These motions

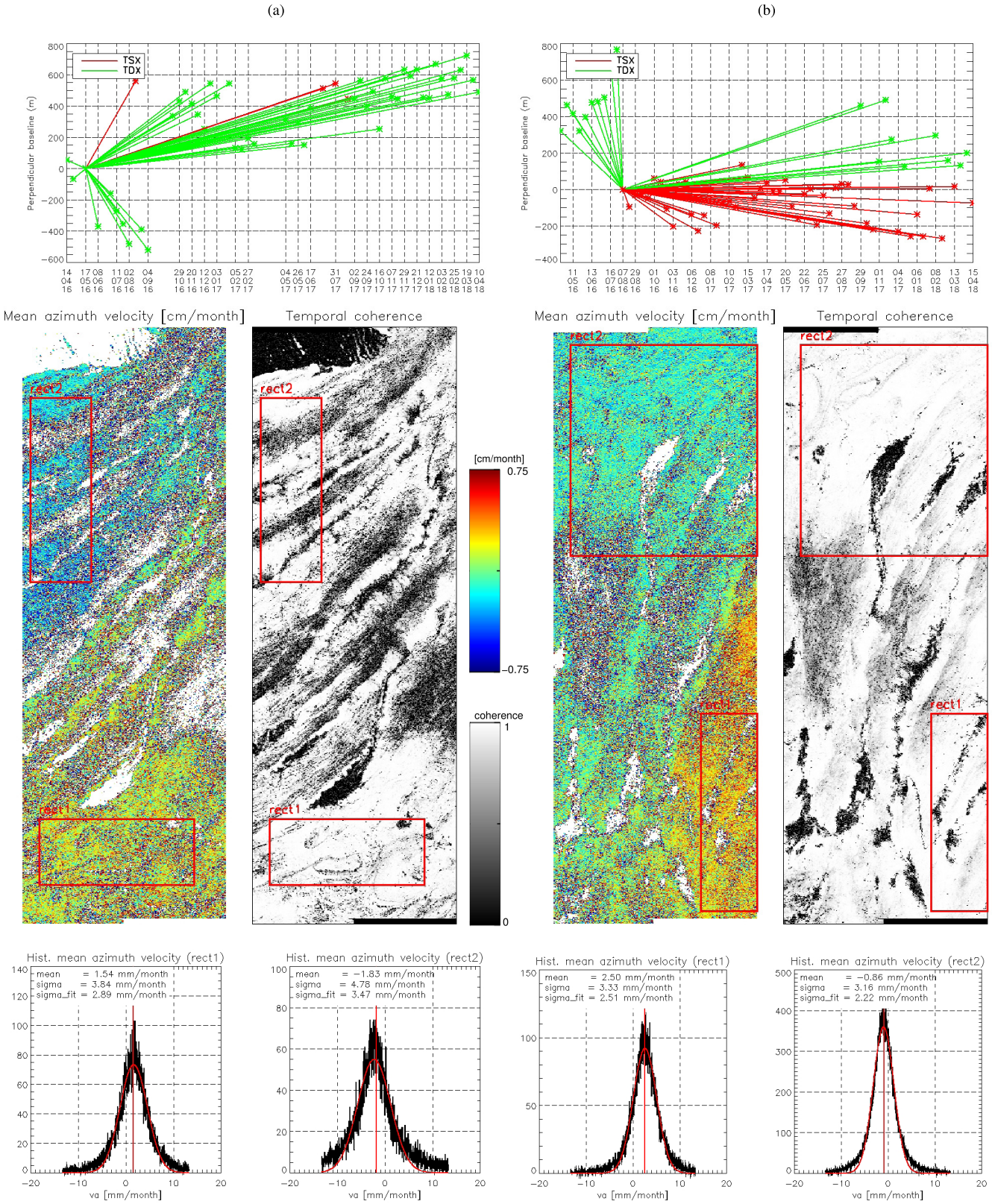

Fig. 17. Time-series TOPS2 results over Balochistan site corresponding to the time frame April 2016 to April 2018. (a) Ascending geometry with a total of 53 images. (b) Descending geometry having a total of 67 images. (Top) Distribution of the perpendicular and temporal baselines for both geometries. (Middle) Retrieved mean azimuth velocity map and the temporal coherence, indicating the areas covered by two rectangles for statistics analysis. Range is horizontal and azimuth is vertical. (Bottom) Histograms of the mean velocity, where a Gaussian fitting (red line) has been performed. The average mean velocity and the standard deviation are provided, as well as the standard deviation result from the Gaussian fit.

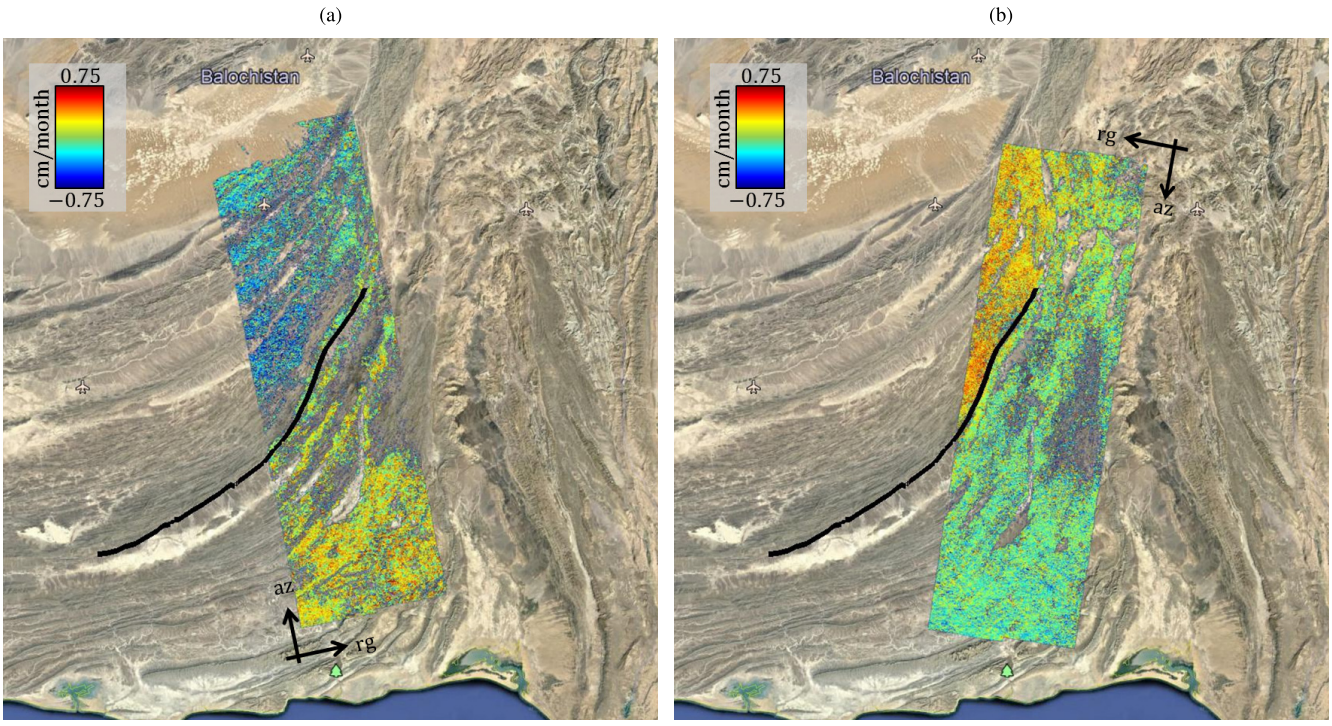

Fig. 18. Result on the estimation of the mean azimuth velocities over Balochistan employing time series for (a) ascending and (b) descending geometries. Black line: surface rupture line (Hoshab fault) derived from Landsat pixel offset tracking applied to coseismic images of the 2013 M_w7.7 earthquake. For both geometries, the postseismic azimuth deformation map presents two areas with clear different behaviors at both sides of this line indicating that the postseismic deformation follows a similar pattern to the coseismic one.

typically result in N-S to northeast–southwest strike-slip motion. After the 2013 shocks, postseismic deformation close to the 2013 Epicenter location is expected, with displacements in N-S to northeast–southwest.

Two stacks of experimental TerraSAR-X TOPS2 acquisitions, in ascending and descending geometries, have been acquired from April 2016 to April 2018. The acquisitions have two subswaths and cover an extension of 85 km × 265 km with 17-m azimuth resolution. Table V details the spectral separation between looks and the ambiguity bands for each subswath. We have analyzed two years of acquisitions in descending geometry with a total of 67 images. In ascending geometry, a total of 53 images were successfully acquired in the same time interval. Fig. 17 (top) shows the distribution of the perpendicular and temporal baselines for both, where note that acquisitions with the TerraSAR-X and TanDEM-X satellites have been made. The master image has been selected following the criterion of minimizing the perpendicular baseline in order to minimize the (range) spectral decorrelation.

Fig. 16 shows interferometric results for the pairs acquired on August 7, 2016 and May 20, 2017, in descending geometry, with a temporal baseline of about 9.5 months. Southern Pakistan is arid and has very little vegetation; therefore, interferograms remained coherent through the observation period. The coherence and the phases of both looks after topographic phase removal are shown, where strong turbulent tropospheric perturbations can be appreciated. The differential phase between looks is almost not affected by the turbulent troposphere. The along-track deformation allows clearly to identify two areas displacing in opposite directions, which confirms postseismic activity.

The mean azimuth velocity can be estimated applying the periodogram operator, introduced in (34), to the multilooked ESD phases of the stack. We define an output resolution for the mean azimuth velocity of 100 m × 100 m, which results roughly in an equivalent number of looks of 1000, similarly as the number of looks assumed in the computation of the performances in Section IV.

Fig. 17 (middle) shows the estimated mean azimuth velocity and temporal coherence for the ascending and descending geometries. Two rectangles over homogeneous areas have been selected to compute the histograms and the mean and the standard deviation of the estimated mean deformation velocity. Fig. 17 (bottom) shows the resulting histograms and Gaussian fitting for each rectangle. Points with a temporal coherence greater than 0.5 have been considered. In the ascending geometry, we obtain standard deviations of about 2.9 to 3.5 mm/month, whereas the expected standard deviation for 53 images is approximately 2.2 mm/month according to the TOPS2 curves of Fig. 12. For the descending geometry, the obtained standard deviation is below 2.5 mm/month, whereas 1.7 mm/month is expected in case of having 67 images, according to the theoretical curves. The differences between expected and measured standard deviations are very likely due to a mismatch of the decorrelation model used for the calculation of the expected performance, as well as due to the inherent assumptions of the HCRB not occurring in a real scenario.

Fig. 18 shows the geocoded maps of the estimated mean azimuth velocities for the descending and ascending geometries. The black line (Hoshab fault) indicates the Surface rupture line derived from Landsat pixel offset tracking applied to coseismic images of the 2013 M_w7.7 Earthquake. For both geometries, the postseismic azimuth deformation map presents two areas with clear different behaviors at both sides of this line, indicating that the postseismic deformation follows a similar pattern to the coseismic one. The same conclusion has been reported from Sentinel-1 time-series analyses in the LOS direction [45], which states that the surface displacements are dominated by horizontal motion of a similar sense to the 2013 earthquake.

The area on the north side of the rupture line is moving toward south–west, a fact which is clearly visible on both geometries, since the motion is quite well aligned with the along-track geometry. On the other hand, the projection of the motion in the southern area is greater for the ascending acquisition.

It is interesting to note that the maximum along-track deformation velocity is about 2.5 mm/month, which, for the largest temporal baseline in the current data set, corresponds to an ESD phase of just 20°. Thanks to the long-term coherence and the exploitation of the time series, it is possible to perform a reliable estimation of the deformation.

VII. Conclusion

Burst-mode acquisitions have been traditionally employed to map large areas by mapping different range subswaths. There have been multiple radar missions which have operated in ScanSAR mode, such as, e.g., RADARSAT-1, ENVISAT-ASAR, and ALOS-PALSAR, or are currently operating, e.g., RADARSAT-2, ALOS-2-PALSAR, COSMO-SkyMed, and TerraSAR-X. The design of the modes has been done employing multiple looks due to SNR reasons (except TerraSAR-X ScanSAR, which is a 1-look system). In this way, the dependence of the azimuth target position could be moderately mitigated. The TOPS mode solved the scalloping and associated effects, making the use of multiple looks not necessary. However, if we compare modes recording bursts of echoes with full-aperture modes (StripMap), the sensitivity to the along-track direction is degraded due to its lower azimuth resolution.

In this contribution, we have proposed the 2-look TOPS concept with the main motivation of overcoming this limitation. The 2-look TOPS mode achieves the same coverage as a single-look TOPS mode at the expense of a degradation of the azimuth resolution by a factor of two, maintaining, however, the number of looks for a given output resolution product. Two different design principles have been presented, the first one, TOPS2, follows a design based on resolution and achieves very similar azimuth sensitivity to StripMap. The second one, TOPS2+, consists in an optimization of the 2-look TOPS mode, which achieves an enhanced azimuth sensitivity. The design is based on selecting larger antenna beam steering angles and is mainly limited by azimuth ambiguities. A quantitative analysis of the ambiguities impact has been provided, including a criterion to select optimal acquisition PRFs. The range ambiguities have been, as well, considered in order to choose the optimal PRF in terms of total ambiguities. For the sake of example, a maximum steering angle of 1.1 ° has been chosen taking TerraSAR-X system parameters, which delivers a gain in the estimation of the azimuth motion of 11 dB (relative variance) with respect to the StripMap mode. The ASR is approximately −21 dB on average (over all subswaths). In case this ratio is not acceptable, either the maximum steering can be relaxed or the processed Doppler bandwidth reduced. We have obtained a gain of about 1 dB when reducing the processed bandwidth by 30%.

The looks can be combined at the interferometric processing stage, reducing this way the residual scalloping. In the case of TOPS2, the resulting residual scalloping is 0.07 dB, whereas for TOPS2+, it amounts 0.4 dB (similar to TOPS, i.e., 0.36 dB). An additional benefit is that ionospheric perturbations can be estimated with continuous coverage (in contrast to TOPS).

The 2-D expected performances in the deformation estimation employing acquisition pairs or time series have been presented, as well as 3-D performances combining ascending and descending geometries. Assuming the TerraSAR-X system and an exponential decorrelation model with a time constant of 40 days, a long-term coherence of 0.1, and a power of the turbulent troposphere of 1 cm^2, we would need 30 TOPS2 images to obtain an accuracy in the mean azimuth velocity of about 4 mm/month. In case of using TOPS2+, the number of images is reduced to 13 for the same accuracy. The same conclusions for the N-S direction can be drawn, when combining acquisitions in ascending and descending geometries.

The methodologies to derive the azimuth displacement have been described and applied to two different scenarios, using real data from TerraSAR-X, with fast deformation (glacier flow) and slow deformation (postseismic ground displacement). In the first case, we have shown the high potential of the exploitation of 2-look modes to perform a local coregistration, removing in that case phase discontinuities due to azimuth displacement. The second case demonstrates the retrieval of a postseismic signal in the along-track direction employing time series, with a two-year stack, delivering accuracies in the mean along-track velocity of a few mm/month.

We would like to stress that the 2-look concept employing burst modes is not only restricted to TOPS operation but can also be employed with ScanSAR. In this case, a design based on the azimuth sensitivity, as done for TOPS2+, is not possible, since the maximum Doppler span is linked solely to the antenna beamwidth. However, in spite of achieving a lower sensitivity than its equivalent TOPS mode, spectral diversity techniques can also be applied.

This contribution has demonstrated the benefits and high potential of the 2-look TOPS concept, especially for geophysical applications, where high azimuth resolution is not required.

Acknowledgments

The authors would like to thank C. González, from DLR, for providing the routines for the calculation of the range ambiguities. They would like to thank K. Hudnut,

from Caltech and Eric Fielding, Jet Propulsion Laboratory, for providing the surface rupture line of the 2013 coseismic event and for discussions regarding the Balochistan site. They would also like to thank the anonymous reviewers for their constructive comments and suggestions, which improved the readability of this paper. The employed TerraSAR-X images have been provided by DLR under proposal MTH0484.

REFERENCES

[1] T. J. Wright, B. E. Parsons, and Z. Lu, "Toward mapping surface deformation in three dimensions using InSAR," *Geophys. Res. Lett.*, vol. 31, 2004, Art. no. L01607. doi: 10.1029/2003GL018827.

[2] R. Michel, J.-P. Avouac, and J. Taboury, "Measuring ground displacements from SAR amplitude images: Application to the landers earthquake," *Geophys. Res. Lett.*, vol. 26, no. 7, pp. 875–878, 1999.

[3] T. Strozzi, A. Luckman, T. Murray, U. Wegmuller, and C. L. Werner, "Glacier motion estimation using SAR offset-tracking procedures," *IEEE Trans. Geosci. Remote Sens.*, vol. 40, no. 11, pp. 2384–2391, Nov. 2002.

[4] K. Tomiyasu, "Conceptual performance of a satellite borne, wide swath synthetic aperture radar," *IEEE Trans. Geosci. Remote Sens.*, vols. GE–19, no. 2, pp. 108–116, Apr. 1981.

[5] F. De Zan and A. M. Guarnieri, "TOPSAR: Terrain observation by progressive scans," *IEEE Trans. Geosci. Remote Sens.*, vol. 44, no. 9, pp. 2352–2360, Sep. 2006.

[6] R. Bamler and M. Eineder, "Accuracy of differential shift estimation by correlation and split-bandwidth interferometry for wideband and delta-k SAR systems," *IEEE Geosci. Remote Sens. Lett.*, vol. 2, no. 2, pp. 151–155, Apr. 2005.

[7] M. Suess, B. Grafmueller, and R. Zahn, "A novel high resolution, wide swath SAR system," in *Proc. Scanning Present Resolving Future, IEEE Int. Geosci. Remote Sens. Symp. (IGARSS)*, vol. 3, Jul. 2001, pp. 1013–1015.

[8] M. Younis, C. Fischer, and W. Wiesbeck, "Digital beamforming in SAR systems," *IEEE Trans. Geosci. Remote Sens.*, vol. 41, no. 7, pp. 1735–1739, Jul. 2003.

[9] G. Krieger, N. Gebert, and A. Moreira, "Unambiguous SAR signal reconstruction from nonuniform displaced phase center sampling," *IEEE Geosci. Remote Sens. Lett.*, vol. 1, no. 4, pp. 260–264, Oct. 2004.

[10] N. Gebert, G. Krieger, and A. Moreira, "Digital beamforming on receive: Techniques and optimization strategies for high-resolution wide-swath SAR imaging," *IEEE Trans. Aerosp. Electron. Syst.*, vol. 45, no. 2, pp. 564–592, Apr. 2009.

[11] M. Villano, G. Krieger, and A. Moreira, "Staggered SAR: High-resolution wide-swath imaging by continuous PRI variation," *IEEE Trans. Geosci. Remote Sens.*, vol. 52, no. 7, pp. 4462–4479, Jul. 2014.

[12] R. Scheiber and A. Moreira, "Coregistration of interferometric SAR images using spectral diversity," *IEEE Trans. Geosci. Remote Sens.*, vol. 38, no. 5, pp. 2179–2191, Sep. 2000.

[13] N. B. D. Bechor and H. A. Zebker, "Measuring two-dimensional movements using a single InSAR pair," *Geophys. Res. Lett.*, vol. 33, 2006, Art. no. L16311. doi: 10.1029/2006GL026883.

[14] P. Prats-Iraola *et al.*, "Repeat-pass interferometric experiments with the tandem-X constellation for accurate along-track motion estimation," in *Proc. IEEE Int. Geosci. Remote Sens. Symp. (IGARSS)*, Jul. 2015, pp. 4077–4080.

[15] P. Prats-Iraola, N. Yague-Martinez, S. Wollstadt, T. Kraus, and R. Scheiber, "Demonstration of the applicability of 2-look burst modes in non-stationary scenarios with TerraSAR-X," in *Proc. 11th Eur. Conf. Synth. Aperture Radar*, Jun. 2016, pp. 1–6.

[16] S. J. Frasier and A. J. Camps, "Dual-beam interferometry for ocean surface current vector mapping," *IEEE Trans. Geosci. Remote Sens.*, vol. 39, no. 2, pp. 401–414, Feb. 2001.

[17] P. Prats-Iraola, R. Scheiber, L. Marotti, S. Wollstadt, and A. Reigber, "TOPS interferometry with TerraSAR-X," *IEEE Trans. Geosci. Remote Sens.*, vol. 50, no. 8, pp. 3179–3188, Aug. 2012.

[18] F. De Zan, P. Prats-Iraola, R. Scheiber, and A. Rucci, "Interferometry with TOPS: Coregistration and azimuth shifts," in *Proc. 10th Eur. Conf. Synth. Aperture Radar*, Jun. 2014, pp. 1–4.

[19] R. Bamler and M. Eineder, "ScanSAR processing using standard high precision SAR algorithms," *IEEE Trans. Geosci. Remote Sens.*, vol. 34, no. 1, pp. 212–218, Jan. 1996.

[20] U. Steinbrecher, T. Kraus, G. C. Alfonzo, C. Grigorov, D. Schulze, and B. Braeutigam, "TerraSAR-X: Design of the new operational wideScanSAR mode," in *Proc. 10th Eur. Conf. Synth. Aperture Radar*, Jun. 2014, pp. 1–4.

[21] A. Meta, J. Mittermayer, P. Prats, R. Scheiber, and U. Steinbrecher, "TOPS imaging with TerraSAR-X: Mode design and performance analysis," *IEEE Trans. Geosci. Remote Sens.*, vol. 48, no. 2, pp. 759–769, Feb. 2010.

[22] J. Mittermayer, S. Wollstadt, P. Prats-Iraola, P. Lopez-Dekker, G. Krieger, and A. Moreira, "Bidirectional SAR imaging mode," *IEEE Trans. Geosci. Remote Sens.*, vol. 51, no. 1, pp. 601–614, Jan. 2013.

[23] J. Curlander and R. Mcdonough, *Synthetic Aperture Radar: Systems and Signal Processing*. Hoboken, NJ, USA: Wiley, 1991.

[24] F. Ulaby and C. Dobson, *Handbook of Radar Scattering Statistics for Terrain*. Norwood, MA, USA: Artech House, 1989.

[25] J. O. Hagberg, L. M. H. Ulander, and J. Askne, "Repeat-pass SAR interferometry over forested terrain," *IEEE Trans. Geosci. Remote Sens.*, vol. 33, no. 2, pp. 331–340, Mar. 1995.

[26] H. A. Zebker and J. Villasenor, "Decorrelation in interferometric radar echoes," *IEEE Trans. Geosci. Remote Sens.*, vol. 30, no. 5, pp. 950–959, Sep. 1992.

[27] R. F. Hanssen, *Radar Interferometry: Data Interpretation and Error Analysis*. Delft, The Netherlands: Delft Univ. Technology, 2001.

[28] P. Prats-Iraola, P. Lopez-Dekker, F. De Zan, N. Yagüe-Martínez, M. Zonno, and M. Rodriguez-Cassola, "Performance of 3-D surface deformation estimation for simultaneous squinted SAR acquisitions," *IEEE Trans. Geosci. Remote Sens.*, vol. 56, no. 4, pp. 2147–2158, Apr. 2018.

[29] A. M. Guarnieri and S. Tebaldini, "Hybrid CramÉr-Rao bounds for crustal displacement field estimators in SAR interferometry," *IEEE Signal Process. Lett.*, vol. 14, no. 12, pp. 1012–1015, Dec. 2007.

[30] F. Rocca, "Modeling interferogram stacks," *IEEE Trans. Geosci. Remote Sens.*, vol. 45, no. 10, pp. 3289–3299, Oct. 2007.

[31] G. Gomba, F. R. González, and F. De Zan, "Ionospheric phase screen compensation for the Sentinel-1 tops and ALOS-2 scanSAR modes," *IEEE Trans. Geosci. Remote Sens.*, vol. 55, no. 1, pp. 223–235, Jan. 2017.

[32] F. Meyer, R. Bamler, N. Jakowski, and T. Fritz, "The potential of low-frequency SAR systems for mapping ionospheric TEC distributions," *IEEE Geosci. Remote Sens. Lett.*, vol. 3, no. 4, pp. 560–564, Oct. 2006.

[33] G. Gomba and F. De Zan, "Bayesian data combination for the estimation of ionospheric effects in SAR interferograms," *IEEE Trans. Geosci. Remote Sens.*, vol. 55, no. 11, pp. 6582–6593, Nov. 2017.

[34] N. Yagüe-Martínez *et al.*, "Interferometric processing of Sentinel-1 TOPS data," *IEEE Trans. Geosci. Remote Sens.*, vol. 54, no. 4, pp. 2220–2234, Apr. 2016.

[35] S. Mancon, A. M. Guarnieri, D. Giudici, and S. Tebaldini, "On the phase calibration by multisquint analysis in TOPSAR and stripmap interferometry," *IEEE Trans. Geosci. Remote Sens.*, vol. 55, no. 1, pp. 134–147, Jan. 2017.

[36] E. Sansosti, P. Berardino, M. Manunta, F. Serafino, and G. Fornaro, "Geometrical SAR image registration," *IEEE Trans. Geosci. Remote Sens.*, vol. 44, no. 10, pp. 2861–2870, Oct. 2006.

[37] F. De Zan, P. Prats-Iraola, and M. Rodriguez-Cassola, "On the dependence of Delta-k efficiency on multilooking," *IEEE Geosci. Remote Sens. Lett.*, vol. 12, no. 8, pp. 1745–1749, Aug. 2015.

[38] D. Just and R. Bamler, "Phase statistics of interferograms with applications to synthetic aperture radar," *Appl. Opt.*, vol. 33, no. 20, pp. 4361–4368, Jul. 1994.

[39] A. M. Guarnieri and S. Tebaldini, "On the exploitation of target statistics for SAR interferometry applications," *IEEE Trans. Geosci. Remote Sens.*, vol. 46, no. 11, pp. 3436–3443, Nov. 2008.

[40] O. Mora, J. J. Mallorqui, and A. Broquetas, "Linear and nonlinear terrain deformation maps from a reduced set of interferometric SAR images," *IEEE Trans. Geosci. Remote Sens.*, vol. 41, no. 10, pp. 2243–2253, Oct. 2003.

[41] T. Nagler, H. Rott, M. Hetzenecker, J. Wuite, and P. Potin, "The Sentinel-1 mission: New opportunities for ice sheet observations," *Remote Sens.*, vol. 7, no. 7, pp. 9371–9389, 2015. [Online]. Available: http://www.mdpi.com/2072-4292/7/7/9371

[42] I. M. Howat, A. Negrete, and B. E. Smith, "The Greenland Ice Mapping Project (GIMP) land classification and surface elevation data sets," *Cryosphere*, vol. 8, no. 4, pp. 1509–1518, Aug. 2014, doi: 10.5194/tc-8-1509-2014.

[43] J.-P. Avouac *et al.*, "The 2013, Mw 7.7 Balochistan earthquake, energetic strike-slip reactivation of a thrust fault," *Earth Planet. Sci. Lett.*, vol. 391, pp. 128–134, Apr. 2014.
[44] R. Jolivet *et al.*, "The 2013 M_w 7.7 Balochistan earthquake: Seismic potential of an accretionary wedge," *Bull. Seismol. Soc. Amer.*, vol. 104, no. 2, pp. 1020–1030, 2014.
[45] K. E. Peterson, W. D. Barnhart, and S. Li, "Viscous accretionary prisms: Viscoelastic relaxation of the Makran accretionary prism following the 2013 Baluchistan, Pakistan earthquake," *J. Geophys. Res. Solid Earth*, vol. 123, no. 11, pp. 10-107–10-123, Oct. 2018. doi: 10.1029/2018JB016057.

Nestor Yague-Martinez received the Ingeniero degree in telecommunication engineering from the Universitat Politècnica de València (UPV), Valencia, Spain, in 2004.

From 2006 to 2015, he was with the Chair for Remote Sensing Technology, Technische Universität München (TUM), Munich, Germany, and also with the Remote Sensing Technology Institute, German Aerospace Center (DLR), Oberpfaffenhofen, Germany, where he was involved in the development of the operational interferometric processor of the TanDEM-X mission. He was with Starlab Barcelona S.L., Barcelona, Spain, from 2011 to 2012, where he was involved in along-track interferometry for ocean surface currents retrieval. In 2015, he joined the Multimodal Algorithms Group, Microwaves and Radar Institute, DLR. His research interests include SAR and InSAR processing and the development of advanced interferometric acquisition modes for the measurement of tectonic and volcanic deformation.

Pau Prats-Iraola (S'03–M'06–SM'13) was born in Madrid, Spain, in 1977. He received the Ingeniero and Ph.D. degrees in telecommunications engineering from the Universitat Politècnica de Catalunya (UPC), Barcelona, Spain, in 2001 and 2006, respectively.

In 2001, he was a Research Assistant with the Institute of Geomatics, Barcelona. In 2002, he was with the Department of Signal Theory and Communications, UPC, where he was involved in airborne repeat-pass interferometry and airborne differential SAR interferometry. From 2002 to 2006, he was an Assistant Professor with the Department of Telecommunications and Systems Engineering, Universitat Autònoma de Barcelona, Barcelona. In 2006, he joined the Microwaves and Radar Institute, German Aerospace Center (DLR), Wessling, Germany, where he has been the Head of the Multimodal Algorithms Group since 2009. His research interests include high-resolution airborne/spaceborne monostatic/bistatic SAR processing, SAR interferometry, advanced interferometric acquisition modes, persistent scatterer interferometry (PSI), SAR tomography, and end-to-end SAR simulation. He has coauthored more than 50 peer-reviewed journal papers in these fields.

Steffen Wollstadt received the Dipl.Ing. (M.Sc.) degree in electrical engineering from the Technical University of Darmstadt, Darmstadt, Germany, in 2005. His M.Sc. thesis was on metamaterial-based microstrip antenna design.

In 2006, he joined the Microwaves and Radar Institute, German Aerospace Center (DLR), Oberpfaffenhofen, Germany. Until 2008, he was with the Satellite Synthetic Aperture Radar (SAR) Systems Department, as a Project Engineer in the System Engineering and Calibration part of the TerraSAR-X ground segment, where he was involved in the TerraSAR-X and TanDEM-X instrument command generation. Since 2009, he has been with the SAR Missions Research Group, Radar Concepts Department, where he has been involved in TOPS Sentinel-1 image quality and SAR performance investigations and in various experiments with TerraSAR-X and TanDEM-X about novel imaging modes and SAR performance improvement. He is responsible for the commanding of experimental TOPS imaging mode acquisitions with TerraSAR-X. His research interests include spaceborne SAR mission and instrument analysis and interferometric problems, including along-track, repeat-pass, and differential interferometry.

Alberto Moreira (M'92–S'96–F'04) received the B.S.E.E. and M.S.E.E. degrees from the Aeronautical Technological Institute (ITA), São José dos Campos, Brazil, in 1984 and 1986, respectively, and the Eng.Dr. degree (Hons.) from the Technical University of Munich, Munich, Germany, in 1993.

From 1996 to 2001, he was the Chief Scientist and an Engineer with the SAR Technology Department, German Aerospace Center (DLR), Oberpfaffenhofen, Germany. Under his leadership, the DLR airborne SAR system has been upgraded to operate in innovative imaging modes, such as polarimetric SAR interferometry and SAR tomography. Since 2001, he is the Director of the Microwaves and Radar Institute, DLR, and a Full Professor in microwave remote sensing with the Karlsruhe Institute of Technology (KIT), Karlsruhe, Germany. His DLR's Institute contributes to several scientific programs and projects for spaceborne SAR missions, such as TerraSAR-X, TanDEM-X, SARLupe, and SARah, as well as Kompsat-6, PAZ, Sentinel-1, BIOMASS, and Tandem-L. The mission TanDEM-X, led by his institute, has generated a global, high-resolution digital elevation model of the earth with unprecedented accuracy. He is the Initiator and a Principal Investigator (PI) for this mission. He has authored or coauthored more than 400 publications in international conferences and journals and eight book chapters, and he holds 41 international patent grants in the radar and antenna field. His professional interests and research areas encompass spaceborne radar end-to-end system design, microwave techniques and system concepts, signal processing, and remote sensing applications.

Dr. Moreira has served as a President of the IEEE Geoscience and Remote Sensing (GRS) Society in 2010. He was a recipient of several international awards, including the IEEE AESS Nathanson Award in 1999 for the Young Radar Engineer of the Year, the IEEE Kiyo Tomiyasu Field Award in 2007, the IEEE W.R.G. Baker Award from the IEEE Board of Directors in 2012, and the IEEE GRSS Distinguished Achievement Award in 2014. He and his colleagues received the GRSS Transactions Prize Paper Awards in 1997, 2001, and 2007 and the GRSS Letters Prize Paper Award in 2015 and 2017. From 2012 to 2017, he has served as a Principal Investigator for the Helmholtz Alliance "Remote Sensing and Earth System Dynamics" and is currently the PI for Tandem-L, a radar mission proposal for the global observation of dynamic processes on earth's surface with unprecedented quality and resolution. He was the Founder and the Chair of the GRSS German Chapter from 2003 to 2008. He has been serving as the Chair for the Major Awards of the GRS Society since 2017. He served as an Associate Editor for the IEEE GEOSCIENCE AND REMOTE SENSING LETTERS from 2003 to 2007. He has been serving as an Associate Editor for the IEEE TRANSACTIONS ON GEOSCIENCE AND REMOTE SENSING since 2005.

Bibliography

Ansari, H., F. De Zan, A. Parizzi, M. Eineder, K. Goel, and N. Adam (2016). "Measuring 3-D Surface Motion With Future SAR Systems Based on Reflector Antennae". In: *IEEE Geoscience and Remote Sensing Letters* 13.2, pp. 272–276. ISSN: 1545-598X. DOI: 10.1109/LGRS.2015.2509440 (cit. on page 24).

Ansari, H., F. De Zan, and R. Bamler (2017). "Sequential Estimator: Toward Efficient InSAR Time Series Analysis". In: *IEEE Transactions on Geoscience and Remote Sensing* 55.10, pp. 5637–5652. ISSN: 0196-2892. DOI: 10.1109/TGRS.2017.2711037 (cit. on page 32).

Attema, E., M. Davidson, N. Floury, G. Levrini, B. Rosich-Tell, B. Rommen, and P. Snoeij (2007). *Sentinel-1 ESA's new European SAR mission*. DOI: 10.1117/12.747146 (cit. on page 16).

Avouac, J-P, F. Ayoub, S. Wei, J-P. Ampuero, L. Meng, S. Leprince, R. Jolivet, Z. Duputel, and D. Helmberger (2014). "The 2013, Mw 7.7 Balochistan earthquake, energetic strike-slip reactivation of a thrust fault". In: *Earth and Planetary Science Letters* (cit. on page 80).

Bamler, R. (2000). "Interferometric stereo radargrammetry: absolute height determination from ERS-ENVISAT interferograms". In: *2000 IEEE Geoscience and Remote Sensing Symposium*. Vol. 2, 742–745 vol.2. DOI: 10.1109/IGARSS.2000.861689 (cit. on page 41).

Bamler, R. and M. Eineder (1996). "ScanSAR processing using standard high precision SAR algorithms". In: *IEEE Transactions on Geoscience and Remote Sensing* 34.1, pp. 212–218. ISSN: 0196-2892. DOI: 10.1109/36.481905 (cit. on page 19).

— (2005). "Accuracy of differential shift estimation by correlation and split-bandwidth interferometry for wideband and delta-k SAR systems". In: *Geoscience and Remote Sensing Letters, IEEE* 2.2, pp. 151–155. ISSN: 1545-598X. DOI: 10.1109/LGRS.2004.843203 (cit. on pages 33, 41, 44, 70, 74).

Bamler, R. and P. Hartl (1998). "Synthetic Aperture Radar Interferometry". In: *Inverse Problems* 14 (cit. on pages 1, 30, 31).

Bara, M., R. Scheiber, A. Broquetas, and A. Moreira (2000). "Interferometric SAR signal analysis in the presence of squint". In: *IEEE Transactions on Geoscience and Remote Sensing* 38.5, pp. 2164–2178. ISSN: 0196-2892. DOI: 10.1109/36.868875 (cit. on page 57).

Barnhart, W.D., G.P. Hayes, R.W. Briggs, R.D. Gold, and R. Bilham (2014). "Ball-and-socket tectonic rotation during the 2013 Mw7.7 Balochistan earthquake". In: *Earth and Planetary Science Letters* 403, pp. 210 –216. ISSN: 0012-821X. DOI: https://doi.org/10.1016/j.epsl.2014.07.001 (cit. on page 80).

Bechor, B. D. and H. A. Zebker (2006). "Measuring two-dimensional movements using a single InSAR pair". In: *Geophys. Res. Lett.* 33, no. 16, (cit. on page 44).

Berardino, P., G. Fornaro, R. Lanari, and E. Sansosti (2002). "A new algorithm for surface deformation monitoring based on small baseline differential SAR interferograms". In: *IEEE Transactions on Geoscience and Remote Sensing* 40.11, pp. 2375–2383. ISSN: 0196-2892. DOI: 10.1109/TGRS.2002.803792 (cit. on pages 31, 55).

Breit, H., T. Fritz, U. Balss, M. Lachaise, A. Niedermeier, and M. Vonavka (2010). "TerraSAR-X SAR Processing and Products". In: *Geoscience and Remote Sensing, IEEE Transactions on* 48.2, pp. 727–740. ISSN: 0196-2892. DOI: 10.1109/TGRS.2009.2035497 (cit. on page 13).

Caputi, W. J. (1971). "Stretch: A Time-Transformation Technique". In: *IEEE Transactions on Aerospace and Electronic Systems* AES-7.2, pp. 269–278. ISSN: 0018-9251. DOI: 10.1109/TAES.1971.310366 (cit. on page 19).

Cardama, A., J. Romeu, J. M. Rius, Ll. Jofre, S. Blanch, and M. Ferrando (1998). *Antenas*. Edicions UPC. ISBN: 84-8301-250-2 (cit. on page 22).

Costantini, M. (1998). "A novel phase unwrapping method based on network programming". In: *IEEE Transactions on Geoscience and Remote Sensing* 36.3, pp. 813–821. ISSN: 0196-2892. DOI: 10.1109/36.673674 (cit. on page 27).

Cumming, I. and F. Wong (2005). *Digital Processing of Synthetic Aperture Radar: Algorithms and Implementation*. Artech House (cit. on page 6).

Curlander, JC. and RN. Mcdonough (1991). *Synthetic Aperture Radar: Systems and Signal Processing*. Wiley, New York (cit. on pages 9, 11–14).

Currie, A. and M. A. Brown (1992). "Wide-swath SAR". In: *IEE Proceedings F - Radar and Signal Processing* 139.2, pp. 122–135. ISSN: 0956-375X. DOI: 10.1049/ip-f-2.1992.0016 (cit. on page 14).

Davidson, G. W. and R. Bamler (1999). "Multiresolution phase unwrapping for SAR interferometry". In: *IEEE Transactions on Geoscience and Remote Sensing* 37.1, pp. 163–174. ISSN: 0196-2892. DOI: 10.1109/36.739150 (cit. on page 27).

Davies, Kenneth (1990). *Ionospheric radio*. 31. IET (cit. on page 77).

De Zan, F. (2011). "Coherent Shift Estimation for Stacks of SAR Images". In: *Geoscience and Remote Sensing Letters, IEEE* 8.6, pp. 1095–1099. ISSN: 1545-598X. DOI: 10.1109/LGRS.2011.2157079 (cit. on page 64).

— (2014). "Accuracy of Incoherent Speckle Tracking for Circular Gaussian Signals". In: *Geoscience and Remote Sensing Letters, IEEE* 11.1, pp. 264–267. ISSN: 1545-598X. DOI: 10.1109/LGRS.2013.2255259 (cit. on page 41).

De Zan, F. and A. Monti Guarnieri (2006). "TOPSAR: Terrain Observation by Progressive Scans". In: *Geoscience and Remote Sensing, IEEE Transactions on* 44.9, pp. 2352–2360. ISSN: 0196-2892. DOI: 10.1109/TGRS.2006.873853 (cit. on pages 19, 20, 55, 70, 72).

De Zan, F., P. Prats-Iraola, and M. Rodriguez-Cassola (2015). "On the Dependence of Delta-k Efficiency on Multilooking". In: *IEEE Geoscience and Remote Sensing Letters* 12.8, pp. 1745–1749. ISSN: 1545-598X. DOI: 10.1109/LGRS.2015.2424272 (cit. on page 44).

De Zan, Francesco and Giorgio Gomba (2018). "Vegetation and soil moisture inversion from SAR closure phases: First experiments and results". In: *Remote Sensing of Environment* 217, pp. 562 –572. ISSN: 0034-4257. DOI: https://doi.org/10.1016/j.rse.2018.08.034 (cit. on page 30).

Derauw, Dominique (1999). "DInSAR and Coherence Tracking Applied to Glaciology:The Example of Shirase Glacier". In: *Proc. FRINGE99, Liege, Belgium.* (Cit. on page 33).

Eineder, M., C. Minet, P. Steigenberger, Xiaoying Cong, and T. Fritz (2011). "Imaging Geodesy – Toward Centimeter-Level Ranging Accuracy With TerraSAR-X". In: *Geoscience and Remote Sensing, IEEE Transactions on* 49.2, pp. 661–671. ISSN: 0196-2892. DOI: 10.1109/TGRS.2010.2060264 (cit. on page 1).

Eineder, M., C. Minet, P. Steigenberger, X. Cong, and T. Fritz (2011). "Imaging Geodesy-Toward Centimeter-Level Ranging Accuracy With TerraSAR-X". In: *IEEE Transactions on Geoscience and Remote Sensing* 49.2, pp. 661–671. ISSN: 0196-2892. DOI: 10.1109/TGRS.2010.2060264 (cit. on page 52).

Elliott, J. R., R. J. Walters, and T. J. Wright (2016). "The role of space-based observation in understanding and responding to active tectonics and earthquakes". In: *Nature Communications* 7, 13844 EP –. DOI: https://doi.org/10.1038/ncomms13844 (cit. on pages 2, 55).

Engen, G. and Y. Larsen (2011). "Efficient Full Aperture Processing of TOPS Mode Data Using the Moving Band Chirp Z -Transform". In: *Geoscience and Remote Sensing, IEEE Transactions on* 49.10, pp. 3688–3693. ISSN: 0196-2892. DOI: 10.1109/TGRS.2011.2145384 (cit. on page 21).

ESA (2018). *Sentinel High Level Operations Plan (HLOP)*. Tech. rep. COPE-S1OP-EOPG-PL-15-0020. Issue 2, Revision 2. Copernicus Space Component Mission Management Team. URL: https://sentinel.esa.int/documents/247904/685154/Sentinel_High_Level_Operations_Plan (cit. on page 55).

Farr, Tom G. et al. (2007). "The Shuttle Radar Topography Mission". In: *Reviews of Geophysics* 45.2. DOI: 10.1029/2005RG000183 (cit. on pages 16, 25).

Fattahi, H., P. Agram, and M. Simons (2017). "A Network-Based Enhanced Spectral Diversity Approach for TOPS Time-Series Analysis". In: *IEEE Transactions on Geoscience and Remote Sensing* 55.2, pp. 777–786. ISSN: 0196-2892. DOI: 10.1109/TGRS.2016.2614925 (cit. on page 65).

Ferretti, A., C. Prati, and F. Rocca (2001). "Permanent scatterers in SAR interferometry". In: *IEEE Transactions on Geoscience and Remote Sensing* 39.1, pp. 8–20. ISSN: 0196-2892. DOI: 10.1109/36.898661 (cit. on pages 1, 29, 31, 55).

Ferretti, A., A. Fumagalli, F. Novali, C. Prati, F. Rocca, and A. Rucci (2011). "A New Algorithm for Processing Interferometric Data-Stacks: SqueeSAR". In: *IEEE Transactions on Geoscience and Remote Sensing* 49.9, pp. 3460–3470. ISSN: 0196-2892. DOI: 10.1109/TGRS.2011.2124465 (cit. on page 32).

Fornaro, G., E. Sansosti, R. Lanari, and M. Tesauro (2002). "Role of processing geometry in SAR raw data focusing". In: *IEEE Transactions on Aerospace and Electronic Systems* 38.2, pp. 441–454. ISSN: 0018-9251. DOI: 10.1109/TAES.2002.1008978 (cit. on page 57).

Fornaro, G., S. Verde, D. Reale, and A. Pauciullo (2015). "CAESAR: An Approach Based on Covariance Matrix Decomposition to Improve Multibaseline–Multitemporal Interferometric SAR Processing". In: *IEEE Transactions on Geoscience and Remote Sensing* 53.4, pp. 2050–2065. ISSN: 0196-2892. DOI: 10.1109/TGRS.2014.2352853 (cit. on page 32).

Frasier, S. J. and A. J. Camps (2001). "Dual-beam interferometry for ocean surface current vector mapping". In: *IEEE Transactions on Geoscience and Remote Sensing* 39.2, pp. 401–414. ISSN: 0196-2892. DOI: 10.1109/36.905248 (cit. on page 21).

Gabriel, Andrew K. and Richard M. Goldstein (1988). "Crossed orbit interferometry: theory and experimental results from SIR-B". In: *International Journal of Remote Sensing* 9.5, pp. 857–872. DOI: 10.1080/01431168808954901 (cit. on pages 25, 27).

Gabriel, Andrew K., Richard M. Goldstein, and Howard A. Zebker (1989). "Mapping small elevation changes over large areas: Differential radar interferometry". In: *Journal of Geophysical Research* 94, pp. 9183–9191. DOI: doi.org/10.1029/JB094iB07p09183 (cit. on pages 25, 29).

Gatelli, F., A. Monti Guamieri, F. Parizzi, P. Pasquali, C. Prati, and F. Rocca (1994). "The wavenumber shift in SAR interferometry". In: *Geoscience and Remote Sensing, IEEE Transactions on* 32.4, pp. 855–865. ISSN: 0196-2892. DOI: 10.1109/36.298013 (cit. on page 30).

Geudtner, D., N. Yague-Martinez, P. Prats, I. Navas-Traver, I. Barat, D. Small, A. Schubert, and A. Monti Guarnieri (2015). "Sentinel-1 InSAR Performance: Results from the Sentinel-1A In-Orbit Commissioning". In: *Proceedings of the ESA FRINGE Workshop, Frascati, Italy*. URL: http://seom.esa.int/fringe2015/les/presentation367.pdf (cit. on page 58).

Ghiglia, Dennis C. and Mark D. Pritt (1998). *Two-Dimensional Phase Unwrapping: Theory, Algorithms, and Software*. Wiley & Sons. ISBN: 978-0-471-24935-1 (cit. on page 27).
Goldstein, R. M. (1995). "Atmospheric limitations to repeat-pass interferometry". In: *Geophysical Research Letters* 22Sept, pp. 2517–2520 (cit. on page 29).
Goldstein, R. M. and H. A. Zebker (1987). "Interferometric radar measurement of ocean surface currents". In: *Nature* 328.6132, pp. 707–709 (cit. on page 25).
Goldstein, R. M., H. A. Zebker, and C. L. Werner (1988). "Satellite radar interferometry: Two-dimensional phase unwrapping". In: *Radio Science* 23.4, pp. 713–720. ISSN: 1944-799X. DOI: 10.1029/RS023i004p00713 (cit. on page 27).
Gomba, G. and F. De Zan (2017). "Bayesian Data Combination for the Estimation of Ionospheric Effects in SAR Interferograms". In: *IEEE Transactions on Geoscience and Remote Sensing* 55.11, pp. 6582–6593. ISSN: 0196-2892. DOI: 10.1109/TGRS.2017.2730438 (cit. on page 78).
Gomba, G., A. Parizzi, F. De Zan, M. Eineder, and R. Bamler (2016). "Toward Operational Compensation of Ionospheric Effects in SAR Interferograms: The Split-Spectrum Method". In: *IEEE Transactions on Geoscience and Remote Sensing* 54.3, pp. 1446–1461. ISSN: 0196-2892. DOI: 10.1109/TGRS.2015.2481079 (cit. on page 29).
Gomba, G., F. Rodríguez-González, and F. De Zan (2017). "Ionospheric Phase Screen Compensation for the Sentinel-1 TOPS and ALOS-2 ScanSAR Modes". In: *IEEE Transactions on Geoscience and Remote Sensing* 55.1, pp. 223–235. ISSN: 0196-2892. DOI: 10.1109/TGRS.2016.2604461 (cit. on pages 76, 78).
Goodman, Joseph W. (2007). *Speckle Phenomena in Optics: Theory and Applications*. Roberts and Company (cit. on page 7).
Gray, A. Laurence, Karim E. Mattar, and George Sofko (2000). "Influence of ionospheric electron density fluctuations on satellite radar interferometry". In: *Geophysical Research Letters* 27.10, pp. 1451–1454. DOI: 10.1029/2000GL000016 (cit. on page 29).
Hanssen, R. F. (2001). *Radar Interferometry: Data interpretation and error analysis*. Delft University of Technology. The Netherlands (cit. on pages 29, 30).
Heidbach, Oliver, Mojtaba Rajabi, Karsten Reiter, and Moritz Ziegler (2016). "World Stress Map 2016". In: *GFZ Data Services*. URL: http://doi.org/10.5880/WSM.2016.002 (cit. on page 2).
Heidbach, Oliver et al. (2018). "The World Stress Map database release 2016: Crustal stress pattern across scales". In: *Tectonophysics* 744, pp. 484 –498. ISSN: 0040-1951. DOI: 10.1016/j.tecto.2018.07.007 (cit. on page 2).
Holzner, J. and R. Bamler (2002). "Burst-mode and ScanSAR interferometry". In: *Geoscience and Remote Sensing, IEEE Transactions on* 40.9, pp. 1917–1934. ISSN: 0196-2892. DOI: 10.1109/TGRS.2002.803848 (cit. on page 56).
Hooper, A. and K. Spaans (2017). "Sentinel-1 Along-Track InSAR for Global Strain Rate Estimation". In: *Proc. FRINGE, June 2017*. URL: http://fringe.esa.int/files/presentation523.pdf (cit. on page 70).
Hooper, Andrew (2008). "A multi-temporal InSAR method incorporating both persistent scatterer and small baseline approaches". In: *Geophysical Research Letters* 35.16. DOI: 10.1029/2008GL034654 (cit. on page 31).
Hooper, Andrew, Howard Zebker, Paul Segall, and Bert Kampes (2004). "A new method for measuring deformation on volcanoes and other natural terrains using InSAR persistent scatterers". In: *Geophysical Research Letters* 31.23. DOI: 10.1029/2004GL021737 (cit. on pages 1, 31, 55).
Howat, I. M., A. Negrete, and B. E. Smith (2014). "The Greenland Ice Mapping Project (GIMP) land classification and surface elevation data sets". In: *The Cryosphere* 8.4, pp. 1509–1518. DOI: 10.5194/tc-8-1509-2014. URL: https://www.the-cryosphere.net/8/1509/2014/ (cit. on pages 78, 79).

Jolivet, R. et al. (2014). "The 2013 Mw 7.7 Balochistan earthquake : Seismic potential of an accretionary wedge". In: *Bulletin of the Seismological Society of America, Seismological Society of America.* (Cit. on page 80).

Jung, H., Z. Lu, A. Shepherd, and T. Wright (2015). "Simulation of the SuperSAR Multi-Azimuth Synthetic Aperture Radar Imaging System for Precise Measurement of Three-Dimensional Earth Surface Displacement". In: *IEEE Transactions on Geoscience and Remote Sensing* 53.11, pp. 6196–6206. ISSN: 0196-2892. DOI: 10.1109/TGRS.2015.2435776 (cit. on page 21).

Just, D. and R. Bamler (1994). "Phase statistics of interferograms with applications to synthetic aperture radar". In: *Appl. Opt., vol. 33, no. 20, pp. 4361–4368* (cit. on pages 27, 31).

Kim, J. S., A. Danklmayer, and K. Papathanassiou (2011). "Correction of ionospheric distortions in low frequency interferometric SAR data". In: *2011 IEEE International Geoscience and Remote Sensing Symposium*, pp. 1505–1508. DOI: 10.1109/IGARSS.2011.6049353 (cit. on page 29).

Krieger, G., N. Gebert, and A. Moreira (2004). "Unambiguous SAR signal reconstruction from nonuniform displaced phase center sampling". In: *IEEE Geoscience and Remote Sensing Letters* 1.4, pp. 260–264. ISSN: 1545-598X. DOI: 10.1109/LGRS.2004.832700 (cit. on pages 14, 25).

Krieger, G., M. Younis, N. Gebert, S. Huber, F. Bordoni, A. Patyuchenko, and A. Moreira (2009). "Advanced Digital Beamforming Concepts for High Performance Synthetic Aperture Radar (SAR) Imaging". In: *Advanced RF Sensors and Remote Sensing Instruments (ARSI)* (cit. on page 14).

Leberl, Franz (1990). *Radargrammetric image processing*. Artech House. ISBN: 0-89006-273-0 (cit. on page 33).

Li, Z., J. P. Muller, P. Cross, P. Albert, J. Fischer, and R. Bennartz (2006). "Assessment of the potential of MERIS near-infrared water vapour products to correct ASAR interferometric measurements". In: *International Journal of Remote Sensing* 27.2, pp. 349–365. DOI: 10.1080/01431160500307342 (cit. on page 29).

Lopez-Dekker, P., H. Rott, B. Chapron, and P. Prats (2018). "Stereo Thermo-Optically Enhanced Radar for Earth, Ocean, Ice, and land Dynamics (STEREOID)". In: *Earth Explorer 10 Mission Proposal. ESA Ref: CEE10/012*. DOI: 10.13140/RG.2.2.25804.46728 (cit. on page 24).

Love, Allan W. (1985). "In memory of Carl A. Wiley". In: *IEEE Antennas and Propagation Society Newsletter* (cit. on page 1).

Madsen, S. N. and H. A. Zebker (1992). "Automated Absolute Phase Retrieval in Across-Track Interferometry". In: *[Proceedings] IGARSS '92 International Geoscience and Remote Sensing Symposium*. Vol. 2, pp. 1582–1584. DOI: 10.1109/IGARSS.1992.578639 (cit. on page 43).

Madsen, S. N., H. A. Zebker, and J. Martin (1993). "Topographic mapping using radar interferometry: processing techniques". In: *IEEE Transactions on Geoscience and Remote Sensing* 31.1, pp. 246–256. ISSN: 0196-2892. DOI: 10.1109/36.210464 (cit. on pages 33, 43).

Massonnet, Didier, Marc Rossi, César Carmona, Frédéric Adragna, Gilles Peltzer, Kurt Feigl, and Thierry Rabaute (1993). "The displacement field of the Landers earthquake mapped by radar interferometry". In: *Nature* 364.6433, pp. 138–142. ISSN: 1476-4687. DOI: 10.1038/364138a0 (cit. on page 29).

Meyer, F., R. Bamler, N. Jakowski, and T. Fritz (2006). "The Potential of Low-Frequency SAR Systems for Mapping Ionospheric TEC Distributions". In: *IEEE Geoscience and Remote Sensing Letters* 3.4, pp. 560–564. ISSN: 1545-598X. DOI: 10.1109/LGRS.2006.882148 (cit. on page 78).

Michel, R., J. P. Avouac, and J. Taboury (1999). "Measuring ground displacements from SAR amplitude images: Application to the Landers earthquake". In: *Geophys. Res. Lett., 26(7), 875–878.* (Cit. on page 33).

Mittermayer, J., S. Wollstadt, P. Prats-Iraola, P. Lopez-Dekker, G. Krieger, and A. Moreira (2013). "Bidirectional SAR Imaging Mode". In: *IEEE Transactions on Geoscience and Remote Sensing* 51.1, pp. 601–614. ISSN: 0196-2892. DOI: 10.1109/TGRS.2012.2202669 (cit. on pages 22, 23).

Monti Guarnieri, A. and S. Tebaldini (2007). "Hybrid Cramér-Rao Bounds for Crustal Displacement Field Estimators in SAR Interferometry". In: *IEEE Signal Processing Letters* 14.12, pp. 1012–1015. ISSN: 1070-9908. DOI: 10.1109/LSP.2007.904705 (cit. on page 76).

— (2008). "On the Exploitation of Target Statistics for SAR Interferometry Applications". In: *IEEE Transactions on Geoscience and Remote Sensing* 46.11, pp. 3436–3443. ISSN: 0196-2892. DOI: 10.1109/TGRS.2008.2001756 (cit. on page 67).

Moore, R. K., J. P. Claassen, and Y. h. Lin (1981). "Scanning Spaceborne Synthetic Aperture Radar with Integrated Radiometer". In: *IEEE Transactions on Aerospace and Electronic Systems* AES-17.3, pp. 410–421. ISSN: 0018-9251. DOI: 10.1109/TAES.1981.309069 (cit. on page 16).

Moreira, A., J. Mittermayer, and R. Scheiber (1996). "Extended chirp scaling algorithm for air- and spaceborne SAR data processing in stripmap and ScanSAR imaging modes". In: *IEEE Transactions on Geoscience and Remote Sensing* 34.5, pp. 1123–1136. ISSN: 0196-2892. DOI: 10.1109/36.536528 (cit. on page 19).

Moreira, A., P. Prats-Iraola, M. Younis, G. Krieger, I. Hajnsek, and K. P. Papathanassiou (2013). "A tutorial on synthetic aperture radar". In: *IEEE Geoscience and Remote Sensing Magazine* 1.1, pp. 6–43. DOI: 10.1109/MGRS.2013.2248301 (cit. on page 1).

Morrison, K., J. C. Bennett, M. Nolan, and R. Menon (2011). "Laboratory Measurement of the DInSAR Response to Spatiotemporal Variations in Soil Moisture". In: *IEEE Transactions on Geoscience and Remote Sensing* 49.10, pp. 3815–3823. ISSN: 0196-2892. DOI: 10.1109/TGRS.2011.2132137 (cit. on page 30).

Oppenheim, Alan W. and Ronald W. Schafer (2007). *Discrete-Time Signal Processing*. Pearson (cit. on pages 34, 36).

Papoulis, Athanasios (1991). *Probability, Random Variables, and Stochastic Processes*. T. McGraw-Hill Series in Electrical Engineering. ISBN: 0-07-048477-5 (cit. on page 33).

Parizzi, Alessandro, Xiao Ying Cong, and Michael Eineder (2009). "First Results from Multifrequency Interferometry. A Comparison of Different Decorrelation Time Constants at L, C and X Band". In: *Proceedings Fringe* (cit. on page 61).

Prats, Pau, Rolf Scheiber, Josef Mittermayer, Adriano Meta, and Alberto Moreira (2010). "Processing of Sliding Spotlight and TOPS SAR Data Using Baseband Azimuth Scaling". In: 48.2, pp. 770–780 (cit. on page 21).

Prats-Iraola, P., R. Scheiber, L. Marotti, S. Wollstadt, and A. Reigber (2012). "TOPS Interferometry With TerraSAR-X". In: *Geoscience and Remote Sensing, IEEE Transactions on* 50.8, pp. 3179–3188. ISSN: 0196-2892. DOI: 10.1109/TGRS.2011.2178247 (cit. on pages 20, 57, 59, 72).

Prats-Iraola, P., M. Rodriguez-Cassola, F. De Zan, R. Scheiber, P. Lopez-Dekker, I. Barat, and D. Geudtner (2015). "Role of the Orbital Tube in Interferometric Spaceborne SAR Missions". In: *Geoscience and Remote Sensing Letters, IEEE* (cit. on page 58).

Prats-Iraola, P., N. Yague-Martinez, S. Wollstadt, T. Kraus, and R. Scheiber (2016). "Demonstration of the Applicability of 2-Look Burst Modes in Non-Stationary Scenarios with TerraSAR-X". In: *Proceedings of EUSAR 2016: 11th European Conference on Synthetic Aperture Radar*, pp. 1–6 (cit. on page 82).

Prats-Iraola, P., P. Lopez-Dekker, F. De Zan, N. Yagüe-Martínez, M. Zonno, and M. Rodriguez-Cassola (2017). "Performance of 3-D Surface Deformation Estimation for Simultaneous Squinted SAR Acquisitions". In: *IEEE Transactions on Geoscience and Remote Sensing* PP.99, pp. 1–12. ISSN: 0196-2892. DOI: 10.1109/TGRS.2017.2776140 (cit. on pages 24, 76).

Pritt, M. D. and J. S. Shipman (1994). "Least-squares two-dimensional phase unwrapping using FFT's". In: *IEEE Transactions on Geoscience and Remote Sensing* 32.3, pp. 706–708. ISSN: 0196-2892. DOI: 10.1109/36.297989 (cit. on page 27).

Proakis, John G. and Dimitris G. Manolakis (1996). *Digital Signal Processing. Principles, Algorithms, and Applications*. Prentice-Hall International (cit. on page 34).

Queiroz de Almeida, F., M. Younis, G. Krieger, and A. Moreira (2018). "Multichannel Staggered SAR Azimuth Processing". In: *IEEE Transactions on Geoscience and Remote Sensing* 56.5, pp. 2772–2788. ISSN: 0196-2892. DOI: 10.1109/TGRS.2017.2783444 (cit. on page 15).

Riaz, M. S., S. Bin, S. Naeem, W. Kai, Z. Xie, S. M. M. Gilani, and U. Ashraf (2019). "Over 100 years of faults interaction, stress accumulation, and creeping implications, on Chaman Fault System, Pakistan". In: *International Journal of Earth Sciences*. DOI: 10.1007/s00531-019-01710-0 (cit. on page 80).

Rocca, F. (2007). "Modeling Interferogram Stacks". In: *Geoscience and Remote Sensing, IEEE Transactions on* 45.10, pp. 3289–3299. ISSN: 0196-2892. DOI: 10.1109/TGRS.2007.902286 (cit. on pages 30, 31, 61).

Rocca, Fabio (2003). "3D motion recovery with multi-angle and/or left right interferometry". In: *Proceedings of the third International Workshop on ERS SAR* (cit. on page 70).

Rodriguez, E. and J.M. Martin (1992). "Theory and design of interferometric synthetic aperture radars". English. In: *IEE Proceedings F (Radar and Signal Processing)* 139 (2), 147–159(12). ISSN: 0956-375X (cit. on page 30).

Rosen, P. A., S. Hensley, I. R. Joughin, F. K. Li, S. N. Madsen, E. Rodriguez, and R. M. Goldstein (2000). "Synthetic aperture radar interferometry". In: *Proceedings of the IEEE* 88.3, pp. 333–382. ISSN: 0018-9219. DOI: 10.1109/5.838084 (cit. on pages 1, 30).

Rossi, Cristian, Fernando Rodriguez Gonzalez, Thomas Fritz, Nestor Yague-Martinez, and Michael Eineder (2012). "TanDEM-X calibrated Raw DEM generation". In: *ISPRS Journal of Photogrammetry and Remote Sensing* 73. Innovative Applications of SAR Interferometry from modern Satellite Sensors, pp. 12 –20. ISSN: 0924-2716. DOI: https://doi.org/10.1016/j.isprsjprs.2012.05.014 (cit. on page 33).

Sack, M., M. R. Ito, and I. G. Cumming (1985). "Application of efficient linear FM matched filtering algorithms to synthetic aperture radar processing". In: *IEE Proceedings F - Communications, Radar and Signal Processing* 132.1, pp. 45–57. ISSN: 0143-7070. DOI: 10.1049/ip-f-1.1985.0006 (cit. on page 19).

Sansosti, E., P. Berardino, M. Manunta, F. Serafino, and G. Fornaro (2006). "Geometrical SAR image registration". In: *Geoscience and Remote Sensing, IEEE Transactions on* 44.10, pp. 2861–2870. ISSN: 0196-2892. DOI: 10.1109/TGRS.2006.875787 (cit. on page 59).

Scheiber, R. and A. Moreira (2000). "Coregistration of interferometric SAR images using spectral diversity". In: *Geoscience and Remote Sensing, IEEE Transactions on* 38.5, pp. 2179–2191. ISSN: 0196-2892. DOI: 10.1109/36.868876 (cit. on pages 44, 59, 70).

Shepherd, A. and the SuperSAR Team (2010). "SuperSAR: A Mission to Detect Earth Surface Deformation in Three Dimensions from a Single Satellite Platform". In: *Geophysical Research Abstracts, Vol. 12, EGU2010-2764, 2010EGU General Assembly 2010* (cit. on page 21).

Steinbrecher, U., T. Kraus, G. Castellanos Alfonzo, C. Grigorov, D. Schulze, and B. Braeutigam (2014). "TerraSAR-X: Design of the new operational WideScanSAR mode". In: *EUSAR 2014; 10th European Conference on Synthetic Aperture Radar*, pp. 1–4 (cit. on page 74).

Strozzi, T., A. Luckman, T. Murray, U. Wegmuller, and C. L. Werner (2002). "Glacier motion estimation using SAR offset-tracking procedures". In: *IEEE Transactions on Geoscience and Remote Sensing* 40.11, pp. 2384–2391. ISSN: 0196-2892. DOI: 10.1109/TGRS.2002.805079 (cit. on page 33).

Sun, G., M. Xing, Y. Wang, Y. Wu, Y. Wu, and Z. Bao (2011). "Sliding Spotlight and TOPS SAR Data Processing Without Subaperture". In: *IEEE Geoscience and Remote Sensing Letters* 8.6, pp. 1036–1040. DOI: 10.1109/LGRS.2011.2151174 (cit. on page 21).

Tarayre, H. and D. Massonnet (1996). "Atmospheric Propagation heterogeneities revealed by ERS-1 interferometry". In: *Geophysical Research Letters* 23.9, pp. 989–992. DOI: 10.1029/96GL00622 (cit. on page 29).

Tomiyasu, K. (1981). "Conceptual Performance of a Satellite Borne, Wide Swath Synthetic Aperture Radar". In: *IEEE Transactions on Geoscience and Remote Sensing* GE-19.2, pp. 108–116. ISSN: 0196-2892. DOI: 10.1109/TGRS.1981.350361 (cit. on pages 16, 55).

Torres, Ramon et al. (2012). "GMES Sentinel-1 mission". In: *Remote Sensing of Environment* 120.0, pp. 9 –24. ISSN: 0034-4257. DOI: 10.1016/j.rse.2011.05.028 (cit. on pages 16, 55).

Touzi, R., A. Lopes, J. Bruniquel, and P. W. Vachon (1999). "Coherence estimation for SAR imagery". In: *IEEE Transactions on Geoscience and Remote Sensing* 37.1, pp. 135–149. ISSN: 0196-2892. DOI: 10.1109/36.739146 (cit. on page 31).

Ulaby, F. and C. Dobson (1989). *Handbook of Radar Scattering: Statistics for Terrain*. Norwood, MA, USA: Artech House (cit. on page 14).

Ulaby, Fawwaz, David Long, William Blackwell, Charles Elachi, Adrian Fung, Christopher Ruf, K. Sarabandi, Jakob Zyl, and Howard Zebker (2014). *Microwave Radar and Radiometric Remote Sensing*. ISBN: 978-0-472-11935-6 (cit. on page 1).

Villano, M., G. Krieger, and A. Moreira (2014). "Staggered SAR: High-Resolution Wide-Swath Imaging by Continuous PRI Variation". In: *IEEE Transactions on Geoscience and Remote Sensing* 52.7, pp. 4462–4479. ISSN: 0196-2892. DOI: 10.1109/TGRS.2013.2282192 (cit. on page 15).

Villano, M., G. Krieger, and A. Moreira (2018). "Nadir Echo Removal in Synthetic Aperture Radar via Waveform Diversity and Dual-Focus Postprocessing". In: *IEEE Geoscience and Remote Sensing Letters* 15.5, pp. 719–723. ISSN: 1545-598X. DOI: 10.1109/LGRS.2018.2808196 (cit. on page 15).

Villano, Michelangelo (2016). "Staggered Synthetic Aperture Radar". PhD thesis. Karlsruhe Institute of Technology (cit. on page 13).

Wadge, G. et al. (2002). "Atmospheric models, GPS and InSAR measurements of the tropospheric water vapour field over Mount Etna". In: *Geophysical Research Letters* 29.19, pp. 11–1–11–4. DOI: 10.1029/2002GL015159 (cit. on page 29).

Wei Xu and I. Cumming (1996). "A region growing algorithm for InSAR phase unwrapping". In: *IGARSS '96. 1996 International Geoscience and Remote Sensing Symposium*. Vol. 4, 2044–2046 vol.4. DOI: 10.1109/IGARSS.1996.516883 (cit. on page 27).

Wicks Jr., Charles W., Daniel Dzurisin, Steven Ingebritsen, Wayne Thatcher, Zhong Lu, and Justin Iverson (2002). "Magmatic activity beneath the quiescent Three Sisters volcanic center, central Oregon Cascade Range, USA". In: *Geophysical Research Letters* 29.7, pp. 26–1–26–4. DOI: 10.1029/2001GL014205 (cit. on page 29).

Wiley, Carl A. (1985). "Synthetic aperture radars: A paradigm for technology evolution". In: *IEEE Transactions on Aerospace and Electronic Systems* 21.3, pp. 440–443 (cit. on page 1).

Williams, Simon, Yehuda Bock, and Peng Fang (1998). "Integrated satellite interferometry: Tropospheric noise, GPS estimates and implications for interferometric synthetic aperture radar products". In: *Journal of Geophysical Research: Solid Earth* 103.B11, pp. 27051–27067. DOI: 10.1029/98JB02794 (cit. on page 29).

Wollstadt, S., P. Prats, M. Bachmann, J. Mittermayer, and R. Scheiber (2012). "Scalloping Correction in TOPS Imaging Mode SAR Data". In: *IEEE Geoscience and Remote Sensing*

Letters 9.4, pp. 614–618. ISSN: 1545-598X. DOI: 10.1109/LGRS.2011.2176716 (cit. on page 20).

Wright, T., M. Garthwaite, H.-S. Jung, and A. Shepherd (2011). "How accurately can current and future InSAR missions map tectonic strain?" In: *FRINGE* (cit. on page 21).

Wright, Tim J., Barry E. Parsons, and Zhong Lu (2004). "Toward mapping surface deformation in three dimensions using InSAR". In: *Geophysical Research Letters* 31.1. L01607, n/a–n/a. ISSN: 1944-8007. DOI: 10.1029/2003GL018827 (cit. on pages 2, 70).

Xu, Wei, Pingping Huang, Yunkai Deng, Jiantao Sun, and Xiuqin Shang (2011). "An Efficient Approach With Scaling Factors for TOPS-Mode SAR Data Focusing". In: *Geoscience and Remote Sensing Letters, IEEE* 8.5, pp. 929–933. ISSN: 1545-598X. DOI: 10.1109/LGRS.2011.2135837 (cit. on page 21).

Yague-Martinez, N., C. Rossi, M. Lachaise, F. Rodriguez-Gonzalez, T. Fritz, and H. Breit (2010). "Interferometric processing algorithms of TanDEM-X data". In: *Geoscience and Remote Sensing Symposium (IGARSS), 2010 IEEE International*, pp. 3518–3521. DOI: 10.1109/IGARSS.2010.5652406 (cit. on page 40).

Yague-Martinez, N., M. Eineder, R. Brcic, H. Breit, and T. Fritz (2010). "TanDEM-X Mission: SAR Image Coregistration Aspects". In: *8th European Conference on Synthetic Aperture Radar*, pp. 1–4 (cit. on page 38).

Yague-Martinez, N., M. Eineder, X. Y. Cong, and C. Minet (2012). "Ground Displacement Measurement by TerraSAR-X Image Correlation: The 2011 Tohoku-Oki Earthquake". In: *IEEE Geoscience and Remote Sensing Letters* 9.4, pp. 539–543. ISSN: 1545-598X. DOI: 10.1109/LGRS.2012.2196020 (cit. on pages 47, 85).

Yague-Martinez, N., P. Prats-Iraola, and F. De Zan (2016a). "Coregistration of Interferometric Stacks of Sentinel-1A TOPS Data". In: *Proceedings of EUSAR 2016: 11th European Conference on Synthetic Aperture Radar*, pp. 1–6 (cit. on page 65).

Yague-Martinez, N., P. Prats-Iraola, F. Rodriguez Gonzalez, R. Brcic, R. Shau, D. Geudtner, M. Eineder, and R. Bamler (2016b). "Interferometric Processing of Sentinel-1 TOPS Data". In: *IEEE Transactions on Geoscience and Remote Sensing* 54.4, pp. 2220–2234. ISSN: 0196-2892. DOI: 10.1109/TGRS.2015.2497902 (cit. on pages 55, 59, 66, 93).

Yague-Martinez, N., F. De Zan, and P. Prats-Iraola (2017). "Coregistration of Interferometric Stacks of Sentinel-1 TOPS Data". In: *IEEE Geoscience and Remote Sensing Letters* 14.7, pp. 1002–1006. ISSN: 1545-598X. DOI: 10.1109/LGRS.2017.2691398 (cit. on pages 61, 111).

Yague-Martinez, N., P. Prats-Iraola, M. Pinheiro, and M. Jaeger (2019a). "Exploitation of burst overlapping areas of TOPS data. Application to Sentinel-1". In: *2019 IEEE Geoscience and Remote Sensing Symposium* (cit. on page 70).

Yague-Martinez, N., P. Prats-Iraola, S. Wollstadt, and A. Moreira (2019b). "The 2-Look TOPS Mode: Design and Demonstration With TerraSAR-X". In: *IEEE Transactions on Geoscience and Remote Sensing* 57.10, pp. 7682–7703. ISSN: 0196-2892. DOI: 10.1109/TGRS.2019.2915797 (cit. on pages 69, 119).

Yoon, Y. T., M. Eineder, N. Yague-Martinez, and O. Montenbruck (2009). "TerraSAR-X Precise Trajectory Estimation and Quality Assessment". In: *IEEE Transactions on Geoscience and Remote Sensing* 47.6, pp. 1859–1868. ISSN: 0196-2892. DOI: 10.1109/TGRS.2008.2006983 (cit. on page 52).

Zebker, H. A. and R. M. Goldstein (1986). "Topographic Mapping from Interferometric Synthetic Aperture Radar Observations". In: *Journal of Geophysical Research-Solid Earth* 91.B5, pp. 4993–4999 (cit. on page 25).

Zebker, H. A. and J. Villasenor (1992). "Decorrelation in interferometric radar echoes". In: *IEEE Transactions on Geoscience and Remote Sensing* 30.5, pp. 950–959. ISSN: 0196-2892. DOI: 10.1109/36.175330 (cit. on pages 30, 31).